Fakultät für Physik der Technischen Universität München
Forschungs-Neutronenquelle Heinz Maier-Leibnitz (FRM II)
Physik Department E13

Development of a dry-chemical extraction process for ^{99}Mo and plasma-aided synthesis of transition metal hexafluorides

Dissertation

Tobias Chemnitz

June 2020

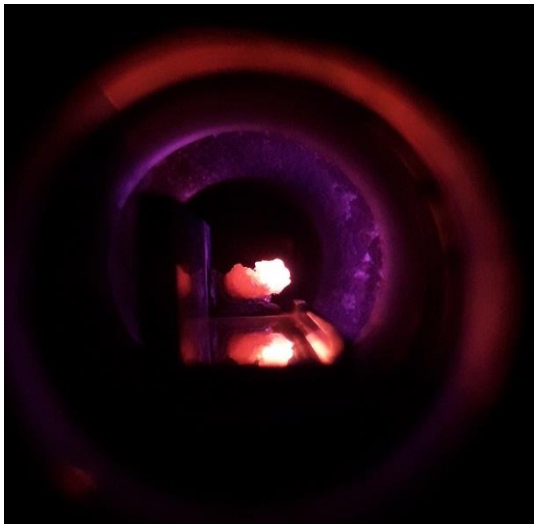

Prof. Dr. Winfried Petry

TECHNISCHE UNIVERSITÄT MÜNCHEN

Physik Department

Lehrstuhl für Funktionelle Materialien (E13)
Forschungs-Neutronenquelle Heinz Maier-Leibnitz

Development of a dry-chemical extraction process for ^{99}Mo and plasma-aided synthesis of transition metal hexafluorides

Tobias Chemnitz

Vollständiger Abdruck der von der Fakultät für Physik der Technischen Universität München zur Erlangung des akademischen Grades eines

Doktors der Naturwissenschaften (Dr. rer. nat.)

genehmigten Dissertation.

Vorsitzender: *apl. Prof. Dr. Norbert Kaiser*
Prüfer der Dissertation:
1. *Prof. Dr. Winfried Petry*
2. *Prof. Dr. Florian Kraus*

Die Dissertation wurde am 26.06.2020 bei der Technischen Universität München eingereicht und durch die Fakultät für Physik am 16.07.2020 angenommen.

"The most exciting phrase to hear in science, the one that heralds new discoveries, is not 'Eureka' but 'Hmmm … that's funny."

Isaac Asimov

Abstract

About 70 years ago, the first report about the use of artificially produced radioisotopes for the treatment of Graves' Disease in 1946 was published. Nuclear medicine has since become an integral part of modern medicine and like no other branch allows the evaluation of the functionality of targeted organs. One isotope thereby has played a substantial role almost from the very beginning: ^{99m}Tc. Being a pure γ-emitter with a short physical and biological half-life, it is perfectly suited for imaging purposes. For that reason, it has evolved to the most important medical radioisotope with over 30 million application per year worldwide. ^{99m}Tc emerges from a β^-−decay of its parent nuclide ^{99}Mo. This isotope also has a rather short half-life of 66 hours and can therefore not be stored, but must continuously be produced. The major production process is hereby the fission of ^{235}U in nine research reactors worldwide. After being irradiated for about six days, the targets are shipped to different processors that extract the ^{99}Mo from the targets in a wet-chemical process. In the course of international efforts to reduce the usage of highly enriched uranium (HEU), the HEU targets used for irradiation were replaced by LEU targets with a degree of enrichment lower than 20 %, thereby increasing the proliferation resistance. On the downside, the reduction of fissionable ^{235}U is accompanied by a significant increase in radioactive waste volume of up to 200 %.

In order to counter this increase in waste volume, a dry-chemical, fluorine-based process was investigated during the course of this thesis. During this process, the irradiated targets will be dissolved using fluorine radicals, thereby converting uranium and molybdenum into their corresponding hexafluorides UF_6 and MoF_6, respectively. For a proof of concept, instead of using irradiated targets, a surrogate material consisting only of uranium and molybdenum was utilized. In order to dissolve these targets, a fluorination line using a microwave plasma for fluorine radical production was designed, built and commissioned. The line allows for the comfortable and safe fluorination of the surrogate material by employing not elemental fluorine, but NF_3 instead. This gas is by far less reactive and toxic, thereby significantly reducing health hazards and corrosion problems. The hexafluorides for their part are collected and pre-separated based on their difference in vapor pressure. In a second step, a selective photochemical process utilizing supercritical CO as a fluorine scavenger converts UF_6 into solid UF_5, whereas MoF_6 stays unaltered, allowing for a convenient separation of the two substances.

As the fluorination of solid uranium and molybdenum proved to be highly efficient, the possibility of an easy access to the hard-to-obtain platinum metal hexafluorides was investigated. It could be shown that the fluorination line can successfully be used for the production of several additional hexafluorides including WF_6, TeF_6, ReF_6 and ReF_7, OsF_6 and IrF_6. As the fluorination line allows the setting of a large number of parameters such as volume flows of NF_3 and Ar, NF_3/Ar ratio, temperature and microwave power, a parameter set allowing for an efficient production of the corresponding hexafluoride was identified in each case. The produced hexafluorides were additionally spectroscopically investigated using IR, Raman, UV/VIS and NMR spectroscopy.

Table of Contents

List of Acronyms

ATR	Attenuated total reflection
CT	Computed tomography
FEP	Fluorinated ethylene propylene
FRM II	Forschungsreaktor München II (Research Neutron Source Munich II)
FTIR	Fourier-transform infrared spectroscopy
HEU	Highly enriched uranium
LEU	Low enriched uranium
LN_2	Liquid nitrogen
MIBI	Methoxyisobutylisonitrile
MPS	Microwave power supply
MRI	Magnetic resonance imaging
NMR	Nuclear magnetic resonance
PCTFE	Polychlorotrifluoroethylene
PET	Positron emission tomography
PFA	Perfluoroalkoxy alkanes
PTFE	Polytetrafluoroethylene
RPS	Remote plasma source
SATP	Standard ambient temperature and pressure
SPECT	Single-photon emission computed tomography
UV/VIS	Ultraviolet/Visible
VDEh	Verein Deutscher Eisenhüttenleute
XRPD	X-ray powder diffraction

Glossary

Torr	Torr, mmHg	pressure	1 Torr	= 133.32 Pa
Curie	Ci	activity	1 Ci	= $3.7 \cdot 10^{10}$ Bq
Standard cubic centimeter per minute	sccm	volume flow	@ and	T = 0° C p = 1013.25 hPa

1 Introduction and Motivation

1.1 Significance of technetium-99m

Over the past decades, nuclear medicine has become to play a key role in modern diagnostics. Thereby, the most widely used isotope for imaging is technetium-99m (^{99m}Tc). Germany alone requires 3 million applications each year, whereas the global demand amounts to over 30 million [1,2]. A safe and reliable production process for ^{99m}Tc is necessary to avoid shortages as they have recurrently taken place over the past years and is therefore a research topic of great interest. Although other nuclear imaging techniques are on the rise such as PET, ^{99m}Tc SPECT will keep its importance in the near future due to considerable lower costs and its high availability as a generator nuclide. Especially private radiological practices, where the major amount of examinations takes place, will most likely not be able to operate PET scanners in a cost-effective manner [3]. Moreover, it is a general misconception, if the advances in the technology of CT and MRI are seen as potential competitors for nuclear imaging. These methods provide high-resolution imaging and deliver valuable information on the appearance of an internal structure but face serious shortcoming as it comes to deliver resilient predictions about its function. Figure 1.1 shows a ^{99m}Tc scintigram of the thyroid gland. Whereas a morphological anomaly of this organ may also be identified in a CT or MRI scan, a statement concerning its metabolic status is not possible.

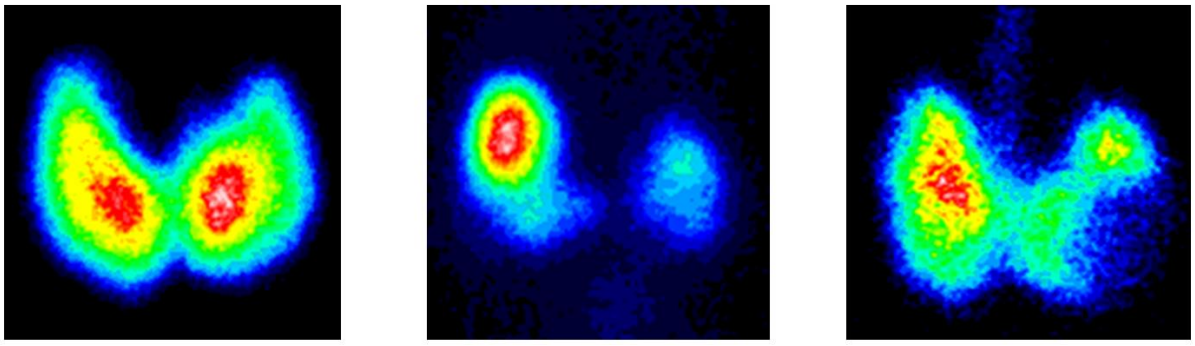

Figure 1.1: ^{99m}Tc scintigram of the thyroid gland. In the very left a normal finding is shown, whereas the middle shows a hot node in the right lobe, the very right a cold node in the left lobe [4].

The ideal radioisotope used for diagnostic purposes possesses certain characteristics: It is a pure γ-emitter with an energy between 100 – 200 keV allowing for a good detectability and limiting the dose of the patient. For the same reason it has a short half-life of up to several hours. The production process is simple and low in cost. Furthermore, it possesses a rich chemistry enabling it to target specific organs and tissues [5]. As one of very few radioisotopes, ^{99m}Tc combines many of the desired properties. The decay scheme in Figure 1.2 depicts its formation as well as its decay. Its mother nuclide molybdenum-99 (^{99}Mo) has a half-life of about 66 hours, allowing for the usage as a generator nuclide und thus convenient shipment to and handling at the hospitals. ^{99m}Tc for its part decays to its ground state ^{99}Tc emitting gamma radiation with an energy of 141 keV with a probability of 89 % after releasing a conversion electron with an energy of 2 keV. For the remaining 11 %, ^{99m}Tc directly relaxes

to its ground state via internal conversion emitting conversion electrons with an energy of 143 keV. The short half-life of 6 hours ensures a fast elimination from the body and thereby a low radiation exposure of the patient.

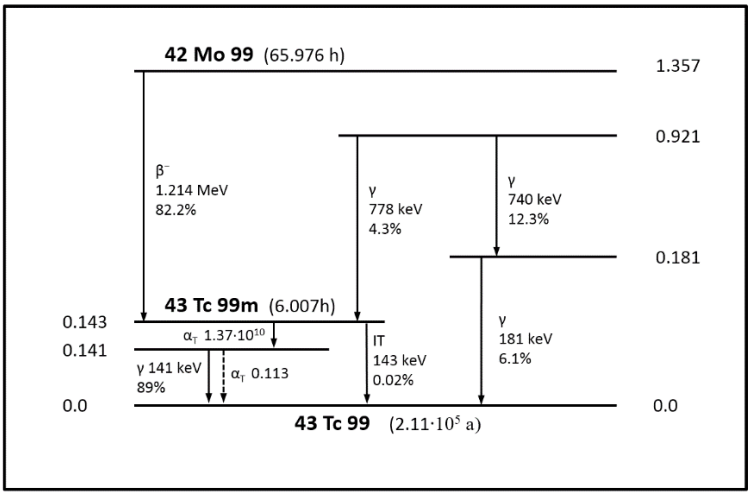

Figure 1.2: Decay scheme for ^{99}Mo and ^{99m}Tc. About 82 % of ^{99}Mo decays directly to ^{99m}Tc via β^--decay. Of this about 89 % decay to its ground state emitting a 141 keV photon used for imaging [6].

However, technetium encounters some difficulties from a chemical perspective. Being a transition metal, a direct bond to carbon atoms is only found in a limited number of organometallic compounds. However, this disadvantage is largely offset by the existence of eight stable oxidation states known for Tc. Important oxidation states are +VII, +V, +IV, +III, +I and 0 [7]. The oxidation state +VII is present in the pertechnetate anion TcO_4^-, which has approximately the same size as the iodide anion I^- and for that reason is suited well for scintigraphy of the thyroid as shown in Figure 1.1, but also for the parathyroid and the salivary glands. Very frequently used is the complex ^{99m}Tc-hexakis-2-methoxyisobutyl isocyanide ^{99m}Tc-HEXAMIBI, in which Tc possesses oxidation state +I and which is used as an agent for myocardial imaging [7,8].

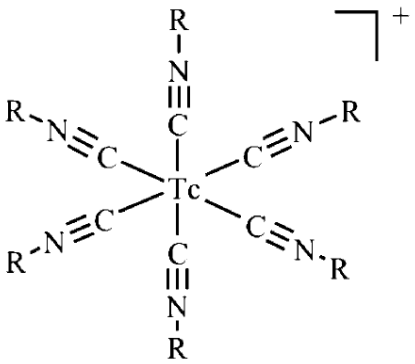

Tc-MIBI

(R = CH_2-C(CH_3)$_2$$OCH_3$)

Figure 1.3: Structure of the Tc-HEXAMIBI complex [7].

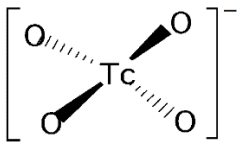

Figure 1.4: Structure of the pertechnetate anion [7].

As the multitude of Tc-related drugs used for medical applications is overwhelming, they shall not be discussed in further detail and the two compounds are only mentioned exemplarily. An overview of the target organ systems is given in Figure 1.5.

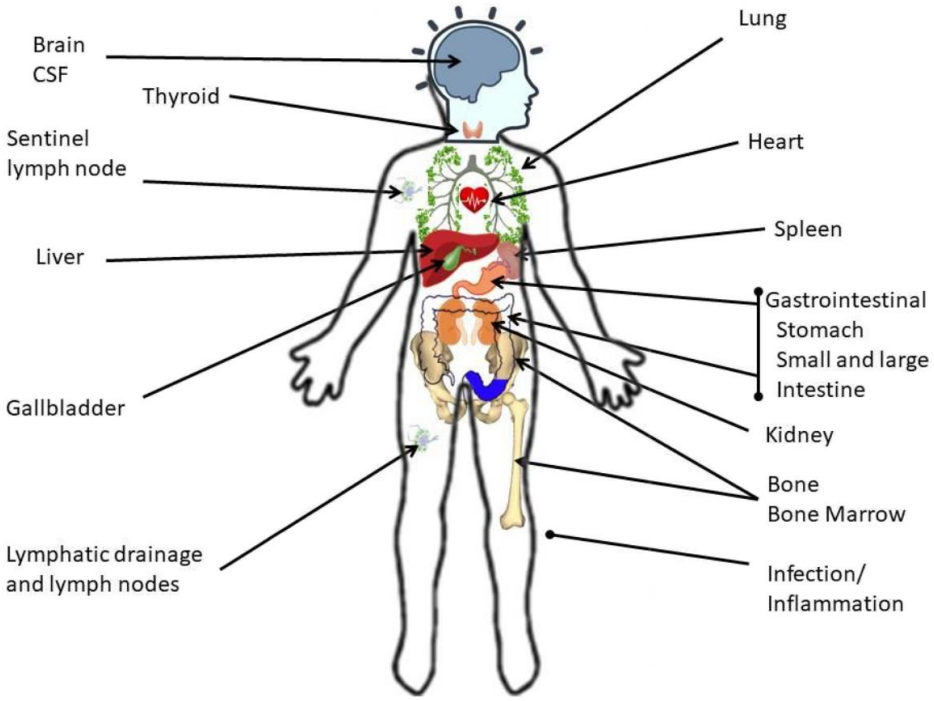

Figure 1.5: Target organ systems for ^{99m}Tc pharmaceuticals [9].

As mentioned before, ^{99m}Tc has a short half-life of only 6 hours and can therefore not be stored directly at the hospital. Instead, the generator principle is used in order to ensure a feasible operation and reliable supply with ^{99m}Tc over an extended period of time that greatly exceeds the half-life of the corresponding radionuclide. Thus, a ^{99m}Tc generator is usually used for a week until being replaced, corresponding to about three half-lives of the parent nuclide ^{99}Mo. At this point, only about 17 % of the original activity of ^{99}Mo remain.

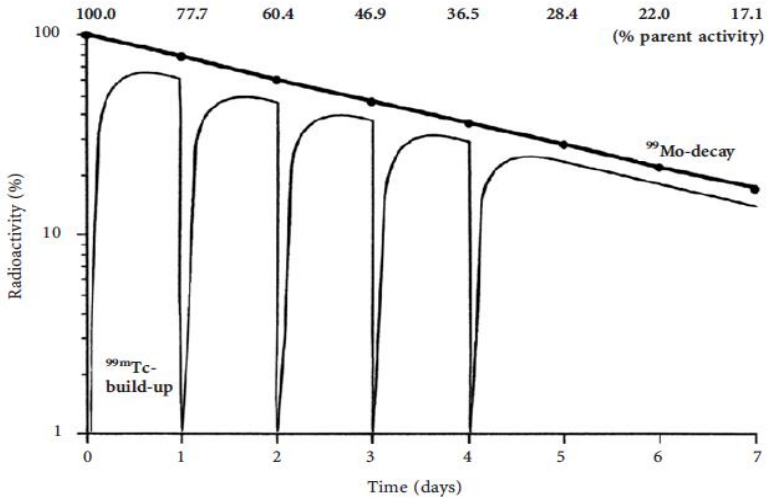

Figure 1.6: Activity of the parent nuclide ^{99}Mo and its daughter ^{99m}Tc, eluded every 24 hours over the course of one week [7].

In the generator, the parent nuclide ^{99}Mo is present in the form of sodium molybdate Na_2MoO_4, which is strongly adsorbed to an alumina column. As an element of group seven, Tc prefers oxidation state +VII in the pertechnetate anion TcO_4^-, which in contrast to the molybdate anion only carries one negative charge. It is therefore only loosely adsorbed to the alumina column and may thereby easily be eluted, using sterile physiological saline solution [10].

The $Na^{99m}TcO_4$ containing solution may then either be directly applied to the patient as it is the case for scintigraphy of the thyroid gland or will be further prepared using ready-made kits. These kits include a reducing agent, often stannous chloride, to adjust the oxidation state of Tc and enable it to bind to the anticipated ligand.

Figure 1.7: DRYTEC ^{99m}Tc generator [11].

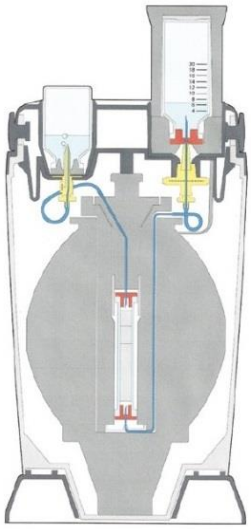

Figure 1.8: Internal view of DRYTEC ^{99m}Tc generator [12].

Depending on the size of the radiological unit and its need for radiodiagnostics, the initial ^{99}Mo activity of a generator may vary between 2.5 and 100 GBq [13].

1.2 Supply chain of ^{99m}Tc

As of 2019, several routes for the production of ^{99m}Tc have been proposed and evaluated with respect to general feasibility, reliability and overall-costs. They can be divided into two main groups based on the production facility, which can be either a reactor or an accelerator. The emphasis of this work is on the production of ^{99m}Tc via the fission route of uranium-235 (^{235}U), as it currently accounts for about 90 % of the global production. However, certain aspects of the extraction process may as well be transferred to other production schemes. A general overview of the different production routes of ^{99}Mo and ^{99m}Tc, respectively, is depicted in Figure 1.9.

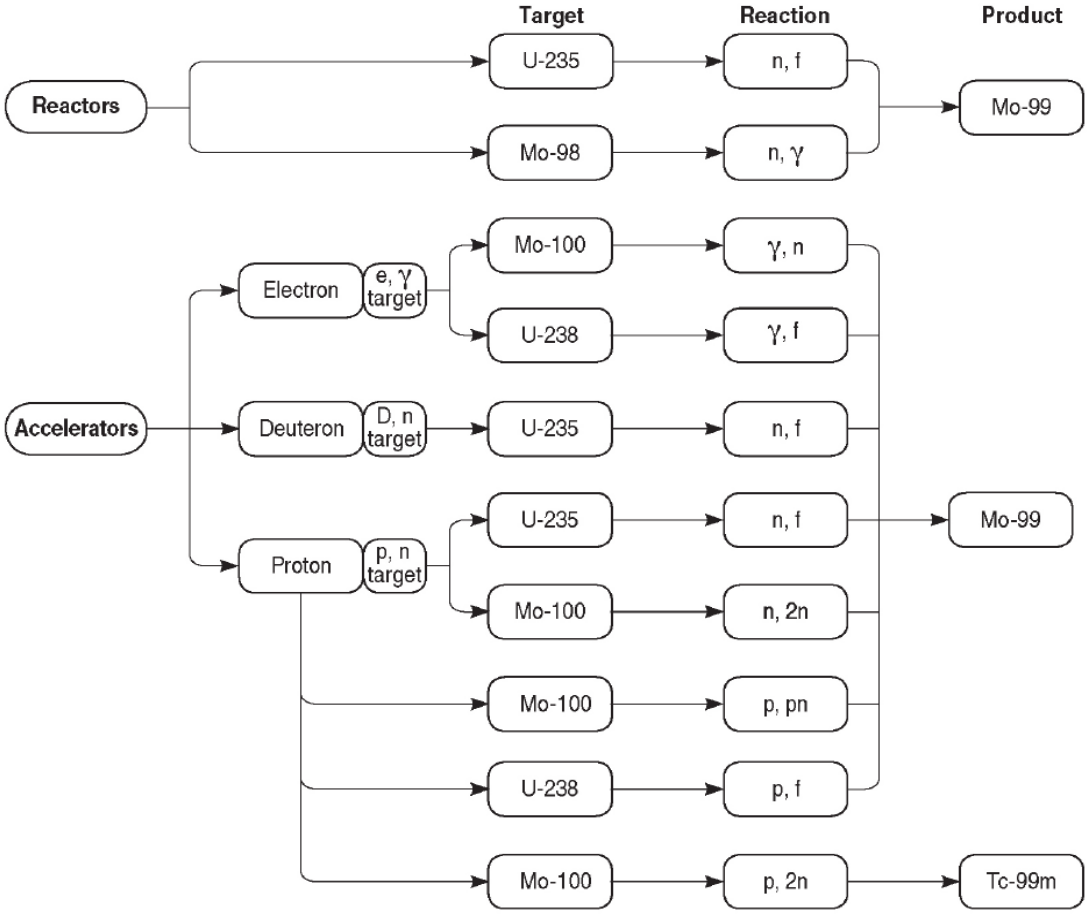

Figure 1.9: Schemes for the production of ^{99}Mo and ^{99m}Tc [14].

The fission route utilizes irradiation targets enriched in ^{235}U. After being irradiated for about six days, these targets are removed from the reactor and shipped to a processor in order to extract the ^{99}Mo along with other radionuclides, for either diagnostic or therapeutic use in nuclear medicine. These radionuclides include iodine-131 (^{131}I), xenon-133 (^{133}Xe) and strontium-89 (^{89}Sr). The purified ^{99}Mo is forwarded to the generator manufacturers, who equip their ready-to-use chromatographic based generators with a sodium molybdate $Na_2{}^{99}MoO_4$ solution. From there it is forwarded to the applying hospitals. The entire supply chain from the reactor to the hospital is depicted in Figure 1.10.

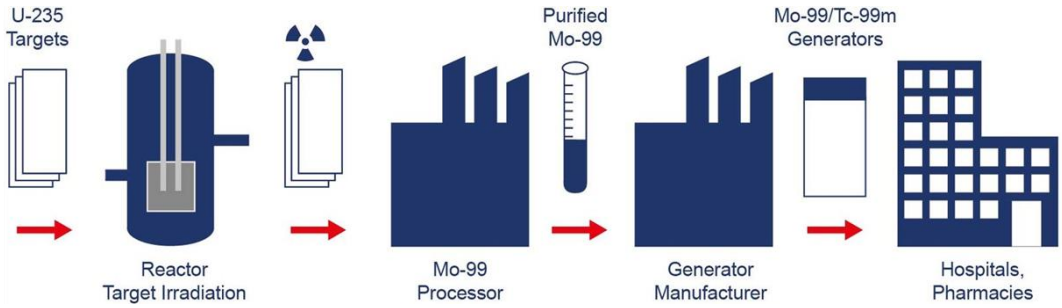

Figure 1.10: ^{99m}Tc supply chain from irradiation based production [15].

In its 2019 report, the High-Level Group on the Security of the Supply of Medical Radioisotopes HLGMR identified the global demand on ^{99}Mo stably staying at 9500 6-day curies per week [16]. In order to ensure a safe supply also in case of an unforeseen problem of a producer, the (n−1) criterion is being applied. This criterion considers the unscheduled shutdown of the largest producer and counters this by an excess capacity of +35 % of the global demand, the so-called outage reserve capacity ORC.

The reactors used for the production of ^{99}Mo as of 2020 are listed in Table 1.1. Due to the efforts to reduce the risks of potential proliferation, all reactors with exception of the ones of the Russian Federation are in the process of converting the irradiation targets to low enriched uranium (LEU) with a degree of enrichment lower than 20 %. One LEU fuel type is already being used for irradiation on a large scale, namely uranium aluminide (UAl_x) dispersion targets in an Al matrix cladded with Al. A second type of targets containing a uranium metal foil also cladded with Al has intensively been investigated and successfully been irradiated. A third fuel type utilizing U_3Si_2-Al dispersion targets has been demonstrated to work on a laboratory scale [17].

Table 1.1: Reactors used for production of ^{99}Mo as of November 2019 [16]. The term weekly capacity refers to the activity produced during operation. However, since all reactors are facing a considerable amount of downtime for revision, the sum of this capacity should not be directly compared with the global demand.

country	reactor	targets	weekly capacity [six-day curies EOP]
Argentina	RA-3	LEU	500
Australia	OPAL	LEU	2150
Belgium	BR-2	HEU/LEU	6500
Czech Republic	LVR-15	HEU/LEU	3000
Germany[1]	FRM II	LEU	2100
Netherlands	HFR	HEU/LEU	6200
Poland	MARIA	LEU	2200
Russia	RIAR/IPC	HEU	890
South Africa	SAFARI	LEU	3000

[1] Delayed to 2021/2022.

As ^{99}Mo has a rather short half-life of 66 hours, its activity is continuously decreasing. The need for a quantity serving as a common reference led to the introduction of the 6-day curie (6-day Ci). This unit is equivalent to the activity of ^{99}Mo six days after it leaves the irradiating facility [3]. In order to minimize the losses of activity due to long transport times of the irradiated targets, many processors are in relative proximity to the irradiation side. The current facilities for the processing of ^{99}Mo as of 2019 are listed in Table 1.2.

Table 1.2: Processing facilities producing bulk ^{99}Mo from irradiated targets as of 2019 [16].

country	processor	weekly capacity [six-day curies EOP]
Argentina	CNEA	500
Australia	ANSTO	2150
Belgium	IRE	3500
Netherlands	Curium	5000
Russia	RIAR/IPC	1350
South Africa	NTP Radioisotopes	3000

The exchange of HEU by LEU targets for ^{99}Mo production is accompanied by several challenges from both, the irradiator's and the processor's side. The former primarily face yield losses due to the decreased uranium content, the latter face higher waste volumes and longer processing times [18]. Lee et al. denominate the increase in waste volume to about 200 % for the target design and the extraction routes being currently used [19]. The extraction routes for their part depend on the deployed fuel type and greatly differ between UAl_x dispersion targets, metal uranium foil targets and U_3Si_2 dispersion targets. UO_2 targets are not discussed hereby as they are currently not used by any major supplier.

The UAl_x dispersion targets consist of uranium aluminide particles enclosed by an aluminum matrix. This meat is sandwiched by two aluminum plates. The uranium loading of this design is comparably low with 2.5-3.0 gU/cm^3 [17], but has been significantly increased with respect to HEU dispersion targets with a loading not exceeding 1.6 gU/cm^3. The processing of UAl_x targets is performed using the alkaline digestion process, a method developed by Ali and Ache [20]. The targets are thereby dissolved using NaOH or KOH, whereas some processors supplementary add $NaNO_3$. Whereas Al and ^{99}Mo are easily dissolved, uranium precipitates in form of UO_2 and $Na_2U_2O_7$, allowing for a separation via filtration. The recovery of ^{99}Mo from the solution occurs through the use of anion exchangers and chromatographic columns [19]. Alternative recovery procedures, e.g. using chelating resins, may be used depending on the processor [21].

The metal uranium foil targets are simple in design and basically consist of an aluminum foil cladded with two aluminum plates. An advantage of this design is its high uranium loading of 19.0 gU/cm^3. As the aluminum cladding is mechanically removed from the foil, only the latter has to be dissolved, thereby significantly reducing the amount of liquid radioactive waste. The dissolution takes place using HNO_3. After the separation of radioiodine from the solution, Mo is precipitated by use of α-benzoin oxime as Mo-α-benzoin oximate [22] and washed with nitric acid. After dissolving the Mo from the precipitate using a solution of H_2O_2 and NaOH, it is absorbed on chromatographic columns [23].

However, as no industrial standard for the manufacturing of this target design has been established, the qualification of uranium foil targets lies within the responsibility of each producer [23]. As of 2015, none of the irradiators mentioned above is using foil-type targets.

The design of the U_3Si_2 dispersion targets is similar to the UAl_x dispersion targets. They also consist of particles, here uranium silicide, enclosed by an aluminum matrix and sealed by an aluminum cladding. These targets have the advantage of high uranium loading of up to 6.0 gU/cm^3 [24]. In addition, they behave well under irradiation. In contrast to UAl_x dispersion targets, the dissolution process is more demanding. Developed in Karlsruhe, it also features the use of NaOH and $NaNO_3$ solution. However, as U_3Si_2 is thereby not readily dissolved, it is further treated with a mixture of HF, H_2O_2 and KIO_3. After this treatment, KOH is added and the solution heated, thereby destroying the H_2O_2 [17,21]. The recovery of ^{99}Mo from this solution is also achieved by the use of ion exchangers and chromatographic columns.

Independent of the details of the utilized process, its ultimate purpose is the production of ^{99m}Tc for medical use. It therefore has to satisfy high requirements concerning its purity. The limits of allowed radiologically active impurities are listed in Table 1.3.

Table 1.3: Limits of radiologically active impurities in the eluate from ^{99}Mo generated by fission from ^{235}U [7].

radionuclide	type of radiation	limit [%]
^{99}Mo	(γ, β^-)	$1 \cdot 10^{-1}$
^{131}I	(γ, β^-)	$5 \cdot 10^{-3}$
^{103}Ru	(γ, β^-)	$5 \cdot 10^{-3}$
^{89}Sr	(pure β^- - emitter)	$6 \cdot 10^{-5}$
^{90}Sr	(pure β^- - emitter)	$6 \cdot 10^{-6}$
α - emitter	–	$1 \cdot 10^{-7}$
γ - emitter	–	$1 \cdot 10^{-2}$

1.3 Production of ^{99}Mo at FRM II

FRM II is a high-flux research neutron source in Garching operated by the Technical University of Munich. In relation to thermal power, it is the most brilliant neutron source worldwide with a maximum undisturbed thermal neutron flux of about $8.0 \cdot 10^{14}$ and is used to conduct research for science, medicine and industry. In addition, FRM II will start the production of ^{99}Mo from irradiation of ^{235}U in 2021. For this purpose, a facility is being installed allowing for the simultaneous irradiation of sixteen rectangular plate-type targets with a respective uranium mass of about 20 g each. They consist of UAl_2 dispersed in an Al matrix, which again is enclosed by an aluminum cladding. The utilized uranium is LEU with a degree of enrichment of 19.75 % [25]. For irradiation, the sixteen targets are placed in a thimble situated in the moderator tank at a distance of about 400 mm to the center of the fuel element. At this position, they are in close proximity to the maximum of the thermal neutron flux. There they are irradiated for six days until they are removed and shipped to a processor, i.e. IRE in Fleurus, Belgium or Curium in Petten, the Netherlands [14]. The irradiation facility is depicted in Figure 1.11.

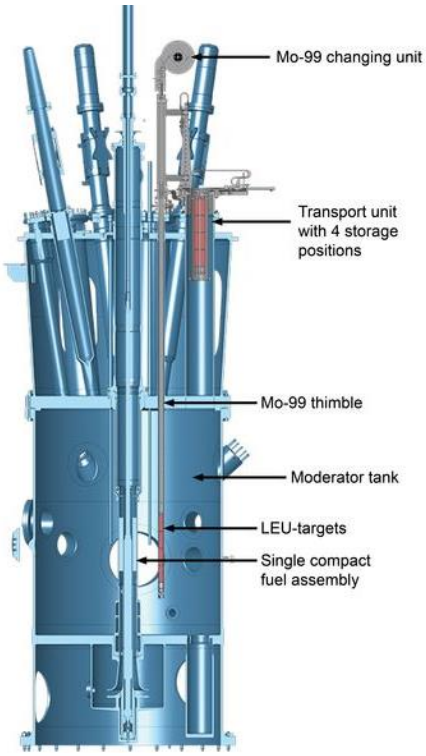

Figure 1.11: Schematic view of the ^{99}Mo irradiation facility at FRM II. Up to 16 targets may be placed in a thimble in close proximity to the fuel element and simultaneously irradiated [26].

In combination with the Jules Horrowitz Reactor (JHR) in France, which will have a weekly capacity of 4800 6-day Ci, FRM II will cover the entire European demand of ^{99m}Tc [16,27]. The commissioning of JHR is planned for 2023, the first irradiation of targets for ^{99}Mo production for 2024.

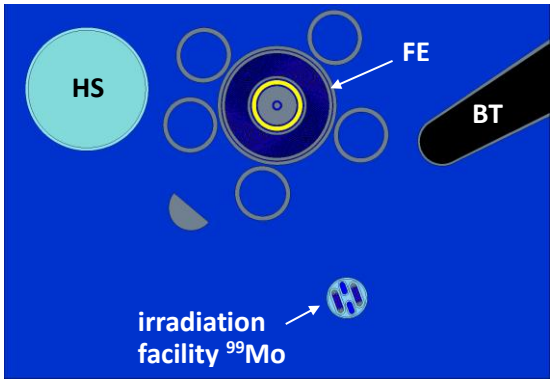

Figure 1.12: The fuel element (FE) surrounded by the tubes of the five shut-down rods, the hot source (HS) and a beam tube (BT). In the lower central part, the irradiation facility for ^{99}Mo [28].

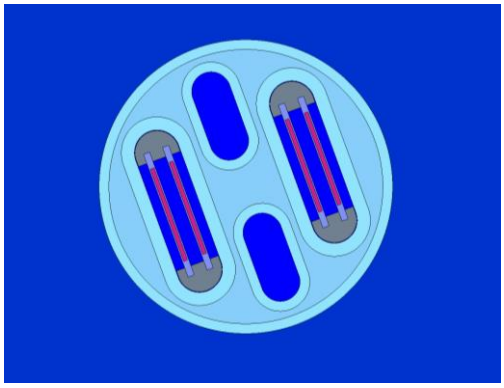

Figure 1.13: Detailed view of the ^{99}Mo irradiation facility [28].

In addition to its ambition of being a major supplier of ^{99}Mo, FRM II also intensively investigates the entire ^{99}Mo cycle, starting with the target production as well as the processing of the irradiated targets. In his PhD thesis, Hollmer developed a manufacturing process for cylindrical monolithic LEU targets, for which he constructed, built and commissioned a sputtering device [29]. As for the metal uranium foil targets, the uranium loading here is of equal amount and in principle, the wet chemical process could also be used for ^{99}Mo recovery. Instead, FRM II takes a different approach and investigates a process that on one hand minimizes the production of corrosive liquid radioactive waste and on the other hand might prove to be suitable for the processing not only of metal foil but also for U_3Si_2 dispersion targets. This process uses a remote plasma source (RPS) in order to create highly reactive fluorine radicals that convert the uranium and molybdenum to their corresponding hexafluorides. These are subsequently separated from each other using a combination of physical and chemical methods.

As a fluorine-based dry-chemical extraction process for ^{99}Mo has to be measured against well-established wet-chemical processes, the following aspects were investigated:

1. The general possibility of the synthesis of the hexafluorides of U and Mo using an RPS.

2. The determination of the etching rate as well as the utilization of the etching agent.

3. The formation of byproducts such as other low-valent fluorides leaving the metals in a lower oxidation state.

4. The possibility of the separation of Mo and U based on physical properties such as a difference in sublimation temperature.

5. The possibility of separating Mo and U by dry-chemical means.

The setting of the technical pre-requisites for this investigation, its implementation and its results will be displayed and illustrated during the course of the following chapters.

2 Theoretical Background

2.1 Nuclide vector

The fission of ^{235}U results in a multitude of isotopes. Thus, a simulation of the exact isotopic composition of the targets after irradiation is of great interest, as it not only specifies the amount of ^{99}Mo and its ratio to non-fissioned uranium, but also allows identifying potential problems during the separation process that may arise from the presence of other elements forming volatile fluorides.

Therefore, a burn-up simulation has been performed with Serpent 2 [30], resulting in the nuclide vector listed in Table 2.1. Here, not the isotopic but the elemental composition is listed, as this is the quantity of interest for a chemical separation process. For this simulation, the 12-group neutron energy spectrum at the ^{99}Mo position was calculated with a full-core model of FRM II [28]. The full-core model includes all reactor components, but the installations are modeled as effective materials in the D_2O reflector tank. For the burn-up calculation, only the new molybdenum target geometry developed by Hollmer [29] was employed and the external source mode was used in Serpent 2. The exact geometry of the target is displayed in Figure 2.1. It consists of a 10 µm outside aluminum cladding, 130 µm uranium foil and a 10 µm inside aluminum cladding. The total mass of uranium amounts to 20.00 g, of which 16.07 g are ^{238}U and 3.93 g are ^{235}U. Minor amounts of ^{234}U and ^{236}U are also present. The source of the simulated neutrons is set into the outer aluminum cladding according to the energy spectrum calculated from the full-core model and randomly distributed in the source volume. After reaching the uranium meat, fission processes are induced and the uranium burn-up and fission product build-up is registered on a daily basis. The mean power released in the phase accounts for 146 kW. After 180 hours, the generated power is set to zero, formally ending the fission process. The decay of the fission products is examined over the following three days [31]. In order to limit their number at this stage, elements with a mass below 1 mg are not listed in Table 2.1, but may still be highly relevant from a radiological perspective.

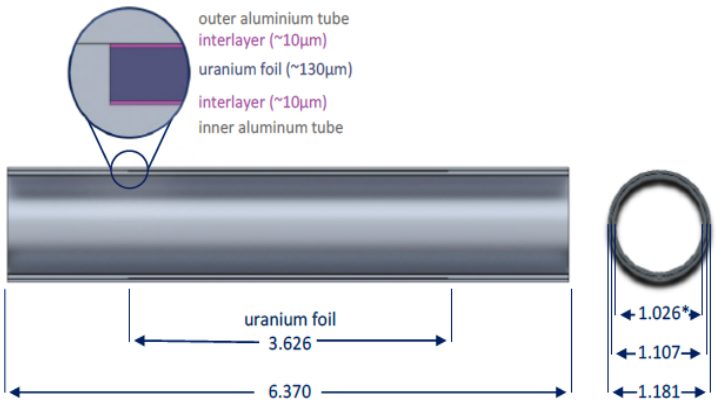

Figure 2.1: The target geometry developed by Hollmer and used for the Serpent 2 simulation [32].

The results of the simulation are in good agreement with previous calculations internally performed at FRM II using MCNP [33]. In addition to the nuclide vector, the corresponding fluorides that are likely to be formed during the fluorination process and their thermodynamic properties are also listed in Table 2.1.

Table 2.1: Element distribution after an irradiation period of 180 hours, 24 hours after end of irradiation with their melting (m.p.) and boiling points (b.p.) and the potential fluorides being produced during the fluorination process with their corresponding melting and boiling points. If the melting point is not accessible under normal conditions, the triple point (t.p.) is given instead. The same holds for the boiling point, where the sublimation point (s.p.) is then given. Only elements with a mass exceeding 1 mg are listed. The thermodynamic data has been taken from [34].

element	mass [mg]	m.p. [°C]	b.p. [°C]	poss. fluorides	m.p. [°C]	b.p. [°C]
Xe	35.5	−112 (t.p.)	−108	XeF_2	129 (t.p.)	114 (s.p.)
				XeF_4	117 (t.p.)	116 (s.p.)
				XeF_6	49.5	75.6
Zr	28.5	1855	4409	ZrF_4	932 (t.p.)	912 (s.p.)
Ce	25.2	798	3443	CeF_4	1430	
Mo	17.5	2623	4639	MoF_6	17.5	34.0
Nd	16.7	1021	3074	NdF_3	1377	2300
Ba	15.5	727	1897	BaF_2	1368	2260
Ru	14.3	2334	4150	RuF_5	86.5	227
				RuF_6	54	
Sr	11.8	777	1382	SrF_2	1477	2460
Cs	11.2	28.5	671	CsF	703	–
La	9.30	918	3464	LaF_3	1493	–
Pr	6.47	931	3520	PrF_3	1395	–
Y	5.03	1522	3345	YF_3	1150	–
Te	4.87	450	988	TeF_6	−37.6 (t.p.)	−38.9 (s.p.)
Tc	3.61	2157	4265	TcF_6	37.4	55.3
Pu	3.32	640	3228	PuF_6	52	–
I	3.25	113.7	184.4	IF_5	9.4	100.5
				IF_7	6.5 (t.p.)	4.8 (s.p.)
Kr	3.06	−157 (t.p.)	−153.2	KrF_2	25 (dec.)	–
Rb	3.04	39.3	688	RbF	833	1410
Sm	2.23	1074	1794	SmF_3	1306	–
Np	1.57	644	3902	NpF_6	–	–
Pm	1.29	1042	3000	PmF_3	–	–
Pd	1.10	1555	2963	PdF_2	952	–

Two very relevant pieces of information may be extracted from this table. First, the mass of each fission product amounts only to 0.18 % on an elemental base with respect to the original target at the most, much less for many others. In the case of molybdenum, the mass of all of its isotopes is only 0.09 % of the mass of the target. This makes high demands on the separation process. Second, molybdenum is not the only fission product with a volatile hexafluoride. Xenon, ruthenium, tellurium, technetium, plutonium, iodine, krypton and neptunium also form fluorides that might be volatile under the conditions in the fluorination chamber. Thus, the etching behavior of tellurium and ruthenium was also investigated. However, this was not the case for xenon and krypton, as gases could not be introduced into the reaction chamber, nor for technetium, plutonium and neptunium, as the laboratory in Marburg had no permission to handle these artificial radioactive elements.

In addition to the elemental composition of the fission products, the exact amount of medical relevant radioisotopes and their development over a period of 70 hours after end of irradiation was also examined and is listed in Table 2.2 as well as depicted in Figure 2.2.

Table 2.2: Predicted mass distribution of different major medical isotopes after an irradiation period of 180 hours and its development over the following 70 hours.

irradiation time [h]	decay time [h]	^{89}Sr [mg]	^{99}Mo [mg]	^{99m}Tc [mg]	^{131}I [mg]	^{133}Xe [mg]	^{153}Sm [mg]
48	–	1.058	1.218	0.250	0.830	1.006	0.044
96	–	2.096	1.953	1.001	1.574	2.563	0.066
144	–	3.106	2.398	2.068	2.208	3.916	0.078
180	–	3.845	2.611	2.998	2.618	4.741	0.083
–	20	3.811	2.113	3.518	2.479	4.917	0.061
–	40	3.767	1.709	3.955	2.321	4.749	0.045
–	60	3.724	1.383	4.310	2.169	4.430	0.034
–	70	3.703	1.244	4.461	2.095	4.247	0.029

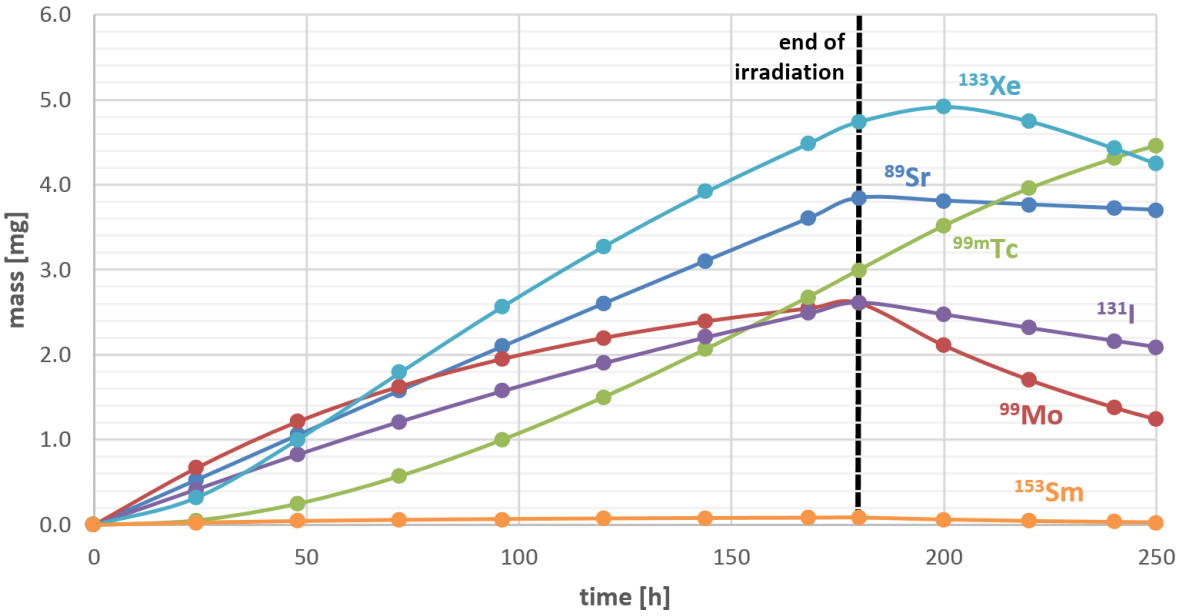

Figure 2.2: Predicted development of the amount of radioisotopes of medical interest during the 180 h irradiation of ^{235}U targets and subsequent decay; visualization of Table 2.2.

2.2 Development of the total activity for HEU and LEU targets

In addition to the waste volume, the total activity as a function of time is also of interest, especially for questions concerning final storage. An additional simulation with Serpent 2 was performed for a slightly changed version of the cylindrical target design described in detail in the previous chapter for both target materials, HEU and LEU [30,35]. The total mass of uranium hereby amounts to 20.21 g. In the case of HEU, 18.78 g are ^{235}U and in the case of LEU, 3.96 g are ^{235}U. The reference scenario is the irradiation of a HEU target for 180 hours with a mean thermal power release of 146 kW. The resulting neutron source rate serves as the normalization for the irradiation of the LEU target. The released mean thermal power of the LEU target thereby amounts to only 40 kW because of the reduced fission rate due to the lower content of ^{235}U.

The activity of ^{99}Mo of one LEU target at the end of irradiation amounts to 61.1 TBq, whereas the activity of ^{99}Mo of one HEU target at the end of irradiation amounts to 231.7 TBq. Thus, a total number of 3.8 LEU targets is necessary in order to produce the same activity as from the use of one HEU target. In order to compare the total activity of the two target types, the produced ^{99}Mo activity in TBq was chosen as a common reference unit. Figure 2.3 shows the development of the total activity for LEU and HEU targets over time per produced TBq ^{99}Mo.

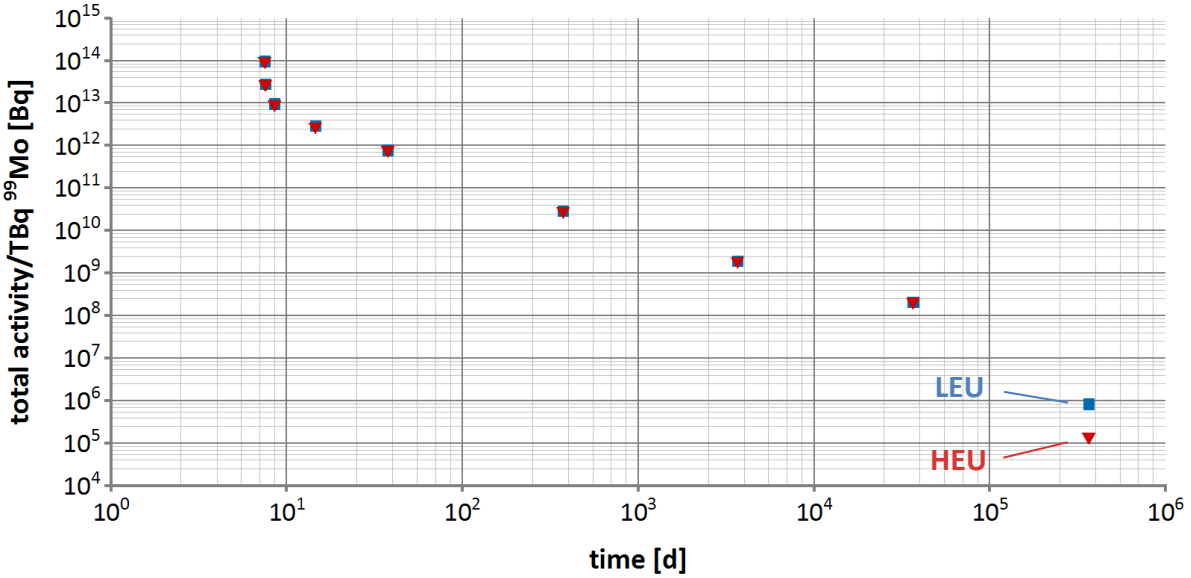

Figure 2.3: Development of the total activity per produced TBq ^{99}Mo for LEU targets (blue squares) and HEU targets (red triangles). The total irradiation time was 180 hours. The activity was calculated for the end of irradiation and certain subsequent points in time: 1hour, 1day, 1 week, 1 month, 1 year, 10 years, 1000 years, and 1000 years.

As expected, the total activity develops very similar for the first 100 years, as this time domain is dominated by the fission products, which are produced in almost identical amounts in both targets types. However, the last data point, which marks 1000 years, shows a significant difference of a factor of almost six between the two target types. This time domain is dominated by the transuranic elements that are produced in significantly higher amounts in LEU targets. Thus, at the end of irradiation, the activity of ^{239}Pu (half life of $24 \cdot 10^3$ years) in LEU targets amounts to 12.6 MBq, whereas in HEU targets it only amounts to 983 kBq.

2.3 Fluorine Chemistry

Fluorine is the lightest of the halogens. It very likely is a colorless gas under standard conditions with a characteristic pungent and unpleasant smell. Being the most reactive of all elements in the periodic table, it was initially believed to be absent in its elementary form in nature. However, Kraus and Günne were able to show the presence of elemental F_2 in antozonite in 2012, a variety of CaF_2, which is also historically known by its German name "Stinkspat" due to its strong odor if cracked [36].

Elemental fluorine is highly toxic and rapidly causes irritation of exposed tissue already at low concentration. Its toxicity is furthermore enhanced by the swift formation of hydrofluoric acid at contact with water or humidity. Hydrofluoric acid for its part is also highly toxic. Because of its high liposolubilty, it easily penetrates the skin and may be absorbed into the blood. Dependent on the extent of the exposure, here it may introduce hypocalcemia and hypomagnesemia due to precipitation of blood calcium and magnesium ions, followed by hyperkalemia as the body tries to maintain ion equilibrium [37]. These conditions may ultimately result in cardiac arrhythmia and cardiac arrest. The inhalation of gaseous HF for its part may lead to chemical burns of the lung and an associated toxic pulmonary edema, but only at very high concentrations and/or reduced protective reflexes. Due to the good solubility of HF in water, it is more likely already absorbed in the upper respiratory tract [38]. In addition, its strong irritation effect and the associated cough prevents a deep inhalation under normal circumstances.

As many high-valent fluorine compounds, such as the transition metal hexafluorides, form HF if in contact with moisture, they must be treated with considerable caution. Fluorides that may potentially be formed during the fluorination of an irradiated target are listed in Figure 2.4.

												GaF_3	GeF_4	AsF_3, AsF_5	SeF_4, SeF_6	BrF_3	Kr, KrF_2
RbF	SrF_2	YF_3	ZrF_4	NbF_5	MoF_6	TcF_6	RuF_6, RuF_3	RhF_6, RhF_3	PdF_2	AgF, AgF_2	CdF_2	InF_3	SnF_4	SbF_5	TeF_6	IF_5, IF_7	Xe, $XeF_{2,4,6}$
CsF	BaF_2	LaF_3															

Lanthanoids	CeF_4	PrF_3	NdF_3	PmF_3	SmF_3	EuF_3	GdF_3	TbF_3	DyF_3	HoF_3	ErF_3		
Actinoids	ThF_4	PaF_3	UF_6	NpF_6	PuF_6	AmF_3	CmF_3						

Figure 2.4: Periodic table showing the fluorides most likely to be formed after the fluorination of an irradiated target [39]. Fluorides presented in black are nonvolatile, whereas fluorides presented in green are volatile. Niobium pentafluoride NbF_5 is presented in yellow, as it is volatile to some extent, but far less than the ones marked in green [40].

The plasma line developed for the fluorination of the uranium targets (see chapter 4.1) proved to be able to easily convert uranium and molybdenum into their corresponding hexafluorides. Thus, in addition to the fluorides listed in Figure 2.4, the synthesis of high-valent fluorides of elements of the sixth period was also of interest. Similar to UF_6, these hexa- and heptafluorides are of high volatility and possess a significant vapor pressure already at ambient temperature [41]. This property makes them easy to sublime and thus allows for a convenient possibility of transferring them from one vessel to another. Table 2.3 lists the melting and boiling points of the hexafluorides belonging to the elements investigated.

Although all hexafluorides listed in this table are potent oxidizing agents, they still show great differences in their reactivity. The oxidizing ability of the hexafluorides of the two homologous metals molybdenum and tungsten is comparably low and lies in the same region as elemental fluorine. ReF_6 and UF_6 already show increased reactivity, whereas especially the platinum metal hexafluorides possess high oxidizing power and therefore must be handled with correspondent caution [42].

Table 2.3: Hexa- and heptafluorides that were investigated for suitability of being synthesized using the plasma-aided fluorination process and their corresponding melting and boiling points [34,43]. The calculated electron affinities of WF_6, ReF_6, OsF_6, IrF_6 and PtF_6 have been taken from [44], for MoF_6, RuF_6 and RhF_6 from [45], for UF_6 from [46] and for atomic fluorine from [47].

compound	melting point [°C]	boiling point [°C]	calc. electron affinity [eV]
WF_6	2.3	17.1	3.16
atomic F	–	–	**3.57**
MoF_6	17.5	34	4.23
ReF_6	18.5	33.8	4.58
UF_6	69.2	56.5 (subl.)	5.1
OsF_6	33.2	47.5	5.92
IrF_6	44	53.6	5.99
RhF_6	70	73.6	6.80
RuF_6	54	–	7.01
PtF_6	61.3	69.1	7.09
ReF_7	48.3	73.7	–

2.4 Material selection

As mentioned before, fluorine and the platinum metal hexafluorides are powerful oxidants. Therefore, careful selection of the involved materials is inevitable in order to provide a safe and reliable operation of the system. NASA has therefore provided its engineers with corresponding design guidelines, which identify the following influencing factors for spontaneous reaction of fluorine with the construction materials [48]:

(1) Initial temperature of the region.

(2) Initial pressure of the region.

(3) Thermal conductivity if the material is a solid.

(4) Exposure surface area with respect to the mass of the substance.

(5) Kinetic or static exposure.

(6) Fluorine concentration in the region.

The following section introduces the employed construction materials and gives a detailed insight into their composition. Only those materials are taken into consideration, which are exposed to the corresponding reactive fluorides. This includes all components of the fluorination and separation line as well as the ones used during the analytical process (also see chapter 4).

2.4.1 Metals

As all metals are attacked by elemental fluorine, the term fluorine-resistant refers to their ability to form a stable and non-volatile protective fluoride layer under the selected conditions. This layer has to be established by a procedure called passivation, during which the metal is exposed to elemental fluorine. It has proven to be effective to start the exposition with an atmosphere of low fluorine content and increasing it over time, until in the final stage pure fluorine is being used. If the planned reaction conditions require the use of elemental fluorine at elevated pressure, passivation should be performed at this pressure increased by an additional 10 %. The entire process should be performed over several days in order to ensure an equal and stable formation of the passivation layer. Amongst other factors such as its crystal structure, the constituents of an alloy significantly affect its resistance to fluorine and other potent fluorination agents. Therefore, a detailed composition of the relevant alloys is given in Table 2.4 to Table 2.6.

Stainless Steel

Two types of austenitic stainless steels show good resistance to dry fluorine in the absence of hydrofluoric acid: AISI 316 and 316L, in the nomenclature of the EN 10027 corresponding to the material numbers 1.4401 and 1.4404, respectively. The major difference between SS316 and SS316L is the lower content of carbon and sulfur of the latter one. This leads to an increased resistance against intergranular corrosion. The detailed composition according to the German steel institute VDEh, which has been responsible for the standardization of steel types, is given in Table 2.4 and Table 2.5. For both steel types, the protective fluoride layer becomes less stable at elevated temperatures [48]. All Swagelok components as well as all KF and CF components used in this work are made from stainless steel AISI 316L.

Table 2.4: Detailed composition of stainless steel 316, material number 1.4401 according to EN 10027 [49].

C ≤ %	Si ≤ %	Mn ≤ %	S ≤ %	P ≤ %	Ni %	Cr %	Mo %	N ≤ %
0.07	1.0	2.00	0.03	0.045	10.0 – 13.0	16.5 – 18.5	2.0 – 2.5	0.110

Table 2.5: Detailed composition of stainless steel 316L, material number 1.4404 according to EN 10027 [50].

C ≤ %	Si ≤ %	Mn ≤ %	S ≤ %	P ≤ %	Ni %	Cr %	Mo %	N ≤ %
0.03	1.0	2.00	0.015	0.045	10.0 – 13.0	16.5 – 18.5	2.0 – 2.5	0.110

Copper is highly resistant to the exposure of dry fluorine. However, it is attacked in presence of moisture, leading to a disintegration of the protective cupric fluoride layer and the formation of hydrofluoric acid [48]. The gaskets for the CF components are made from soft-annealed copper.

Nickel, also known as Alloy 200, shows good corrosion resistance similar to that of Monel to elemental fluorine up to 540 °C, provided the absence of oxygen. However, its resistance to aHF as well as hydrofluoric acid is inferior to that of Monel [51,52]. Some storage containers and the original reaction tube are made from nickel.

Monel, also known as Alloy 400, in German metal nomenclature 2.4360, is an alloy consisting of about two-thirds of nickel and about one-third of copper with some iron. The detailed composition according to [53] is listed in Table 2.6. Monel shows the highest resistance to fluorine, especially under high pressure and if the absence of moisture cannot be guaranteed [51]. It is therefore the material of choice under these conditions. The high resistivity comes at the cost of demanding processing procedures. Monel tends to very easily strain-harden, leading to an increased abrasion of the deployed tools [54]. Another drawback limiting its wider use are the associated high costs. Components made from Monel are usually between twice and three times as expensive as their stainless-steel counterparts. The sample carrier is made from Monel, as it is directly exposed to the fluorine radicals in the reaction chamber.

Table 2.6: Detailed composition of Monel, also known as Alloy 400 [53].

C ≤ %	Si ≤ %	Mn ≤ %	S ≤ %	Ni ≥ %	Ti ≤ %	Al ≤ %	Cu %	Fe %
0.15	0.50	2.00	0.02	63	0.30	0.50	28 – 34	1.0 – 2.5

2.4.2 Polymers

Most polymers are heavily attacked by fluorine and are therefore completely unfeasible for the process. An exception are fully fluorinated polymers and under certain conditions also polymers, where fluorine atoms are partly substituted by chlorine atoms. Favorably, a similar passivation procedure as for metals must be applied to polymers, even if fully fluorinated. As their service temperature and service pressure are lower compared to metals, the same holds for the passivation conditions. The passivation procedure ensures the elimination of all potential carbon double bonds as well as the substitution of potential hydrogen by fluorine atoms. It also eliminates potential monomers that have not exhaustively reacted.

Polytetrafluoroethylene **(PTFE)** is a homopolymer of tetrafluoroethylene (TFE) and also known under its brand names Teflon® or Dyneon™. Its chemical structure is shown in Figure 2.5. It is a thermoplastic with outstanding chemical resistance to many highly corrosive agents such as hydrogen fluoride and hydrofluoric acid. After passivation with gaseous fluorine at increasing fluorine content and pressure, PTFE shows great resistance even to agents with a high fluorination potential such as elemental fluorine and the platinum metal hexafluorides. The service temperature of PTFE is 260 °C under ambient pressure, above this temperature it shows increased reactivity and outgassing, which is an undesirable property in high vacuum application [55]. However, it is known to be attacked by elemental fluorine already at lower temperatures, so in this case the operating temperature should not exceed 180 °C, especially under low-pressure conditions. PTFE is used for the stem tips of some of the smaller membrane valves as well as for the spacer disks of the measuring cell (see chapter 3.3.1).

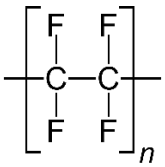

Figure 2.5: Molecular structure of PTFE.

Polychlorotrifluoroethylene **(PCTFE)** is a homopolymer of chlorotrifluoroethylen (CTFE), which structurally differs from TFE by the substitution of a fluorine atom by a chlorine atom. Its chemical structure is shown in Figure 2.6. PCTFE is a thermoplastic and, as PTFE, possesses high chemical resistance to most corrosive agents. However, the substitution of one fluorine atom in favor of a chlorine atom improves its processibility, as PCTFE is injection-moldable. This is not the case for PTFE. Unfortunately, this property comes at the cost of decreased chemical resistance against fluorine and agents with a high fluorination potential. PCTFE is used for the stem tips of all ½ inch membrane valves of the fluorination line. Having a glass transition temperature of about 45 °C [56], heating of the valves should be limited to about 60 °C, allowing for the sublimation of UF_6.

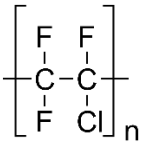

Figure 2.6: Molecular structure of PCTFE.

Perfluoroalkoxy alkanes **(PFA)** are copolymers of tetrafluoroethylene and perfluoroethers, which also possess the outstanding chemical resistance of PTFE. Their chemical structure is shown in Figure 2.7. In difference to PTFE, PFA can be processed via methods as melt-extrusion as well as injection molding [56]. As for PTFE, the service temperature is 260 °C and here again, increased reactivity and outgassing is observed above this temperature. The major advantage of this polymer is its translucency, ideally suiting it for the use as the cold traps of the fluorination line. However, some of the platinum metal hexafluorides show a very high diffusion rate into PFA. This is especially the case for IrF_6.

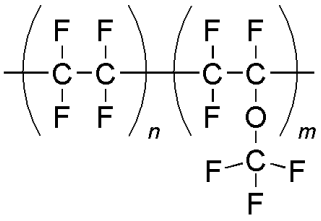

Figure 2.7: Molecular structure of PFA.

Fluorinated ethylene propylene **(FEP)** is a statistical copolymer of tetrafluoroethylene and hexafluoropropylene. The service temperature is 200 °C and thereby slightly lower than that of PTFE and PFA [57]. FEP is utilized for the tubes used for NMR and Raman spectroscopy. However, some of the hexafluorides show a relatively high diffusion rate into FEP at ambient temperature. If they are to be stored at this temperature, other materials should be chosen for the containing vessels. However, low temperature storage seems to be possible. Samples of IrF_6 have been stored in FEP tubes at −40 °C for 4 months without showing signs of degradation. These FEP tubes were additionally enclosed in steel tubes filled with argon, in order to avoid diffusion of moisture from the lab atmosphere into the tubes.

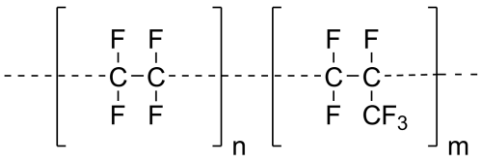

Figure 2.8: Molecular structure of FEP.

Perfluoroelastomers **(FFKM)** are the only known fully fluorinated elastomers of today. Brand names include Kalrez® or Perlast®. Due to the great variety of perfluoroelastomers and the different interlacing types, the declaration of a specific chemical structure is not possible. The impact of the exact composition of the elastomer does not emerge at room temperature. However, it does at elevated temperatures. Figure 2.9 shows an FFKM O-ring made of Parofluor V8920-75 after being used for sealing the sapphire window of the reaction chamber, therefore being located in close proximity to the plasma source. Whereas even prolonged exposure at temperatures below 100 °C did not change the appearance of the material, exposure at 200 °C for only two hours led to a significant degradation of the material. Figure 2.10 shows an O-ring made of Perlast G75H, a FFKM composition especially designed for plasma cleaning processes. Here, no signs of degradation can be identified. Although its exact composition is not accessible, the black color does most likely originate from the addition of elemental carbon to the polymer [58] seemingly facilitating the reaction with the fluorine species at elevated temperatures.

Figure 2.9: FFKM O-ring made of Parofluor V8920-75 showing clear signs of degradation after NF_3 plasma exposure at a temperature of 200 °C for 2 hours.

Figure 2.10: FFKM O-ring made from Perlast G75H without any signs of degradation after NF_3 plasma exposure at a temperature of 210 °C for 2 hours. The black deposits show to be removable.

2.4.3 Glass and ceramics

For the visual inspection as well as the spectroscopic analysis, materials have to be used, that are transparent in the optical spectrum (including UV and IR). However, they have to be resistant to fluorine as well, as many of the investigated hexafluorides possess a comparable or even higher fluorination potential. This immensely limits the number of eligible materials and especially excludes all silicon-based glasses due to the following, exemplary reaction:

$$SiO_2 + 2\ MF_6 \rightarrow 2\ MOF_4 + SiF_4 \qquad (1)$$

M hereby includes the majority of the transition metals investigated (e.g. U, Mo, Re, etc.). This would lead to an unnecessary contamination of the reaction product as well as to a slow decomposition of the window material. Therefore, the material choice is limited to sapphire and single crystals of alkaline and earth alkaline fluorides. A comparison of their spectroscopic properties identifies BaF_2 as being superior to the others, especially due to its much higher cutoff-wavelength. From an optical perspective, BaF_2 is also superior to Al_2O_3 in several aspects. Its transmittance is higher and its cutoff wavelengths, i.e. the wavelength at which the transmittance falls below 10 %, are lower in the UV-range (135 nm vs. 147 nm) and higher in the IR-range (15125 nm vs. 6451 nm). Therefore, it can be used for both, IR and UV/VIS measurements. For BaF_2, its transmittance falls under 10 % at 711 cm^{-1}, under 1 % at 663 cm^{-1} and under 0.1 % at 628 cm^{-1}. The transmission spectra of both materials are shown in Figure 2.11 and Figure 2.12, an enlarged part of the spectrum of BaF_2 in the region between 400 and 750cm^{-1} is shown in Figure A.1 in chapter A.1.1.

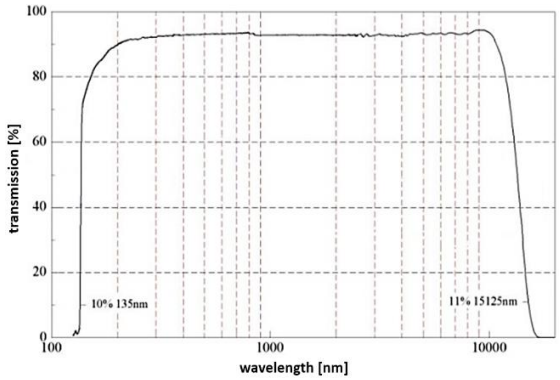

Figure 2.11: IR spectra of a BaF_2 window with a thickness of 2 mm as purchased from Korth Kristalle GmbH [59].

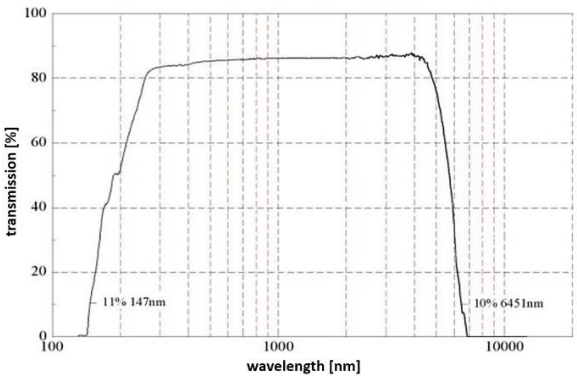

Figure 2.12: IR spectra of a sapphire Al_2O_3 window with a thickness of 2.5 mm as purchased from Korth Kristalle GmbH [60].

However, BaF_2 faces two major disadvantages. The first one is its high sensitivity to temperature gradients and rapid heating or cooling and the resulting risk of cracking of the crystal. The second one, which is by far more serious, is the formation of barium monohydrofluoride $BaF_2 \cdot HF$ in the presence of hydrogen fluoride with a completely different transmission pattern, as can be seen in Figure 2.13. The transition metal hexafluorides easily react with moisture, releasing HF in the process. These two properties complicate the use of BaF_2 as a window material, since it always binds water on its surface when exposed to air. In order to remove this moisture, surfaces have to be heated before exposed to fluorides. However, the heating has to be performed with a low rate of temperature change in order to avoid cracking of the crystal.

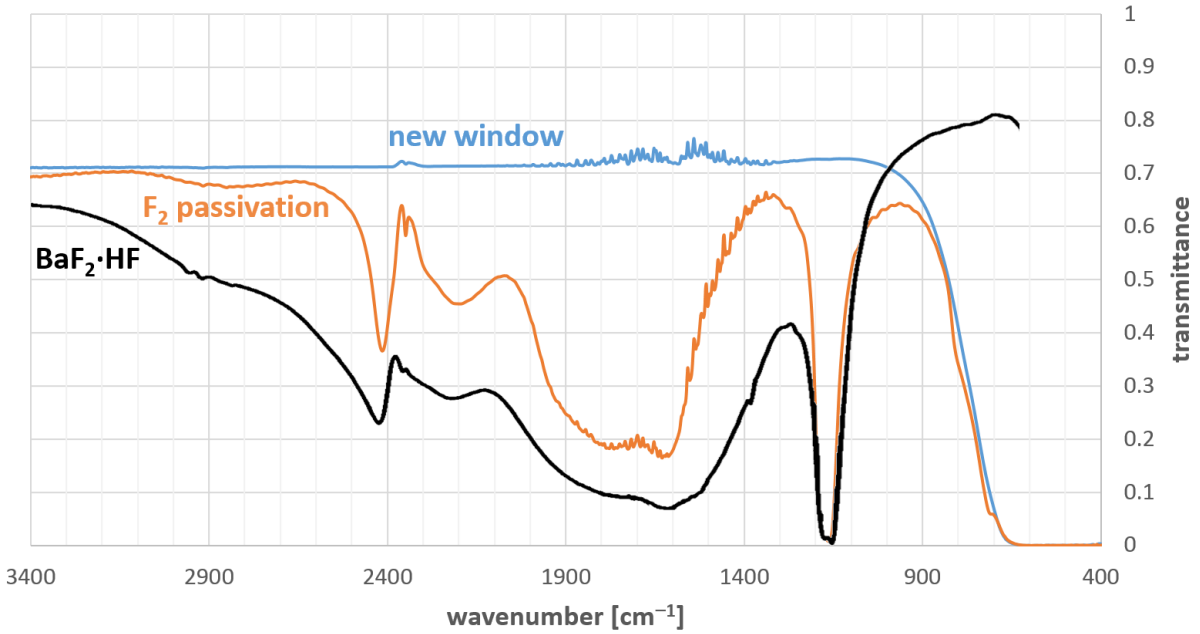

Figure 2.13: IR spectra of a new BaF_2 window (blue graph) and after exposition to fluorine for passivation (orange graph). The black graph is the recorded IR spectra of $BaF_2 \cdot HF$ samples dried at 30 °C [61].

Despite these disadvantages, the very low cut-off wave number of BaF_2 gives the opportunity to distinguish between MoF_6 and UF_6 even at low pressure, as UF_6 has its most prominent absorption band at 625 cm^{-1}. On the contrary, MoF_6 shows almost no absorption at all at that wavenumber. All other alkaline and earth alkaline fluorides have higher cut-off wavenumbers. However, quantitative analysis in this spectral region is not possible due to the low transmittance of BaF_2.

3 Analytical Methods

The following chapter gives a short overview on the applied analytical methods, which were used to identify the synthesized compounds. The focus here lies on spectroscopic methods as they allow for a fast quantitative analysis.

Spectroscopic methods make use of the ability of molecules to interact with electromagnetic radiation under certain conditions. During this electromagnetic interaction, energy is transferred between the incident wave and the molecule, changing its state as well as the spectrum of the radiation. The different spectral regions correlate to specific molecular transitions as shown in Figure 3.1 and Table 3.1.

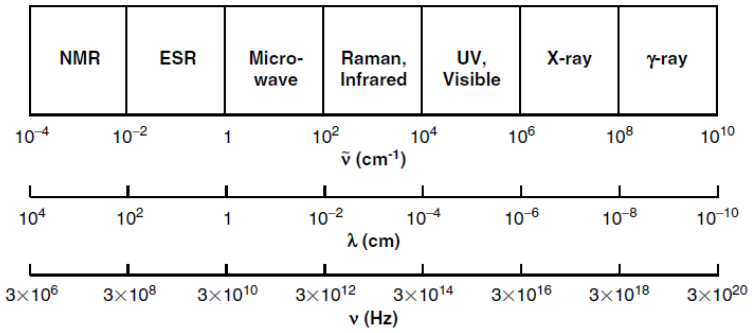

Figure 3.1: The different spectroscopic methods and the corresponding range of the electromagnetic spectrum used for measurement expressed by the wavenumber $\tilde{\nu}$, the wavelength λ and the frequency ν [62].

Due to historical reasons, two different units are being used as the independent variable in spectroscopy, namely the wavelength λ and the wavenumber $\tilde{\nu}$. Both parameters are linked according to

$$\tilde{\nu} = \frac{1}{\lambda} \qquad (2)$$

Whereas the wavenumber is usually favored in IR and Raman-spectroscopy, the wavelength is typically used in UV/VIS spectroscopy. However, deviations of this unwritten convention are possible depending on the date of the publication of interest.

Table 3.1: Spectroscopic methods and the origin of their corresponding signal [62].

spectroscopic method	wavenumber $\tilde{\nu}$ [cm^{-1}]	wavelength λ [cm]	origin	interaction principle
X-ray	$10^6 – 10^8$	$10^{-8} – 10^{-6}$	inner electronic transitions	diffraction
UV/Visible	$10^4 – 10^6$	$10^{-6} – 10^{-4}$	valence electronic transitions	absorption
Raman	$10^2 – 10^4$	$10^{-4} – 10^{-2}$	vibrational transitions	scattering
Infrared	$10^2 – 10^4$	$10^{-4} – 10^{-2}$	vibrational transitions	absorption
NMR	$10^{-4} – 10^{-2}$	$10^2 – 10^4$	nuclear spin level transitions	resonance

The energy of the electronic, vibrational and rotational modes of a molecule differ by about three orders of magnitude, thus the Born-Oppenheimer approximation guarantees that these terms contributing to the total energy of the molecule can be treated separately [63]:

$$E_{total} = E_{el} + E_{vib} + E_{rot} \quad (3)$$

This allows the introduction of independent quantum numbers for each of the corresponding excitation modes. Electronic and rotational states shall not be treated here, as they are only of minor significance for the analysis performed during the experiments of this thesis. In order to describe the vibrational excitations, the chemical bonds between the atoms of a molecule may be approximated by the quantum mechanical model of the one-dimensional harmonic oscillator in proximity to its equilibrium state and its energy levels calculated by:

$$E_n = \left(n + \frac{1}{2}\right)\hbar\omega \quad (4)$$

Obviously, the energy levels in this model are evenly spaced. In combination with the selection rule for the harmonic oscillator $\Delta n = \pm 1$, only one absorption band should be observed for a given vibratory motion [64]. The shortcoming of this model is the asymmetry of the real potential, which can be countered by the introduction of the Morse potential also allowing for an analytical solution of the Schrödinger equation and whose energy levels may be calculated by:

$$E_n = \hbar\omega_0 \cdot \left(n + \frac{1}{2}\right) - \frac{\hbar^2 {\omega_0}^2}{4D_0} \cdot \left(n + \frac{1}{2}\right)^2 \quad (5)$$

In this case, the energy levels are no longer evenly spaced and the selection rules also permit additional values, so that $\Delta n = \pm 1, \pm 2, \ldots$ allowing for the existence of overtones [65]. However, as the difference in energy of the different levels decreases with n, the overtones may not exactly be observed as a multiple of the fundamental excitation but rather at a slightly shifted position.

A spectroscopic measurement does not provide a sharp line, but instead a profile with a certain width, usually described by the full width at half maximum FWHM. Thus, different distributions must be used to fit the measured profile, depending on the aggregation state of the sample [66]. The Gaussian profile is described by (6) and is well suited to describe excitations in solids:

$$y = y_0 + \frac{A}{w\sqrt{\pi/2}} \cdot e^{-2\frac{(x-x_c)^2}{w^2}} \quad (6)$$

The Lorentzian profile is described by (7) and is the best choice to fit excitations in gases [66]:

$$y = y_0 + \frac{2A}{\pi}\frac{w}{4(x-x_c)^2 + w^2} \quad (7)$$

Liquids are best described by a Voigt profile, a convolution of a Gaussian and a Lorentzian profile [66]. In order to facilitate the evaluation, the computationally intensive convolution is often substituted by a superposition of both profiles. This so-called Pseudo-Voigt profile is given by:

$$y = y_0 + A\left[m_u \frac{2}{\pi}\frac{w_L}{4(x-x_c)^2 + {w_L}^2} + (1-m_u)\frac{\sqrt{4\ln 2}}{\sqrt{\pi} w_G} e^{-\frac{4\ln 2}{{w_G}^2}(x-x_c)^2}\right] \quad (8)$$

3.1 X-ray Powder Diffraction

X-ray powder diffraction (XRPD) is one of the oldest methods in crystal structure analysis and has been used for over a century. Different models may be used to explain the physical principle behind this method, although the models of Bragg and Laue are the ones being commonly consulted [67]. Both are equivalent in principle, but Bragg's feels more intuitive and thus shall be the one presented here. In his proposed model, the atoms of a crystal generate a family of lattice planes. At each of these, an incident beam is partly reflected and may interfere with a second beam reflected on a neighboring plane of the same family. Constructive interference is only possible, if the optical path difference of both beams is an integer multiple of the wavelength. As the path difference is given by $2 \cdot d \cdot \sin\theta$, the arising equation is known as Braggs law [68]:

$$n \cdot \lambda = 2 \cdot d \cdot \sin\theta \qquad (9)$$

Herein, λ denominates the wavelength of the incident radiation and n is a positive integer, which may be interpreted as the order of diffraction. d is the interplanar distance and θ the glancing angle. Figure 3.2 illustrates the situation explicated above.

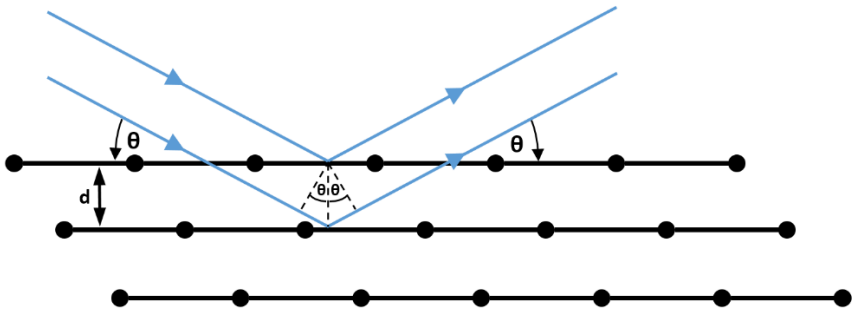

Figure 3.2: Reflection of an incident beam on a family of lattice planes.

Technically spoken, the validity of Bragg's law as described in equation (9) is limited to single crystals. However, a powder may be interpreted as a mixture of crystallites that from an atomic perspective are still very large. The corresponding powder diffraction pattern is therefore identical with the superposition of the patterns for all orientations possible of the corresponding single crystal [67].

The instrument used for XRPD analysis was a *STOE STADI MP* by the STOE company and is shown in Figure 3.3. It can utilize the monochromatic characteristic x-rays, in particular the $K_{\alpha 1}$ lines of cobalt, copper or molybdenum with a wavelength of 1.7902 Å, 1.5406 Å and 0.7107 Å, respectively. The diffractograms of all investigated samples were acquired using molybdenum $K_{\alpha 1}$ radiation.

Figure 3.3: The *STOE STADI MP* X-ray powder diffractometer as used for all XRPD measurements [69].

Two different measuring modes were used at the *STADI MP*. For the first one, the transmission mode, the sample is placed on a flat sample carrier. Samples that are neither sensitive to moisture or oxygen, can be measured most easily by placing them on scotch tape. For many of the high-valent fluorides, the collection of a powder diffractogram is non-trivial. Most of them are highly reactive and sensitive to moisture as well as oxygen. They also appear to react with the adhesive of the scotch tape over time, which prohibits long-term measurements. For these samples, the second measuring mode, the Debye-Scherrer mode, is more appropriate. Thereby, the sample is filled into a thin glass capillary with an inner diameter of 0.3 mm, preferably inside a glovebox. The capillary is afterwards melted off using a red hot tungsten wire and additionally dipped into molten pitch in order to ensure the integrity of the seal. In the case of hexafluorides being the subject of investigation, the capillaries have to be thoroughly dried in order to avoid the formation of SiF_4 according to equation (1) and thus a disruption of the capillary.

In order to assign the reflections of a recorded diffractogram, they are matched with the database of the International Centre for Diffraction Data ICDD. This database is a collection of powder diffraction patterns, which have either been experimentally determined or calculated based on the crystal structure obtained by single crystal diffraction. Each ICDD file is graded and assigned with a quality mark. The marks and their underlying description are listed in Table 3.2.

Table 3.2: Quality marks of the powder diffraction patterns as defined by the ICDD [70,71].

index	meaning	description
S (also *)	Star	well characterized chemically and crystallographically, no unindexed lines, average $\Delta 2\Theta \leq 0.03°$
I	Indexed	well characterized chemically, no unindexed strong lines, average $\Delta 2\Theta \leq 0.06°$
O	Low precision	poorly characterized, with editorial comment explaining the reason
B	Blank	does not meet the criteria for *, I or O
C	Calculated	author calculated d values from single-crystal structural parameters, for which the structural refinement R-factor was < 0.10

3.2 Ultraviolet-Visible spectroscopy

In ultraviolet-visible (UV/VIS) spectroscopy, the absorption in the visible spectrum between 380 and 720 nm as well as its adjacent regions is measured. Excitation in the visible range is typical for colored gases and often finds its origin in the transition of electrons from bonding and non-bonding into anti-bonding molecular orbitals [72]. Quantitative analysis using UV/VIS spectroscopy is also based on applying Lambert-Beers law [73]. However, as UV/VIS spectroscopy has only been performed for qualitative analysis, i.e. the identification of compounds, it will instead be introduced in chapter 3.3.1.

For the experiments, all UV/VIS measurements were performed on a *SPECORD 210 PLUS* of the analytic jena AG covering a total spectral range of 190 to 1100 nm, which is shown in Figure 3.4.

Figure 3.4: The double-beam photometer *SPECORD 210 PLUS* as used for all UV/VIS measurements, covering the wavelength region from 190 to 1100 nm.

Figure 3.5 shows the optical components of the *SPECORD 210 PLUS*. The UV light is generated by a deuterium lamp, the light of the visible spectrum by a halogen lamp. The light passes through a filter wheel, allowing for the suppression of the unrequested wavelengths and is split into different wavelength using a diffraction grating. The exit slit allows for an adjustment of the resolution on the one hand and for the intensity of the signal on the other hand. The use of the smallest slit of 0.5 nm will result in the highest resolution, but may not be able to detect very small concentrations due to the increased signal-to-noise ratio. On the other hand, the largest slit of 4 nm may not be able to resolve very fine structured spectra. The beam splitter splits the incident beam into two beams, one for the measurement of the sample, the other one for the reference measurement [74].

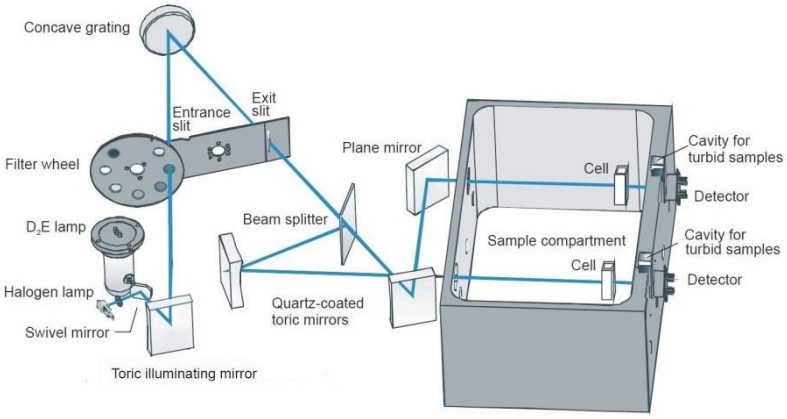

Figure 3.5: Optical diagram of the *SPECORD 210 PLUS* [74].

3.3 Infrared spectroscopy

IR spectroscopy uses the electromagnetic spectrum between approximately 1 µm and 100 µm. This wavelength corresponds to an energy between 0.01 eV and 1 eV and therefore allows transitions between different vibrational levels of a molecule. In order to be IR-active, i.e. capable of being excited by infrared radiation, the dipole moment of a molecule needs to change during the vibrational motion [75]. For this reason, diatomic molecules do not show absorption and cannot be investigated using IR spectroscopy. From the range of different methods, only transmission and attenuated total reflection (ATR) measurements shall be introduced in more detail as they have been used for analysis.

3.3.1 Transmission IR spectroscopy

In IR transmission spectroscopy, an incident beam of known intensity is rayed through the investigated sample and the transmitted intensity is measured.

Figure 3.6: The physical principal of IR transmission spectroscopy. The incident beam with the intensity I_0 excites transitions between vibrational levels and is thereby attenuated to the intensity I [62].

The Lambert-Beer law describes the attenuation of the incident beam [62]:

$$I = I_0 \cdot e^{-\varepsilon c d} = I_0 \cdot e^{-\tau} \qquad (10)$$

This equation is derived based on the assumption of non-overlapping cross sections of the bodies interacting with the radiation and is therefore satisfied very well especially for gases. Thereby, I_0 und I are the intensities of the incident and the transmitted beam, respectively. The exponential argument denotes the molar attenuation coefficient ε, the molar concentration c and the path length d. It is called the optical depth τ and arises from (10) as the negative *natural* logarithm of the transmittance T. However, in spectroscopy, the quantity of interest is not the optical depth but the absorbance, which is defined as the negative *decadic* logarithm of the transmittance [76]:

$$A = \log_{10}\left(\frac{I_0}{I}\right) = -\log_{10} T = \frac{\tau}{\ln 10} \qquad (11)$$

The background correction plays an important role for the investigated samples, especially for quantitative analysis, and has to be executed in two steps. The first part respects the transmission of the window material itself and may easily be performed by recording the spectrum of the empty measuring cell. In addition, it also accounts for reflection of the incident light on the windows of the measuring cell, which does not reach the detector and is lost for the measurement. The second part has to be performed on the acquired spectrum, as the window material may experience a chemical alteration and

thus also a change in its reflectivity especially, in case of the highly reactive platinum metal fluorides.

All transmission IR spectroscopy measurements of the gas phase were performed on a *Tensor 37 FTIR* using a purpose-built measuring cell. The spectrometer is shown in Figure 3.7; the measuring cell is described in detail in chapter 4.3.

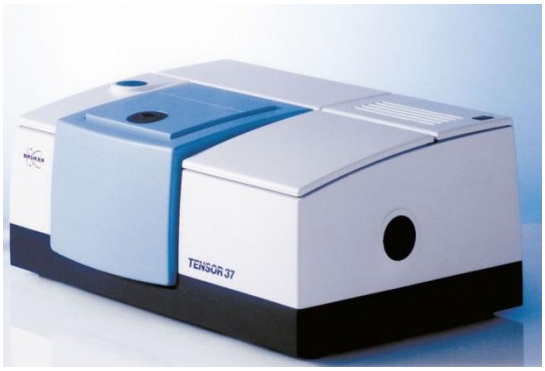

Figure 3.7: The *TENSOR 37* as used for the acquisition of the IR spectra for the hexafluorides as well as for other gas phase IR spectroscopic measurements [77].

Figure 3.8 shows the optical path of the IR radiation from the source to the detector. The radiation is generated using a silicon carbide heating element (A), which is then passed through a collimator (B) and a filter (C) on a beam splitter made of KBr. The beam splitter and its two gold-plated mirrors form in principle a Michelson interferometer [72]. The movement of one of the two mirrors leads to a continuously changing interference pattern of the original wave packet. This radiation is deflected by different mirrors (F) through the windows of the sample compartment (G) and passes through the sample that is to be measured (H). After passing the sample, the radiation passes through the second window (G') and is finally deflected onto the detector. The detector is based on deuterated L-alanine doted triglycine sulfate (DLaTGS). This signal may be transformed from the time domain into the frequency domain by Fourier transform [78].

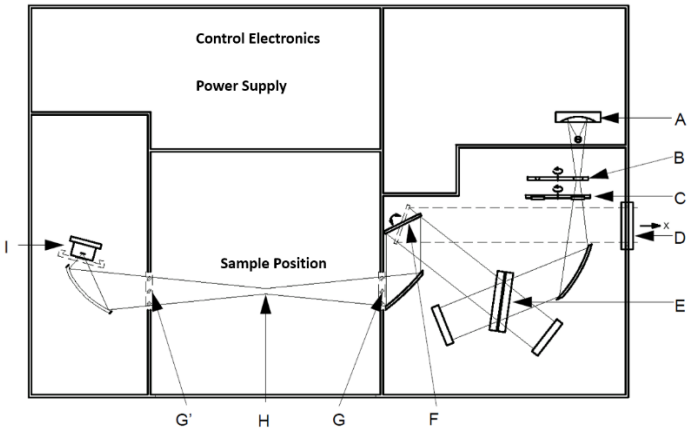

Figure 3.8: Optical diagram of the *TENSOR 37* [78].

3.3.2 ATR IR spectroscopy

In difference to transmission IR spectroscopy, during ATR IR spectroscopy the infrared radiation is not passed through the sample. Instead, this method uses the principle of attenuated total reflection. The centerpiece of an ATR IR spectrometer is a crystal made from a material with a high refractive index such as germanium or diamond [79]. The sample, which is to be investigated, is placed on this crystal. Liquid samples do not need further adjustment, whereas solid samples have to be pressed onto the crystal using the implemented stamp. The infrared radiation is coupled into this ATR crystal and experiences internal total reflection as it passes through it, if the sample has a lower refractive index than the crystal. However, the IR radiation is not instantly reflected at the sample-crystal interface, but expands into the sample for about 2 to 15 µm as an evanescent wave [80]. This wave attenuates exponentially, but is able to interact with the sample, thereby exciting its vibrational modes. The corresponding wavenumbers are suppressed in the observed spectrum.

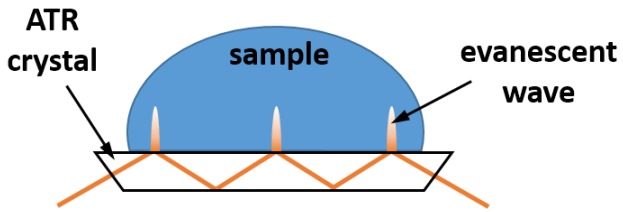

Figure 3.9: The principle behind ATR IR spectroscopy.

The strength of the signal depends on the contact pressure on the one hand and on the number of reflections on the other hand.

The spectrometer used for ATR IR spectroscopy was a *Bruker Alpha*, which was situated in a glovebox and therefore allowed measurements under argon atmosphere. As argon itself as an atom is IR inactive and the moisture in the glovebox was kept at a very low level, the noise in the spectrum was thereby significantly reduced. For all measurements performed on the *Alpha*, a diamond crystal was used.

Figure 3.10: The *Bruker Alpha*, as used for all ATR IR measurements performed during the experiments [81].

3.4 Raman spectroscopy

Raman spectroscopy is closely related to IR spectroscopy, but instead of detecting the absorption of photons, it observes the change in energy of scattered photons [72]. The sample to be investigated is thereby irradiated with a linearly polarized laser in the visible or near-infrared spectrum of frequency ν_0. During this irradiation, the molecule is excited to a virtual state and de-excites after a short period to a different energy level. This state is no real excited state but rather finds its origin in the interaction of the laser with the molecule's electron cloud causing temporary polarization. Thus, in order to be Raman-active, the polarizability of a molecule needs to change during vibration [62].

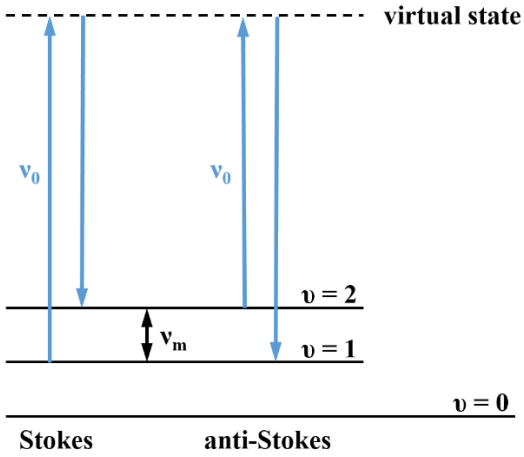

Figure 3.11: The excitation from a real vibrational state υ to a virtual state via laser irradiation with a frequency ν_0. The energy of the photon differs prior to and after the scattering process by ν_m [62].

This change in energy of the scattered photon distinguishes the inelastic Raman scattering from elastic Rayleigh scattering. Only a fraction of scattering events ($\sim 10^{-5}$) is inelastic in nature. Raman scattering therefore is a rather weak phenomenon, which is why overtones and combination bands are usually not observed in Raman spectra [82]. The frequency ν_0 is chosen in a way that the virtual state lies well below the first excited electronic state. If the molecule gains energy during the scattering process, the corresponding signal found at $(\nu_0 - \nu_m)$ is on the so-called Stokes side, if it loses energy, the signal found at $(\nu_0 + \nu_m)$ is on the anti-Stokes side. For that reason, the quantity measured is not the actual wavenumber, but rather its shift with respect to the incident radiation. Figure 3.12 illustrates this principle, especially the difference to transmission IR spectroscopy [62,83].

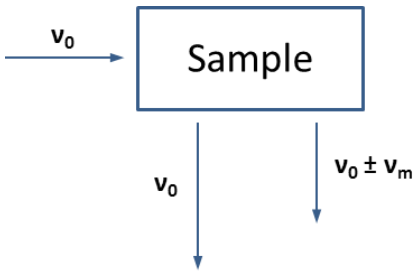

Figure 3.12: The physical principle of Raman spectroscopy [62].

The intensity of the scattered signal depends on a number of parameters, namely the frequency ν and intensity I_0 of the incident beam, the number of scattering particles N and the change in polarizability α in dependence of the wave vector q is according to [72] described by equation (12):

$$I \sim \nu^4 \cdot I_0 \cdot N \cdot \left(\frac{\partial \alpha}{\partial q}\right)^2 \qquad (12)$$

All Raman measurements were performed on a *Mono Vista CRS+*, as it is shown in Figure 3.13. This spectrometer allows for the irradiation of the sample at four different wavelengths of 488, 532, 785 and 1064 nm. The samples were condensed into FEP tubes with an inner diameter of 1.6 mm and a wall thickness of 0.8 mm. Some of the hexafluorides that under standard conditions would only be existent in the gas phase can thereby be measured in the liquid state. In addition, these tubes may also be used for NMR spectroscopy, allowing the acquisition of different spectra and thereby complementary information on the same sample.

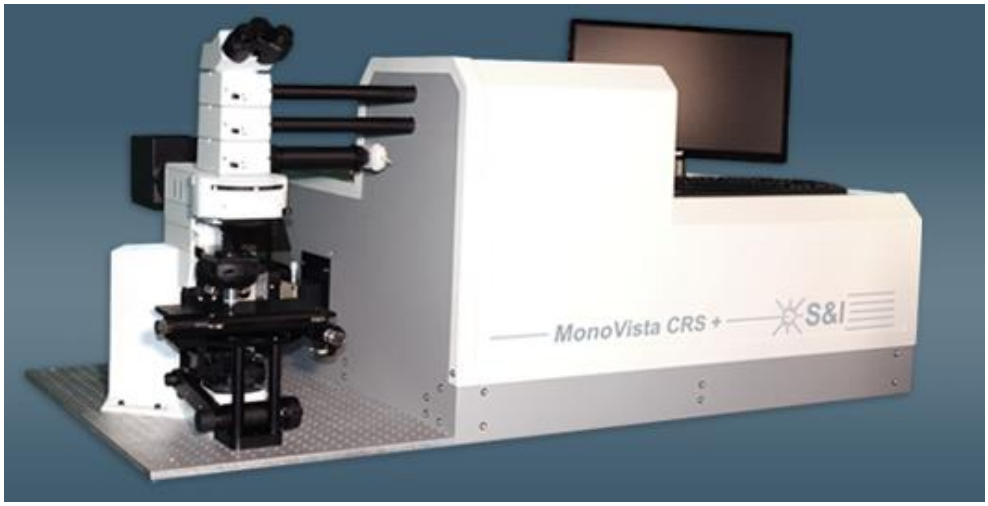

Figure 3.13: The *MonoVista CRS+* as used for the acquisition of all Raman spectra measured during the experiments [84].

The FEP tubes themselves are manufactured from an FEP hose with an inner diameter of 1.6 mm and an outer diameter of 3.0 mm cut into pieces of a length of 180 mm each. These pieces are put into a glass tube with an inner diameter of 3.2 mm, which is then heated to a temperature of 400 °C causing the FEP to melt. Gently pressing the FEP hose into the glass tube forms a plug sealing off one side of the FEP. Having undergone passivation as described in chapter 2.4.1, these tubes have the advantage of being resistant to even the platinum metal hexafluorides and sustaining an internal pressure of more than 8 bar. For investigation, the synthesized volatile hexafluorides are condensed into these FEP tubes. During the condensation process, the lower end of the tube is inserted into a Dewar and cooled with liquid nitrogen whereas the upper part is melted off using a heat gun set to a temperature of 500 °C.

Figure 3.14: FEP tube as used for Raman and NMR spectroscopy.

FEP itself is Raman active and its spectrum is depicted in Figure 3.15. Very characteristic is the series of three peaks between 1180 and 1400 cm^{-1}. As none of the hexafluorides shows bands in this region, this band series is well suited for identifying the presence of FEP in the spectrum.

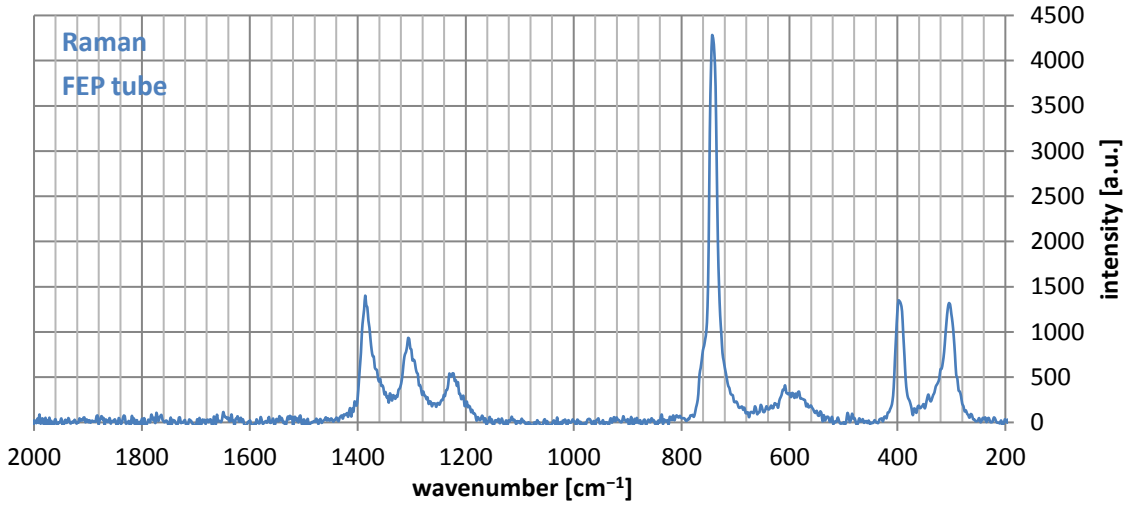

Figure 3.15: Raman spectrum of an empty FEP tube as it is shown in Figure 3.14 measured with a laser wavelength of 532 nm and a groove density of 300 g/mm.

The entire Raman spectrum shows the presence of eight bands, whereas one of these is only visible as a shoulder in the band at 303.2 cm^{-1}. One additional band may be present at the left side of the band at 741.4 cm^{-1}, as a shoulder is also visible there. All fitting was performed using Voigt profiles; the corresponding fitting plots are shown in Figure A.2 to Figure A.4. The knowledge of the FEP spectrum is crucial for the analysis of the spectra of the hexafluorides, as their ν_5 fundamental is in the vicinity of the prominent band at 741.1 cm^{-1}.

Table 3.3: Positions of the bands in the Raman spectrum of FEP as shown in Figure 3.12.

wavenumber [cm^{-1}]
303.2
325.7
395.7
598.7
741.4
1223.5
1304.4
1383.4

3.5 Nuclear Magnetic Resonance Spectroscopy

Nuclear magnetic resonance (NMR) spectroscopy has become one of the leading experimental identification methods, especially in molecular chemistry. In combination with ICP-MS and IR spectroscopy, it allows the identification of the molecular structure of an investigated substance. However, only atoms possessing a nuclear spin different from zero are accessible to this investigative method and are therefore called NMR active [85]. As all NMR spectroscopy has been performed with respect to ^{19}F, which possesses a nuclear spin of I = ½, the following remarks will apply for spin ½ nuclei. These nuclei are characterized by possessing only two spin states, called the α spin state and the β spin state [86]. The z-component of the angular momentum vector is given by

$$\mu_z = \gamma m \hbar \qquad (13)$$

with the gyromagnetic ratio γ and the magnetic quantum number m. As m can take values from m = I, I−1,…,−I, only two values are allowed for spin ½ nuclei, which are $\mu_z = +½\gamma\hbar$ and $\mu_z = -½\gamma\hbar$. Fluorine possesses the advantages of being isotopically pure, as ^{19}F is its only stable nucleus and furthermore has a high gyromagnetic ratio of 40.078/2π MHz/T [34]. The energy of a magnetic dipole in an external homogenous magnetic field is given by:

$$E = -\ \mu_z \cdot B_{eff} \qquad (14)$$

Therefore, the degenerate energy level of a spin ½ nuclei splits, if exposed to an external magnetic field. The exact strength of this magnetic field largely depends on the electronic environment of the fluorine atom. This phenomenon is called diamagnetic shielding. Thus, a nucleus being subject to diamagnetic shielding does not entirely experience the external magnetic field B_0, but rather a reduced magnetic field B_{eff}. This field is weaker than the field of a deshielded nucleus, also resulting in a decrease in energy difference between the two spin states.

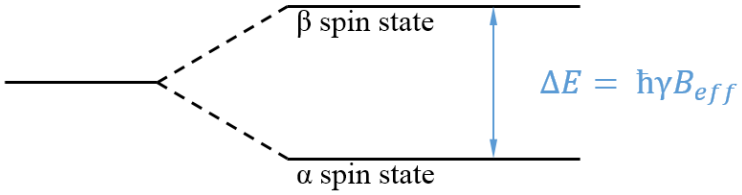

Figure 3.16: Splitting of a degenerate spin state into an α spin state of lower and a β spin state of higher energy in the presence of an external magnetic field.

As the α spin state is of lower energy as the β spin state, the latter is not as densely populated. The population density is given by a Maxwell-Boltzmann distribution [86]:

$$\frac{N_\beta}{N_\alpha} = e^{-\frac{\hbar\gamma B_{eff}}{k_B T}} \qquad (15)$$

The difference in the population of the two spin states gives rise to the recordable signal, as the z-components of the other spins cancel out. As the spin of the nucleus is not aligned parallel to the external magnetic field, it is precessing around the magnetic field lines with the Larmor frequency

$$\omega_L = -\gamma B_{eff} \quad (16)$$

By irradiating the investigated compound with a short RF pulse of a carefully chosen length at this resonance frequency, the precession may be shifted into the perpendicular plane. After switching off the exciting radiofrequency, the system will return to its original state within the spin-spin relaxation time T_2, emitting radiation for its part, which is recorded [87]. By repeating this procedure several times, the signal-to-noise-ratio may be significantly enhanced. The resulting signal is transformed from the time domain into the frequency domain using Fourier transformation [88].

In order to decouple the energy difference between the two spin states and the corresponding frequency from the applied magnetic field, the *chemical shift* δ is introduced. This quantity is measured in parts per million and is always given with respect to a reference compound [87]. For ^{19}F-NMR this reference compound usually is $CFCl_3$:

$$\delta = 10^6 \cdot \frac{\nu - \nu_{CFCl_3}}{\nu_{CFCl_3}} \quad (17)$$

All NMR measurements on the hexafluorides were performed using FEP tubes as already described in chapter 3.4. The FEP tube for its part is additionally placed into a standardized NMR glass tube. The spectrum of both components without any content measured against $CFCl_3$ is shown in Figure 3.17.

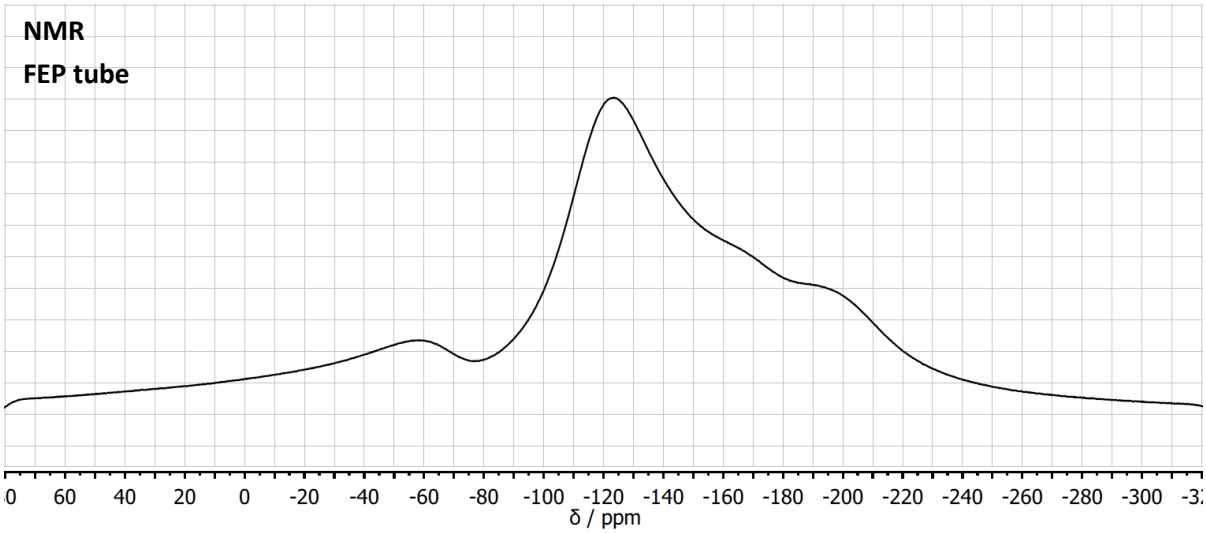

Figure 3.17: NMR spectrum of an empty FEP tube in glass tube, showing a very broad signal peaking at −122 ppm with respect to $CFCl_3$.

One of the major drawbacks of NMR spectroscopy is the necessity of the sample being available in a diluted or liquid form, although the recording of a gas phase NMR is also an alternative for compounds with sufficient vapor pressure. However, experiments performed trying to quantify the amounts of UF_6 and MoF_6 in a mixture of the two hexafluorides gave different results, even if the same sample was repeatedly measured. This method therefore proved to be unsuited for quantitative analysis aiming at the determination of the ratio of the two hexafluorides.

3.6 Microwave plasma atomic emission spectroscopy

Atomic emission spectroscopy (AES) uses the characteristic radiation emitted by excited atoms when they return to their ground state. The excitation thereby takes place between electronic states, the electrons move between two electronic orbitals [89].

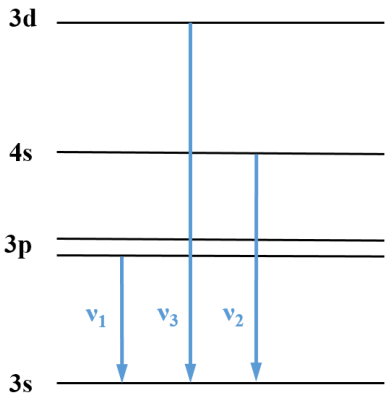

Figure 3.18: The emitted radiation in AES finds its origin in the transition of electrons between different atomic orbitals [89].

As the population of the excited states again is given by a Maxwell-Boltzmann distribution, high temperatures are preferable in order to increase this population, thereby generating a strong signal and improving the detection limits. Different methods of providing this temperature have been established, inductively coupled plasma (ICP-AES) and microwave plasma (MP-AES) being two very commonly used techniques [89].

All AES measurements were performed on an *Agilent 4200 MP-AES*. The energy necessary for excitation is hereby provided by a nitrogen plasma at a temperature of about 5000 K, whereas the plasma for its part is created by an industrial magnetron. The liquid sample is introduced as an aerosol in the center of the plasma and after passing through a monochromator, the emitted radiation is detected by a CCD detector [90].

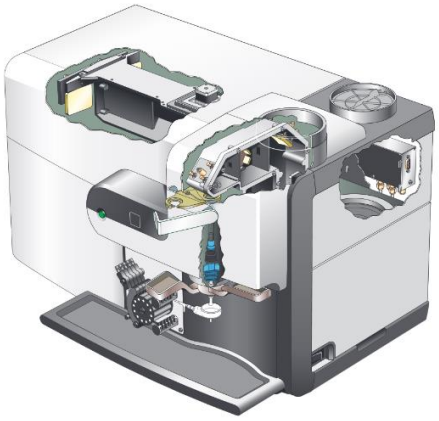

Figure 3.19: The *Agilent 4200 MP-AES*, as used for the performed AES measurements [91].

The method is well suited for the determination of the concentration of uranium and molybdenum in solution. Both elements show an almost entirely linear dependency between their concentration in the solution and the resulting intensity of the signal.

4 Instrumentation and applied methods

4.1 Microwave Plasma Fluorination Line

All of the investigated fluorides were synthesized using fluorine radicals generated by microwave radiation in a newly designed system, hereinafter referred to as fluorination line. It consists of the following major subsystems:

The gas supply, the remote plasma source (RPS), the reaction tube, the pipelines and cold traps, the absorption system and the pumping unit. The system is completed by several peripheral devices. These include control units for the mass flow controllers (MFCs), the readout device for the pressure sensors, the control unit for the oven, the power supply for the microwave as well as PC, keyboard and screen, which are necessary to operate the control software for the RPS. The wiring of the system is housed in a separate control cabinet.

The use of three MFCs allows the control of the gas flow rate and thus the exact composition of the process gas. The process gas is fed into the RPS, where fluorine, hydrogen and oxygen radicals are formed, depending on its exact composition. The use of oxygen potentially allows the synthesis of oxyfluorides, whereas the use of hydrogen allows the removal of potential oxide layers on the substrate.

The actual fluorination takes place in the heatable reaction tube. The cold traps are located downstream and allow the deposition of the reaction product. Operation of the cold traps at different temperatures allows for a separation of synthesized fluorides based on a difference in vapor pressure at a given temperature. The use of the last cold trap as a “getter trap” has proven to be advantageous in order to remove residues and impurities from the system.

Further downstream, the fluorine absorbers are located, which bind unconsumed reactive fluorine species and thereby protect the subsequent pumps. They consists of two 40 x 150 mm tubes filled with soda lime, that is, a mixture of calcium hydroxide, sodium hydroxide and potassium hydroxide. Temperature sensors at different positions of the tube show the position of the reaction front and thereby the exhaustion of the absorber.

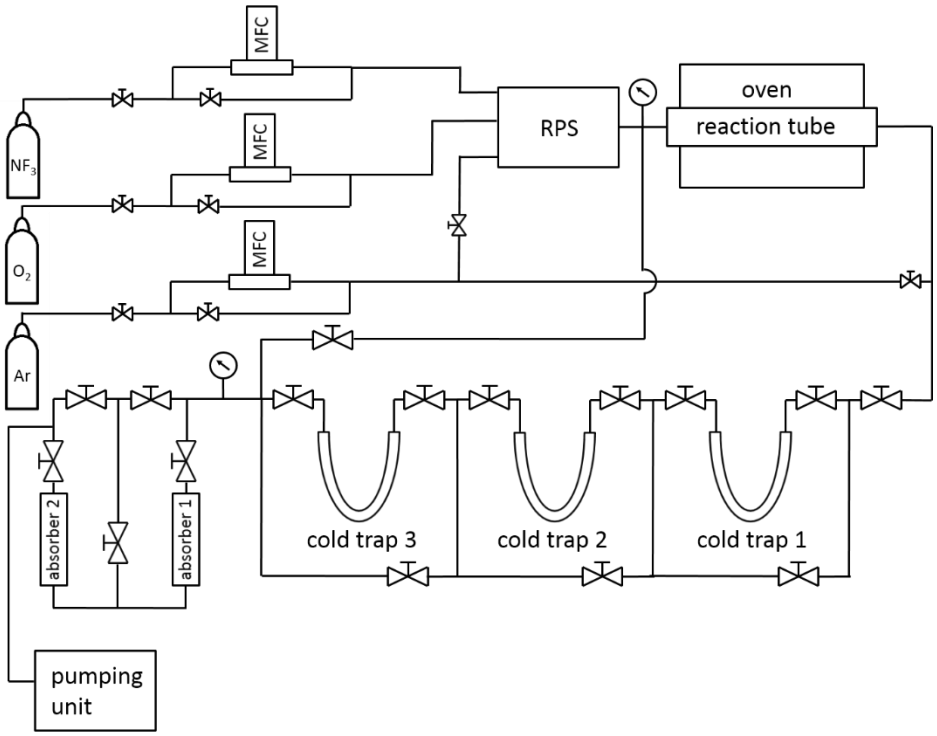

Figure 4.1: Flow chart of the fluorination line. The composition of the gas flow is regulated by three mass flow controllers, one for argon, oxygen/hydrogen and nitrogen trifluoride each. The process gas reaches the remote plasma source, where fluorine and oxygen radicals are generated. The fluorination takes place in the reaction tube, which can be heated. The reaction product is deposited in the subsequent cold traps and can be removed via extraction ports situated behind each cold trap. Subsequently to the cold traps, two fluorine absorbers are located, which bind unconsumed reactive fluorine species and thereby protect the pumping unit.

Figure 4.2: General view of the system in the labs of the AG Kraus at the Philipps-Universität Marburg.

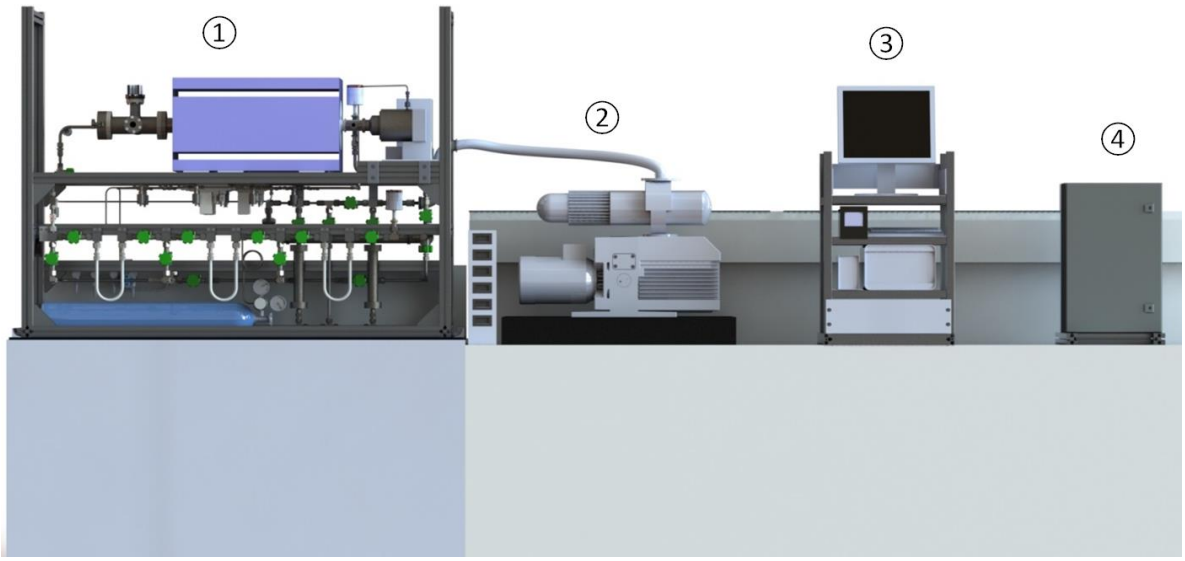

Figure 4.3: General view of the fluorination line as a CAD model (frontal view). The fume hood, in which the line is actually situated, has been removed for clarity. It consists of the core piece (1), the pumping unit (2), the control unit (3) for the peripheral controllers and evaluation units for the RPS, the MFCs, the oven, the pressure sensors as well as the control cabinet (4).

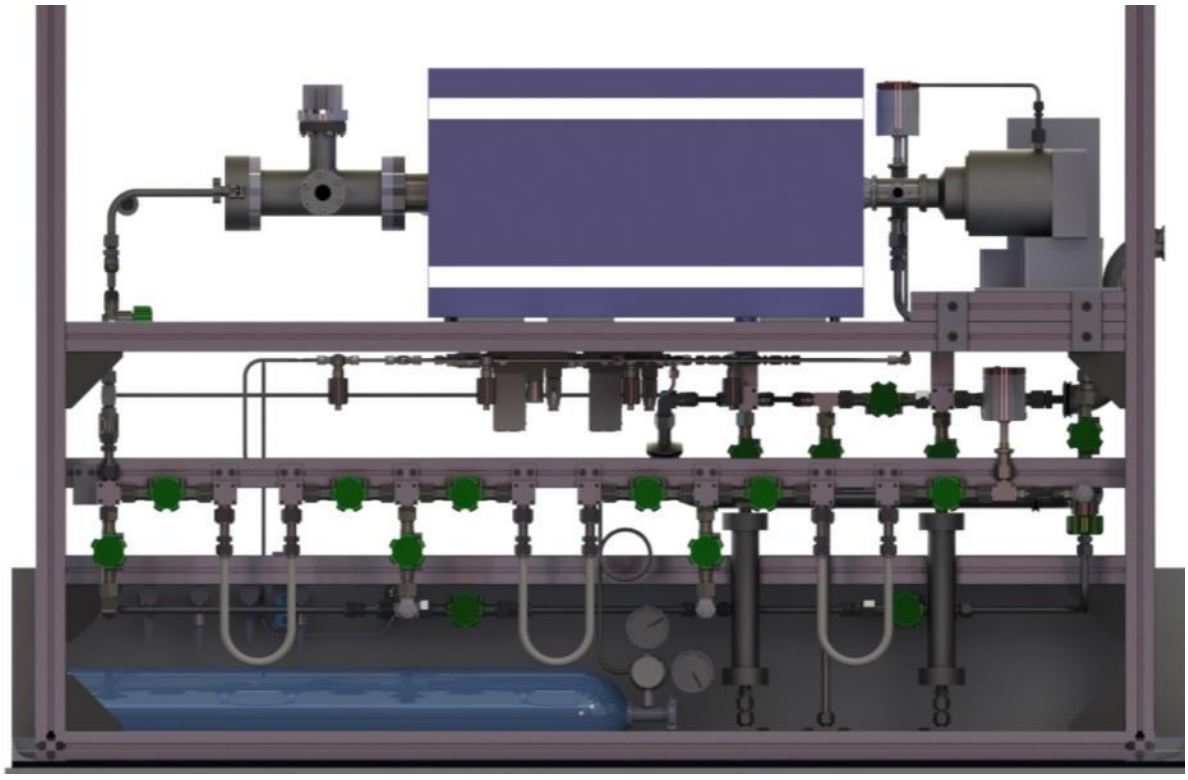

Figure 4.4: Core part of the line without peripheral components as a CAD model (front view).

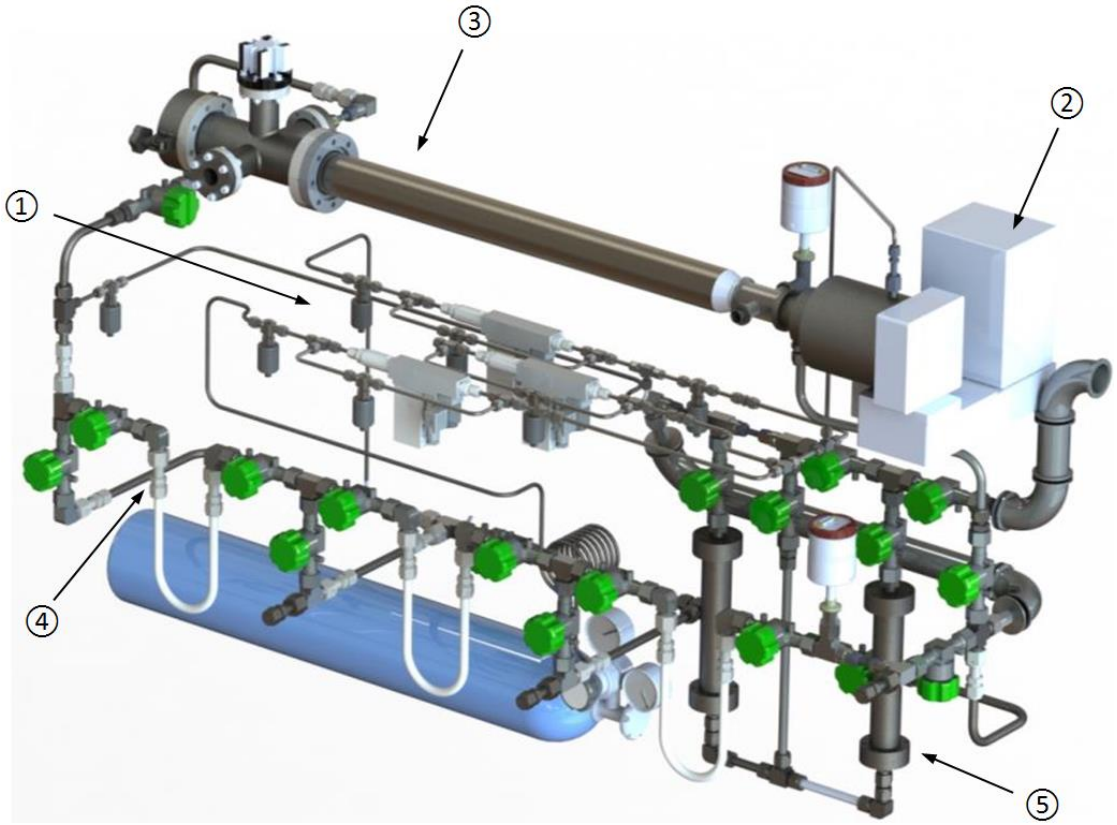

Figure 4.5: Core part of the line as a CAD model. The entire supporting structure as well as the oven has been removed for clarity. It consists of the following subsystems: the gas supply (1), the RPS (2), the reaction tube (3), the cold traps with bypass (4) and the absorption system (5).

4.1.1 Vacuum and gas supply system

In order to ensure a stable process, a dynamic equilibrium concerning pressure and gas flow has to be established. The supply with the required process gases is controlled by three MFCs manufactured by the Bronkhorst Company. Currently, these are driven over an RS232 interface with the Readout and Control System E-8501-0-2A, likewise of the Bronkhorst Company. For a later process with implementation of a programmable logic controller, the MFCs are also equipped with an EtherCAT port. The readout of the pressure takes place by two capacitive sensors CERAVAC Transmitter CTR100N of Oerlikon Leybold with a maximum pressure range of 100 Torr and 10 Torr, respectively. Thereby, the 100 Torr sensor is located directly subsequent to the RPS, whereas the 10 Torr sensor is located downstream of the third cold trap (see Figure 4.5).

MFC 1 supplies the RPS with the fluorine containing process gas, namely NF_3, although other process gases would also be suitable (see following chapter). In order to ensure a high life time, MFC 1 is equipped with FFKM gaskets. The volume flow may be adjusted between 2 and 200 sccm.

MFC 2 supplies the RPS with argon. The volume flow of NF_3 as well as the ratio of NF_3 and argon have a major impact on the etching rate. Furthermore, argon is used for purging the line after the fluorination process and to ensure a counter flow when opening the extraction port. This minimizes the intrusion of oxygen and moisture. The gaskets of MFC 2 are made of Viton. Also in this case, the volume flow may be adjusted between 2 and 200 sccm.

MFC 3 supplies the line with either oxygen (synthesis of oxyfluorides) or hydrogen (removal of potential oxide layers on the substrate by hydrogenation). The volume flow of this MFC may be adjusted between 60 and 10,000 sccm.

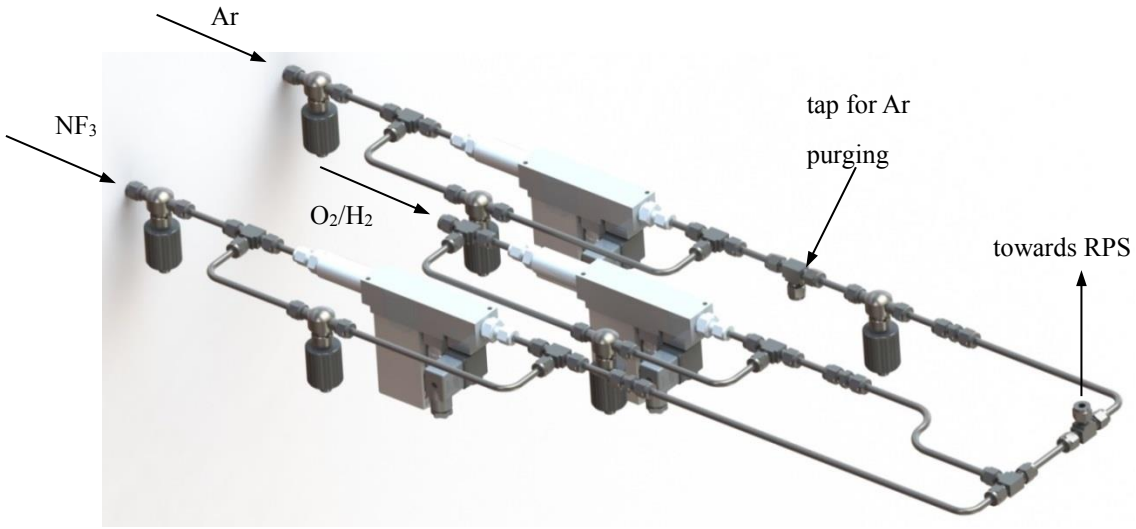

Figure 4.6: The gas supply for argon, NF_3 and oxygen/hydrogen using MFCs. Each MFC can be bypassed. An additional tap in the argon line allows the independent purge of the lower part of the system, which includes the cold traps and the extraction ports.

4.1.2 Remote Plasma Source (RPS) and reaction chamber

The remote plasma source (RPS) is the model MA3000C-193BB manufactured by the MUEGGE company. It is the component responsible for establishing the plasma by using microwaves with a frequency of 2.45 GHz to crack the N−F bonds in the etching agent thereby creating fluorine radicals. The grade of dissociation exceeds 95 %. According to the technical specifications, the model requires high flow rates of the process gas of at least 500 sccm. However, it could be shown during operation, that the RPS can be operated safely at much smaller flow rates of as low as 2 sccm. A potential negative effect on the etching rates could not be observed.

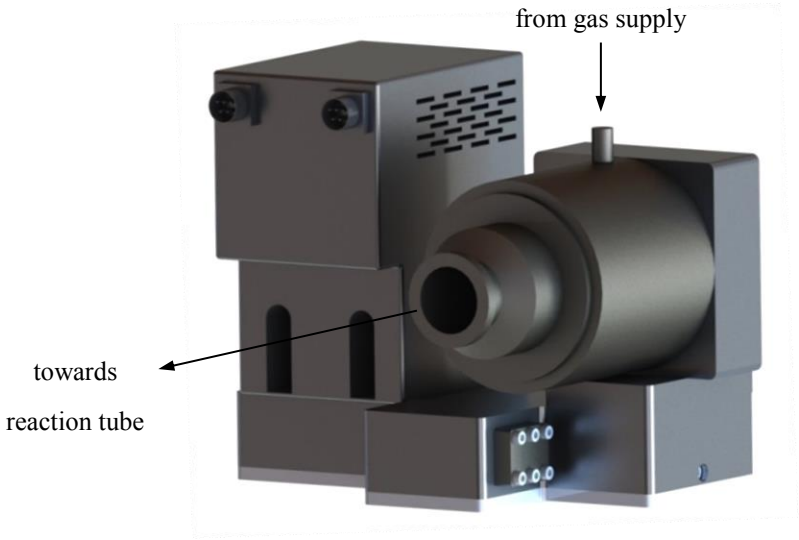

Figure 4.7: Remote Plasma Source MA3000C-193BB of the MUEGGE Company as a CAD model. The fluorine radicals are generated in this device via microwave radiation.

The RPS itself is powered by the microwave power supply MX3000D-117KL (MPS) manufactured by the MUEGGE Company, which can operate at a maximum output of 3000 W. It is controlled via PC, which runs the Windows-based control software shown in Figure 4.8. However, the input signal for the MPS is based on CAN bus, so a signal converter is interposed between the PC and the MPS.

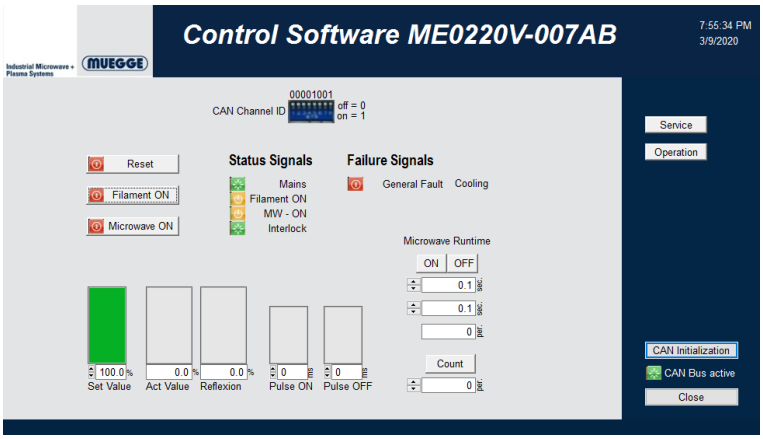

Figure 4.8: Interface of the control software of the RPS allowing for activation, deactivation and power setting.

Both components, the RPS and the MPS, depend on sufficient cooling in order to ensure safe operation. Therefore, the monitoring of the temperature and the flow rate of the cooling water for both components

is automated. As soon as its temperature leaves a precisely defined window, an interlock shuts down the MPS preventing an overheating on one hand as well as a condensation of air moisture on the electronic components on the other hand. The interlock is also triggered, if the flow rate falls below 4 L/min. If the pressure of the cooling water exceeds 4 bar, magnet valves at the entry switch of the feed pipe in order to protect the system from damage and leakage.

According to the specifications of the RPS, three different fluorine containing etching agents may be used in the RPS: nitrogen trifluoride NF_3, sulfur hexafluoride SF_6 and carbon tetrafluoride CF_4. In addition, elemental fluorine may also be used. Their chemical structure is shown in Figure 4.9 to Figure 4.12, whereas the corresponding bond strength for homolytic cleavage is listed in Table 4.1.

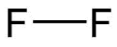

Figure 4.9: Molecular structure of F_2.

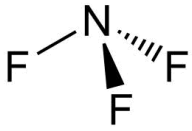

Figure 4.10: Molecular structure of NF_3.

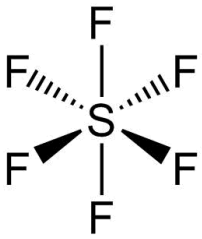

Figure 4.11: Molecular structure of SF_6.

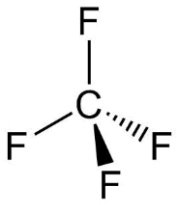

Figure 4.12: Molecular structure of CF_4.

An evaluation of the bond strength identifies NF_3 as being well suited for use in the RPS. Its nitrogen-fluorine bond is weaker as the corresponding sulfur-fluorine bond in SF_6 and the carbon-fluorine bond in CF_4. Therefore, the dissociation of NF_3 is nearly complete, resulting in a higher fluorine radical concentration compared to the other etching gases. Only the bond strength of F_2 is even lower, but comes at the cost of the by far higher toxicity and much more difficult manageability due to reactivity and corrosivity.

Table 4.1: Bond strength for homolytic cleavage of the different potential etching agents [92,93].

etching agent	specific bond	bond strength [kJ/mol]	bond strength [eV]
F_2	F – F	159	1.65
NF_3	NF_2 – F	238.5	2.47
SF_6	SF_5 – F	420	4.35
CF_4	CF_3 – F	546.0	5.66

NF_3 holds the further advantage to be cracked into volatile components not leaving residues in the fluorination system. Sulfur has a strong affinity to form polymeric molecules, which may accumulate in critical components such as the membrane valves. The same holds for CF_4. For the etching processes

in the semiconductor industry, it is usually applied in combination with oxygen in order to avoid the formation of polymeric residues.

All of the etching agents aside from elemental fluorine have the disadvantage of a very high global warming potential (GWP[1]), as can be seen in Table 4.2. It also shows the direct correlation of the strength of the fluorine bond with the lifetime of the etching agent.

Table 4.2: Lifetime and GWP of potential etching agents [92,95,96]. ITH stands for integration time horizon, i.e. the period of time, for which the warming potential is taken into consideration. The number indicates the years taken into consideration for the calculation. All values are normalized with respect to CO_2 (GWP = 1), which has a lifetime of 100 years.

etching agent	lifetime [a]	GWP, ITH_{100}	GWP, ITH_{500}	GWP, ITH_{∞}
NF_3	740	10,000	14,000	18,000
SF_6	3,200	23,000	32,000	230,000
CF_4	50,000	6,000	9,000	850,000

Despite its advantage of leaving no residues in the system, NF_3 still forms a number of volatile compounds under plasma conditions. In order to identify these components, the plasma line was operated for 45 minutes at the absence of a target in the reaction chamber and the reaction products collected by freezing them out using liquid nitrogen. Figure 4.13 shows the IR spectrum of the content of the first cold trap, which was cooled to a temperature of −200 °C. When being warmed to room temperature, the compounds completely enter the gas phase. However, the pressure stays well below the pressure expected, if the reaction products were entirely deposited in the cold traps. Therefore, they must possess a considerable vapor pressure at −200 °C and be highly volatile, greatly reducing the number of the species in question.

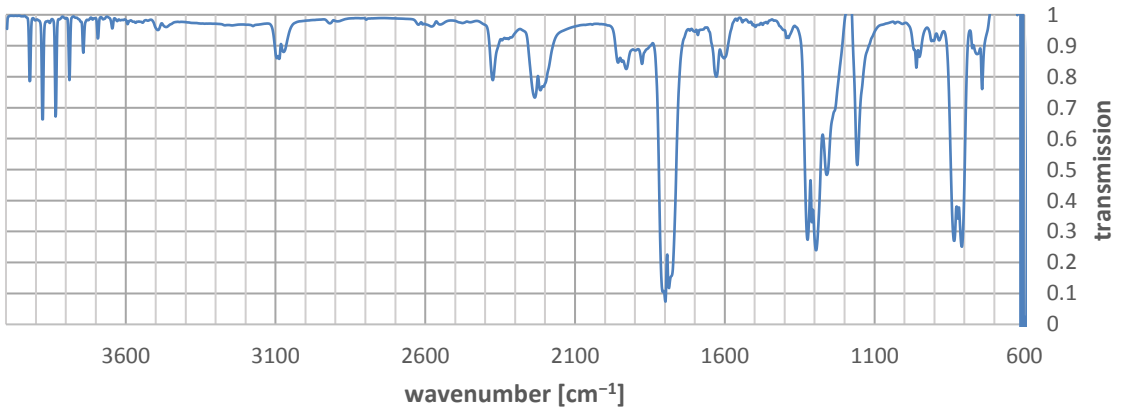

Figure 4.13: IR spectrum of the content of the first cold trap held at −200 °C without a target in the reaction chamber. Fluorination took place for 45 minutes at an Ar flow of 10 sccm and an NF_3 flow 10 sccm.

[1] The Global Warming Potential (GWP) is "an index, based on the radiative properties of greenhouse gases, measuring the radiative forcing following a pulse emission of a unit mass of a given greenhouse gas in the present-day atmosphere integrated over a chosen time horizon, relative to that of carbon dioxide." [94].

The seven bands in the region between 3600 and 4000 cm^{-1} can be identified as the p-branch of the rotational excitations of hydrogen fluoride being approximately equidistant with $46 \pm 2\ cm^{-1}$. Unfortunately, none of the other bands could be assigned. Compounds, which seemed likely to be formed such as tetrafluorohydrazine N_2F_4, could not be identified. Some of these signals are also found in the synthesized hexafluorides, allowing the conclusion that they are not to be assigned to these reaction products.

The concentration of fluorine radicals and the etching rate depend on a large variety of parameters. The most influential of these parameters are:

- system pressure
- position of the substrate
- temperature
- mixture etching gas/inert gas
- flow profile

Fluorine radicals are a highly reactive species and therefore only have a very limited lifetime. Two mechanisms are responsible for their recombination: surface recombination particularly at low pressures in the low one-digit mbar region and volume recombination as the dominating process at higher pressures [92]. The process of surface recombination takes place in two steps. First, a fluorine atom is absorbed on the surface. Subsequently, it can either be thermally desorbed and continue its existence as a fluorine radical or it can interact with another fluorine atom, forming a F_2-molecule, which for its part desorbs from the surface. The process of volume recombination is also a three-body reaction involving two fluorine atoms and one atom of the carrier gas [92].

The influence of the system pressure and the position of the substrate is depicted in Figure 4.14. Two conclusions can be deduced from that diagram in order to minimize recombination losses. First, the pressure of the process should be kept as low as possible. Second, the substrate must be placed closely to the exit of the RPS and unnecessary tubing in between has to be avoided.

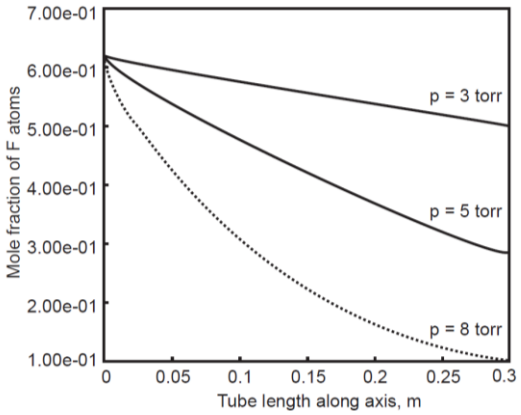

Figure 4.14: Mole fraction of fluorine atoms as a function of the length of the tube they are injected in [92].

The reaction chamber was originally intended to be a 700 mm long nickel tube, which was located in an oven and that is depicted as part ① in Figure 4.15. The idea behind this setup was the ability of heating the substrate, which proved to be necessary for the synthesis of some of the platinum metal fluorides. However, the first experiments revealed the need for a reduction of the distance of the substrate to the RPS. This instance led to an adjustment of the position of substrate carrier in favor of the 4-way cross indicated as part ② in Figure 4.15. As this component was equipped with a sapphire window, this position also provided the possibility of the observation of the substrate during the fluorination process.

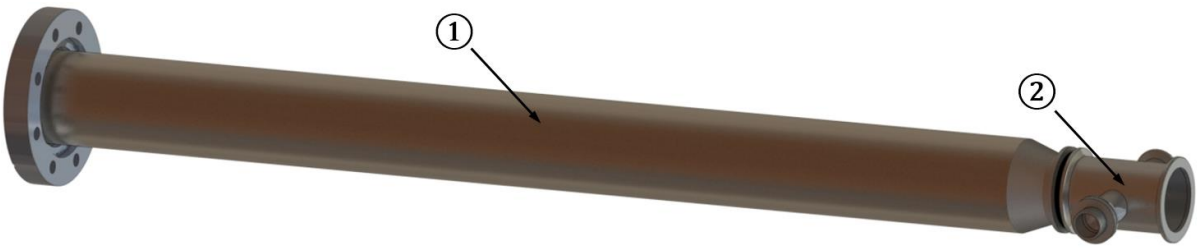

Figure 4.15: The originally intended reaction chamber (1) and the 4-way cross (2) used instead after the first unsuccessful trial. A sapphire window allowed the observation of the fluorination.

The term reaction chamber hereinafter always refers to the 4-way cross. Due to the design of the chamber, the temperature of the substrate is not accessible during the etching process. The use of a pyrometer seemed to be problematic, as the emissivity of the substrate material was expected to change during the course of the reaction. Instead, the wall temperature of the reaction chamber was measured on its upper and the lower side. Although this temperature may be used to gain some knowledge about the course of the reaction, it must not be taken as a measure for the temperature of the substrate material. The sapphire window used to observe the reaction consists of a sapphire disc soldered to a KF flange. Unfortunately, the soldering metal proofed not to be fluorine resistant and decomposed over time, as can be seen in Figure 4.16 and Figure 4.17.

Figure 4.16: New sapphire window.

Figure 4.17: Sapphire window after being used for approximately 100 hours of fluorination.

However, the decomposition extends over a period of several tens of hours, so a regular exchange of the window was possible. An advanced version of the reaction chamber should address this problem by abdicating the utilization of a soldering metal at all.

As mentioned before, the flow profile also has a major impact on the etching process. First experiments with a corundum boat showed non-satisfying results due to an incomplete reaction of the deployed substrate. A simulation of the flow profile using SolidWorks verified the assumption of a limited interaction of the flow with the substrate in the shaded region of the boat (see Figure 4.19).

Figure 4.18: CAD model of the corundum boat used in the first set of experiments.

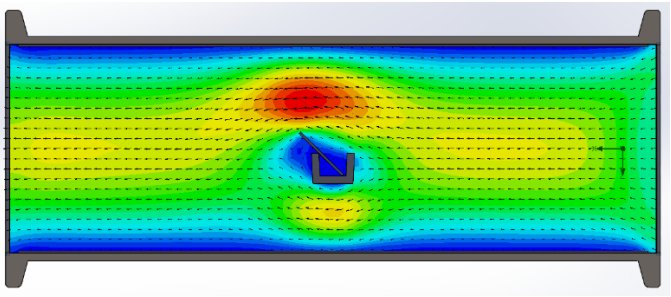

Figure 4.19: Flow profile of the etching gas with substrate being deployed in a standard corundum boat.

The introduction of a sample holder made from Monel significantly improved the flow profile and the interaction of the etching gas with the substrate. In addition, it proved to be easier to free from absorbed water and also allowed a residue-free cleaning. Especially the last quality is of major interest if it comes to the fluorination of uranium and the associated deposition of thorium fluoride (see chapter 5.2.2).

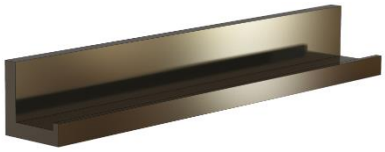

Figure 4.20: CAD model of the adapted sample holder made from Monel.

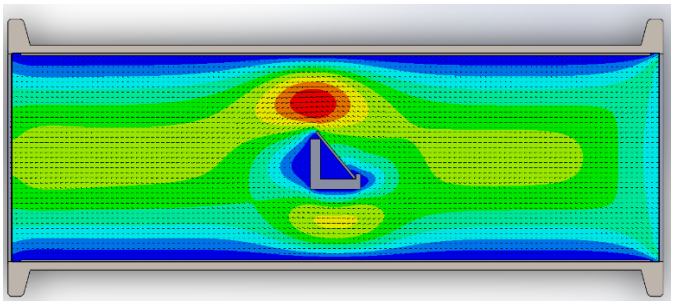

Figure 4.21: Flow profile of the etching gas with substrate being deployed in the Monel sample holder.

The sample holder proves to be resistant to the fluorine radicals in the gas stream even if exposed at elevated temperatures for a prolonged time. In experiments deploying uranium and molybdenum as a substrate material, no reduction of mass within the limits of the accuracy of the scale of 0.5 mg was observed. However, apparently it is attacked by the high-valent fluorides of some of the platinum metals such as ruthenium and palladium (see chapters 6.1 and 6.3).

4.1.3 Pipelines and cold traps with bypass

The pipelines lead from the reaction tube further downstream to the cold traps, in which the deposition of the synthesized fluorides takes place. The pipelines are made from stainless steel 1.4404 with a diameter of ½ inch. A smaller diameter would lead to higher pressure losses, so it is questionable whether the RPS could stably be operated. As only membrane and bellow-seal valves have been proven to work reliable in the presence of fluorine, all of the valves used are membrane valves of the type 6L-ELD8-77X-P of the Swagelok Company. The pressure in this part of the system is measured subsequent to the third cold trap CERAVAC Transmitter CTR 100N with a pressure range from $1.3 \cdot 10^{-3}$ to $1.3 \cdot 10$ mbar.

The cold traps are made from PFA and feature a simple U-tube design. They are being passivated before use at a pressure of 1 bar for 24 hours with pure fluorine in order to eliminate all non-fluorinated constituents and thereby to guarantee the chemical inertness of the material. All cold traps can be bypassed. This allows purging the system with argon before the resublimation process on one hand and switching to another cold trap, if the deposited product negatively affects the gas flow rate leading to an increased pressure on the other hand. The number of cold traps allows for the deposition of the synthesized fluorides as well as for their separation based on a difference in vapor pressure. Different frigorific mixtures such as isopropanol and dry ice as well as isopropanol cooled with a cryostat were used in order to precisely adjust the temperature of the cold traps. Subsequent to each cold trap is an extraction port (see Figure 4.22), which is capped with a stainless-steel plug during operation. The extraction port allows for the sublimation of the content of the cold traps into a storage container or into the measuring cell (see chapter 4.4). However, as UF_6 may react explosively with isopropanol even at low temperature, extensive caution is recommended during the extraction process. Depending on the demanded temperature, liquid perfluorocarbons may pose a safer alternative as a frigorific agent, but they become highly viscous at lower temperatures.

With respect to vacuum tightness, the polymer-metal connection of the cold traps and the line is the weak part of the system. As a transparent design is beneficial during the characterization phase of the process, this disadvantage was accepted. However, a further development of the line should introduce cold traps made from stainless steel.

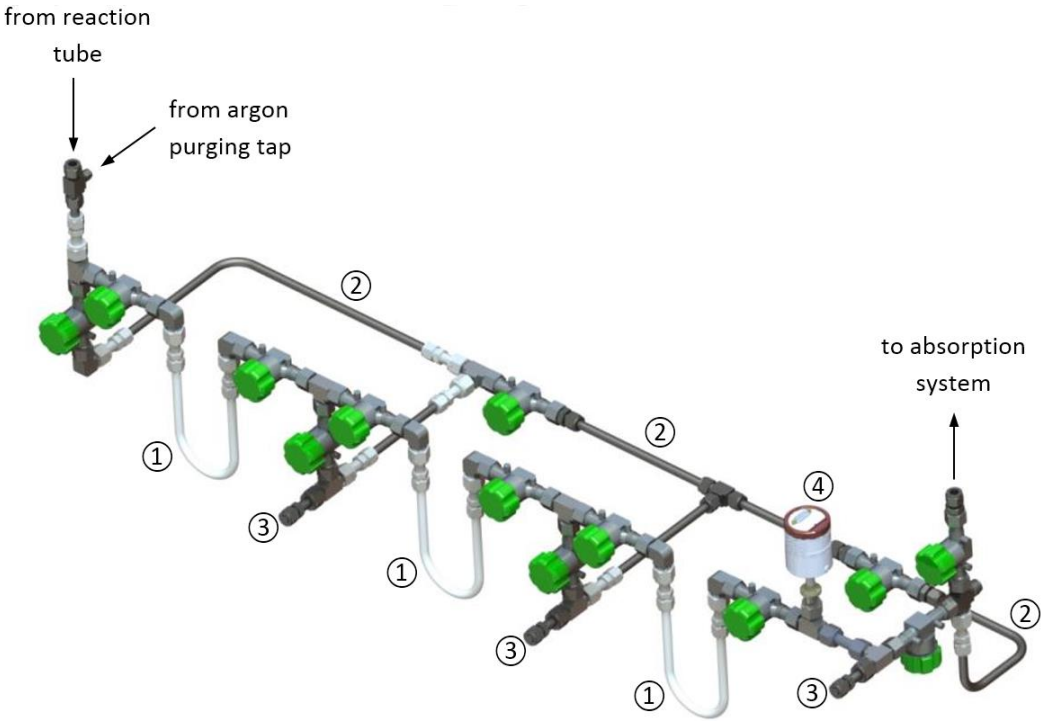

Figure 4.22: CAD model of the lower part of the system including the cold traps. Each of the cold traps (1) can be bypassed (2). The bypasses also allow the purging after the fluorination process in order to remove residues from the system. The extraction ports (3) serve as taps to empty the cold traps through sublimation. The pressure is measured by a CERAVAC pressure sensor (4).

4.2 Separation line

The possibility of a separation of MoF_6 and UF_6 based on the irradiation with near-UV light at a wavelength 395 nm and the simultaneous use of CO as a fluorine atom scavenger was investigated at a second line, hereinafter referred to as separation line. It allowed the investigation of the advantages and disadvantages of the use of CO in different states of matter: gaseous, liquid and supercritical as well as the acquisition of the IR spectra partially used for the evaluation of the different separation techniques. It may be used in different configurations. Figure 4.23 shows the configuration for all low-pressure experiments up to 3 bar. Here, the line consists of two ports allowing the connection of the cylinders containing UF_6 and MoF_6 ① and a third one for the connection of the measuring cell ②. The pressure is measured by a piezo-resistive sensor ③. This part may be switched off by a ⅜ inch valve ④, whereas valve ⑤ supplies the line with argon. Valve ⑥ allows the supply with CO. The tee ⑦ is sealed on top with a sapphire window allowing the irradiation with UV-light. Filter ⑧ collects all solid reaction products that originate from irradiation. The cold trap ⑨ allows for the deposition of the hexafluorides as well as for the condensation of CO. The measuring cell may also be connected to port ⑩, allowing for the investigation of reaction products while being purged with argon from ⑪. The pressure in this downstream part of the line is measured by ⑫, whereas the soda lime filled absorber ⑬ protects the pump from reactive fluorine species.

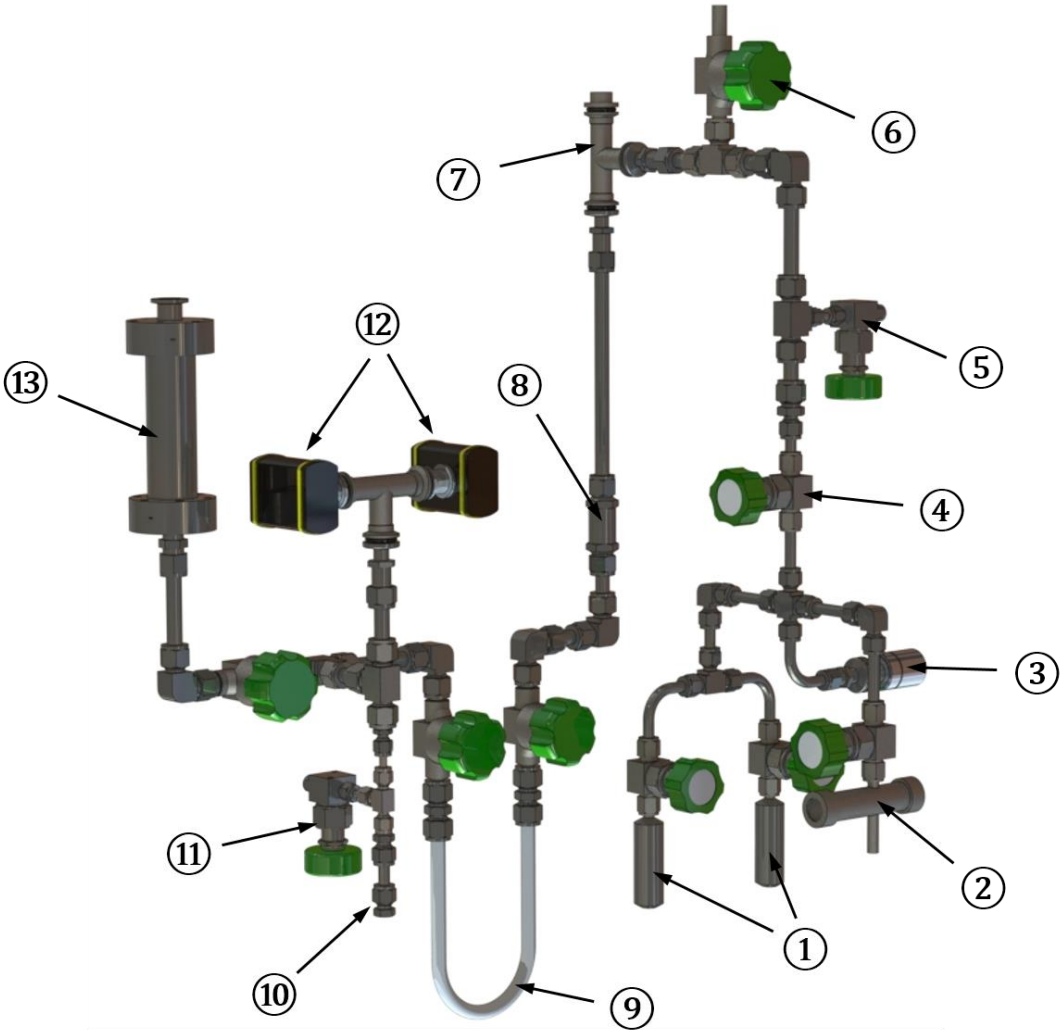

Figure 4.23: CAD model of the separation line for the investigation of the chemical separation of UF_6 and MoF_6.

The high-pressure section of the line is indicated by a red frame in Figure 4.24. It may be easily connected to the line at the port that would usually hold the measuring cell and allows high-pressure experiments up to 70 bar. It consists of the high-pressure container, which has already been described in detail, and several standard components of the Swagelok company. These include three membrane valves, a miniature sample cylinder with a capacity of 50 ml and a 100 bar pressure gauge. The membrane valves are type SS-4H with stainless steel tem tips and a maximum pressure of 68.9 bar indicating the pressure, under which the valve can still be opened safely. The sample cylinder holds the same maximum pressure but was tested from company side at a pressure of 150 bar.

The UV-LED is a Roschwege Star-UV395-10 from the Roschwege Company. It has its maximum intensity at 395 nm and emits its radiation in a narrow band with a half-width of 12 nm. Its electrical power consumption of 10 W results in a radiant flux of 2.2W. Its viewing angle, i.e. the angle at which the relative intensity has declined to 50 %, is 115°. To protect the LED from overheating, it is mounted on an aluminum dissipater, which for its part is actively cooled by a fan.

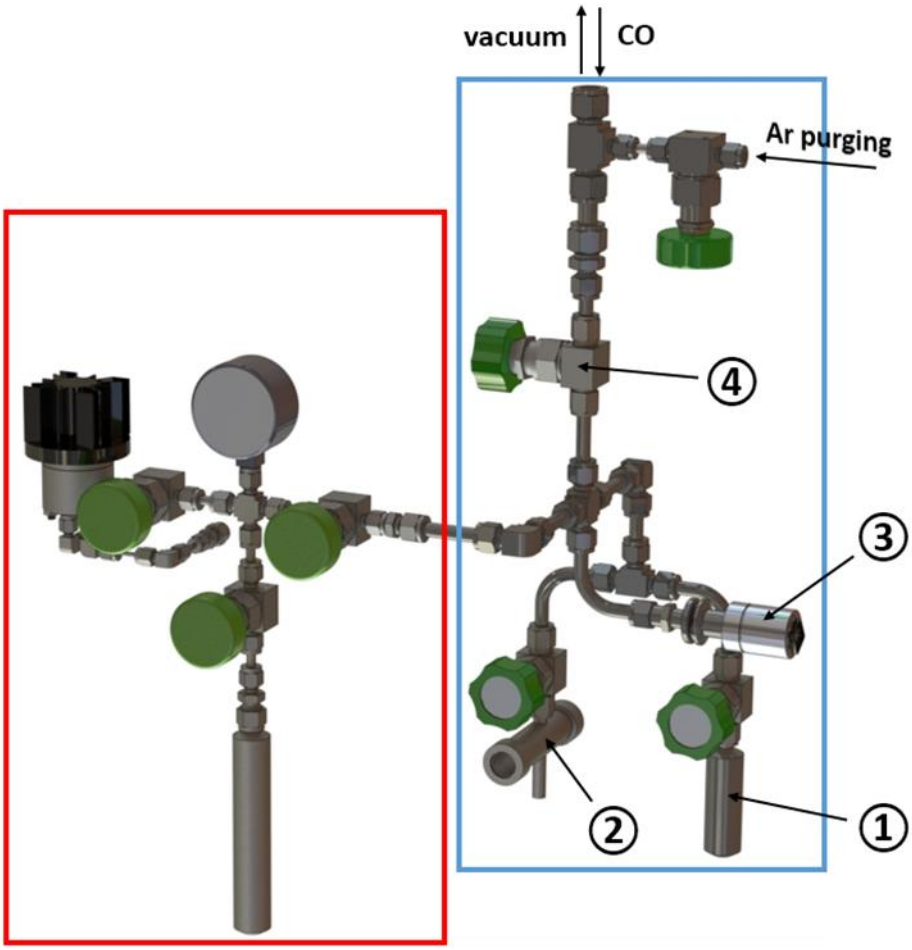

Figure 4.24: Section of the separation line for the separation of UF_6 and MoF_6 using supercritical CO. The red framed part is the high-pressure part, whereas the blue framed part belongs to the low-pressure section, as depicted in Figure 4.23.

The high-pressure section is described in detail in chapter 5.5.3, which covers the separation experiments using supercritical CO.

4.3 High-pressure container

The high-pressure container was designed to allow the irradiation of MoF_6 and UF_6 under high pressure up to 100 bar, thus allowing the use of supercritical CO for the separation process. It has a total volume of 3.8 ml and consists of five parts: The pressure hull ① serves as the reaction vessel and has a cold finger ② at its center that can be flushed with liquid nitrogen. The cold finger is sloped in order to eliminate all shaded regions and ensure the UV radiation illuminates the entire inside. It has a blind hole at the bottom side allowing the insertion of a thermocouple. On the top side, the container is confined by a 5 mm sapphire window ③, sealed with an FFKM O-ring ④ made from Perlast G92E and held in place by a steel lid ⑤. The pressure hull is manufactured from a solid piece of stainless steel in order to avoid any weak spots from welding seams. Both, pressure hull and cold finger possess a receptacle for a thermocouple. A nozzle connects is equipped with a ¼ inch membrane valve.

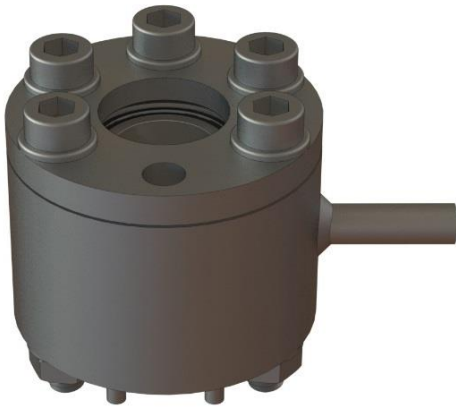

Figure 4.25: High-pressure container, front screw removed for better visibility

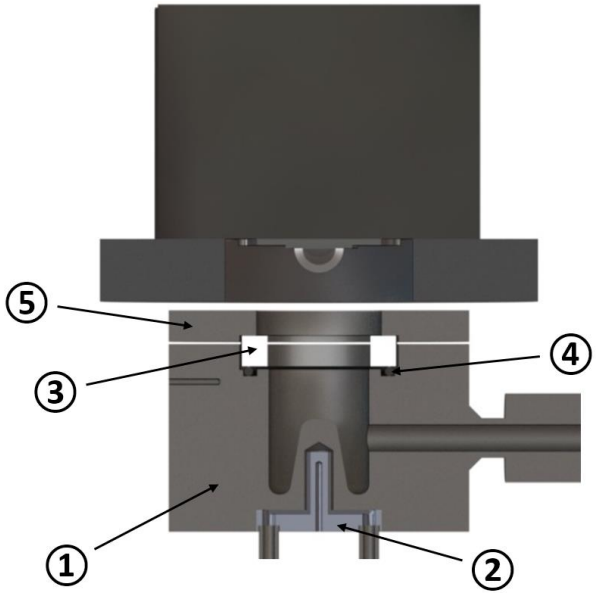

Figure 4.26: Longitudinal sectional view of the high-pressure container with the UV-LED on top

The weak spot of the high-pressure container is the sapphire window, which however is essential for the irradiation process. In order to maximize the applicable stress, the c-axis of the crystal is aligned parallel to the axis of the window. According to [97], the maximum pressure load on a clamped window may be calculated by:

$$p = \left(\frac{T}{0.866 \cdot D}\right)^2 \cdot F_A \qquad (18)$$

T being the thickness of the window, D the diameter of its unclamped part and F_A the rupture modulus of the window material. This formula includes a safety factor of 4, which is reasonable for materials with brittle fracture behavior. With a thickness of 5 mm, an unclamped diameter of 20 mm and a rupture modulus of 276 MPa, the maximum applicable pressure evaluates to 230 bar. In order to validate the calculations, the high-pressure section of the line was tested with argon at a pressure of 80 bar for six hours. The system therefore holds a sufficient pressure reserve capacity, as the separation experiments were performed at pressures not exceeding 45 bar.

4.4 Measuring cell for IR and UV/VIS spectra acquisition

All of the investigated hexafluorides possess a relatively high vapor pressure at room temperature and are highly sensitive to oxygen and moisture, favoring transmission spectra acquisition. Therefore, a special measuring cell was manufactured and used for the acquisition of all IR and UV/VIS transmission spectra of the hexafluorides. It is manufactured from a solid piece of stainless steel AISI 316 entirely without welding. Considering corrosion resistance, Monel would be the better choice, but is also much more demanding in the manufacturing process.

Figure 4.27: CAD model of the measuring cell used for acquisition of IR and UV/VIS spectra.

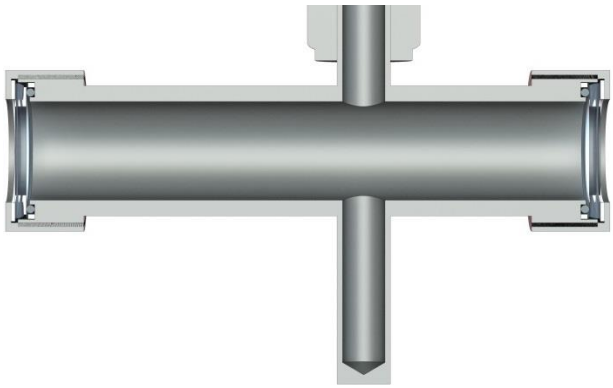

Figure 4.28: Longitudinal sectional view of the measuring cell.

The windows are made of either BaF_2 or sapphire single crystals, which are sealed to the trunk with FFKM O-rings. Teflon spacer discs prevent the windows from being damaged by contact with the steel trunk, if the shells are accidentally tightened to fast. The resulting optical path length is 100 mm. The fluorides of interest can either be transferred from the cold traps simply using their intrinsic pressure or by condensation into the cylindrical depot (1) using liquid nitrogen. After the removal of the liquid nitrogen, the compound heats up to room temperature and equilibrium between the solid and the gas phase emerges. The leakage rate of the measuring cell was determined to be smaller than:

$$Q_L < \; 3 \cdot 10^{-7} \; \frac{mbar \cdot l}{s}$$

The major advantage of the measuring cell is the possibility of the acquisition of IR spectra and UV/VIS spectra on the same sample. The typical time frame including the extraction of the fluorides from the line to the measuring cell, transport to both spectrometers and the subsequent measurement did not exceed 30 minutes. Based on the volume of the measuring cell of about 28.2 cm^3, this leads to an intrusion from the outside atmosphere of fewer than 0.02 mbar. The smallest quantities of gas measured were corresponding to 5 mbar, leading to a contamination due to leakage from the outside atmosphere of less than 0.4 vol%.

4.5 Standard components

4.5.1 Pressure sensors

Three different types of pressure sensors have been used for the process and shall be explained in more detail: capacitive and piezo resistive sensors as well as Bourdon tube gauges. All three types directly measure pressure and are therefore independent of the gas type. In addition, they all show a basic resistance to fluorine and the hexafluorides.

Capacitive sensors have a flexible membrane with an opposing electrode that both form a plate capacitor. In case of the CERAVAC CTR 100 N, the membrane is made from Inconel, a nickel-based alloy and therefore shows very good resistance against corrosion. Its displacement results in a shift of the voltage, which is evaluated by an internal electronic circuit and translated into a pressure reading. Depending on the stiffness of the membrane, capacitive sensors can cover different pressure ranges. Independent of the absolute pressure range, they can cover about four orders of magnitude, e.g. from 0.1 to 1000 mbar. The uncertainty of the CERAVAC is 0.2 % of its reading. Its major disadvantage is the high price.

Figure 4.29: The CERAVAC CTR 100 N is a capacitive pressure sensor and is the type being used on the fluorination line [98].

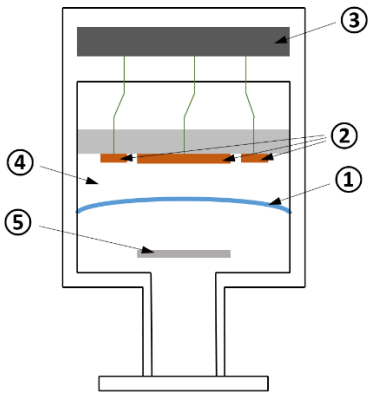

Figure 4.30: Internal view of a capacitive sensor. The membrane (1) and the opposing electrodes (2) form a plate capacitor, whose displacement is evaluated by the electronics (3). The section behind the membrane (4) is an ultra-high vacuum. A baffle (5) protects the membrane from abrupt pressure changes.

Piezo resistive sensors also possess a thin membrane. On its far side, a number of piezo elements are mounted, whose electrical resistance changes under stress. If pressure is applied to the sensor, the deformation of the membrane is directly transmitted onto the piezo elements changing their electric resistance. As they form a Wheatstone bridge circuit, this is associated with a change in voltage. An internal electronic circuit translates this change of voltage into a pressure reading. The uncertainty of the used VSC43MV is smaller than 0.3 % f.s., which corresponds to 4.2 mbar. After being exposed to UF_6 and MoF_6 for several weeks, the piezo resistive sensors show a zero-shift of about 3 %. However, the actual change during one single experiment is negligible.

Figure 4.31: The VSC43MV is a piezo resistive pressure sensor [99].

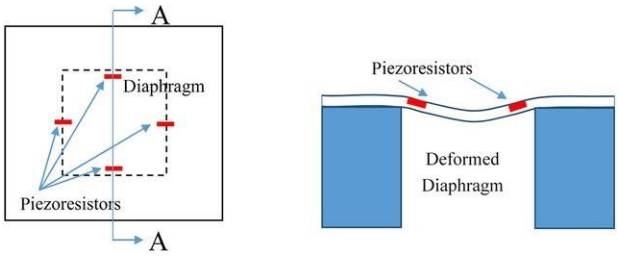

Figure 4.32: Four piezoresistive elements form a Wheatstone bridge and change their resistance, if the membrane is deflected [100].

A **Bourdon tube gauge** is a pressure sensor consisting of a flattened tube that changes its shape when pressurized. The deformation of the tube is mechanically transmitted by a drawbar to the needle, which indicates the corresponding pressure on a scale reading. In case of the used PGI-63C-BG100-LAQX, the tube is made from stainless steel 316L and shows good corrosion resistance. This type was applied for the separation line and has an uncertainty of 1.5 % f.s., which corresponds to 1.5 bar.

Figure 4.33: The PGI-63C-BG100-LAQX used for the high-pressure section is a Bourdon tube gauge [101].

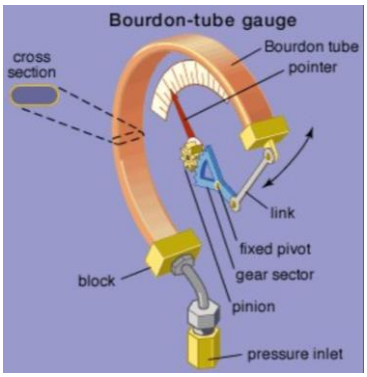

Figure 4.34: Internal view of a Bourdon type pressure sensor [102].

The advantages and disadvantages of the three different sensors types are listed in Table 4.3.

Table 4.3: Advantages and disadvantages of the described sensor types.

sensor type	advantages	disadvantages
capacitive	• independence from applied gas • pressure range three orders of magnitude • highest precision of the three types	• very cost intensive
piezo resistive	• comparable low costs • pressure range three orders of magnitude	• lower corrosion resistance than capacitive sensors • lower precision than capacitive sensors • zero-point shift over operation time
Bourdon tube	• high corrosion resistance in case of appropriate material choice • applicable for high-pressure • low costs	• lowest precision of the three types • lowest pressure range of the three

4.5.2 Valves

Two different types of valves have proven reliable when working with fluorine: membrane (or diaphragm) valves and bellows-sealed valves.

The **membrane valves** used in the line consist of a stainless steel AISI 316L diaphragm mounted to a 316L stem. The stem tip has a PCTFE insert that presses against the valve body if the valve is closed. The membrane itself is tightened to the valve body by PTFE coated stainless steel AISI 316L gaskets. All wetted components are therefore resistant to the hexafluorides, if properly passivated before use. The most critical component is the PCTFE insert in the stem tip. These valve type has the major advantage of a very small dead volume, thereby reducing potential sedimentation and deposition of the fluids passing through.

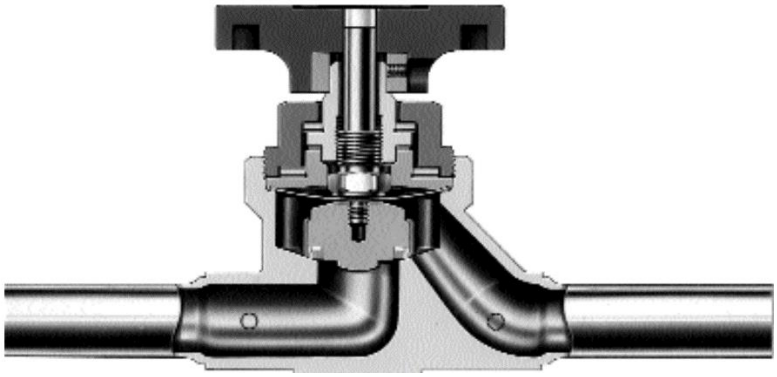

Figure 4.35: Sketch of a membrane valve of the LD16 series as used in the fluorination line [103].

The **bellows-sealed valves** used in the separation line consist of a stainless steel AISI 316 stem with a stainless steel 1.4546 stem tip inserted into a bellows fabricated from stainless steel AISI 321. This assembly is welded together; therefore, no gaskets are used, reducing the risk of leakage. All wetted components are therefore resistant to fluorine and the hexafluorides, again, if properly passivated before the first use. The main disadvantage compared to membrane valves is the increased dead volume and the therefore increased evacuation times. In addition, the bellow harbors the danger of a deposition of the fluids passing through.

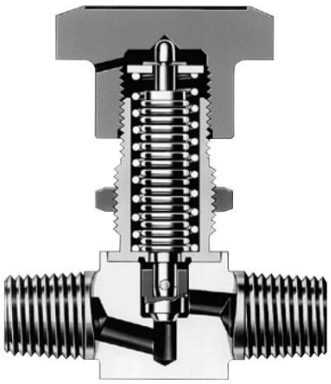

Figure 4.36: Sketch of a bellows-sealed valve of the H Series as used for the separation line [104].

Common to both types is the direction change of the current passing through the valve, as they do not possess a straight through boring as e.g. ball valves.

5 Dry-chemical separation of uranium hexafluoride from molybdenum fluorides

The following chapter summarizes the results of the experiments performed during the investigation of a dry-chemical separation of uranium and molybdenum. All methods are based on a precedent conversion of the metals into their corresponding hexafluoride. After this conversion, the subsequent separation was investigated for the following procedures:

- Separation based on a difference in vapor pressure
- Separation using CO
- Separation using SO_2

The conversion and separation was investigated with samples of different compositions of uranium and molybdenum, hereinafter referred to as UMo samples. These samples were produced by CERCA, a wholly-owned subsidiary of Framatome. In order to investigate the influence of the molybdenum content on the separation process and to qualify the analytical methods, samples with four different mass ratios of uranium and molybdenum were produced. These weight ratios were chosen as 95 : 5, 99 : 1, 99.5 : 0.5 and 99.9 : 0.1. The molybdenum content of samples of the latter composition closely resembles the one of an irradiated target. In order to increase readability, the samples are denominated according to their molybdenum content, e.g. UMo5 contains 95 % uranium and 5 % molybdenum, UMo05 contains 99.5 % uranium and 0.5 % molybdenum, et cetera.

In addition to the chemical analysis done by CERCA, three samples of each ratio were dissolved in nitric acid and hydrogen peroxide in order to determine their molybdenum content using ICP-MS. The results of this analysis are listed in Table 5.1. As the 95 : 5 samples show the greatest uncertainty with respect to the molybdenum content, these samples were excluded from the investigation of the process.

Table 5.1: Analysis of the composition of the surrogate samples. Uncertainties on the Mo content determined by ICP-MS are given as one standard deviation based on the t-distribution due to the small sample size of six samples.

composition U : Mo	denomination	CERCA [wt% Mo]	ICP-MS [wt% Mo]
95 : 5	UMo5	13.7 ± 0.6	10.31 ± 1.91
99 : 1	UMo1	1.1 ± 0.3	1.139 ± 0.029
99.5 : 0.5	UMo05	0.5 ± 0.3	0.591 ± 0.070
99.9 : 0.1	UMo01	< 0.3	0.125 ± 0.014

The evaluation of the efficiency of the separation process depends on a reliable determination of the content of uranium and molybdenum or the corresponding hexafluorides, respectively. Unfortunately, only a very limited number of analytical methods is suited for this purpose. The typical mass of an

UMo sample accounts for 500 to 4000 mg. Table 5.2 gives an overview over the mass and amount of substance formed for the complete fluorination of a sample with a mass of 1000 mg.

Table 5.2: Nominal mass and amount of substance of UF_6 and MoF_6 being produced.

composition U/Mo	U [mg]	Mo [mg]	UF_6 [mg]	UF_6 [mmol]	MoF_6 [mg]	MoF_6 [mmol]
95 : 5	950	50	1405	3.992	109.4	0.521
99 : 1	990	10	1464	4.159	21.88	0.104
99.5 : 0.5	995	5	1471	4.179	10.94	0.052
99.9 : 0.1	999	1	1477	4.196	2.188	0.010

Two important conclusions may be derived from this table. First, the mass of the synthesized MoF_6 is more than twice as high as of the deployed molybdenum increasing its detectability. Second, based on the amount of substance, the ratio of UF_6 : MoF_6 is decreased to about 400 : 1 in contrast to the metal based ratio of about 1000 : 1. This circumstance plays into the hands of the transmission based spectroscopic methods as the absorbance is direct proportional to the concentration of a substance.

5.1 Fluorination of molybdenum

5.1.1 General aspects of molybdenum and its fluorides

Molybdenum is a silvery-grey hard metal with great tensile strength. It is chemically stable on air due to passivation and is not attacked by non-oxidizing acids for the same reason. However, it is vividly attacked by oxidizing acids as concentrated sulfuric acid or aqua regia [105]. Molybdenum does not form binary hydrides, permitting a potential hydrogenation of the uranium-molybdenum alloy. As an element of group 6, it has the electron configuration [Kr] $4d^5 5s^1$ and thus a sufficient number of valence electrons to form a hexafluoride. The oxidation state +VI, which it holds in that compound, is also the most important one [105]. Aside from MoF_6, three other thermodynamically stable binary fluorides of molybdenum are known: MoF_3, MoF_4 and MoF_5.

Table 5.3: Physico-chemical properties of the fluorides of molybdenum [34,105,106].

	MoF_3	MoF_4	MoF_5	MoF_6
molar mass	152.9 g/mol	171.9 g/mol	190.9 g/mol	209.9 g/mol
melting point	> 600 °C	dec.	45.7 °C	17.5 °C
boiling point	–	–	213.6 °C	34.0 °C
appearance (SATP)	brownish-yellow solid	pale green solid	yellow solid	colorless liquid

MoF_3 is a yellow-brownish solid that may be synthesized via reduction of MoF_6 with elemental Mo at 400 °C [105]. Different colors are described at other temperatures and vary from grey-green at 700 °C to dark red at 850 °C [107]. LaValle et al. also describe its synthesis via reduction of MoF_5 with elemental molybdenum powder also at 400 °C [108].

MoF_4 is a light green solid, whose preparation was first described by Peacock et al. by reacting $Mo(CO)_6$ with fluorine at −75 °C [109]. The synthesized compound was of olive green color and is believed to be a mixture of MoF_4 and MoF_5. Heating it in a vacuum to 170 °C allowed for the removal of the volatile MoF_5, leaving MoF_4 behind [107]. The occurrence of a mixed-valent Mo_2F_9 could never be proven, and thermal analysis as well as magnetic susceptibility measurements rather contradict its existence [107].

MoF_5 is a sunflower-yellow solid and may easily be prepared by the reduction of MoF_6 using CO and ultraviolet radiation [110]. It was described to disproportionate into MoF_4 and MoF_6 at 150 °C by Edwards and Peacock in [111], but more recent studies performed electron diffraction at overheated MoF_5 vapor at 275 °C [112].

MoF_6 is a colorless liquid at room temperature. Due to its relatively low chemical reactivity compared to other transition metal hexafluorides, it is one of the few commercially available hexafluorides of the transition metals [113]. MoF_6 is diamagnetic [105].

The vapor pressure of MoF_6 according to Cady and Hargreaves [114] may be calculated for the different temperature ranges by:

−60 °C to −8.7 °C	$p = 1.33 \cdot 10^{\left(10.216 - \frac{2166.5\ K}{T[K]}\right)}\ mbar$	(19)
−8.7 °C to 17.4 °C	$p = 1.33 \cdot 10^{\left(8.533 - \frac{1722.9\ K}{T[K]}\right)}\ mbar$	(20)
17.4 °C to 34 °C	$p = 1.33 \cdot 10^{\left(7.766 - \frac{1499.9\ K}{T[K]}\right)}\ mbar$	(21)

It should be noted, authors publishing before 1967 often use °K, being the official thermodynamic unit at that time. Figure 5.1 shows the vapor pressure curve over the entire domain covered by the equations mentioned above.

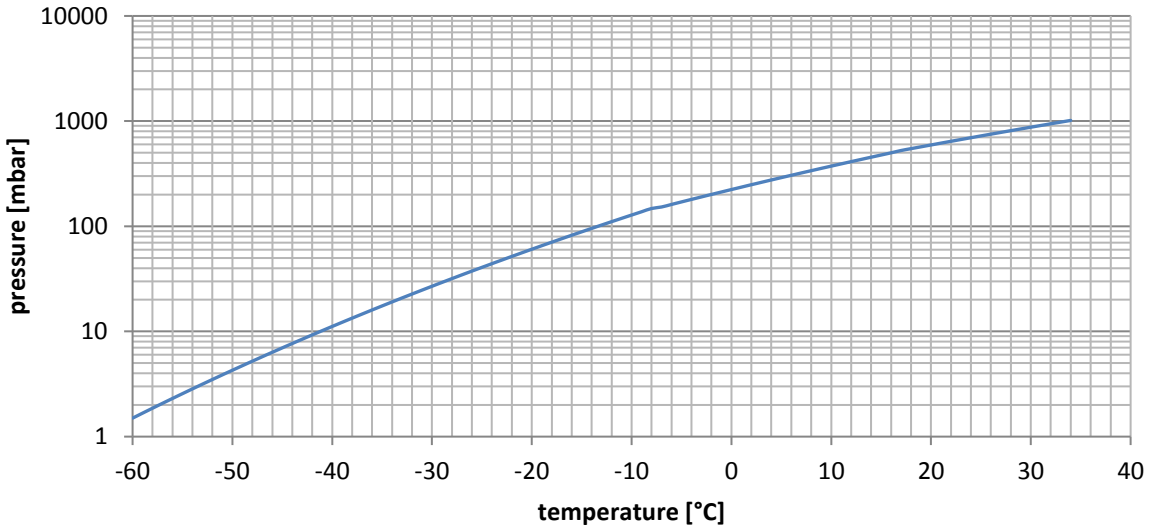

Figure 5.1: The vapor pressure of molybdenum hexafluoride MoF_6 derived from the equations mentioned above.

The crystal structure of MoF_6 changes at −9.7 °C. Below that temperature, MoF_6 is orthorhombic, between this temperature and its melting point at 17.5 °C, it is present in the cubic crystal system [107].

5.1.2 Reaction conditions

Molybdenum is easily fluorinated and can be presented in a massive form such as a sheet. Good etching results were achieved with a NF_3 : Ar ratio of 35.0 sccm : 35.0 sccm, resulting in an average etching rate of 45 mg/min and a calculated utilization of NF_3 of 60 %. Additional information on other volume flows of the etching agent can be derived from Table 5.4.

Figure 5.2: Molybdenum sheet before fluorination with a mass of 1957.5 mg.

Figure 5.3: Molybdenum sheet after fluorination for 55 minutes at 300 W with a mass 298.3 mg.

The shape of the target after fluorination clearly resembles the shape of the gas flux. However, the thickness of the sheet was reduced over the entire area exposed. As molybdenum was the first element to be fluorinated, the experiments were performed using a corundum boat. However, the shape of the boat accounts for regions shaded from the gas flow thereby leading to an incomplete reaction and the formation of the low-valent MoF_3 (see Figure 5.4 and Figure 5.5). This effect could be reduced by the introduction of the Monel carrier, which reduces the shaded regions and increases the exposed area of the substrate (also see chapter 4.1.2).

Figure 5.4: Residues in the corundum boat after fluorination, identified as MoF_3 by XRPD (also see Figure A.5).

Figure 5.5: Enlarged view of the residues.

Depending on the utilized refrigerant, MoF_6 is deposited in different forms. The use of an isopropanol/dry ice bath results in crystal growth at the height, where the cold trap enters the cold bath and powder on its lowest point, whereas the use of liquid nitrogen results in the deposition of powder only. Figure 5.6 shows deposited MoF_6 in the first cold trap.

Figure 5.6: Deposited MoF_6 in the first cold trap.

As molybdenum was the first element to be investigated, different parameters were altered to see their qualitative impact on the process. The exact course of the etching process depends on a variety of parameters. The most influential ones were expected to be the temperature in the reaction chamber, the applied power of the RPS, the shape and position of the substrate, the absolute flow of the etching agent NF_3, the absolute flow of argon as a carrier gas and the ratio of the two. Unexpectedly, the etching time also seems to have a significant impact on the etching rate. The entirety of these parameters spans a seven-dimensional parameter space, in all likelihood being unique to each element. Its detailed investigation would therefore go beyond the scope of this work. Instead, a qualitative approach was chosen to identify a promising set of etching parameters knowing that this set should be subject to further optimization.

All samples were cleaned prior to the etching experiments using half-concentrated hydrochloric acid. In order to minimize the influence of the substrate shape, all targets were of rectangular shape with dimensions 53 x 7 mm and a thickness of 0.5 mm. However, the identical positioning of the corundum boat and the Monel carrier could not completely be assured, as a slight tilt around their longitudinal axis already might significantly alter the flow profile. Thus, as mentioned before, an enhanced version of the reaction chamber should include a positioning mechanism ensuring an identical positioning of the target. The results from the etching experiments are listed in Table 5.4 and additionally visualized in Figure 5.7 and Figure 5.8.

Table 5.4: Experiments investigating the etching behavior and its dependency on applied power, etching time and process gas composition.

Exp. No	power [W]	time [min]	Ar/NF_3 [sccm]	etching rate [mg/min]	MoF_3 residues	crucible heated	sample holder
8	300	9	100/60	3.9	no	no	Monel carrier
9	300	20	100/60	4.2	no	no	Monel carrier
10	300	30	100/60	18.0	yes	no	Monel carrier
11	300	40	100/60	9.8	no	no	Monel carrier
12	300	40	100/60	27.5	yes	no	Monel carrier
13	3000	39	35/35	45.2	no	no	Monel carrier
5	300	10	100/60	6.2	no	no	corundum boat
2	300	48	200/60	34.6	yes	yes	corundum boat
6	900	10	100/60	22.3	no	no	corundum boat
4	900	22.5	100/60	77.8	yes	yes	corundum boat
7	1800	10	100/60	86.5	yes	no	corundum boat

The reaction takes place without additional heating. However, as the etching rate increases with a prolonged reaction time even at otherwise unaltered conditions, an acceleration of the reaction at elevated temperatures may be assumed. In this case, the exothermic nature of the reaction would heat up the target thereby enhancing the reaction. The etching rate as a function of total reaction time at an applied power of 300 W is depicted in Figure 5.7.

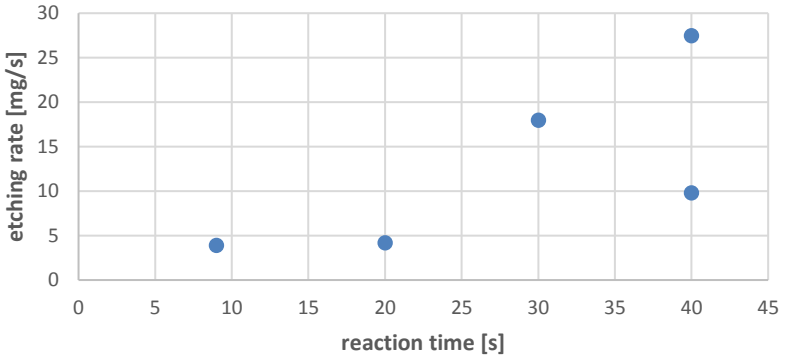

Figure 5.7: Etching rate as a function of reaction time. The applied power was 300 W, volume flow of argon was 100 sccm and volume flow of NF_3 was 60 sccm. The Monel carrier was used for positioning of the sample.

The etching rate rapidly increases with the applied power of the plasma source. There are two possible explanations to this observation. According to the specifications of the manufacturer, the dissociation rate of the process gas NF_3 is only guaranteed to exceed 95 % for every power setting at a volume flow of at least 500 sccm. At a flow as low as 160 sccm, the dissociation might not be complete at low power but increase with higher power. The second explanation also involves an increased heating of the target especially in an earlier stage of the fluorination, thereby enhancing the reaction. It was noticed during the experiments, that a high power output of the RPS also increases the temperature of the walls of the reaction chamber, even if only an argon plasma is burning. This observation eliminates the possibility of an additional introduction of energy into the gas flow by an exothermic reaction. As both explanations do not contradict each other, a combination of them also seems possible.

As a result of this finding, all separation experiments as well as the fluorination attempts of the other elements described in chapter 6 were performed at the maximum power of the RPS of 3000 W.

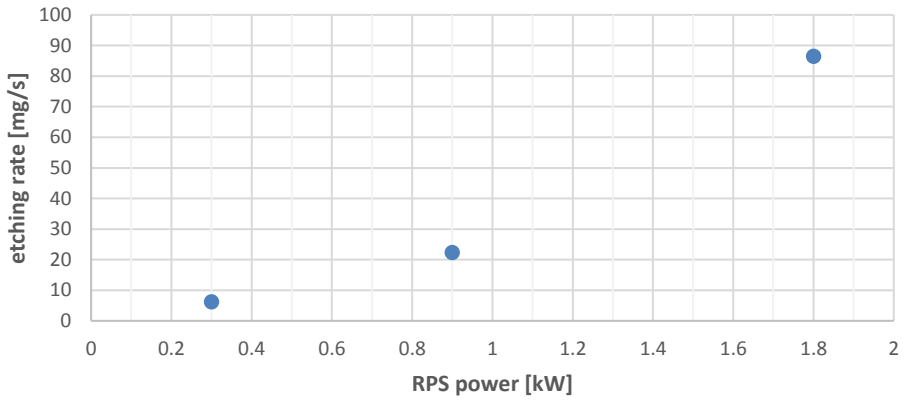

Figure 5.8: Etching rate as a function of applied power of the RPS. Volume flow of argon was 100 sccm, volume flow of NF_3 was 60 sccm and the samples were kept exposed to the etching agent for 10 minutes. A corundum boat was used for the positioning of the samples.

5.1.3 UV/VIS spectroscopy

Spectroscopy on MoF_6 in the ultraviolet and visible range was performed at different pressures, whereas Figure 5.9 shows the recorded spectrum at 592 mbar, which is just below its vapor pressure at room temperature. As MoF_6 is a colorless gas, no distinct absorption is expected in the visible range.

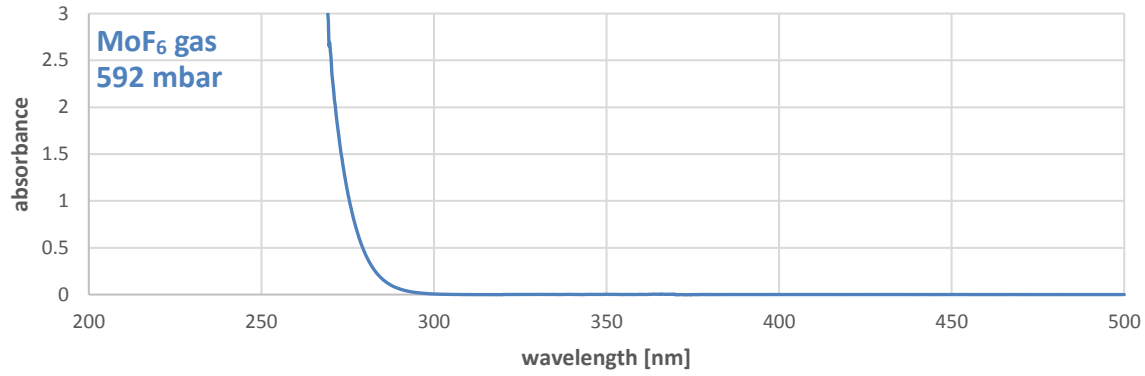

Figure 5.9: UV/VIS spectrum of MoF_6 acquired with the measuring cell at a pressure of 592 mbar, shortly below the vapor pressure at 22 °C. Slit width was 0.5 nm, acquisition speed 0.2 nm/s. The optical path length is 100 mm. No absorption bands are recorded above 500 nm.

However, a very weak interaction in the range between 320 and 380 nm was observed. It was well above the background as observed in the nearby region between 400 and 500 nm. Whether it is assigned to MoF_6 or must be allocated to minor impurities, cannot be answered at this point. But even in case the absorption bands could be assigned to MoF_6, their location and unincisiveness makes UV/VIS spectroscopy unsuitable for the distinction between MoF_6 and UF_6.

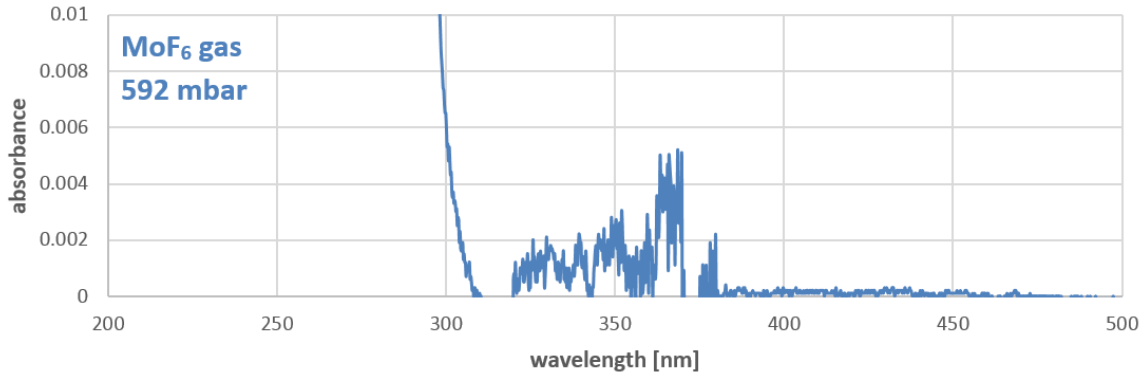

Figure 5.10: High resolution of the spectrum of Figure 5.9.

5.1.4 IR spectroscopy

In order to verify the successful synthesis of MoF_6, the general conformity of the measured IR spectrum with literature spectra must be verified. For the acquisition of its IR spectrum, MoF_6 was collected in the first cold trap and afterwards transferred via sublimation into the measuring cell. As the absorbance of a single band greatly differs depending on whether it is a fundamental, binary or tertiary combination band, spectra were collected at different pressures in order to allow a distinct analysis especially for overlapping bands. The general spectral verification was performed close to the vapor pressure of MoF_6 in order to be able to also resolve the weaker bands. It must be pointed out that for this spectrum the transmittance is considerably too high and by far exceeds the measurement uncertainty of the spectrometer. However, as this measurement is not used for quantitative analysis but only to show the conformity of the two spectra thus verifying the successful synthesis of MoF_6, no negative impact arises from this deviation. The acquired spectra are in good conformity with literature, as is shown in Figure 5.11. No additional bands are observed except for the ones 2350 and 2450 cm^{-1}, which can be assigned to CO_2 always present as the IR is not placed under inert atmosphere.

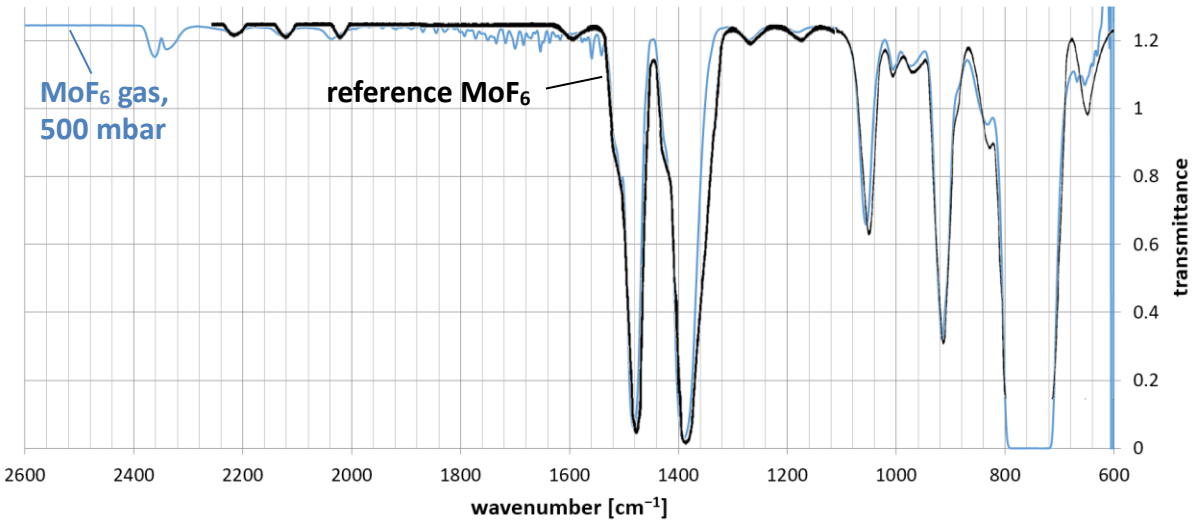

Figure 5.11: IR transmission spectrum of MoF_6 synthesized using the fluorination line at 500 mbar recorded using the measuring cell on the TENSOR 37 (blue graph). Optical path length was 100 mm. The reference spectrum (black graph) of MoF_6 from 2 - 40µm was taken from [115]. A spectrum without superimposed literature data can be found in Figure A.6

According to [115], as an seven-atom octahedral molecule, MoF_6 has six normal frequencies of which two are IR-active. As a binary combination, eight frequencies are permitted.

Two bands from the literature spectrum are not found, the ones at 648 cm^{-1} and 1585 cm^{-1}. However, four bands could not be assigned in the literature data: at 455 cm^{-1}, 648 cm^{-1}, 970cm^{-1} and 1175 cm^{-1}. It may therefore be assumed, that the band at 648cm^{-1} does not belong to MoF_6. The band at 1585 cm^{-1} lies in a region with intense noise from the BaF_2 window, possibly resulting in an interference with the signal. But as the wavenumber of the band considerably deviates from the calculated position by more than 60 cm^{-1} as seen from Table 5.5, it seems questionable whether this assignment is correct. Decomposition of the binary band at 1482 cm^{-1} has been performed in Figure A.9 and shows two additional minor bands at 1507 and 1519 cm^{-1}. The latter one would be a far better assignment to the calculated one at 1524 cm^{-1}.

As the bands between 720 and 790 cm^{-1} cannot be dissolved any further at 500 mbar, additional measurements were performed at 6 mbar, resulting in the spectrum shown in Figure 5.12. Here, the absorbance is plotted, as it is easier to evaluate. Figure 5.13 shows the same spectrum as well as a plot of three superimposed Gaussian functions approximating the measured spectrum.

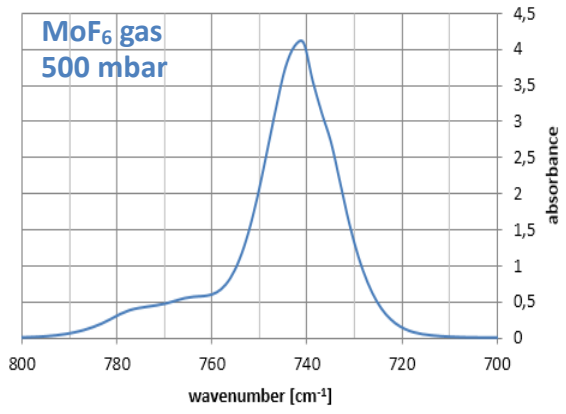

Figure 5.12: Absorbance of the IR spectrum of MoF_6 at 500 mbar in the range between 700 and 800 cm^{-1}.

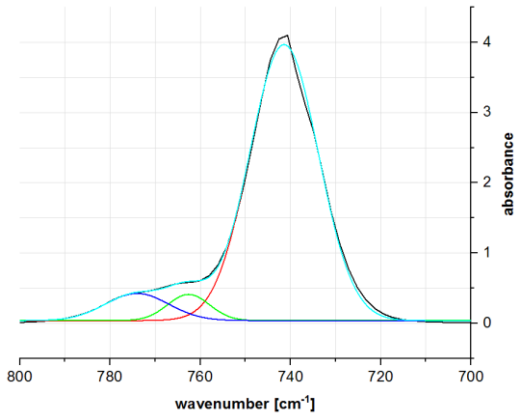

Figure 5.13: Spectral analysis of the absorbance of the IR spectrum of MoF_6 as shown in Figure 5.12.

As several of the intense bands show shoulders, they were decomposed into superposition of Lorentzian functions, which can be found in the appendix. A list of all bands and their comparison with the results from Burke et al. is shown in Table 5.5 [115].

Table 5.5: Comparison of the positions of the bands in the IR spectrum of MoF_6 found during this work with those found and calculated in the work of Burke et al. [115]. Values in parenthesis are technically forbidden, n.o. = not observed.

assignment	Burke et al. wavenumber [cm^{-1}]	this work wavenumber [cm^{-1}]
ν_3	741	741
$2\,\nu_4 + \nu_6$	764	763
$3\,\nu_4$	777	774
$\nu_1 + \nu_5 - \nu_6$	833	833
$\nu_2 + \nu_6$	882	875
$\nu_2 + \nu_4$	913	915
$(\nu_1 + \nu_6)$	970	975
$\nu_1 + \nu_4$	1002	1003
$\nu_3 + \nu_5$	1052	1055
–	1175	1181
$2\,\nu_4 + \nu_3$	1265	1269
$\nu_2 + \nu_3$	1385	1389
$\nu_1 + \nu_3$	1480	1482
–	–	1507
$2\,\nu_2 + \nu_6$	1585	1519
$2\,\nu_3 + \nu_4$	1740	n.o.
$2\,\nu_2 + \nu_3$	2030	2034
$2\,\nu_1 + \nu_2$	2125	2127
$3\,\nu_3$	2215	2218

5.1.5 Raman spectroscopy

Raman spectroscopy was performed on the content of the first cold trap in the liquid phase in FEP at a laser wavelength of 532 nm and a groove density of 1800 g/mm. It is in good agreement with the spectrum reported from literature. In order to determine their position, the acquired spectrum was fitted stepwise using pseudo-Voigt profiles, which gave a total number of five bands that could be assigned to MoF_6. The by far strongest of these signals is found at 741.1 cm^{-1} and may be assigned as the ν_1 fundamental. Two additional clearly distinguishable signals are found 645.9 and 323.2 cm^{-1} and may be assigned as the ν_2 and the ν_5 fundamental, respectively. Two rather weak signals at 247.2 and 386.4 cm^{-1} and originate from overtones and combination bands of the stated fundamentals.

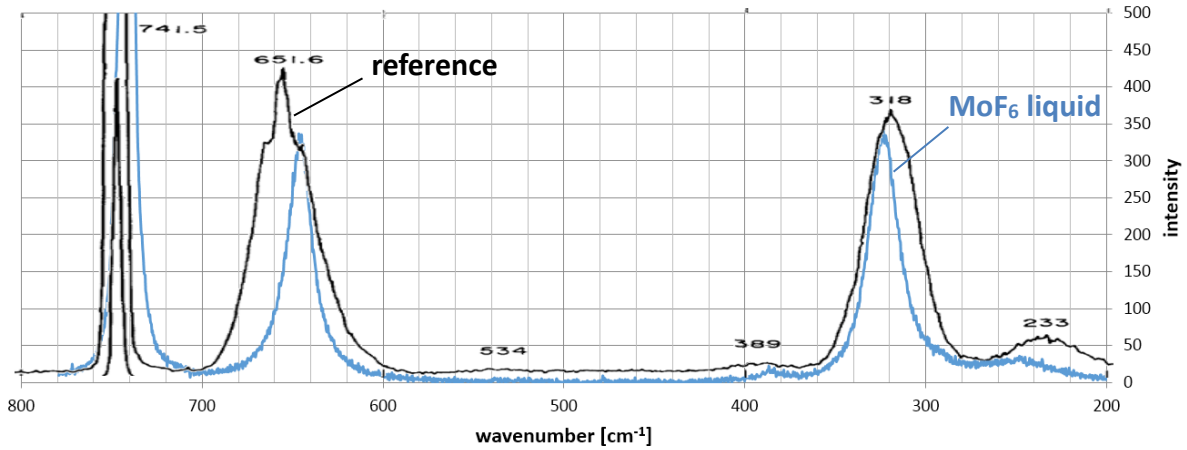

Figure 5.14: Raman spectrum of the reaction product of the fluorination of molybdenum sheets (blue graph). The sample was measured in the liquid phase at a temperature of 22 °C under intrinsic vapor pressure. The black graph shows the reference Raman spectrum of MoF_6 gas at a temperature of 70 °C and a pressure of 2 bar [116].

Table 5.6 lists the observed band positions from the Raman spectrum as well as those already reported in literature. The position of the fundamentals is in very good agreement with those reported by Burke et al., which were also measured in the liquid phase. The positions reported by Claassen et al. show greater deviations, as these were measured in the gas phase and may therefore be subject to liquid-to-vapor frequency shifts. In addition, the positions of the overtones show a significant discrepancy (233 vs. 247.2 cm^{-1}) or may not be observed at all (534 cm^{-1}).

Table 5.6: Comparison of the observed band position in the Raman spectrum of MoF_6. The samples of Burke at al. [115] were measured in the liquid phase, whereas the samples of Claassen et al. [116] were measured in the gas phase.

assignment	Burke et al. wavenumber [cm^{-1}]	Claassen et al. wavenumber [cm^{-1}]	this work wavenumber [cm^{-1}]
$2\ \nu_6$	–	233	247.2
ν_5	322	318	323.2
$\nu_4 + \nu_6$	–	389	386.4
$2\ \nu_4$	–	534	–
ν_2	645	651.6	645.9
ν_1	741	741.5	741.1

In combination with the IR data, the fundamentals are found at ν_1 at 741.1, ν_2 at 645.9, ν_3 at 741.5 and ν_5 at 323.2 cm^{-1}. As ν_4 and ν_6 may not be directly measured, they are not given here.

5.1.6 NMR spectroscopy

As MoF_6 is present in the liquid phase, acquisition of ^{19}F NMR was uncomplicated. The main signal is found at 283.2 ppm w.r.t. $CFCl_3$, with a total number of six satellites. These are located at 283.3, 283.5 and 283.7 ppm as well as 283.2, 283.0 and 282.8 ppm, respectively. Molybdenum has a total number of seven stable isotopes, of which only two possess a nuclear spin different from zero. These are ^{95}Mo and ^{97}Mo, both with I = 5/2, with a natural abundancy of 15.9 and 9.6 %, respectively. They cause heteronuclear spin-spin coupling with ^{19}F and therefore are the origin of the satellites. The position of the main signal is in very good accordance with the position at 282.9 ppm w.r.t $CFCl_3$ reported in the review article of Seppelt [117].

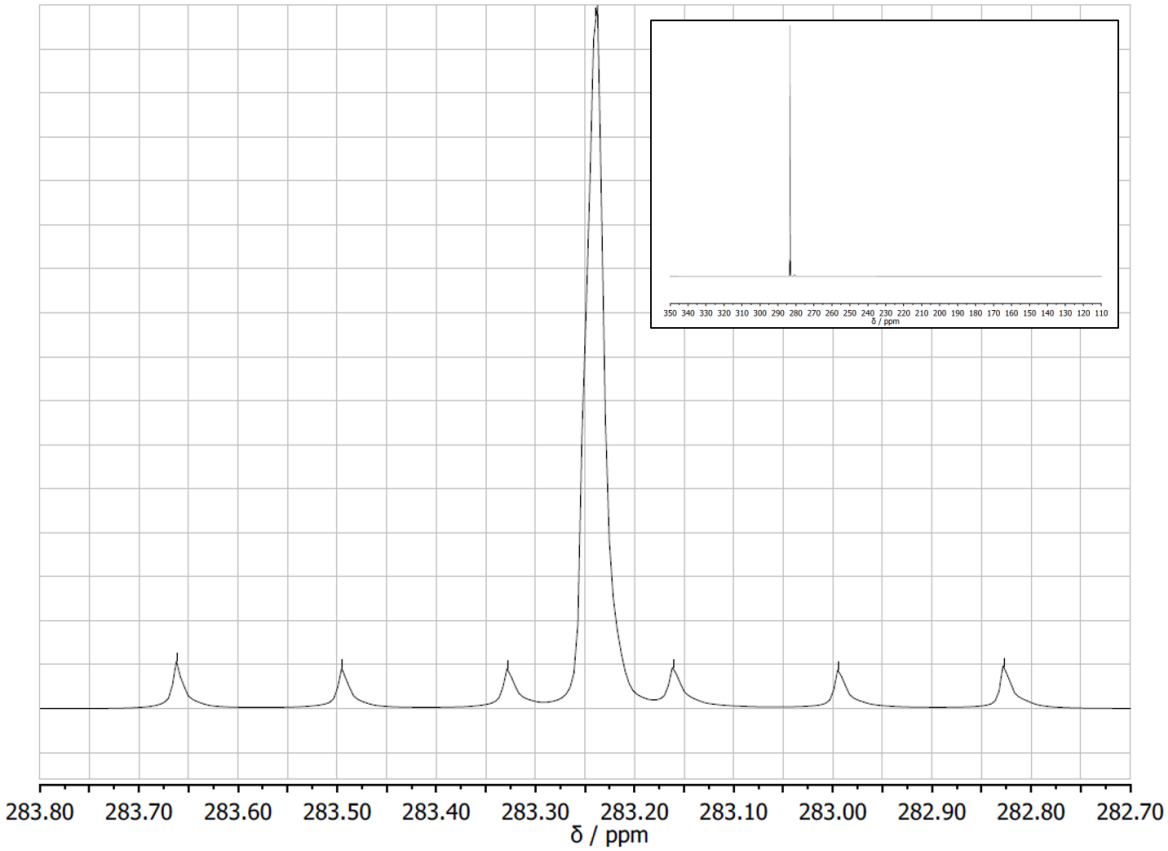

Figure 5.15: ^{19}F NMR spectrum of MoF_6 in the liquid phase measured at room temperature.

5.2 Fluorination of uranium

5.2.1 General aspects of uranium and its fluorides

Uranium is a primordial radionuclide and the element with the highest atomic number that is naturally occurring in significant amounts. It consists mainly of two isotopes, ^{235}U (0.72 %) and ^{238}U (99.28 %). Elemental uranium is a silvery base metal, which loses its metallic gloss over a period of days, if exposed to air. It thereby starts to develop a golden appearance, turning bluish as time passes until a thickening black oxide layer is being formed. This oxide layer is not protective of the underlying material, causing thin sheets to completely be transformed into uranium oxide. Fine uranium powder is pyrophoric and may only be handled under inert atmosphere, for example in a glovebox. Uranium is the third of the actinoid elements and has the electron configuration [Rn] $5f^3 6d^1 7s^2$, thus easily being able to reach oxidation state +VI. The known thermodynamically stable binary fluorides of uranium are listed in Table 5.7. Additional compounds between UF_4 and UF_5 such as U_2F_9 or U_4F_{17} are known, but shall not be considered here [118].

Table 5.7: Physico-chemical properties of the thermodynamically stable binary fluorides of uranium [105,119,120].

	UF_3	UF_4	UF_5	UF_6
molar mass	295.0 g/mol	314.0 g/mol	333.0 g/mol	352.0 g/mol
melting point	1495 °C (dec.)	960 °C	348 °C	64.1 °C
boiling point	–	–	disp.	56.5 °C
appearance (SATP)	black	bright green solid	pale grey-blue solid (β)	colorless solid

UF_4 is an intermediate product occurring during the preparation of elemental uranium from its oxides and is also known as green salt. It may be synthesized directly from the elements, but on an industrial scale it is primarily facilitated through the hydrofluorination of UO_2 [121]. UF_4 is only slightly soluble in water and hydrolyzes on moist air forming different possible uranium compounds and hydrofluoric acid. This contributes to the toxicity of UF_4 if incorporated [122].

UF_5 plays an important role in the studies on the dry-chemical separation process due to the low vapor pressure of its solid phase. It is thermodynamically stable but starts disproportionation into U_2F_9 and UF_6 at a temperature of 150 °C. UF_5 exists in two polymorphs, α-UF_5 being the high-temperature and β-UF_5 being the low-temperature modification, marked by a transition temperature of 125 °C [120,123]. The vapor pressure of solid α-UF_5 according to Wolf [120] is given by:

$$p = 1.33 \cdot 10^{\left(13.994 \pm 1.119 - \frac{(8001 \pm 664)K}{T[K]}\right)}\ mbar \qquad (22)$$

The pressure calculated by this equation evaluates to $2 \cdot 10^{-11}$ mbar at 50 °C and therefore is completely negligible at the temperatures occurring during the process. As β-UF_5 crystallizes in form of a three-dimensional infinite network structure with an 8-coordinated uranium atom, its vapor pressure should be even lower as that of α-UF_5, which crystallizes in form of one-dimensional linear chains [124].

UF_6 is the only known binary uranium compound with a comparably low boiling point, drawing high interest from nuclear industry for enrichment processing. In the gaseous state, UF_6 is a covalent molecule with octahedral structure. The uranium atom is in its center of mass, the fluorine atoms surrounding it and being located at the corners of the octahedron. Despite its high molar mass, rather large size and high boiling point, the gaseous phase of UF_6 only shows minor deviation from ideal gas behavior [125]. As UF_6 was a subject of great interest during the last century, numerous sources for the calculation of its vapor pressure exist. According to Llewellyn [126] it can be calculated by:

$$-19\ °C \text{ to } 65\ °C \qquad p = 1.33 \cdot 10^{\left(-\frac{2751K}{T[K]} - 75.0 \cdot e^{-\frac{2560K}{T[K]}} - 1.01 \cdot \log(T[K]) + 13.797\right)}\ mbar \qquad (23)$$

$$65\ °C \text{ to } 100\ °C \qquad p = 1.33 \cdot 10^{\left(-\frac{1946K}{T[K]} - 0.00492 \cdot T[K] + 0.934 \cdot \log(T[K]) + 8.123\right)}\ mbar \qquad (24)$$

Oliver et al. [127] used the modified Antoine equation in different temperature regimes to describe its vapor pressure by:

$$0\ °C \text{ to } 64.0\ °C \qquad p = 1.33 \cdot 10^{\left(6.38363 + 0.0075377 \cdot T[°C] - \frac{942.76}{T[°C] + 183.416}\right)}\ mbar \qquad (25)$$

$$64.2\ °C \text{ to } 91.9\ °C \qquad p = 1.33 \cdot 10^{\left(6.99464 - \frac{1126.288}{T[°C] + 221.963}\right)}\ mbar \qquad (26)$$

Both equations show minor differences in the calculated pressure by up to 4 % in the thermal regions mentioned. As own measurements with respect to vapor pressure have not been performed, no statement can be given which of the characterizations holds the higher accuracy. However, for the experiments the exact value of the vapor pressure is irrelevant as it serves as a mean to determine, whether UF_6 was completely transferred into the gaseous phase. Figure 5.16 shows the vapor pressure curve over the entire domain covered by the equations mentioned above.

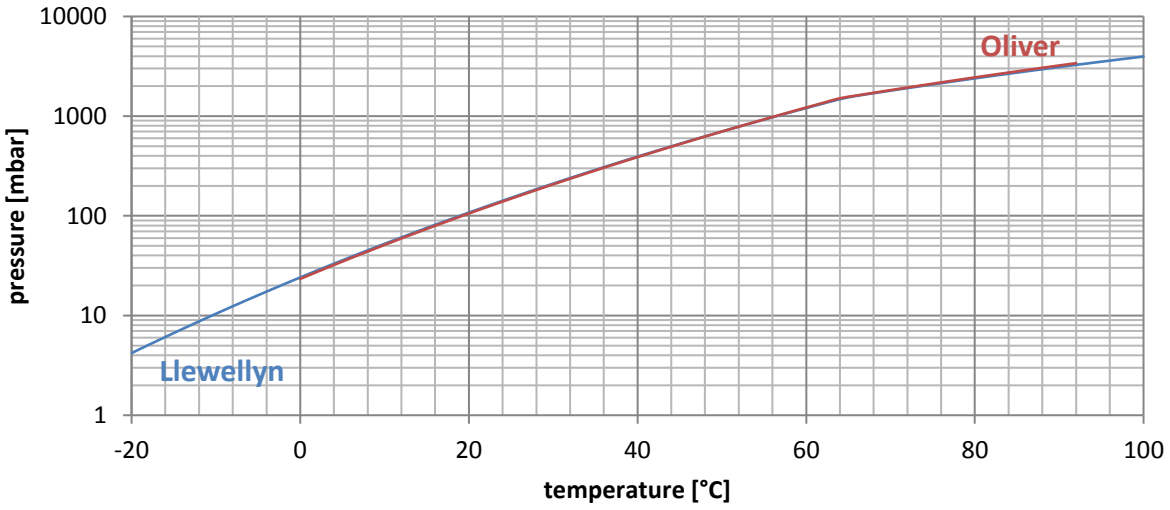

Figure 5.16: Vapor pressure of UF_6 according to Llewellyn (blue graph) and Oliver (red graph). The absolute difference between both characterizations does not exceed 4 %.

5.2.2 Reaction conditions

Uranium is very easily fluorinated and can be presented in a massive form such as a sheet or an ingot. Due to its high affinity to oxygen, it is favorable to free the material from any oxide layer by inserting it into a solution of half-concentrated nitric acid for 60 seconds and rinsing it with distilled water and acetone afterwards. However, experience of the working group of high-density fuel development at FRM II proposes a different cleaning procedure to be more efficient [128]. Thus it seems suitable, to deploy a mixture of 10 % H_2O_2 and 15 % SurTec 138 (a cleaning solution on KOH basis) for the sample preparation of future experiments, if the impact of a potential oxide layer is to be minimized.

The course of the fluorination reaction of uranium shows a behavior highly depended on the flow rate of the etching agent. Therefore, the results using a high volume flow and a low volume flow are described separately. Hereinafter, low flow refers to a mass flow of NF_3 of below 30.0 sccm, whereas high flow to a mass flow of at least 30.0 sccm.

Table 5.8: Experiments performed with UMo samples and their corresponding process data.

composition	sample mass [mg]	Ar-NF_3 [sccm]	time [min]	residual mass [mg]	reaction yield [%]	etching rate [mg/min]
UMo05	1272.93	20 - 20	34.3	176.33	86.15	32.0
UMo05	2217.46	25 - 25	48.5	152.72	93.11	42.6
UMo05	1974.10	35 - 35	39.5	85.93	95.65	47.8
UMo01	1229.20	20 - 20	51.5	78.80	93.59	22.3
UMo01	4472.04	25 - 25	114.5	265.98	94.05	36.7
UMo01	3033.35	35 - 35	64.5	201.97	93.34	43.9

High volume flow

In the investigated configuration of the reaction chamber, a volume flow ratio of NF_3 : Ar of 35.0 sccm : 35.0 sccm provokes a glowing of the target, several minutes after the ignition of the plasma (see Figure 5.17). However, the target does not glow continuously but rather in short intervals of about one to two minutes, after which the glow expires for about the same amount of time. Further increase of the volume flow of NF_3 increases the brightness of the glowing, indicating a higher temperature and thus an accelerated reaction.

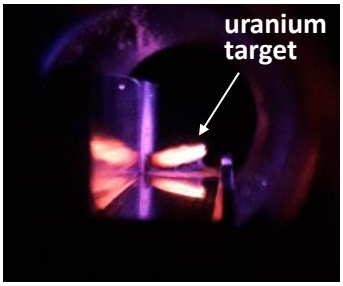

Figure 5.17: Uranium target at a volume flow of 35 sccm NF_3 and 35 sccm Ar. The target starts to glow after about 12 minutes after igniting the plasma.

During the reaction, the target is constantly dissolved to more than 95 %. Several trials with UMo1 targets even showed complete dissolution with only non-volatile reaction products remaining on the Monel carrier, as shown in Figure 5.18 and Figure 5.19.

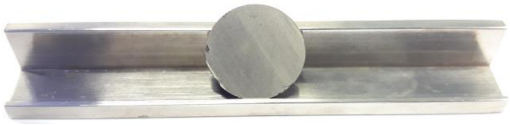

Figure 5.18: Uranium target before fluorination.

Figure 5.19: Residues after fluorination at a NF_3 flow of 35 sccm with complete consumption of the uranium target. The white powder is AlF_3 as shown by XRPD.

These products originate from the radioactive decay of uranium on one hand (also see Table 5.9) and on the other hand are impurities from the production process. For instance, a white residue always present after fluorination could be identified as aluminum fluoride AlF_3 by XRPD (also see Figure A.16). Consultation of the processor identified the corundum crucibles used during the melting process as the most probable cause. Molten uranium is known to be highly oxophilic and according to [129] even able to corrode alumina by reducing it to elemental aluminum as described by reaction (27)

$$3\ U\ (l)\ +\ 2\ Al_2O_3\ \rightarrow\ 3\ UO_2\ +\ 4\ Al \qquad (27)$$

In addition to AlF_3, other compounds were also identified by gamma-spectroscopy. As they are found independent of the volume flow, their analysis is presented at the end of this passage.

During the course of the reaction, the pressure sensor next to the reaction chamber records a considerable different pressure dependent on whether or not the Monel carrier is loaded with a uranium sample. The same holds for the upper temperature sensor. Figure 5.20 shows the course of the pressure, Figure 5.21 the course of the temperature for an empty carrier as well as for a carrier loaded with an UMo05 sample with a mass of 1974 mg. In order to compare their results, both trials were performed under identical conditions. Even for the empty reaction chamber, the cold traps were equipped with refrigerants of identical temperature compared with the UMo run. The reaction chamber was initially evacuated and the trial was started with the introduction of 35.0 sccm argon to the reaction chamber. After 300 seconds, the plasma was ignited, resulting in a slight pressure jump. After an additional 180 seconds, 35.0 sccm NF_3 were introduced to the chamber.

As expected, until this point no difference in the course of the pressure occurred between the two settings. However, during the following course of the UMo run, the pressure started to decrease after several seconds, staying well below the pressure in the empty run. This is a strong indication of a reaction with a decrease in volume. It follows a comparable static phase, which is than replaced by an oscillation phase with rapid pressure rises and drops, as can be seen in Figure 5.22. During this phase, a decrease in pressure is accompanied by an increase in the brightness of the glow of the target as well as a rise in temperature.

In summary, if the course of pressure and temperature is known for a run without a target, an estimation of the progress of the fluorination reaction seems to be possible even without visual inspection of the target.

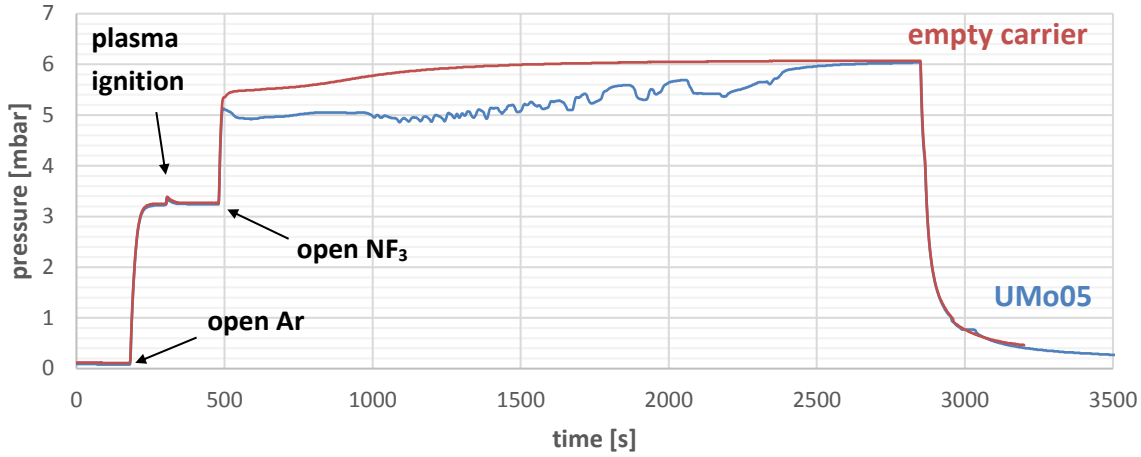

Figure 5.20: Comparison of the pressure pattern of a mixture of 35.0 sccm Ar and 35.0 sccm NF_3 with a UMo05 sample with a mass of 1974 mg on the Monel carrier (blue graph) and with the Monel carrier alone (red graph).

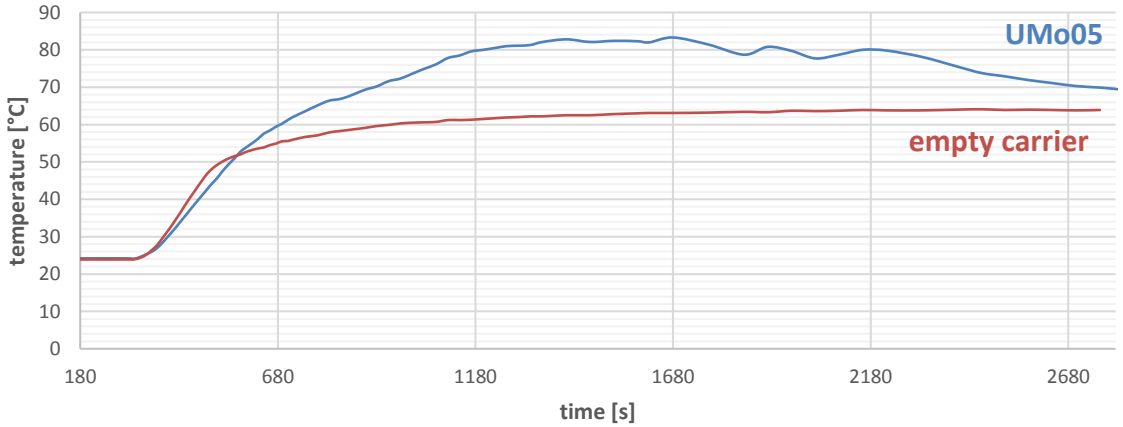

Figure 5.21: Comparison of the temperature pattern of the same sample on the Monel carrier (blue graph) and with the Monel carrier alone (red graph).

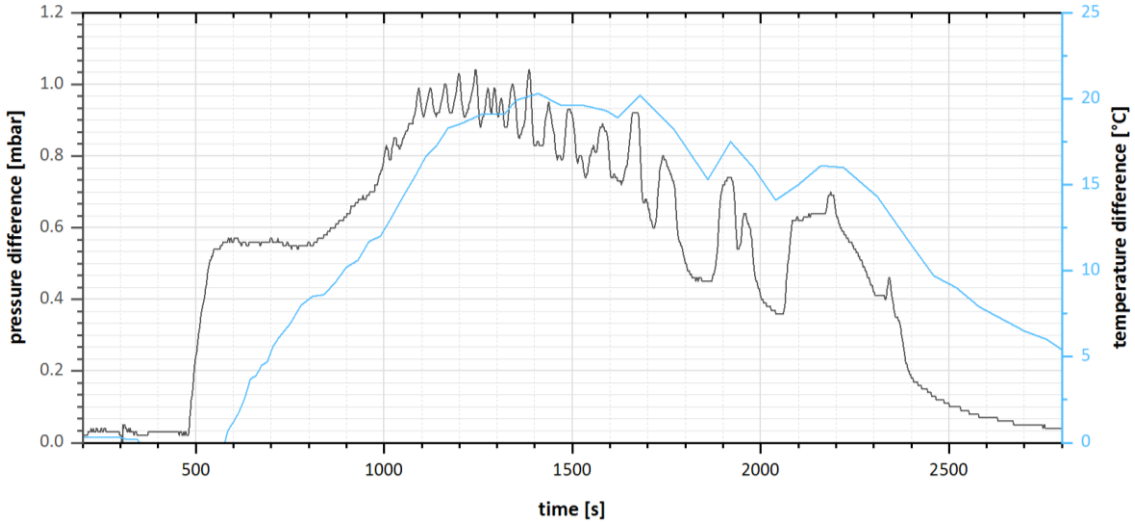

Figure 5.22: The difference in pressure and temperature between the Monel carrier exposed empty and with an UMo01 sample during the fluorination process. A decrease in pressure (= increase in pressure difference) is accompanied by an increase in the brightness of the glow of the target as well as a rise in temperature.

Low volume flow

At a low flow, no glowing of the target was observed, indicating a much lower temperature of the target during the course of the reaction (see Figure 5.23).

Figure 5.23: Dissolution of a target at a low flow of the etching agent, here at 20 sccm Ar and 20 sccm NF_3.

In addition to the appearance of the target during the reaction, also the outcome of the reaction shows difference behavior. As during a high flow reaction, UF_6 is deposited in the cold traps. However, the reaction yield is slightly lower as for the high flow reaction, as it never exceeds 93 %. The explanation for this observation can be found in the concurrent formation of another compound. As the target continuously diminishes, this compound is deposited in its shade and can be identified as UF_4 by XRPD. The deposition exclusively occurs on the walls of the Monel carrier in the slipstream region of the target, as can be seen from Figure 5.26 and Figure 5.27. This observation indicates the necessity for a relative local deficit of fluorine radicals. Additionally, it supports the idea of UF_6 being reduced to UF_4 by oxidation of elemental metallic uranium.

Figure 5.24: Uranium target before fluorination.

Figure 5.25: Residues after fluorination at a NF_3 flow of 25 sccm.

Figure 5.26: Cleared residues after removal of the covering AlF_3 layer.

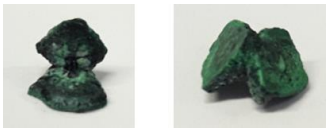

Figure 5.27: The residues of Figure 5.26 after removal from the Monel carrier and rinsing them with isopropanol.

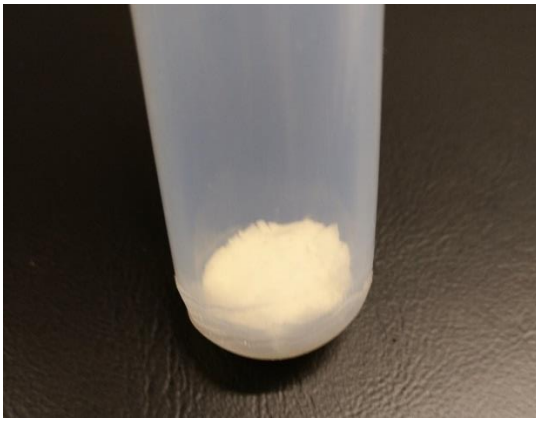

Figure 5.28: UF_6 powder after condensing it from one cold trap into an FEP tube, identified by IR and NMR spectroscopy.

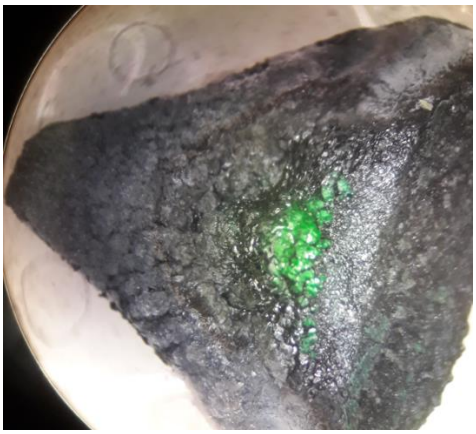

Figure 5.29: UF_4 left on the Monel carrier after fluorination, identified by XRPD (see Figure A.17). The entire chunk consists of UF_4, as samples of different parts have been analyzed. Note the greenish color under the black covering.

Residues found at low and high flow

Significant amounts of ^{234}Th and ^{234m}Pa, accounting for about 40 % of the activity initially present in the targets, were identified in the residues at the Monel carrier by gamma spectroscopy. For this measurement, the Monel carrier was completely masked with Scotch tape after extraction from the reaction chamber, thereby fixating the residues. The deployed UMo target had a total uranium mass of 2727 mg, resulting in an activity of 33.6 kBq of ^{238}U. As both isotopes, ^{234}Th and ^{234m}Pa, are initially in secular equilibrium with their parent and grandparent nuclide ^{238}U, respectively, the activity of all three is initially identical. After the fluorination and complete transformation of uranium to UF_6, ^{234}Th is no longer reproduced from the decay of ^{238}U and its activity decreases over time. The activities listed in Table 5.9 were measured 48.5 hours after extraction. An extrapolation to the time of the fluorination process gives an activity of 14.1 kBq for ^{234}Th, equivalent to about 42 % of the activity initially present.

Under the conditions in the reaction chamber, thorium is most likely to form thorium tetrafluoride ThF_4, a white solid, which is stable to the exposure of both, oxygen and moisture. Protactinium on the other hand is most likely to form protactinium pentafluoride PaF_5, a white, highly hygroscopic solid, which is reported to react with moisture to form diprotactinium(V)-oxidoctafluoride Pa_2OF_8 [130]. Table 5.9 shows that ^{234}Th and ^{234m}Pa are only present on a picogram and femtogram scale, respectively. This circumstance prevents the analysis of their exact chemical composition as these amounts will neither be detected by XRPD nor by µRFA.

The presence of ^{234}Th and ^{234m}Pa and the absence of ^{238}U at the same time suggests the suitability of the process to separate volatile from non-volatile fluorides already at this stage of the process.

Table 5.9: Composition of the powdery white residues after uranium fluorination as measured from gamma spectroscopy.

nuclide	activity [kBq]	specific activity [Bq/g]	corr. mass [mg]
^{231}Th	0.09 ± 0.01	$1.89 \cdot 10^{16}$	$(4.54 \pm 0.36) \cdot 10^{-12}$
^{234m}Pa	13.93 ± 0.45	$2.56 \cdot 10^{19}$	$(5.44 \pm 0.18) \cdot 10^{-13}$
^{234}Th	13.34 ± 0.97	$8.57 \cdot 10^{14}$	$(1.56 \pm 0.11) \cdot 10^{-8}$

5.2.3 UV/VIS spectroscopy

As UF_6 is a colorless gas, it would be expected to show no absorption in the visible range of the electromagnetic spectrum. However, it shows strong absorption in the UV-range below 300 nm. A strong decrease in absorbance follows, reaching a minimum at about 340 nm and increases again reaching a maximum at about 368 nm. A plateau with almost constant absorbance follows between 375 and 390 nm, after which it decreases until at about 420 nm at which point no further absorption is observed. The absorption in the latter region is related to the photodissociation of UF_6 into UF_5 and fluorine and will be described in further detail in chapter 5.5.1.

The UV/VIS spectrum acquired from UF_6 synthesized in the fluorination process is in very good agreement with the data from Lewis et al. in [131] and does not show any additional absorption, thereby underlining the absence of a major amount of impurities. Both graphs are depicted in Figure 5.30.

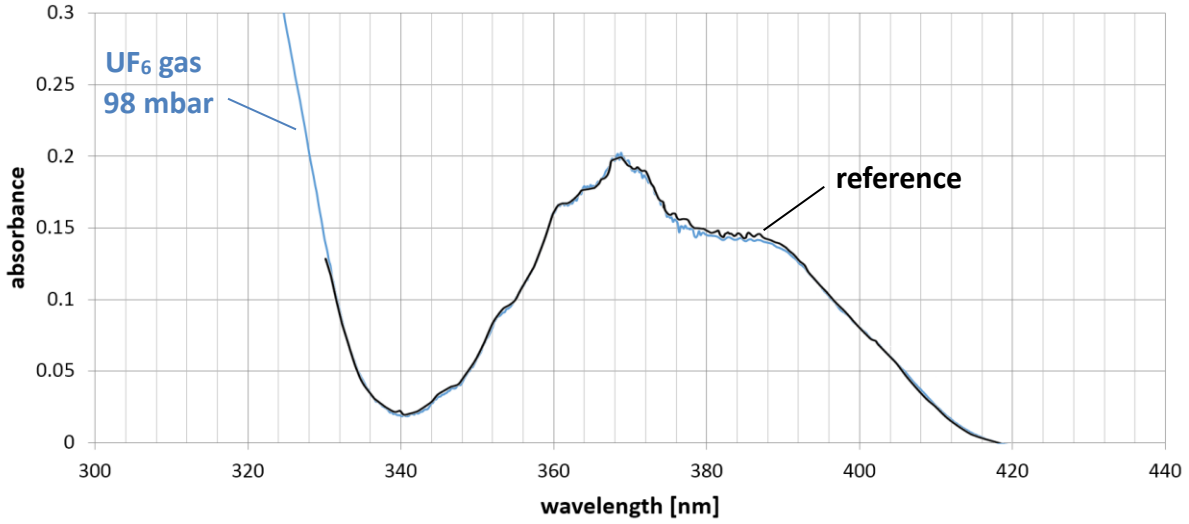

Figure 5.30: The blue graph depicts the spectrum of gaseous UF_6 synthesized in the MPFL, measured at 298K and 98 mbar with 100 mm optical path. The black graph shows the spectrum of UF_6 vapor at 298 K and 2 mbar with 8.25 m optical path [131].

5.2.4 IR spectroscopy

The spectrum acquired with the measuring cell is in good agreement with the data from literature. As the transmittance of the BaF_2 is down to 0.3 % at 640 cm^{-1}, the ν_3 fundamental at 640 cm^{-1} could be observed, its exact position could however not be determined. This band can be observed down to pressures of about 1 mbar and may therefore be used to detect even small amounts of UF_6. One additional band may be found at 741.4 cm^{-1} that is not found in the reference spectrum. As UF_6 was the second hexafluoride to be synthesized subsequent to MoF_6, this band may be assigned as the ν_3 fundamental of traces of MoF_6.

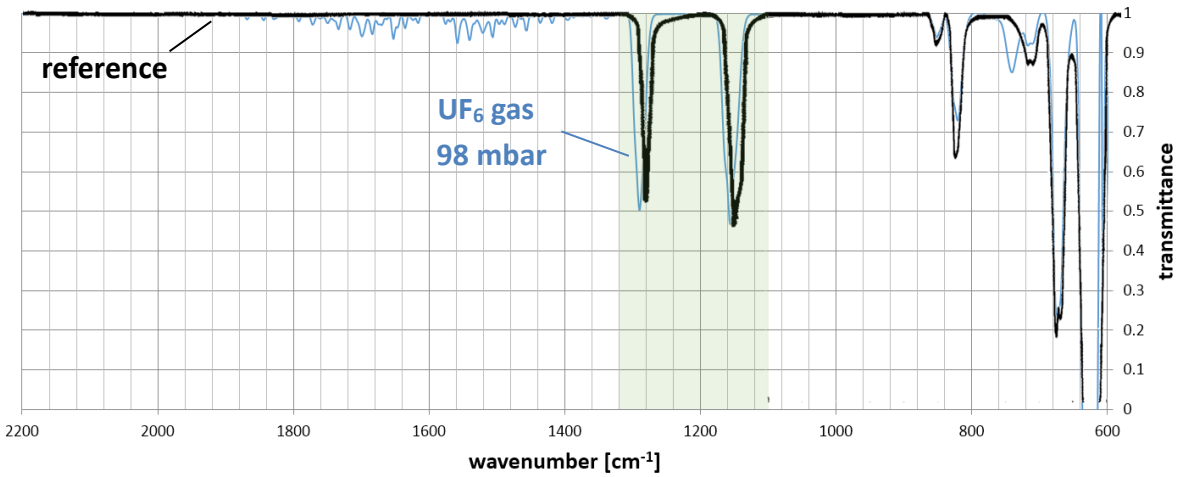

Figure 5.31: The blue graph shows the IR spectrum of the content of the first cold trap after the fluorination of a uranium sheet acquired with the measuring cell at 98 mbar. The black graph shows the IR spectrum of UF_6 as reported by Burke et al. [115]. A spectrum without superimposed literature data may be found in Figure A.18.

An additional measurement with a resolution of 2 cm^{-1} reveals a more detailed structure in many of the combination bands. Thus, the bands at 674, 825, 850, 1157 and 1290 cm^{-1} actually may be observed as a doublet or split into their PQR branches, respectively. The band at 1159 cm^{-1} has been assigned by Burke et al. belonging to either a binary or to a ternary combination band. However, they are actually resolved as the three branches of one single binary combination band and assigned to the calculated positions. A detailed decomposition of the bands may be found in Figure A.23. The same holds for the structure at the combination band at 1290 cm^{-1} that also may be decomposed into its three PQR branches. The corresponding analysis is depicted in Figure A.24.

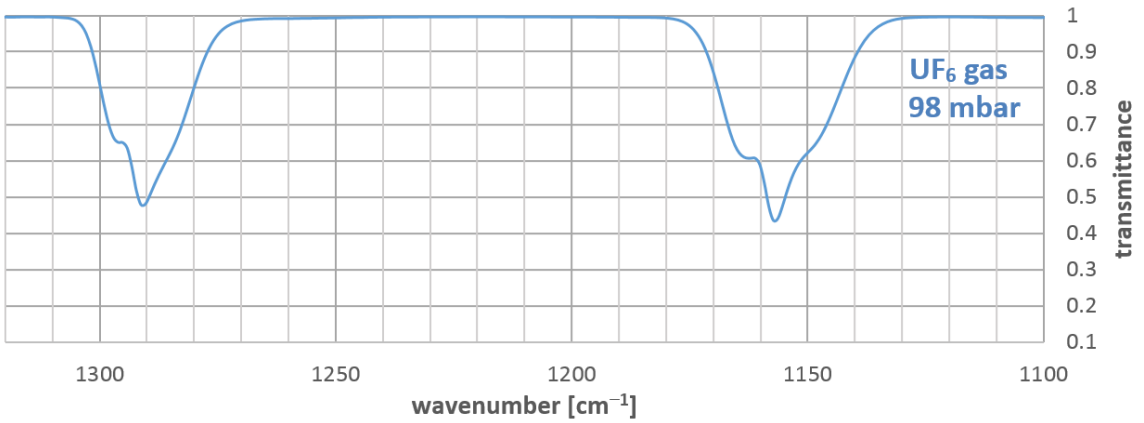

Figure 5.32: Measurement with a higher resolution of 2 cm^{-1} of the region between 100 and 1320 cm^{-1} (highlighted in green in Figure 5.31), revealing a more complicated structure of the two combination bands than originally observed.

The observed band at 674 cm^{-1} is a doublet located at 670 and 676 cm^{-1}, the band at 825 cm^{-1} is also a doublet located at 821 and 828 cm^{-1} and the band at 850 cm^{-1} a superposition of its PQR branches located at 847, 853 and 858 cm^{-1}. The decomposition of these bands is depicted in Figure A.19 to Figure A.21. There are some signs of the band at 1662 cm^{-1}, but due to considerable noise in that region, no clear assignment is possible. Table 5.10 lists the bands that have been observed by Burke et al. and their assignment as well as the position, at which they would be expected based on the combination of the fundamentals. In comparison, the last column lists the positions found during the measurements of this work.

Table 5.10: The position and assignment of the bands observed by Burke et al. as well as their calculated position. The position of the ν_3 fundamental at 623 cm^{-1} is the observed perturbed value, the position at 640 cm^{-1} the unperturbed value. The last column lists the position of the bands found analyzing the IR spectra of UF_6 during the experiments of this thesis. The exact position of the ν_3 fundamental could not be determined (n.d.). Many of the bands were only identified as a single one by Burke but are actually a superposition of several branches of one band. Positions found in this work not assigned in the previous work are denominated with n.o. (= not observed).

assignment	Burke obs. wavenumber [cm^{-1}]	Burke calc. wavenumber [cm^{-1}]	this work wavenumber [cm^{-1}]
ν_3	623 (640)	–	n.d.
$\nu_2 + \nu_6$, P	674	641	670
$\nu_2 + \nu_6$, R	n.o.	–	676
$\nu_2 + \nu_4$, P	715	711	710
$\nu_2 + \nu_4$, R	n.o.	–	718
$\nu_3 + \nu_5$, P	825	840	821
$\nu_3 + \nu_5$, R	n.o.	–	828
$\nu_1 + \nu_4$, P	n.o.	–	847
$\nu_1 + \nu_4$, Q	850	856	853
$\nu_1 + \nu_4$, R	n.o.	–	858
$\nu_2 + \nu_3$, P	n.o.	–	1148
$\nu_2 + \nu_3$, Q	1159	1151	1157
$\nu_2 + \nu_3$, R	n.o.	–	1164
$\nu_1 + \nu_3$, P	n.o.	–	1285
$\nu_1 + \nu_3$, Q	1288	1296	1291
$\nu_1 + \nu_3$, R	n.o.	–	1297
$2\,\nu_3 + \nu_4$	n.o.	1480	n.o.
$2\,\nu_1 + \nu_2$	n.o.	1512	n.o.
$2\,\nu_2 + \nu_3$	n.o.	1662	n.o.
$3\,\nu_3$	n.o.	1920	n.o.

5.2.5 Raman spectroscopy

Raman spectroscopy was performed on a sample from the sample cylinder. Thus, the acquired spectrum is not from a single fluorination experiment but rather represents a cross section over several trials. As the sample was enclosed in an FEP tube, the spectrum shows additional signals originating from FEP.

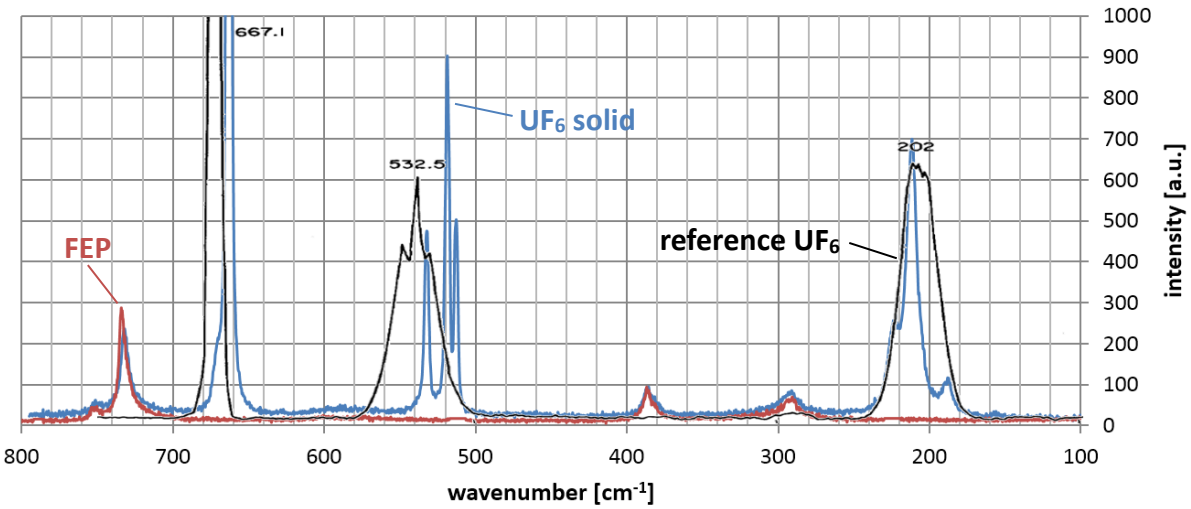

Figure 5.33: Raman spectrum of UF_6 solid (blue graph) at a temperature of 22 °C under intrinsic pressure. The black graph shows the Raman spectrum of UF_6 gas at a temperature of 85 °C and a pressure of 2 bar [116]. For comparison, the spectrum of FEP (red graph) is also shown.

The structure of the UF_6 spectrum reported by Claassen et al. [116] shows considerable deviations from the one acquired during the course of this thesis. Whereas these may be accounted for by the different state of the measured samples (gas vs. solid), the deviations regarding the measurements of McDowell et al. [132] are more puzzling, as they have also been measured on a solid sample at room temperature. One possible explanation is the formation of small crystals with a preferred orientation. As solid UF_6 is present in an orthorhombic crystal structure, it shows different bands depending on the orientation of the crystal.

Table 5.11: Comparison of the fundamental bands reported by McDowell et al. with the positions determined during the experiments of this thesis. The FWMH $\Delta_{1/2}$ is given for 298 K.

assignment	McDowell et al. wavenumber [cm^{-1}]	this work wavenumber [cm^{-1}]
ν_5, P	–	188.1
ν_5, Q	200.3 ($\Delta_{1/2}$ = 19 cm^{-1})	211.8
ν_5, R	–	224.1
ν_2, P	–	512.8
ν_2, Q	534.1 ($\Delta_{1/2}$ = 15 cm^{-1})	518.7
ν_2, R	–	532.4
ν_1	667.1	663.1

5.2.6 NMR spectroscopy

NMR spectroscopy was first performed on UF_6 in the solid phase, but did not provide expedient data. Thus, additional measurements were done on the liquid phase under intrinsic pressure by heating the sample to a temperature of 348 K.

UF_6 in the liquid phase shows a single peak at a chemical shift of 765.0 ppm w.r.t. $CFCl_3$. This in good accordance with the position reported of 764.0 ppm w.r.t. $CFCl_3$ by Seppelt in [133]. An additional, very weak peak may be identified at 759 ppm. It most probably originates from gaseous UF_6 also present in the FEP tube due to the high vapor pressure of UF_6 at 348 K. A chemical shift of 10.6 ppm for the signal of UF_6 in the vapor phase relative to its liquid phase has also been reported by Ursu et al. [134]. However, they did not provide information about the used reference compound.

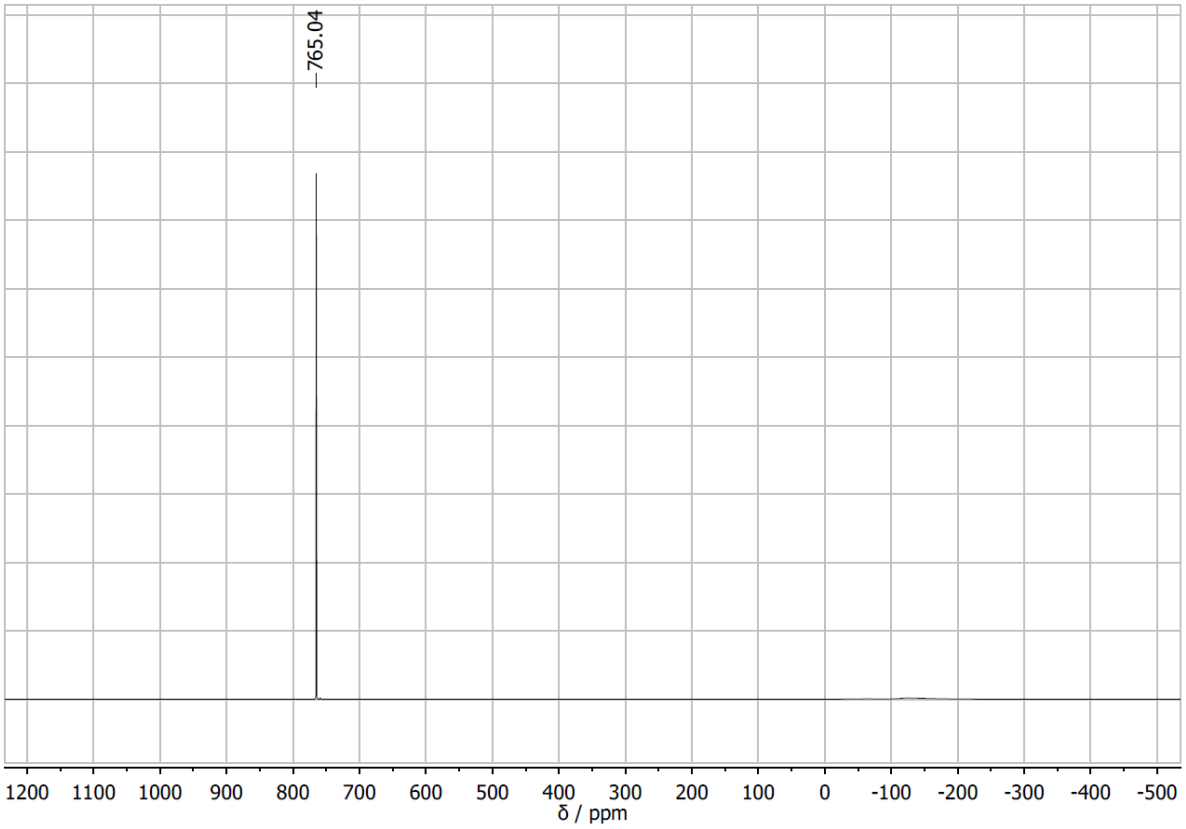

Figure 5.34: NMR spectrum of UF_6 in the liquid phase under intrinsic pressure measured at a temperature of 348K.

5.3 Acquisition of IR reference spectra

In order to determine the efficiency of a separation process of UF_6 and MoF_6, the exact composition of a mixture of both compounds before and after the separation must be determined. Thereby, the measurement must not alter the composition, a fact that eliminates methods such as ICP-MS or MP-AES. In contrast, IR spectroscopy using the measuring cell is well suited for this purpose. In order to be used quantitatively, a number of spectra must be acquired at different pressures and ideally, the spectrum of each compound has distinct absorption bands in regions, where the other component does not show absorption altogether. For UF_6, this is the case at 1290.3 cm^{-1} and 1157.3 cm^{-1}. The same holds for MoF_6 at 1388.7 cm^{-1} and 1481.3 cm^{-1}. The strong band of UF_6 at 675.0 cm^{-1} may only be used with reservations for quantitative analysis, as the transmittance of the BaF_2 windows is already down to 2.3 % inducing a too large uncertainty at that wavenumber. Figure 5.35 shows both spectra in the relevant region. All reference and subsequent experimental spectra were collected with the same resolution of 4 cm^{-1}, the results are therefore only valid for this parameter. A different resolution may result in deviant values for the transmittance.

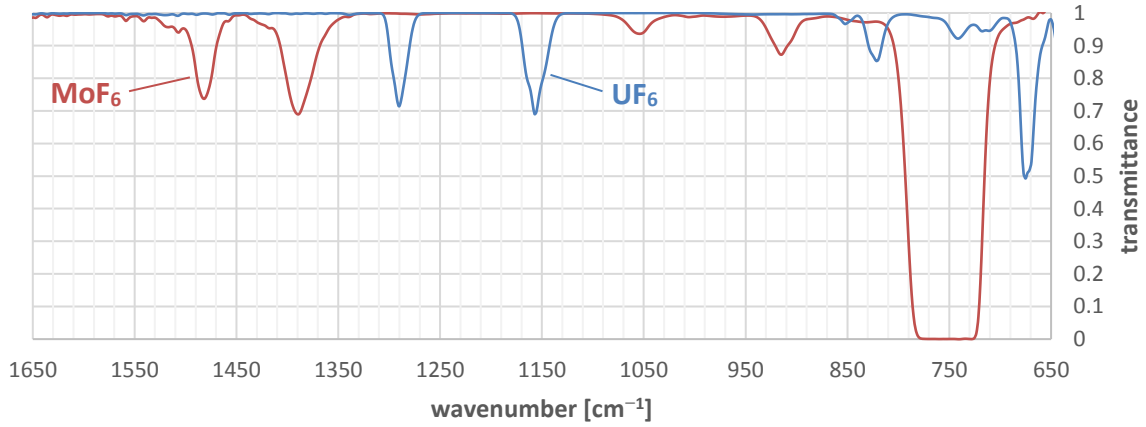

Figure 5.35: IR transmission spectrum of MoF_6 (red graph) and UF_6 (blue graph). Both spectra show distinct absorption bands in the overtone region that do not overlap and that are therefore utilizable for a quantitative analysis.

The UF_6 and MoF_6 produced in the fluorination line and stored in Swagelok miniature sample cylinders ① and ② can be transferred to the measuring cell using the separation line as shown in Figure 5.36. The system pressure was measured using a piezo sensor VSC42MV of the Thyracont company ③. This sensor features a linear pressure-voltage characteristic and is fairly resistant to MoF_6 and UF_6. Careful opening the valves of the sample cylinder allows to set a specific pressure in the measuring cell ④. In order to prevent contamination of the content of the sample cylinders, the hexafluoride left in the connecting pipes was not resublimed after closing the valve of the measuring cell. Instead, it was pumped off into the absorber. The measuring cell was then disconnected from the line and an IR transmission spectrum was collected. For MoF_6, the transmission spectrum was measured for eight different pressures, two times each with exception of two measurements, resulting in a total number of 14 spectra. For UF_6, the same was done for seven different pressures two measurements each, resulting in a total number of also 14 spectra. As neither UF_6 nor MoF_6 show any absorption in the region between 3200 and 2500 cm^{-1}, this region was used for the background correction of the measured spectra and the arithmetic mean of the transmittance in this range defined as the offset, by which all values were corrected.

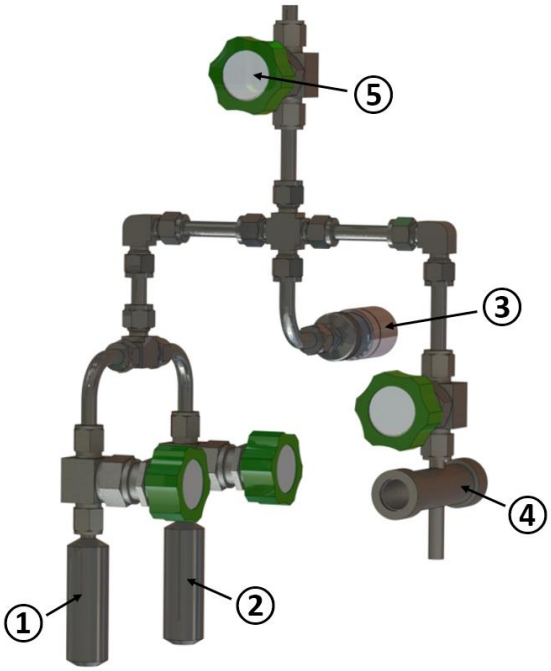

Figure 5.36: Part of the separation line used for the acquisition of the IR reference spectra. UF_6 and MoF_6 are taken from the miniature storage cylinders (1) and (2), transferred to the measuring cell (4), in which the pressure is monitored using a piezo pressure sensor (3). A membrane valve (5) shuts this part off from the vacuum pumps.

As mentioned before, the systematic error introduced by usage of the ideal gas law is comparably small. Combining it with the Lambert-Beer law allows for the conclusion of the pressure from the absorbance according to:

$$\varepsilon = \frac{A \cdot R \cdot T}{p \cdot d} \cdot \log_{10} e = 0.434 \cdot \frac{A \cdot R \cdot T}{p \cdot d} \qquad (28)$$

Hereby, ε indicates the molar attenuation coefficient, A the measured absorbance, R the universal gas constant, T the temperature of the gas, p the pressure in the measuring cell and d the length of the measuring cell. Thus, for the wavenumbers mentioned above, the molar attenuation coefficients of the binary combination bands of MoF_6 and UF_6 are listed in Table 5.12. The attenuation coefficients over the range from 650 to 2050 cm^{-1} for both hexafluorides may be found in Figure A.29 and Figure A.30.

Table 5.12: Molar attenuation coefficients of MoF_6 and UF_6 combination bands used for quantitative analysis. Error is given as one standard deviation.

compound	wavenumber [cm^{-1}]	molar attenuation coefficient ε [m^2/mol]
MoF_6	1481.3	0.2867 ± 0.0028
MoF_6	1388.7	0.3498 ± 0.0031
UF_6	1290.3	0.3113 ± 0.0012
UF_6	1157.3	0.3428 ± 0.0015

These coefficients serve as a mean to calculate the pressure of UF_6 and MoF_6 from IR spectroscopy in the following experiments using the measuring cell by solving equation (28) for p.

5.4 Separation by difference in vapor pressure

The idea behind this separation method is based on the difference in vapor pressure of MoF_6 und UF_6 at low temperatures. In the case of UF_6, the temperature range known of being described by equation (23) ends at −19 °C. Although extrapolation down to a temperature as low as −80 °C is highly speculative, it nevertheless shows the divergent trend of both graphs in this temperature regime. Hereby, the forms of the equations for the vapor pressure according to both, Llewellyn [126] and Oliver [127] were evaluated in order to increase their informative value. The less favorable result for the separation process arises from the equation found by Llewelyn and is therefore depicted in Figure 5.37.

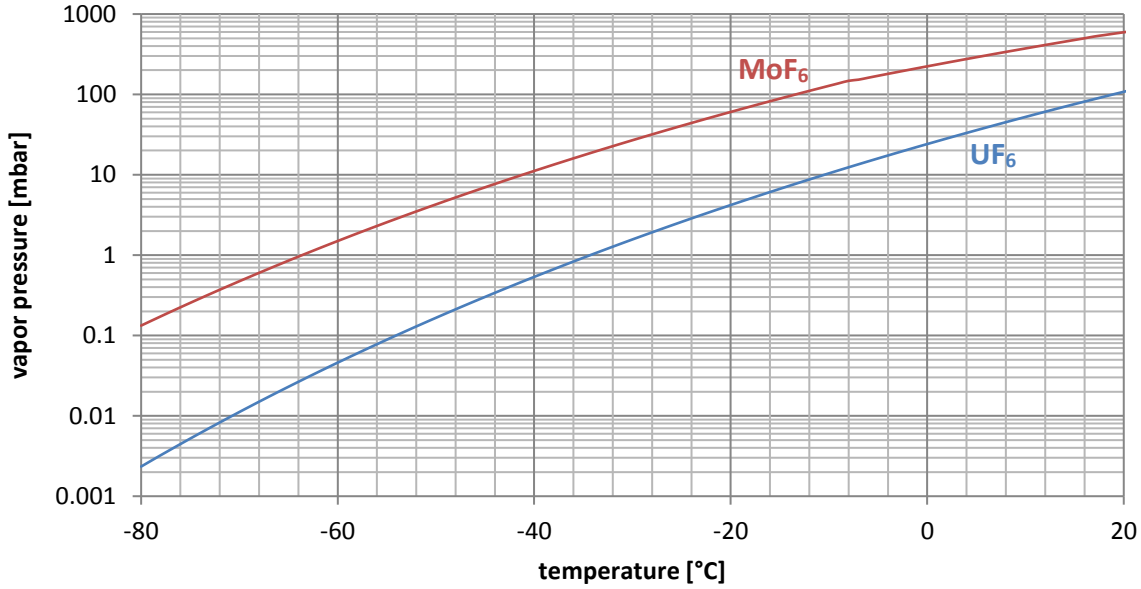

Figure 5.37: Vapor pressure curve of MoF_6 (red graph) and UF_6 (blue graph).

The graphs show the tendency to diverge at lower temperatures, a circumstance that is further illustrated by calculation of the ratio between both vapor pressures as listed in Table 5.2.

Table 5.13: Vapor pressure of UF_6 und MoF_6 at different temperatures and the ratio of both pressures.

temperature [°C]	vapor pressure UF_6 [mbar]	vapor pressure MoF_6 [mbar]	$p(MoF_6)/p(UF_6)$
−10	10.42	127.91	12.3
−30	1.57	26.90	17.2
−50	0.17	4.28	25.8
−70	0.01	0.47	42.4

The following calculations will relate the etching rate and the temperature of the cold trap to the uranium deposition rate. As the fluorination of 1 mol U leads to the formation of 1 mol UF_6, its molar flow may be calculated by:

$$\dot{n}_{UF_6} = \frac{\dot{m}_U}{M_U} \qquad (29)$$

$\dot{m}_U$ thereby being the etching rate of uranium. The molar flow of the etching agent into the reaction chamber may be calculated from the volume flow by:

$$\dot{n}_{NF_3,MFC} = \frac{\dot{V}_{NF_3,MFC}}{V_M} \quad (30)$$

as both, the unit sccm and the molar volume V_M are defined at a pressure of 1013.25 hPa and a temperature of 0 °C. According to equation (31), 2 mole NF_3 will form 1 mol UF_6. The same holds for MoF_6:

$$2\ NF_3 + U \rightarrow N_2 + UF_6 \quad (31)$$

$$2\ NF_3 + Mo \rightarrow N_2 + MoF_6 \quad (32)$$

The molar flow of unreacted NF_3 at the cold traps will therefore amount to:

$$\dot{n}_{NF_3,CT} = \frac{\dot{V}_{NF_3,MFC}}{V_M} - 2 \cdot \left(\frac{\dot{m}_U}{M_U} + \frac{\dot{m}_{Mo}}{M_{Mo}}\right) \quad (33)$$

The total molar flow is the sum of the molar flows of the constituents NF_3, Ar, UF_6 and MoF_6:

$$\dot{n}_{tot} = \sum_i n_i = \frac{\dot{V}_{NF_3,MFC}}{V_M} - \frac{\dot{m}_U}{M_U} - \frac{\dot{m}_{Mo}}{M_{Mo}} + \frac{\dot{V}_{Ar}}{\dot{V}_M} \quad (34)$$

Based on the ideal gas law, it may be assumed the static pressures of the individual components p_i behaving directly proportional to their molar flows $\dot{n}_i$:

$$\frac{p_i}{p_{tot}} = \frac{\dot{n}_i}{\dot{n}_{tot}} \quad (35)$$

The static partial pressure of the two hexafluorides MF_6 (M = U, Mo) may therefore be calculated by:

$$p_{MF_6} = \frac{\dot{m}_M}{M_M} \cdot \left(\frac{\dot{V}_{NF_3,MFC}}{V_M} - \frac{\dot{m}_U}{M_U} - \frac{\dot{m}_{Mo}}{M_{Mo}} + \frac{\dot{V}_{Ar}}{\dot{V}_M}\right)^{-1} \cdot p_{tot} \quad (36)$$

If the static partial pressure of the hexafluoride is higher than its corresponding vapor pressure at that temperature, it is to be expected to partly deposit in the cold traps. If the static partial pressure on the other hand is much lower than its vapor pressure at this temperature, the hexafluoride is expected to stay in the gas phase. For the process, the cold traps can be operated cascading at decreasing temperature, in order to successively freeze out UF_6 and thereby enrich MoF_6 in the gas phase.

One of the challenges in the determination of the amount of the hexafluorides recovered was due to the low molybdenum content of the UMo01 samples. In order to keep MoF_6 at an easy detectable level, the mass of the targets was significantly increased. Obviously, the amount of UF_6 was likewise increased in return. For that reason, the use of the measuring cell proved to be unsuitable for the determination of the uranium content. Instead, both hexafluorides were hydrolyzed and the solution investigated using MP-AES. This was achieved by closing the valves of the cold traps and exchanging

the frigorific mixtures in favor of liquid nitrogen after the termination of the fluorination process. As the vapor pressures of both UF_6 and MoF_6 are insignificant at this temperature, a safe disassembly of the cold traps from the fluorination line under constant LN_2 cooling was possible. Subsequent to the disassembly, LN_2 was removed and an immediate addition of deionized water to the cold trap conducted. As reaction (37) is highly exothermic, the amount of water added must be sufficient to absorb the thermal energy released. Especially at amounts of UF_6 exceeding 3000 mg, this measure must be performed unhesitatingly and yet with caution in order to avoid a boiling retardation. The solution process itself is slow, as different uranium oxyfluorides are formed, protecting the remaining UF_6 from a contact with water. The color gradient thereby suggests these to include solid UO_2F_2 as well an orange substance, which is suspected to be UOF_4, as Wilson describes its preparation from UF_6 with dilute solutions of water in a HF slurry [135].

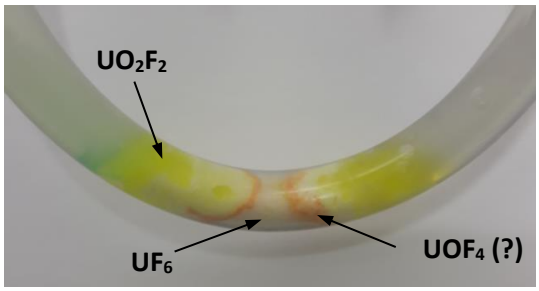

Figure 5.38: PFA cold trap with deposited UF_6 after addition of deionized water. The white substance in the center part is UF_6, whereas the yellow substance on the both outer ends is UO_2F_2. The orange substance in-between the two was not characterized, but from its color as well as the reaction environment, it is assumed to be UOF_4.

During hydrolysis, uranium hexafluoride forms uranyl fluoride UO_2F_2 and HF according to:

$$UF_6 + 2\ H_2O \rightarrow UO_2F_2 + 4\ HF \qquad (37)$$

The reaction of MoF_6 with water for its part is not well characterized. According to [107], an "ill-defined product forms which shows no Mo-F stretching vibration in the Raman spectrum" with excess water, which here definitely is the case. Surprisingly, a solution of pure MoF_6 in water does not show any color of all. This behavior is in strong contrast to MoF_6 coming in contact with traces of moisture, which is known to form a compound due to its strong color known as molybdenum blue. Molybdenum blue for its part is not a uniform compound either but rather a subsumption for molybdenum oxide hydroxides of the general formula $Mo_xO_y(OH)_z$ [136]. Here, molybdenum holds an oxidation number between +V and +VI. As the colorless solution of MoF_6 in water changes its color to blue after addition of zinc, at may be assumed that molybdenum therein stays in oxidation state +VI. In conjunction with the absence of Mo−F bonds, it seems reasonable to assume the formation of molybdic acid H_2MoO_4 according to:

$$MoF_6 + 4\ H_2O \rightarrow H_2MoO_4 + 6\ HF \qquad (38)$$

Table 5.14 lists the target and process data of the performed experiments. For experiments 1 to 3, the target material was UMo1, for the experiments 4 to 7 it was UMo05 and for experiments 8 to 10, UMo01 was applied. Experiment 1 was the only one using IR spectroscopy for analysis of the deposited compounds in the cold traps. Starting with experiment 3, MP-AES was used as an analytical method for all subsequent experiments. Table 5.15 to Table 5.17 list the results for each individual experiment and have to be read vertically. Given is the deployed NF_3/Ar ratio, as well as the applied and reacted mass of Mo. The masses have been calculated multiplying the target mass with the Mo content determined by ICP-MS as listed in Table 5.1. The three lines below the temperature of each cold trap list the mass fractions of the reacted uranium or molybdenum found in that cold trap.

Table 5.14: Basic conditions of the experiments performed investigating the separation based on the difference in vapor pressure. Experiment 1 to 3 use UMo1 as a substrate, experiment 4 to 7 use UMo05 and experiment 8 to 10 use UMo01.

Exp. No.	NF_3/Ar [sccm/sccm]	m_{sample} [mg]	$m_{reacted}$ [mg]	reaction yield [%]	reaction time [min]	etching rate [mg/min]
1	20/20	3265.8	–	–	42:20	–
2	25/25	2156.7	2124.9	98.53	26:20	80.7
3	35/35	2754.2	2753.6	99.98	28:45	95.8
4	20/20	1272.9	1096.6	86.15	34:15	32.0
5	25/25	2217.5	2064.7	93.11	48:30	42.6
6	25/25	537.5	497.4	92.54	23:30	21.2
7	35/35	1974.1	1888.2	95.65	39:30	47.8
8	20/20	1229.2	1150.4	93.59	51:30	22.3
9	25/25	4472.0	4206.1	94.05	114:30	36.7
10	35/35	3033.4	2831.4	93.34	64:30	43.9

As expected, an increase in the volume flow of the etching agent likewise results in an increase of the etching rate. However, both parameters do no correlate linearly. Furthermore, the impact of the exact positioning of the target becomes obvious. The targets of experiments 2 and 3, which were positioned at an angle of attack of 45° show significantly increased etching rates compared with the subsequent experiments, in which for their part the targets were aligned parallel to the gas flow.

Table 5.15: Separation experiments using UMo1 targets. Experiment 1 was performed using the measuring cell and IR spectroscopy for U and Mo mass determination, experiment 2 was not able to deposit any UF_6 or MoF_6 and experiment 3 was the first to use MP-AES for U and Mo mass determination. The content of the third cold trap of the second experiment was not analyzed, as it was used for an additional separation experiment (n.d. = not determinded).

Exp. No.	1	2	3
NF_3/Ar [sccm/sccm]	20/20	25/25	35/35
mass Mo, applied [mg]	32.7	24.6 ± 0.6	31.37 ± 0.80
mass Mo, reacted [mg]	–	24.2 ± 0.6	31.36 ± 0.80
T_{CT1} [°C]	− 74	− 37	− 59.0
fraction of Mo [%]	20.7	0.0	22.83 ± 0.60
fraction of U [%]	–	0.0	90.05 ± 1.07
mass ratio Mo [%]	–	0.0	0.29 ± 0.00
T_{CT2} [°C]	− 73	24	− 200
fraction of Mo [%]	–	–	41.61 ± 1.11
fraction of U [%]	–	–	5.41 ± 0.11
mass ratio Mo [%]	–	–	8.13 ± 0.16
T_{CT3} [°C]	− 200	− 200	–
fraction of Mo [%]	27.4	n.d.	–
fraction of U [%]	0.3	n.d.	–
mass ratio Mo [%]	52.3	–	–

Table 5.16: Separation experiments using UMo05. All experiments used MP-AES for mass determination of U and Mo.

Exp. No.	4	5	6	7
NF_3/Ar [sccm/sccm]	20/20	25/25	25/25	35/35
mass Mo, applied [mg]	7.52 ± 0.89	13.11 ± 1.55	3.18 ± 0.38	11.67 ± 1.38
mass Mo, reacted [mg]	6.48 ± 0.77	12.20 ± 1.45	2.94 ± 0.35	11.16 ± 1.32
T_{CT1} [°C]	− 69.3	− 68.2	− 60.5	− 66.4
fraction of Mo [%]	13.73 ± 1.63	24.75 ± 2.95	7.35 ± 0.92	13.53 ± 1.61
fraction of U [%]	91.79 ± 1.56	94.96 ± 0.89	61.75 ± 1.16	90.02 ± 0.94
mass ratio Mo [%]	0.09 ± 0.00	0.15 ± 0.00	0.07 ± 0.00	0.09 ± 0.00
T_{CT2} [°C]	− 66.0	− 65.4	− 200	− 69.0
fraction of Mo [%]	0.00 + 0.09	0.06 ± 0.03	73.25 ± 8.80	1.72 ± 0.21
fraction of U [%]	0.00 + 0.01	0.02 ± 0.01	27.24 ± 0.30	2.76 ± 0.06
mass ratio Mo [%]	0.09 + 60.00	2.08 ± 1.74	1.57 ± 0.04	0.37 ± 0.01
T_{CT3} [°C]	− 200	− 200	–	−200
fraction of Mo [%]	51.54 ± 6.14	29.99 ± 3.56	–	34.41 ± 4.08
fraction of U [%]	4.00 ± 0.08	3.20 ± 0.04	–	4.09 ± 0.65
mass ratio Mo [%]	7.12 ± 0.15	5.28 ± 0.08	–	4.77 ± 0.71

Table 5.17: Separation experiments using UMo01. All experiments used MP-AES for mass determination of U and Mo.

Exp. No.	8	9	10
NF_3/Ar [sccm/sccm]	20/20	25/25	35/35
mass Mo, applied [mg]	1.54 ± 0.17	5.59 ± 0.63	3.79 ± 0.42
mass Mo, reacted [mg]	1.44 ± 0.16	5.26 ± 0.59	3.54 ± 0.40
T_{CT1} [°C]	− 66.2	− 69.2	− 67.3
fraction of Mo [%]	5.08 ± 0.90	20.64 ± 2.43	18.28 ± 2.12
fraction of U [%]	84.58 ± 1.96	93.81 ± 2.00	90.10 ± 1.99
mass ratio Mo [%]	0.01 ± 0.00	0.03 ± 0.00	0.03 ± 0.00
T_{CT2} [°C]	− 67.9	− 67	− 70.2
fraction of Mo [%]	1.11 ± 0.71	0.15 ± 0.19	1.30 ± 0.32
fraction of U [%]	3.44 ± 0.03	0.00 ± 0.00	2.80 ± 0.03
mass ratio Mo [%]	0.04 ± 0.03	8.79 ± 10.61	0.06 ± 0.01
T_{CT3} [°C]	− 200	− 200	− 200
fraction of Mo [%]	74.48 ± 8.45	80.78 ± 9.23	64.19 ± 7.27
fraction of U [%]	7.72 ± 0.06	4.23 ± 0.10	4.81 ± 0.08
mass ratio Mo [%]	1.19 ± 0.02	2.33 ± 0.07	1.64 ± 0.04

The data listed in Table 5.15 to Table 5.17 show a relatively large uncertainty for the Mo and U content in the cold traps that originates from the large uncertainty of the Mo content of the UMo targets. Nevertheless, it allows drawing several conclusions about a separation based on difference in vapor pressure. Figure 5.39 is a visualization of the recovery of uranium in the first cold trap in dependency of its temperature and the etching rate. Hereby, all available data from UMo01 to UMo1 targets have been used, as the small molybdenum content is not expected to significantly affect the etching rate or the uranium deposition. In order to allow for a better visualization, error bars have only been plotted for the uranium recovery.

The diagram underlines the major impact of both, the etching rate and the cold trap temperature as well as their mutual influence on the deposition. At a given temperature, the uranium recovery will decrease with a decreasing etching rate. Similar, at a given etching rate, the uranium recovery will increase with decreasing temperature. High etching rates thereby seem to be able to compensate for relatively high temperatures, as is illustrated by a uranium recovery of 90 % at a temperature of −59 °C and an etching rate of 96 mg/min for experiment 3, compared to a recovery of 62 % at −61 °C and 21 mg/min for experiment 6. However, at a temperature as high as −37 °C, a deposition could not be achieved at all even at comparably high etching rates of 81 mg/min.

One observation of major importance is the successful recovery of almost two thirds of the employed molybdenum in the last cold trap for the UMo01 sample. As these samples closely represent the Mo content in an irradiated target, these results should also be applicable for them. In addition, the Mo ratio could be increased by a factor of between 10 and 20 from originally 0.12 % to between 1.2 and 2.3 %.

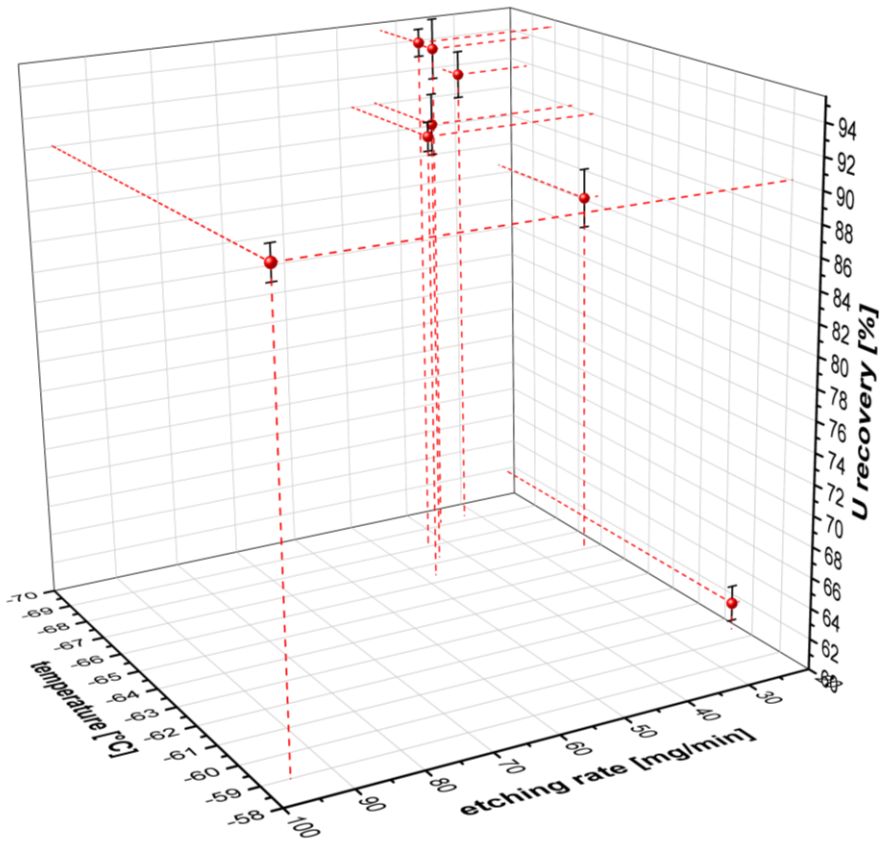

Figure 5.39: Recovery of uranium in the first cold trap in dependency of etching rate and cold trap temperature for all targets.

As stated before, the static partial pressure of UF_6 may be calculated using equation (36). On the other hand, the vapor pressure of UF_6 may be derived from equation (22). Under the premise of a dynamic equilibrium, the vapor pressure of UF_6 at a given temperature is the fraction of its total static pressure that will not be deposited in the cold trap. The following table gives an overview of the calculated recovery rate based on these assumptions and the observed recovery rate.

Table 5.18: Calculated and observed recovery of uranium in the first cold trap of the separation experiments. Experiment 2 and 3 used UMo1, experiments 4 to 7 used UMo05 and experiments 8 to 10 targets UMo01 targets.

Exp. No.	etching rate [mg/min]	T_{CT1} [°C]	total static pressure [mbar]	static pressure UF_6 [mbar]	vapor pressure [mbar]	calc. recovery [%]	obs. recovery [%]
2	80.7	−37.0	3.82	0.708	0.74	0.0	0.0
3	95.8	−59.0	4.47	0.656	0.0525	92.0	89.2
4	32.0	−69.3	3.76	0.305	0.0124	95.9	91.8
5	42.6	−68.2	4.05	0.352	0.0146	95.8	95.0
6	21.2	−60.5	4.35	0.176	0.0429	75.6	61.8
7	47.8	−66.4	5.00	0.342	0.0189	94.5	90.0
8	22.3	−66.2	4.98	0.276	0.0194	93.0	84.6
9	36.7	−69.2	4.34	0.322	0.0126	96.1	93.8
10	43.9	−67.3	5.35	0.335	0.0165	95.1	90.1

This very simple model does not take several important aspects into account, such as a changing etching rate over time or a sublimation rate towards the end of the reaction, when the static partial pressure of UF_6 falls below the vapor pressure. However, it allows for a qualitative understanding of the correlation of the etching rate on one hand and the temperature of the first cold trap on the other.

Whereas a high deposition in the first cold trap is desirable for uranium, this is not the case for molybdenum. Preferably, no Mo would be deposited in this trap at all. However, for all experiments, the presence of MoF_6 was also observed at temperatures not suggesting a deposition. The model used for uranium and based on the ratio of partial static pressure and the vapor pressure hereby completely fails to make any meaningful predictions. Instead, the recovery behavior does show some similarities to uranium. Low etching rates in combination with relatively high temperatures lead to relatively low depositions. Thus, a temperature of −66 °C at an etching rate of 22 mg/min lead to a Mo deposition of only 5 % for experiment 8, but at the same time was able to remove 85 % of U. It seems that comparably high temperatures in combination with low etching rates are able to minimize the deposition losses of MoF_6 in the first cold trap.

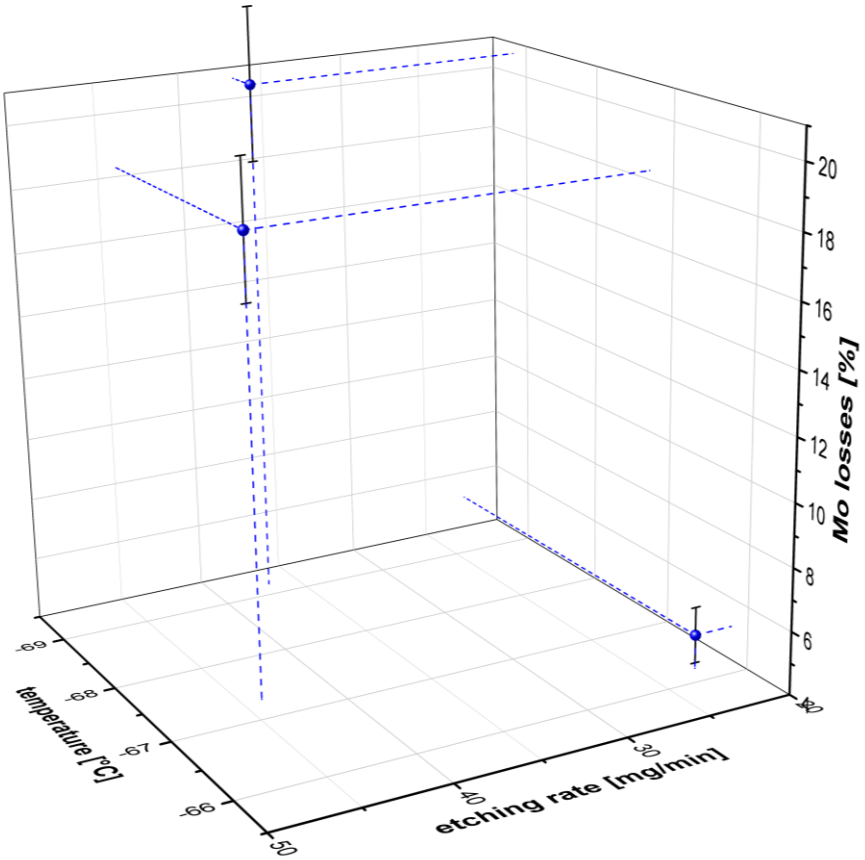

Figure 5.40: Losses of molybdenum in the first cold trap in dependency of etching rate and cold trap temperature for UMo01 targets.

The same calculations according to equation (36) as performed for uranium are listed in the following Table 5.19. The vapor pressure of MoF_6 has been extrapolated from equation (19).

Table 5.19: Calculated and observed recovery of molybdenum in the first cold trap of the separation experiments. Experiment 2 and 3 used UMo1, experiments 4 to 7 used UMo05 and experiments 8 to 10 UMo01 targets.

Exp. No.	etching rate [mg/min]	T_{CT1} [°C]	total static pressure [mbar]	static pressure MoF_6 [mbar]	vapor pressure [mbar]	calc. recovery [%]	obs. recovery [%]
2	80.7	−37.0	3.82	0.0072	14.6	0.0	0.0
3	95.8	−59.0	4.47	0.0066	1.67	0.0	22.8
4	32.0	−69.3	3.76	0.0015	0.52	0.0	13.7
5	42.6	−68.2	4.05	0.0018	0.59	0.0	24.8
6	21.2	−60.5	4.35	0.0009	1.42	0.0	7.4
7	47.8	−66.4	5.00	0.0017	0.73	0.0	13.5
8	22.3	−66.2	4.98	0.0003	0.74	0.0	5.1
9	36.7	−69.2	4.34	0.0003	0.52	0.0	20.6
10	43.9	−67.3	5.35	0.0003	0.65	0.0	18.3

A potential, yet unfortunately unattractive explanation would be the solution of MoF_6 in UF_6. As both compounds crystalize in the orthorhombic crystal system, it seems plausible, that MoF_6 would diffuse into UF_6. Figure 5.41 shows the phase diagram of the two hexafluorides. The diagram does not cover the entire temperature range down to −70 °C. However, it does show the existence of a solid phase s_2 at high mole fractions of UF_6, forming a UF_6-MoF_6 mixed crystal. If a diffusion of MoF_6 into UF_6 is indeed causing its deposition at relatively high temperatures, additional investigations are necessary to determine, whether the deposition behavior may be modified by an appropriate choice of the cooling profile.

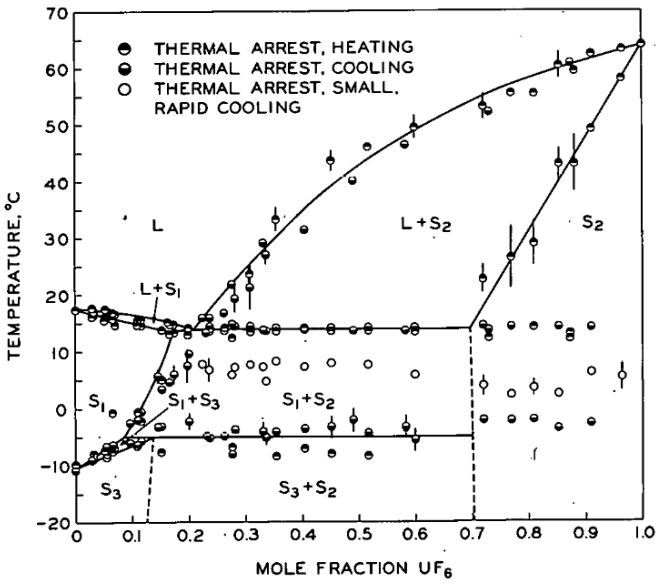

Figure 5.41: The phase diagram of the UF_6-MoF_6 system as reported by Trevorrow et al. [137] .

5.5 Separation by irradiation and usage of carbon monoxide

5.5.1 General aspects

As carbon monoxide was utilized in different aggregation states during the separation experiments, its phase diagram is depicted in Figure 5.42.

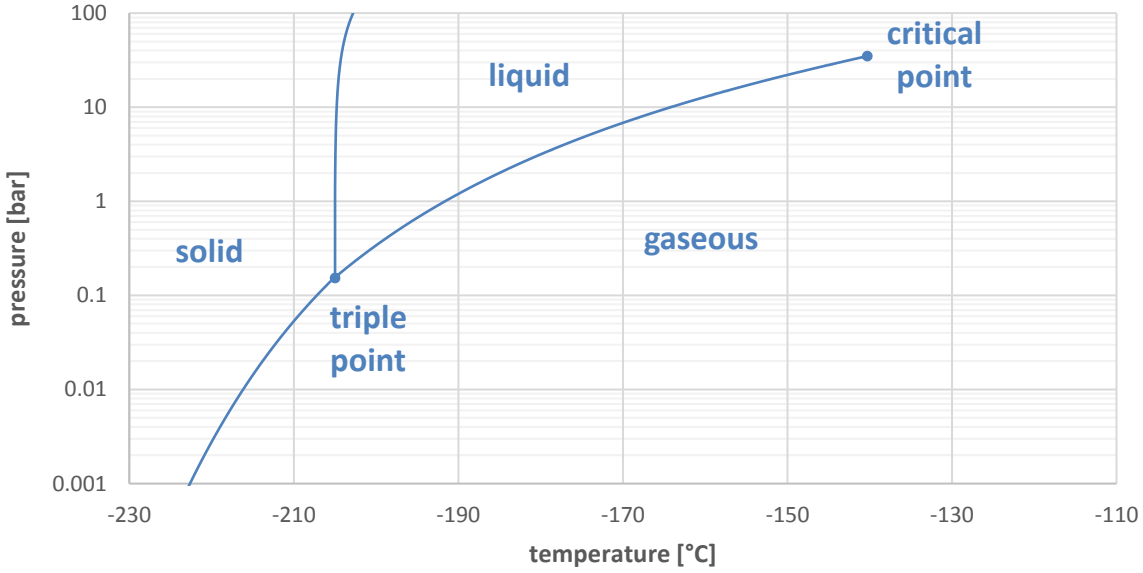

Figure 5.42: Phase diagram of carbon monoxide [138].

Gaseous carbon monoxide is known to react with UF_6 under UV irradiation under the formation of β-UF_5 and carbonyl fluoride COF_2 according to [139]:

$$2\ UF_6\ +\ CO\ \xrightarrow{h\cdot\nu}\ 2\ UF_5\ +\ COF_2 \qquad (39)$$

The same reaction is known to take place for MoF_6 and CO under UV irradiation:

$$2\ MoF_6\ +\ CO\ \xrightarrow{h\cdot\nu}\ 2\ MoF_5\ +\ COF_2 \qquad (40)$$

UV lamps with an emission spectrum containing wavelengths below 260 nm are suitable for the reduction of both hexafluorides. However, MoF_6 and UF_6 show a different absorption behavior in the UV-A as well as the visible range. The UV/VIS spectrum of UF_6 shows an additional absorption between 340 and 420 nm, with a maximum at 368 nm. MoF_6 on the other hand shows no absorption in this region at all. CO does not show relevant absorption in the range between 210 and 1100 nm as can be seen from the spectrum in Figure A.32. Borsella et al. [140] investigated the photodissociation of UF_6 in dependence of the excitation wavelength as well as the induction time in showing a minimum of the latter at a wavelength of 389 nm. Figure 5.43 shows their findings, depicting the reciprocal induction time of UF_5 as a function of irradiation wavelength.

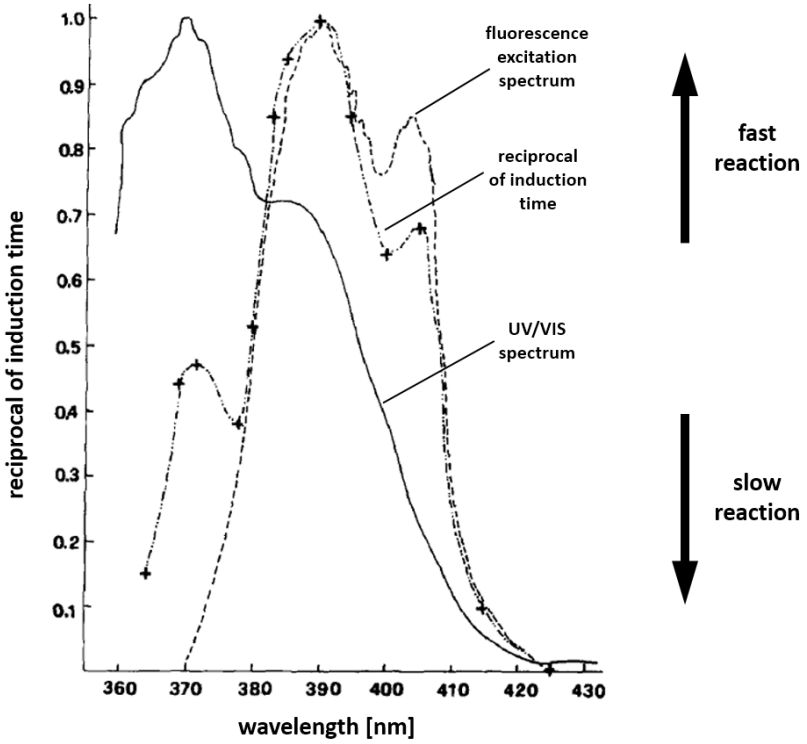

Figure 5.43: Reciprocal of induction time of UF_5 formation as a function of the wavelength (chain dotted line). The continuous line depicts the UV/VIS spectrum [140].

As the reciprocal induction time shows a maximum at 390 nm indicating an accelerated reaction at this wavelength, all irradiation experiments were performed using an LED with an emission maximum at 395 nm. At this wavelength, UF_6 also shows significant absorption in the UV/VIS spectrum in contrast to MoF_6 showing only minor absorption above 300 nm. Both spectra are depicted in Figure 5.44. This fact indicates reaction (39) being greatly accelerated compared to reaction (40).

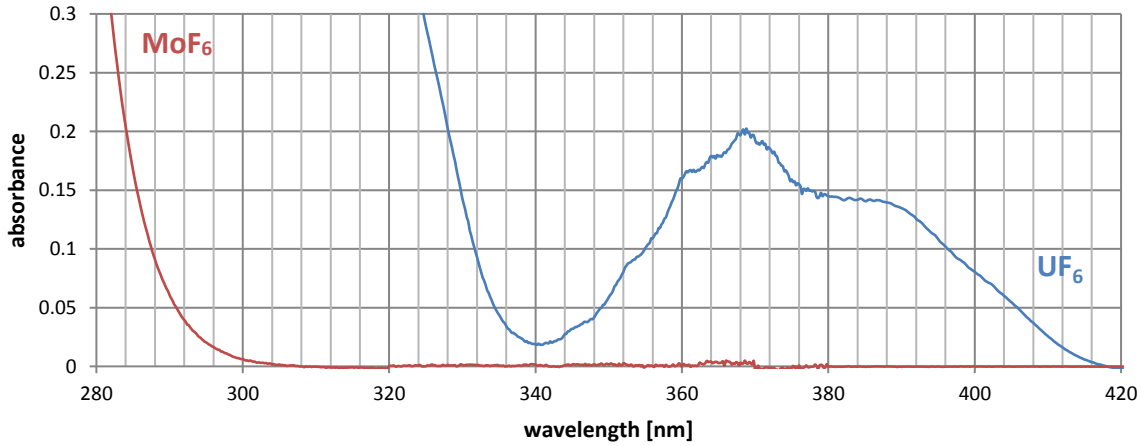

Figure 5.44: The UV/VIS spectrum of UF_6 at 80 mbar (blue graph) and MoF_6 at 592 mbar (red graph). MoF_6 does not show any absorption at all in the region around the irradiation wavelength of 395 nm.

As for the separation of UF_6 and MoF_6 from non-reacted CO, COF_2 and UF_5, the thermodynamic properties of the latter three are very favorable for a separation based on the difference in their vapor pressure. They are listed in the following Table 5.20.

Table 5.20: Comparison of the physico-chemical properties of COF_2, CO and β-UF_5 [34]. As can be seen, the former two are highly volatile, allowing for a feasible separation from UF_5 and MoF_6.

	COF_2	CO	UF_5 (β)
molar mass	66.0 g/mol	28.0 g/mol	333.0 g/mol
density	2.7 g/l	1.1 g/l	6.45 g/cm^3
melting point	−111.3 °C	−205.0 °C	348 °C
boiling point	−84.6 °C	−191.5 °C	disp.
appearance (SATP)	colorless gas	colorless gas	pale greenish or grey-blue solid

According to Wolf et al. [120], the vapor pressure of UF_5 has already dropped to 0.55 mbar at 282 °C and is therefore expected to be completely negligible in the temperature range used for the separation below −60 °C. The other two components on the other hand are much more volatile than both hexafluorides. The following Figure 5.55 shows the vapor pressures of the components that are most similar concerning their thermodynamic behavior. Thereby, data for COF_2 was actually recorded in the displayed range [141], whereas the data for MoF_6 was extrapolated as before in chapter 5.4. Although the numbers are therefore tainted with a certain degree of uncertainty, the general trend of both curves being separated by several orders of magnitude is still observable.

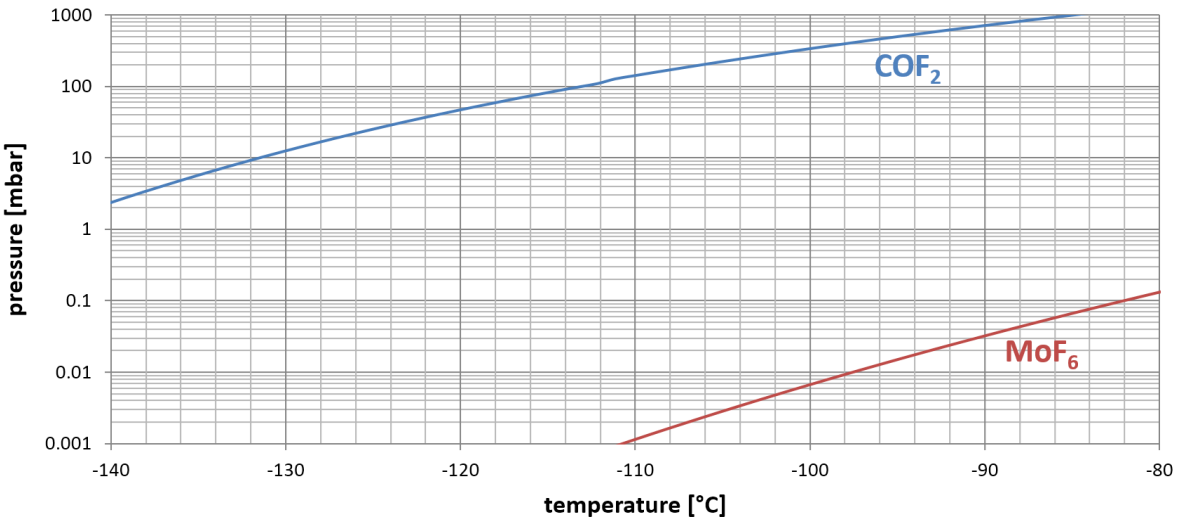

Figure 5.45: The vapor pressure curves of MoF_6 and COF_2. The data for MoF_6 has been calculated by extrapolation of equation (20), whereas the data for COF_2 has been calculated by the equation given by Pace and Reno.

A separation of MoF_6 and UF_6 under static conditions using gaseous CO was simultaneously investigated by Stene during the course of her thesis [142]. However, the total irradiation time in this setup was 48 hours and involved an exchange of reacted for fresh CO after 24 hours. This period for only one processing step is rather long compared to the half-life of ^{99}Mo of 66 hours. It was therefore investigated, whether the reaction time could be significantly decreased by using CO at a higher density. The included liquid and supercritical CO. However, the use of either one of the two comes at the cost of a significantly increased complexity of the processing system as the process involves either very low temperatures or high pressures.

5.5.2 Static separation using liquid CO

During these experiments, it was investigated whether the reaction could be accelerated by use of the reducing agent in the liquid phase. The wavelength of the UV-light source was identical to previous experiments as the spectral maximum still lay at 395 nm. As CO boils at −191.5 °C under normal pressure, the reaction had to take place under liquid nitrogen cooling.

Two experiments were performed in order to investigate this concept. For both experiments, a composition of UF_6 and MoF_6 was condensed into the measuring cell and characterized by IR spectroscopy. Afterwards, the measuring cell was connected to the line again, opened and its content carefully resublimed into the cold trap using LN_2, thereby ensuring the hexafluorides were frozen out at its lowest point. Subsequently, CO was condensed into the cold trap entirely covering the mixture of UF_6 and MoF_6, which then was irradiated with the UV-LED for 30 minutes, as is shown in Figure 5.46. During the entire time, there were no signs of the mixture dissolving in the liquid CO. After the irradiation period, the cold trap was evacuated again. As CO still has a vapor pressure of about 700 mbar at −200 °C, it could be pumped off from the cold trap without need for the removal of the LN_2, thereby ensuring that MoF_6 and UF_6 remain in the solid phase. After the CO being completely pumped off, the LN_2 was removed and the mixture of UF_6 and MoF_6 again condensed into the measuring cell in order to collect an IR spectrum for comparison with the initial composition. No residues were visible in the cold trap; especially there were no signs of deposited UF_5.

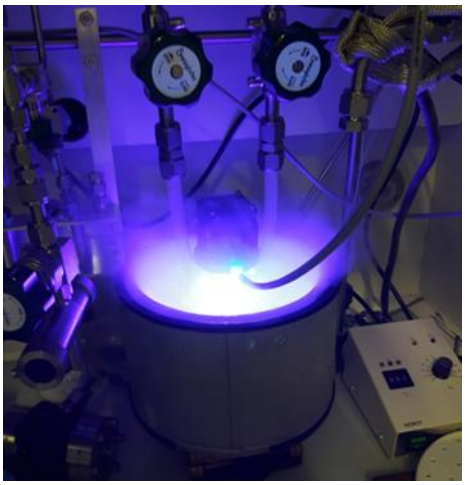

Figure 5.46: Investigation of the reaction of MoF_6 and UF_6 with liquid CO at a temperature of 75 K under irradiation at a wavelength of 395 nm.

In order to allow for quantitative analysis, baseline correction was performed for all IR spectra using the arithmetic mean of the transmittance between 2600 and 3200 cm^{-1}, as all spectra showed no absorption in this region. The resulting masses of both hexafluorides prior and after the separation attempt are listed in Table 5.21. The mass calculations were performed using reference spectra according to chapter 5.3. However, whereas the absorbance of the MoF_6 bands at 1388 and 1481 cm^{-1} gave consistent results for both, the spectra before and after the separation attempt, the bands of UF_6 at 1157 and 1290 cm^{-1} were consistent before but showed different absorbance for the spectra after separation attempts. This difference was significant and exceeded the confidence levels. It could furthermore be observed in both experiments. It may therefore be assumed a compound being formed

during the reaction that shows absorption in this region. Therefore, the absorption band at 675 cm^{-1} was used for uranium mass determination instead the one at 1157 cm^{-1}, giving consistent results.

Table 5.21: Calculated masses of the hexafluorides based on the transmittance measured using IR spectroscopy.

Exp. No.	initial mass UF_6 [mg]	final mass UF_6 [mg]	Ratio [%]	initial mass MoF_6 [mg]	final mass MoF_6 [mg]	ratio [%]
1	37.0 ± 0.1	31.1 ± 0.1	84.1 ± 0.9	18.9 ± 0.1	16.0 ± 0.1	84.7 ± 0.7
2	35.3 ± 0.1	32.9 ± 0.1	93.2 ± 1.1	17.7 ± 0.1	15.0 ± 0.1	84.7 ± 0.7

The IR spectrum collected after the first separation experiment shows a shoulder on the left side of the 1157 cm^{-1} band that originally was not present and therefore substantiates the decision of this band to be discarded for mass calculations. Additional bands also show the presence of COF_2.

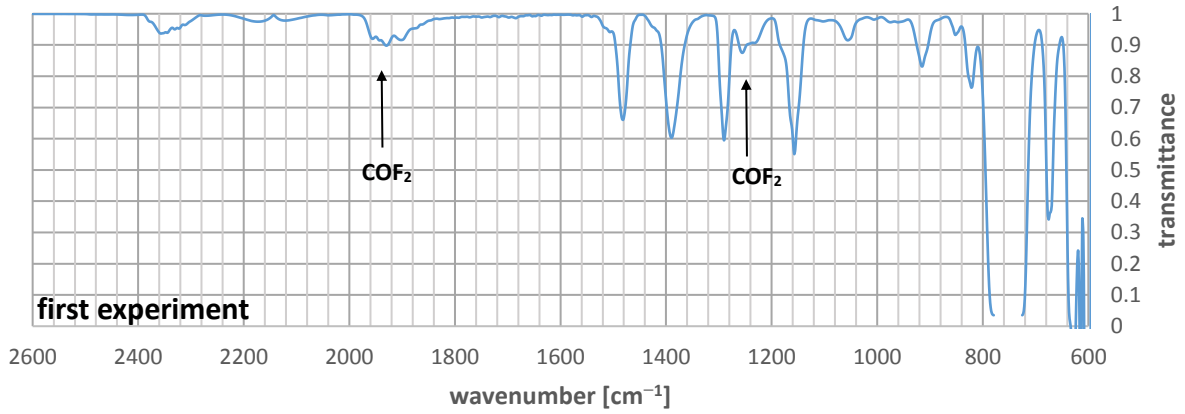

Figure 5.47: IR spectrum of the first experiment after UV irradiation. The spectrum shows the presence of COF_2.

However, these bands are not present in the IR spectrum of the second separation experiment.

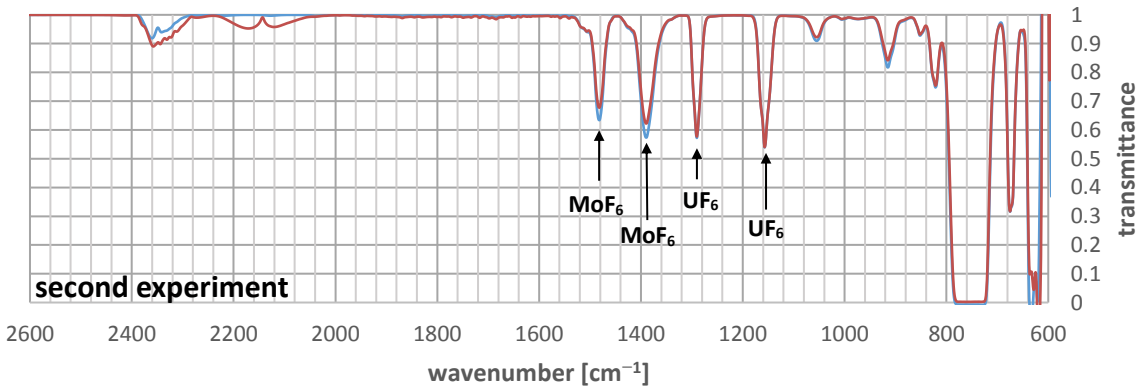

Figure 5.48: IR spectrum of the second experiment before UV irradiation (blue graph) and after irradiation (red graph). The bands belonging to MoF_6 show less gain in transmittance than the bands of UF_6, indicating a shift in the ratio of both compounds in disfavor of MoF_6.

The findings of these two experiments do not paint a consistent picture. The presence of COF_2 in the first experiment strongly suggests a reduction of UF_6. This is in accordance with the significantly lower amount of UF_6 found compared to the second experiment. The second experiment on the other hand shows no traces of COF_2, but does show the presence of CO. As CO is more volatile as COF_2, it seems unlikely that COF_2 was completely evaporated during the second trial. Instead, it was more likely not formed. In that case, there was no reduction of UF_6 in the beginning.

5.5.3 Static separation using supercritical CO

As a separation could not be achieved with CO in the liquid phase at low temperatures, supercritical CO was the next subject of investigation. The critical point of CO is characterized by a pressure of 34.98 bar, a temperature of 134.45 K and a density of 11.1 mol/L [143]. Thus, the high-pressure container described in chapter 4.3 was used to perform a total number of four experiments. The conditions of the individual trials are shown in Table 5.22.

Table 5.22: Basic conditions of the experiments performed investigating the separation using irradiation of the samples in supercritical CO. A total number of four experiments was performed. However, two experiments did not give any results as they experienced O-ring failure due to low temperature.

Exp. No.	mass UF_6 [mg]	mass MoF_6 [mg]	T_{wall} [°C]	T_{finger} [°C]	pressure [bar]	remarks
1	44.6 ± 0.1	18.0 ± 0.1	−16	−69	42 ± 1	IR, XRPD, µXFS
2	44.4 ± 0.1	16.2 ± 0.1	−69	−133	−	FFKM failure
3	39.0 ± 0.1	16.4 ± 0.1	−18	−88	−	FFKM failure
4	39.7 ± 0.1	16.4 ± 0.1	0	−33	56 ± 1	MP-AES

As performed in the experimental setup using liquid CO, a mixture of MoF_6 and $UF_6$was condensed into the measuring cell and prior to each experiment characterized by IR-spectroscopy. Thereby, the exact composition and the ratio of MoF_6/UF_6 before the experiment was known using the reference spectra described in section 5.3. After the spectroscopic analysis, the measuring cell was reconnected to the line and its content resublimed into the high-pressure container, which was cooled with liquid nitrogen at the cold finger to as low a temperature as possible. Thereby, a high temperature gradient between the walls and the cold finger ensures MoF_6 and UF_6 only to condense at the latter. The high-pressure container was subsequently sealed off via the bellow-sealed valve ①.

The limiting factor of this procedure was the temperature of the FFKM O-ring, as its lowest operating temperature is −15 °C. The second and third trial with wall temperatures of −69 °C and −18 °C, respectively, led to O-ring failure and a rapid decompression of the high-pressure container. However, no dangerous situation arose from this circumstance, as the entire setup was additionally confined in a special housing as a precautionary measure.

In a second step after transferring the hexafluoride mixture into the high-pressure container, dried CO was condensed into the storage container ② using liquid nitrogen. Valve ⑤ was closed, LN_2 removed and the pressure rise monitored with the pressure gauge ③. The evolving pressure has to exceed the critical pressure of CO considerably. After reaching equilibrium, valve ① was shortly opened to let the CO enter the high-pressure container and immediately closed again.

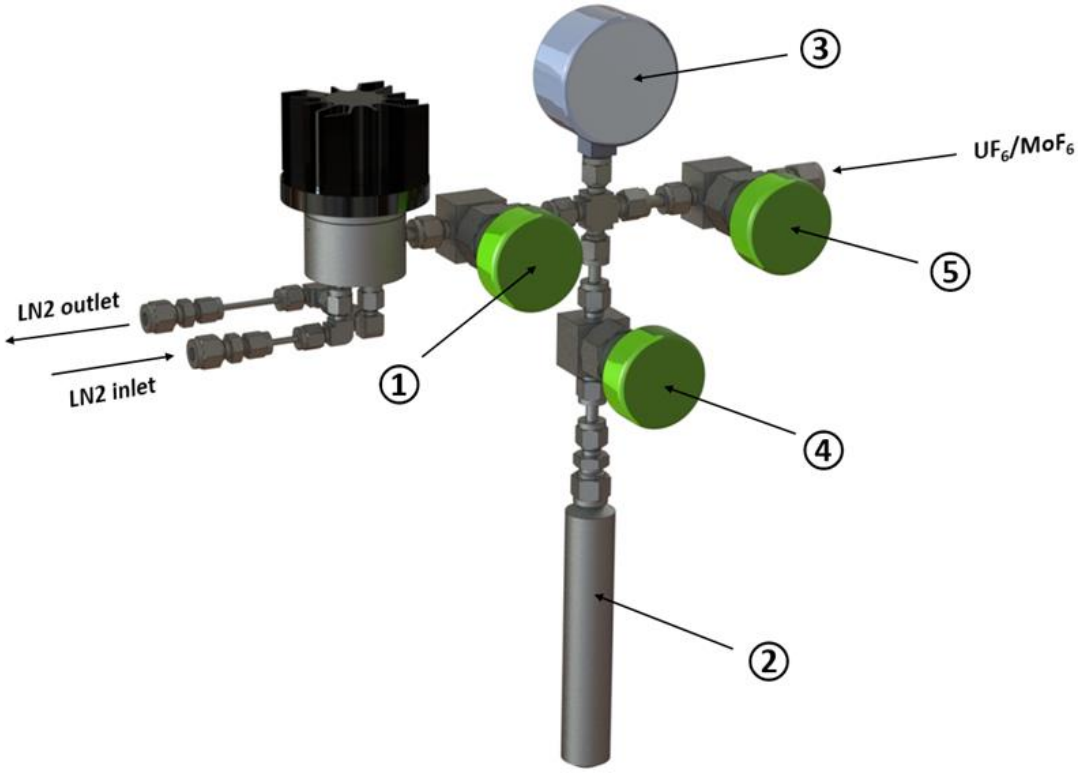

Figure 5.49: CAD model of the high-pressure section of the separation line, consisting of the high-pressure container that can be cooled with LN_2 and is described in chapter 4.3, a storage container for the condensation of CO (2) and a pressure gauge with a measuring range of 100 bar. Each part of the section may be separated from all other components by one of the three bellows-sealed valves (1), (4) and (5).

The high-pressure container was heated to 20 °C and its content was irradiated for 60 minutes with light of 395 nm wavelength. During this process, its temperature rose to about 33 °C due to the heat input of the radiation. The irradiation process itself was hallmarked by the evolution of thin filaments from the cold finger that rose towards the sapphire window. During the course of the irradiation, their increasing number led to the formation of a fluffy cloud finally covering the entire window. This cloud was of a light blueish-white color and was most probably finally blocking the major part of the incident radiation, thereby reducing the efficiency of the irradiation at this point. The changing appearance of the content of the pressure chamber during irradiation is shown in Figure 5.50.

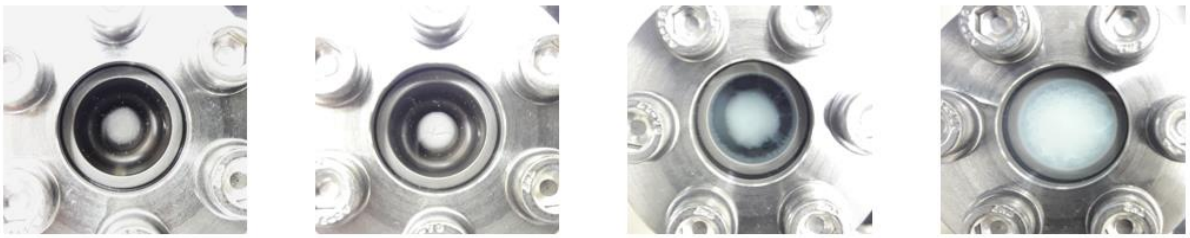

Figure 5.50: View from above into the high-pressure container during the UV irradiation. From left to right: (1) white UF_6/MoF_6 mixture sublimed at the cold finger in the center of the chamber; (2) after venting the container with supercritical CO; (3) after irradiation for 7 minutes and (4) after irradiation for 60 minutes.

The treatment of the reaction products after the termination of the irradiation differed between the first and the fourth experiment. For the first trial, the cold finger was cooled down to −69 °C in order to freeze out remaining MoF_6. The wall temperature reached −16 °C, however without O-ring failure. All constituents volatile at that temperature were extracted and analyzed using IR spectroscopy. The results are shown in Figure 5.51. The spectrum shows the presence of different constituents. As expected, these include unreacted CO and as well as COF_2. Rather surprisingly, the spectrum also shows the presence of oxalyl fluoride $(COF)_2$. This compound is most probably produced due to the photolytic decomposition of COF_2 and subsequent recombination according to

$$COF_2 \xrightarrow{h\cdot\nu} COF\cdot + \cdot F \qquad (41)$$

$$2\ COF\cdot + 2\ \cdot F \rightarrow (COF)_2 + F_2 \qquad (42)$$

The entire spectrum of the extract is shown in Figure 5.51 from 600 to 4000 cm^{-1} and its comparison with literature data of $(COF)_2$ may be found in Figure A.33.

Additionally, a considerable amount of MoF_6 was found. Based on the absorbance at 1388 cm^{-1} and 1481 cm^{-1}, this amount corresponds to about 2.0 mg MoF_6 or about 11 % of the originally deployed amount. Apparently, a lower temperature has to be chosen in order to minimize the losses of MoF_6 during this phase of the process. Alternatively, the procedure described for the forth experiment may be adopted.

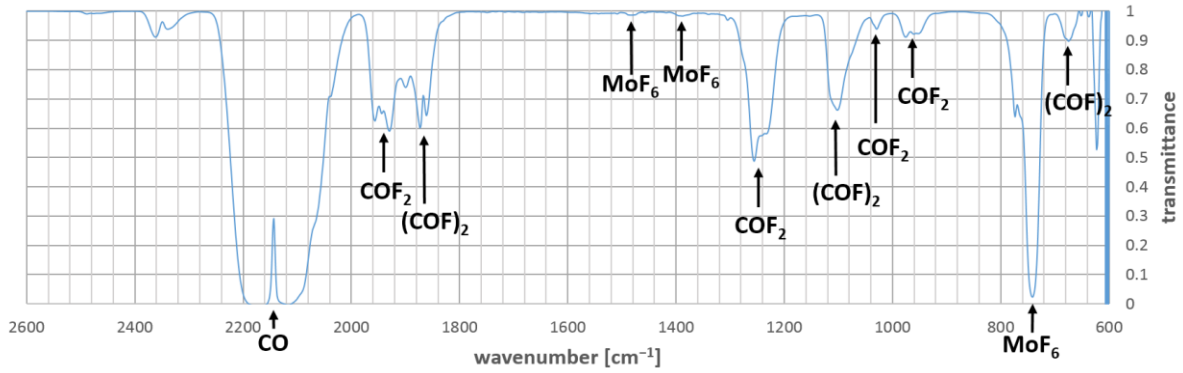

Figure 5.51: IR spectrum of the contents condensed into the storage container after end of irradiation of the UF_6/MoF_6 mixture. As expected, CO and COF_2 may be identified. Additionally, also oxalyl fluoride $(COF)_2$ and MoF_6 are present.

The next step of the separation process was initialized by a shut-off of the cooling system and heating of the high-pressure chamber to 61 °C, thereby expelling all volatile components. Subsequent resublimation in the measuring cell using LN_2 allowed for the measurement of these components, whose spectrum is depicted in the red graph of Figure 5.52. Quantitative analysis of this spectrum is only possible for MoF_6 and reveals a rate of recovery of about 22.0 %. Quantitative statements concerning the presence of UF_6 are not possible as its bands overlap with the ones of $(COF)_2$. The blue graph depicts the hexafluoride mixture prior to the irradiation. In summary, the spectrum showed IR spectroscopy not being the most practicable analytical method for quantitative analysis of the content of UF_6 and MoF_6 due to the high number of additional bands of other reaction products, which partly overlap with the positions of the bands of the two hexafluorides.

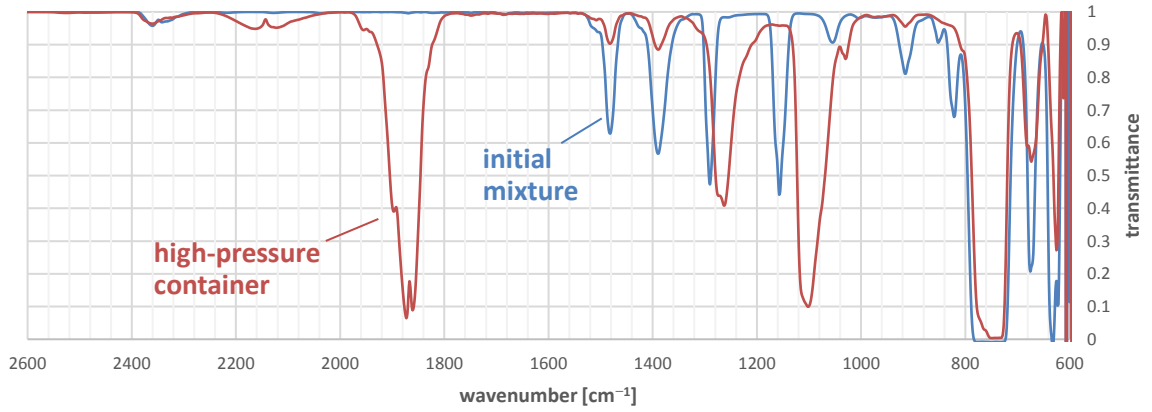

Figure 5.52: IR spectrum of the UF_6/MoF_6 mixture before separation (blue graph) and content of the high-pressure container after heating to 45 °C and sublimation into the measuring cell (red graph).

The fluffy residues in the high-pressure container were recovered under argon atmosphere, filled into a glass capillary and analyzed using XRPD. The corresponding powder diffractogram is shown in the following Figure 5.53. All reflections may be assigned to β-UF_5, underlining the absence of a major amount of crystalline impurities. This finding is in accordance with additional spectroscopic measurements using µXFS and MP-AES.

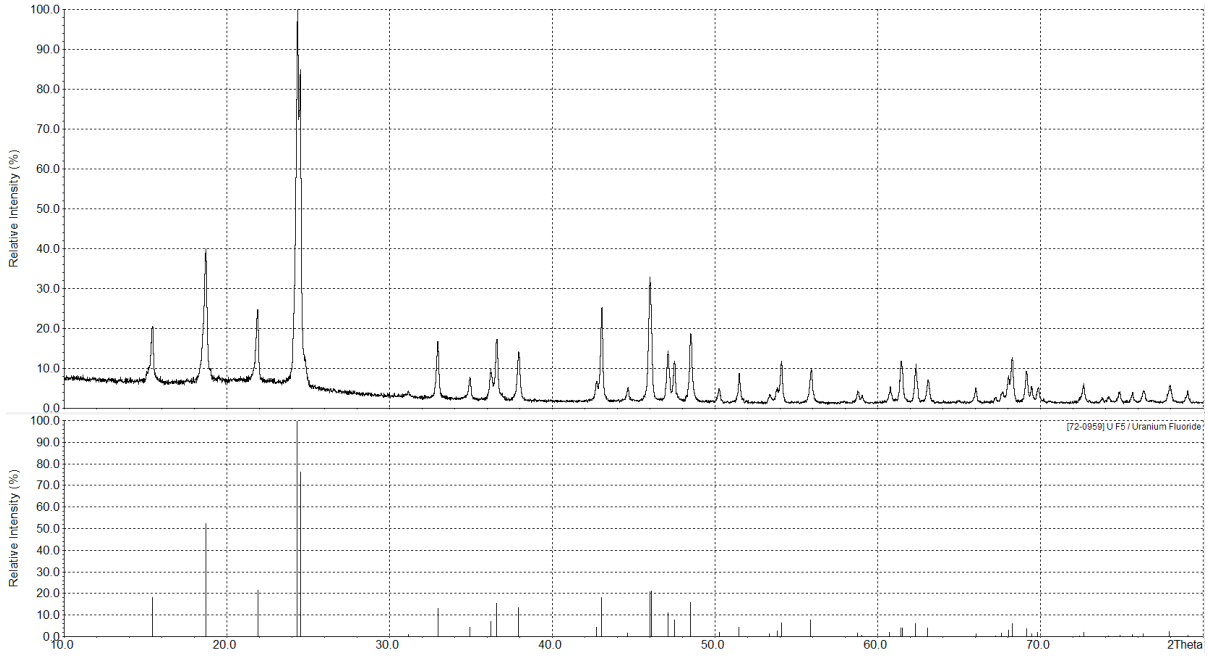

Figure 5.53: Powder diffractogram of the powdery residues of after UV radiation. Reflexes are in good agreement with β-UF_5. Reference data taken from ICDD-File [72-0959] rated with quality mark C.

µXFS was performed on a second sample in addition to XRPD. The corresponding spectrum is shown in Figure 5.54 and shows the presence of uranium and molybdenum. The additional peaks originate from the X-ray tube, which uses a rhodium anode. A quantitative analysis shows the mass-based uranium content to amount to 98.5 % and the molybdenum content to 1.5 %. However, these numbers should be treated somehow carefully, as the signals of molybdenum and uranium partly overlap. Thus, the main signals for Mo mass determination may only be seen as a shoulder of the U signal. However, the result is in good agreement with the data from the fourth experiment (see Table 5.23).

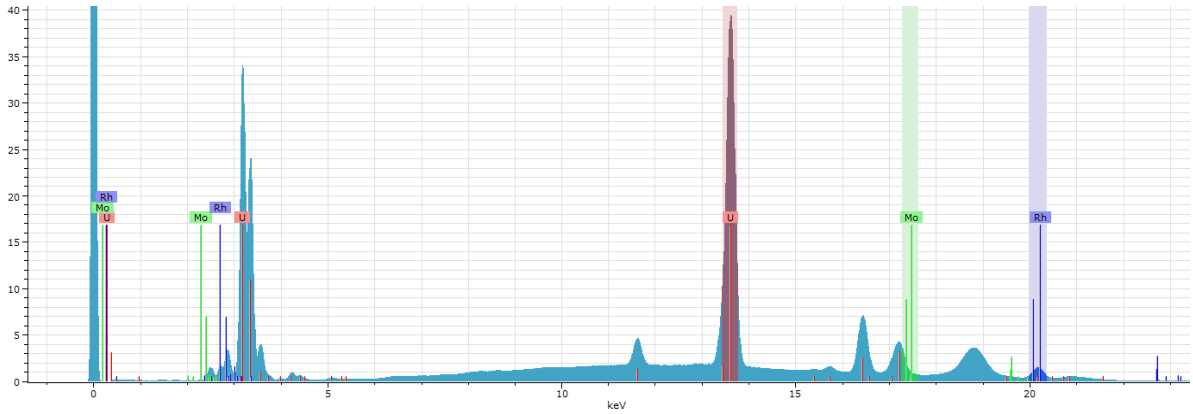

Figure 5.54: µXFS spectrum of the powdery residues after UV radiation, however not performed on the same sample that has been used to perform XRPD.

For the forth experiment, the cold finger was not cooled down again, but the storage container instead by the use of LN_2. By slowly opening valve ①, the volatile components were released and collected in the storage container. After a sufficient period for resublimation, valve ① was closed again and valve ⑤ opened instead allowing all highly volatile components, in particular CO and COF_2, to be pumped off. Afterwards, the container was disconnected from the line, vented and filled with water, dissolving MoF_6 and unreacted UF_6. The emerging solution was analyzed using MP-AES. The content of the high-pressure container could be analyzed after dissolving it with diluted HNO_3. The amount of uranium and molybdenum prior to the reaction as well as the amounts found in the storage container and the high-pressure container are listed in Table 5.23.

Table 5.23: Results of the fourth separation experiment using supercritical CO. Analytical method prior to separation was gas phase IR spectroscopy, after separation MP-AES.

	mixture before	storage container (Mo side)	high-pressure container (U side)
U [mg]	26.8 ± 0.3	2.99 ± 0.60	20.96 ± 0.63
Mo [mg]	7.5 ± 0.3	7.35 ± 0.06	0.08 ± 0.06
wt% Mo	21.9 ± 0.7	71.2 ± 1.7	0.4 ± 0.3

The uranium mass in the storage container amounts to 11.1 % and the molybdenum mass in the high-pressure container to 0.9 % of the original mass, respectively. On the molybdenum side, this implies 98.0 % of the molybdenum being recovered and at the same time 88.9 % of the uranium being removed. On the uranium side, 78.2 % of the uranium was recovered and at the same time 98.9 % of the molybdenum removed. The losses in uranium may be explained as not all UF_5 could be recovered from the high-pressure container.

5.6 Recovery of uranium from uranium silicide U_3Si_2

5.6.1 General aspects

Two fluorination experiments were performed in order to investigate the general suitability of the fluorination line for a potential separation of uranium and silicon, especially under the impression of the difficulties faced by the process developed at ANL.

The fluorination of uranium silicide is expected to lead to the formation of uranium hexafluoride UF_6 and silicon tetrafluoride SiF_4 according to:

$$26\ NF_3\ +\ 3\ U_3Si_2\ \rightarrow\ 13\ N_2\ +\ 9\ UF_6\ +\ 6\ SiF_4 \qquad (43)$$

The vapor pressure for SiF_4 was investigated by Pace and Mosser [144] and may be calculated by:

$$p = 1.33 \cdot 10^{\left(-5.5025\ -\ \frac{894.93}{T\ [K]}\ +\ 5.9593 \cdot \log_{10} T\right)}\ mbar \qquad (44)$$

A comparison of the vapor pressure of UF_6 and SiF_4 at a given temperature is depicted in Figure 5.55. Here, as in chapter 5.4, the extrapolation for the vapor pressure of UF_6 was conducted according to Llewellyn. The high difference of several orders of magnitudes allows highly efficient pre-separation based on vapor pressure.

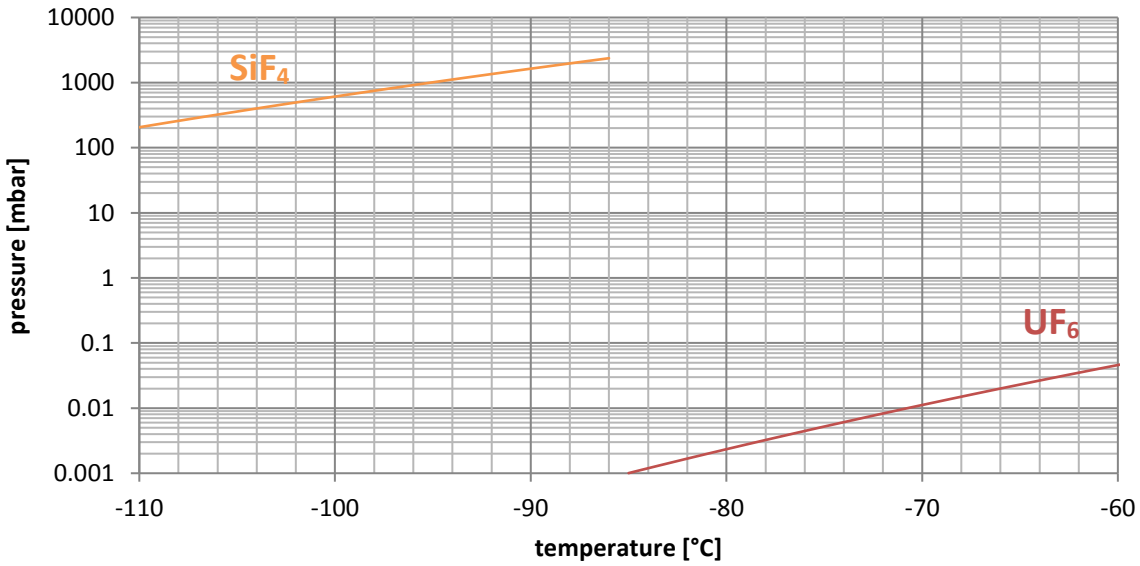

Figure 5.55: The vapor pressures of SiF_4 (orange graph) and UF_6 (red graph).

5.6.2 Reaction conditions

For both experiments, U_3Si_2 was presented in form of a slug (see Figure 5.57) and the cold traps were held at different temperatures. The slug was produced via plasma arc melting using a stoichiometric amount of uranium and silicon. After melting, the slug was shattered and one of the fragments was grounded in order to perform XRPD on the resulting powder. Thereby it was ensured that actually U_3Si_2 was formed during the melting process (also see the powder diffractogram in Figure A.34).

Table 5.24: Basic conditions of the etching experiments with U_3Si_2 as a substrate material. A total number of two experiments was performed, both giving similar results.

Exp. No.	sample mass [mg]	Ar [sccm]	NF_3 [sccm]	time [min]	residual mass [mg]	reaction yield [%]	etching rate [mg/min]
1	671.13	30	30	23	0.05	99.99	29.2
2	692.18	various	various	–	0.00	100.00	–

Uranium silicide shows an even fiercer reaction with NF_3 than elemental uranium. However, the general behavior during the reaction is similar. At high fluxes of NF_3 : Ar of 35.0 sccm : 35.0 sccm, the slug starts glowing within minutes after ignition of the plasma and also shows intense sparking. The glowing lasts for the entire reaction until the target material was completely consumed. Major amounts of residues are not present and the carrier showed no change in mass within the accuracy of the scale of 0.5 mg. At lower flows of NF_3 : Ar of 15.0 sccm : 15.0 sccm, the slug also starts glowing and sparking, although not as intense.

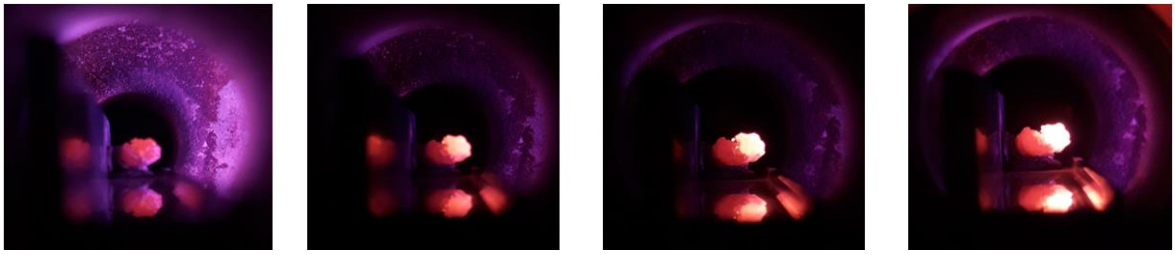

Figure 5.56: Slug of U_3Si_2 at different volume flows of NF_3. Argon was constantly kept at 15.0 sccm, whereas the volume flow of NF_3 was set from left to right to 20.0, 30.0, 40.0 and 50.0 sccm. The brightness significantly increases with increased flow of the etching agent, indicating an increased temperature and thus an increased reaction rate.

In addition, the formation of a dark solid in the shaded regions occurs, most likely UF_4 as observed in the fluorination experiments of elemental uranium. However, this solid could completely be converted into volatile products by changing to a flow of 30.0 sccm of pure NF_3 during the further process. Therefore, also in this case no residues were visible and again, no change of mass within the accuracy of the scale.

Figure 5.57: Uranium silicide slug before fluorination.

Figure 5.58: Residues of the uranium silicide slug after fluorination for 23 minutes.

In order to investigate the suitability of a separation based on a difference in vapor pressure, the first cold trap was held at a temperature of −90 °C using an isopropanol/ LN_2 slush whereas the second and third cold trap were cooled to about −200 °C using liquid nitrogen. The IR spectrum of the first cold trap is in good accordance with UF_6 but shows two additional signals, one at 920 and one at 1028 cm^{-1}. The former rather weak one may not explicitly be assigned, whereas the latter is very strong and can clearly be matched with the ν_3 fundamental vibration of SiF_4 [145]. The pressure of UF_6 calculated by the absorbance at 1157 and 1290 cm^{-1} evaluated to 81.9 mbar. However, as SiF_4 also shows absorption in that region, the UF_6 band at 675 cm^{-1} is also used for pressure determination and evaluates to 80.5 mbar. In the most unfavorable case, the pressure attributed to SiF_4 does not exceed 7 mbar, as the pressure in the measuring cell evaluated to 87.4 mbar. This corresponds to only about 0.5 % of the entire amount of SiF_4 produced during the reaction. The portion of recovered uranium in the first cold trap was determined for the second experiment using MP-AES and amounts to 611.6 mg.

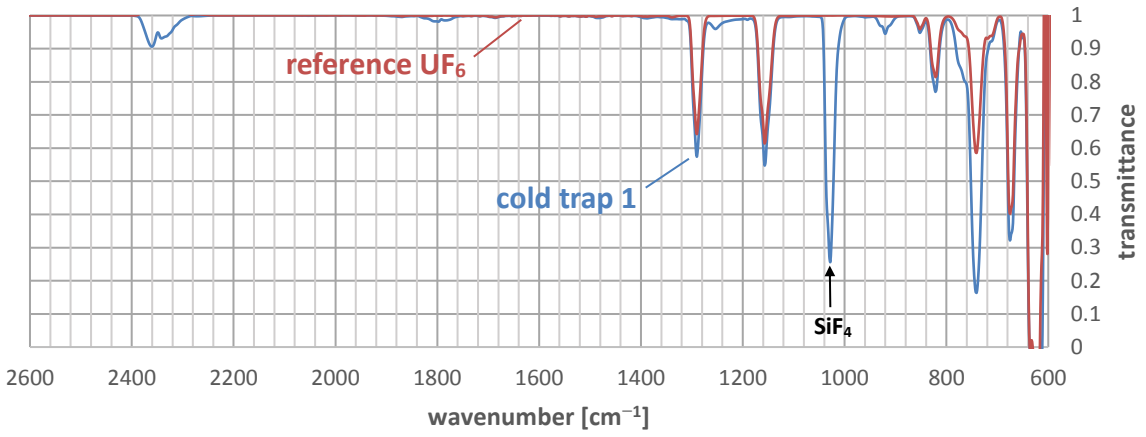

Figure 5.59: The IR spectrum of the first cold trap held at 180 K (blue graph) and the reference spectra of UF_6 (red graph). The pressure in the measuring cell was 87.4 mbar, the reference spectrum was taken at 66 mbar.

The portion of uranium in the second cold trap was also determined for the second experiment using MP-AES and amounts to 11.5 mg. As other components such as HF are also present in the measuring cell, a quantitative mass determination of SiF_4 based on pressure was not possible.

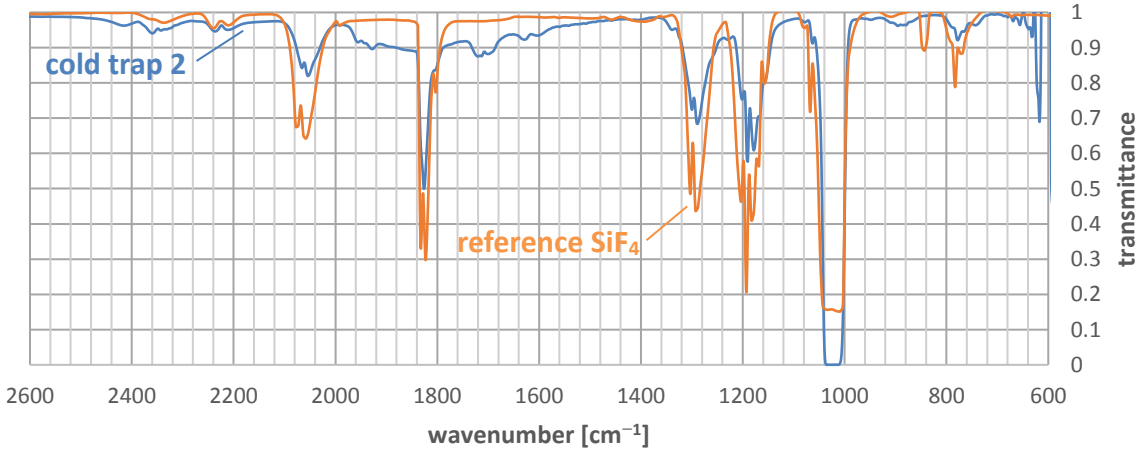

Figure 5.60: The IR spectrum of the second cold trap held at 80 K (blue graph) and the reference spectra of SiF_4 (orange graph). The pressure in the measuring cell was 134.6 mbar, the reference spectrum was taken from NIST Chemistry WebBook [146].

6 Synthesis of high-valent fluorides of transition metals and main group elements

To date, 16 molecular hexafluorides have been synthesized and are to a large extent well characterized [113]. These include nine transition metal hexafluorides (Mo, Tc, Ru, Rh, W, Re, Os, Ir, Pt), four main group element hexafluorides (S, Se, Te, Xe) and three actinoid hexafluorides (U, Np, Pu).

Due to the promising results of the first fluorination experiments with molybdenum and uranium, the idea was born to study its potential on the fluorination of other transition metals, of which the existence of high-valent fluorides is known. Thereby, the platinum metals are of special interest. Many of the synthesis routes of their penta-, hexa- and heptafluorides include the use of elemental fluorine, autoclave technology as well as elevated temperatures with the corresponding challenges concerning safety, laboratory equipment and experimental expertise of the personal engaged. The MPFL would provide an elegant way to obtain these compounds.

The following chapter summarizes the experimental data collected for the fluorination of additional elements. They are thereby ordered according to their position in the periodic table. First, the fluorination experiments performed with the 4d transition metals ruthenium, rhodium and palladium are described. These are followed by the 5d transition metals rhenium, osmium, iridium and platinum and concluded with the main group element tellurium. For each element, a short introduction is given, followed by a description of its binary fluorides and how they are synthesized according to literature. Afterwards, the reaction conditions are provided and what fluoride could thereby be obtained. These include the ratio of argon and NF_3 as well as the temperature to which the reaction chamber was heated. In addition, the etching rate and the utilization of NF_3 are provided, if possible. The latter is calculated by assuming a complete reaction according to

$$M + 2\ NF_3 \rightarrow MF_6 + N_2 \qquad (45)$$

In addition, spectral data is provided wherever possible. This includes IR, UV/VIS, Raman and NMR spectroscopy. However, as the focus of this part of the work lay on the general suitability of the process for obtaining these compounds, the evaluation of the spectral data has not been performed in greatest detail.

6.1 Ruthenium

6.1.1 General aspects of ruthenium and its fluorides

Ruthenium is a silver-white, hard and brittle platinum metal. A considerable amount of ruthenium in the same order of magnitude as molybdenum is formed during the fission process. The fluorination and deposition behavior of this element therefore is of high relevance for the separation process. The metal is insoluble in all mineral acids including aqua regia below 100 °C [105]. Ruthenium has the electron configuration [Kr] $4d^7 5s^1$ and may therefore be present in oxidation state +VIII in certain compounds such as RuO_4. However, its preferred oxidation states are +III and +IV . Ruthenium forms four different thermodynamically stable binary fluorides, which are listed in Table 6.1 [147].

Table 6.1: Physico-chemical properties of the thermodynamically stable binary fluorides of ruthenium [34,43,105,148]. If no data could be found in literature, this is indicated by n.d. (= no data).

	RuF_3	RuF_4	RuF_5	RuF_6
molar mass	158.1 g/mol	177.1 g/mol	196.1 g/mol	215.1 g/mol
melting point	650 °C (dec.)	n.d.	86.5 °C	54 °C
boiling point	–	n.d.	227 °C	200 °C (dec.)
appearance (SATP)	brown solid	yellow or pink solid	green solid	dark or red brown solid

RuF_3 is a brown solid and can be produced by reduction of RuF_5 using iodine [149]. It is insoluble in water, but soluble in acidic solutions [34].

RuF_4 is also a solid. Its optical appearance has been described as either yellow [34] or deep pink [149,150]. It is described to react with water [34]. Its synthesis has been described by Casteel and Bartlett in [150], starting with the dissolution of K_2RuF_6 in anhydrous HF and subsequently reacting it with AsF_5.

RuF_5 is being described as a green solid by Holloway et al., which melts to a viscous liquid. The dissolution of RuF_5 in water results in the formation of a brown solution, of which hydrated ruthenium dioxide precipitates. Its synthesis from the elements has been described using pure fluorine at a temperature between 280 °C and 900 °C [148] or 20/80 % fluorine/helium mixture at 300 – 450 °C [151].

RuF_6 is described as a dark brown [149] or red-brown [150] solid and extremely sensitive to moisture [149]. It is synthesized by inductively heating metallic ruthenium in a fluorine atmosphere at 400 mbar in quartz container cooled with liquid nitrogen [152].

6.1.2 Reaction conditions and results

One experiment was performed investigating the fluorination behavior of ruthenium. The applied ruthenium was introduced as a powder with a mesh size of 20 micron and produced by Alfa Products - Thiokol/Ventron division. The experimental conditions are summarized in Table 6.2.

Table 6.2: Basic conditions of the etching experiment on ruthenium as a substrate material. The volume flow of NF_3 was kept constant the entire time, the argon flow was however varied, in order to identify an effect on the deposition rate in the cold traps.

Exp. No.	sample mass [mg]	Ar [sccm]	NF_3 [sccm]	time [min]	residual mass [mg]	reaction yield [%]	etching rate [mg/min]
1	306.42	8 − 16	2	100	36.7	88.0	2.7

At ambient temperature, neither an observable reaction of the substrate nor a deposition in the cold traps was observed. The argon flow was varied between 8 and 16 sccm in order to identify a potential effect on the etching rate. At the same time, the volume flow of NF_3 was kept constant. Visual inspection of the cold traps did not show any deposition. However, an increase of the temperature of the reaction chamber to 190 °C after one hour of unsuccessful fluorination attempts induced sparking of the powder, which was soon followed by a deposition of a solid of emerald green color in the first cold trap. The reaction time and etching rate in Table 6.2 refer to the time the reaction chamber was held at the elevated temperature.

Figure 6.1: Ruthenium powder on the Monel carrier before fluorination.

Figure 6.2: Residues of ruthenium after fluorination for 100 minutes at an elevated temperature of 190 °C.

Figure 6.3: Residues of ruthenium after being exposed to the lab atmosphere for 15 minutes.

The removal of the residues left on the Monel carrier from the chamber is accompanied by a strong smell of hydrogen fluoride. They are very sensitive to moisture and rapidly hydrolyze on air, as seen in Figure 6.2 and Figure 6.3. Therefore, a repeated weighing of the residues was not possible, as they rapidly changed their mass. Furthermore, they are completely soluble in water and form a light-brown solution that changes its color to black over a period of days as seen in in Figure 6.4 and Figure 6.5.

Figure 6.4: Solution of the residues on the Monel carrier dissolved in aqua dest.

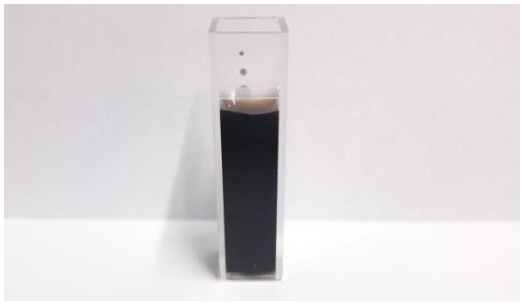

Figure 6.5: The same solution after a period of 150 hours.

The exact nature of this compound remains unknown, as the color does not match any of the known binary fluorides, except maybe for RuF_4. RuF_3 may be discarded, as it is insoluble in water.

The reaction product depositing in the first cold trap almost has an oily appearance and does not show the powdery or crystal form that has been observed for deposition of the hexafluorides. It is of emerald green color as seen in Figure 6.6, but is reluctant to sublimation into another FEP tube. However, it melts into a viscous liquid when heated with a heat gun set to 100 °C, suggesting its melting point to lie in the region of 80 °C − 100 °C. This is in good agreement with the reported melting point of RuF_5 of 86.5 °C.

Figure 6.6: Reaction product of the fluorination of ruthenium in the first cold trap, which was cooled using LN_2. The deposition is of emerald green color, suggesting it to be RuF_5.

Addition of water to the component after extraction from the cold trap leads to the immediate formation of a black precipitate in a yellowish-brown solution in accordance with the description of Holloway [148]. All experimental observations are therefore in good agreement with what has been reported in literature for RuF_5.

However, the same does not hold for the spectral data. ATR-IR spectroscopy provides the spectrum shown in Figure 6.7 (blue graph). The reference data from literature was recorded on RuF_5 synthesized by the decomposition of $KrF^+RuF_6^-$ in anhydrous HF. In order to at least qualitatively resemble the measured spectrum, the reference spectrum was shifted by 30 cm^{-1}. No additional information about the conditions of the recording is given. A discussion about the origin of the discrepancy between the two spectra would therefore be highly speculative.

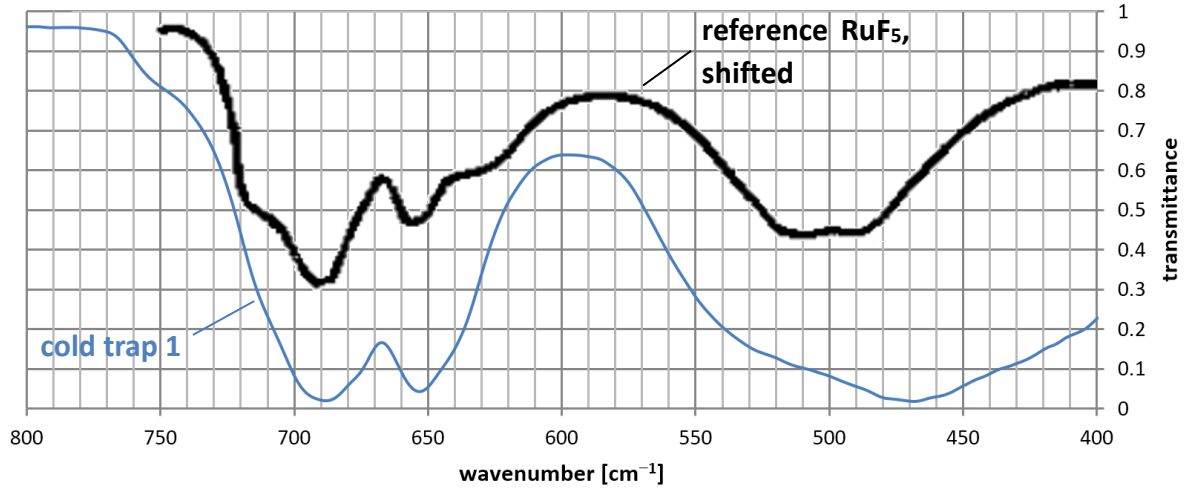

Figure 6.7: IR spectrum of the reaction product of the fluorination of ruthenium powder taken from the first cold trap (blue graph). The sample was measured in the solid phase under argon atmosphere using the ATR method. A comparison of the spectrum with data from literature [153] (black graph) only shows a qualitative similarity and only, if the reference spectrum is shifted by 30 cm^{-1}.

In summary, the recovery of RuF_6 was unsuccessful. However, there are indications of its initial synthesis during the fluorination process. According to [123], RuF_6 tends to react with nickel. In accordance, a slight reduction in the mass of the Monel carrier after the removal of the residues and subsequent cleaning with water could indeed be observed. It therefore seems possible, that RuF_6 was initially formed, but due to its highly instable nature was reduced to RuF_5 shortly afterwards.

6.2 Rhodium

6.2.1 General aspects of rhodium and its fluorides

Rhodium is a silvery-white and ductile platinum metal. It is characterized by its chemical inertness and in compact form is resistant to acids. As a fine powder, rhodium is dissolved by concentrated sulfuric acid and aqua regia [105]. Rhodium has the electron configuration [Kr] $4d^8$ $5s^1$ and thus prefers the oxidation states +I and +III. Higher oxidation states are also found, but have a tendency to be decreasingly stable with increasing state [149]. Rhodium forms four different thermodynamically stable binary fluorides, which are listed in Table 6.3 [147].

Table 6.3: Physico-chemical properties of the thermodynamically stable binary fluorides of rhodium [34,149,154,155]. If no data could be found in literature, this is indicated by n.d. (= no data).

	RhF_3	RhF_4	RhF_5	RhF_6
molar mass	159.9 g/mol	178.9 g/mol	197.9 g/mol	216.9 g/mol
melting point	n.d.	290 °C (disp.)	95.5 °C	70 °C
boiling point	n.d.	–	n.d.	73.6 °C
appearance (SATP)	red solid	purple or sandy-brown solid	ruby red solid	black solid

RhF_3 is a red solid and may be synthesized by the fluorination of $RhCl_3$ with elemental fluorine at 500 °C [149]. It is insoluble in water [155].

RhF_4 has been described by Sharpe as a purple-red solid using a synthesis dissolving rhodium hydroxide in hydrobromic acid and subsequent treatment with BrF_3. If exposed to water, it gives a blue-green solution, of which an olive green substance precipitates, supposedly the hydrated dioxide [156]. However, Rao and Bartlett doubt that compound to be RhF_4. They describe it as a sandy-brown solid that rapidly hydrolyses in moist air. It was obtained by a several day fluorination of RhF_3 at 250 °C [154].

RhF_5 is a dark red solid and may either be synthesized from the elements at 400 °C and 6 bar or by reacting RhF_3 with fluorine at 400 °C [149]. An alternative reaction route involves the decomposition of RhF_6 at room temperature to RhF_5 and elemental fluorine [157].

Chernick et al. describe RhF_6 to be of black color in the solid state and of deep red-brown color, when in the gas phase. Their reaction route is similar to the one of RuF_6 [158]. However, the synthesis has also be recorded for the need of more extreme conditions by reacting rhodium with elemental fluorine at 250 °C and 30 bar [149]. RhF_6 is able to react even with carefully dried glass [105]. It decomposes at room temperature into RhF_5 and elemental fluorine, but seems to be stable at 0 °C [158].

6.2.2 Reaction conditions

Two experiments were performed investigating the fluorination behavior of rhodium. For the first trial, rhodium powder was pressed into three small briquettes with a diameter of 2.5 mm each, in order to eliminate the possibility of powder losses during the evacuation process. For the second experiment, the rhodium was not compressed but exposed as a plain powder. The rhodium powder was produced by Heraeus and had a metal-based purity of more than 99.90 %.

Table 6.4: Basic conditions of the etching experiments on rhodium as a substrate material. The volume flow of NF_3 was kept constant for both experiments; the argon flow was however varied during the first experiment, in order to identify an effect on a potential deposition in the cold traps.

Exp. No.	sample mass [mg]	Ar [sccm]	NF_3 [sccm]	time [min]	residual mass [mg]	reaction yield [%]	etching rate [mg/min]
1	298.8	6 − 10	2	60	299.2	–	–
2	195.6	8	2	60	–	–	–

The first experiment was performed without any heating for 60 minutes. During that time, the volume flow of NF_3 was kept constant at 2 sccm, whereas at the same time the flow of argon was varied in order to identify a potential effect of the ratio of the etching agent and the carrier gas. Neither a deposition in the cold traps nor a change in the optical appearance of the briquettes after their extraction from the reaction chamber could be observed. However, the extraction was accompanied by a slight smell of hydrogen fluoride.

The second experiment was initiated by the treatment of the powder with an Ar plasma for 180 minutes at an Ar volume flow of 100 sccm, followed by a hydrogenation for 90 minutes at an H_2 volume flow of 500 sccm. The actual fluorination attempt was performed with an Ar : NF_3 ratio of 8 sccm : 2 sccm. During the entire procedure, the reaction chamber was heated to 160 °C. The extraction of the powder from the reaction tube after the end of the reaction is again accompanied by the strong smell of hydrogen fluoride. Visual inspection of the powder shows it to be strongly agglomerated.

Figure 6.8: Rhodium pellets as used for the first fluorination experiment.

Figure 6.9: Residues of rhodium after fluorination at 160 °C for 60 minutes.

During the course of the reaction, traces of a red brown precipitate in the first cold trap, which is shown in Figure 6.10. However, its recovery was unsuccessful, as the windows of the measuring cell almost entirely lost their transparency, when the content of the cold trap was transferred to it.

Exposure of the residual powder of the second experiment to water changes the color of the water to light yellow, as can be seen in Figure 6.11.

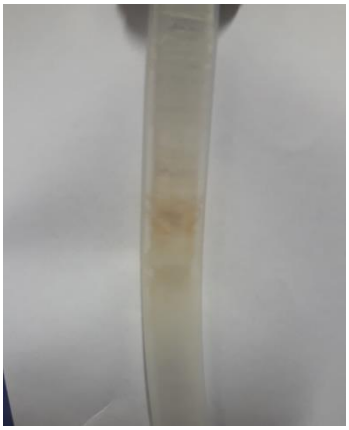

Figure 6.10: Brown precipitate in the first cold trap. LN_2 was used as a frigorific agent.

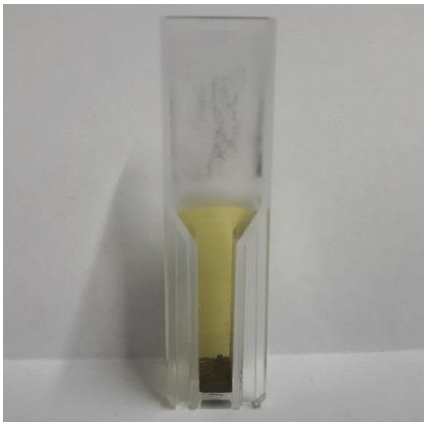

Figure 6.11: Formation of a yellow solution, after exposure of the Rh residues from the reaction chamber to water.

Adding 6M HCl and KCl to the solution and subsequently heating it, led to the formation of a light red solution. UV/VIS spectroscopy performed on it shows two distinct absorption bands at 405 and 517 nm, respectively. This is in good accordance with the $[RhCl_6]^{3-}$ anion, which according to Svecova et al. shows absorption bands at 404 and 519 nm [159]. Both spectra are shown in Figure 6.12.

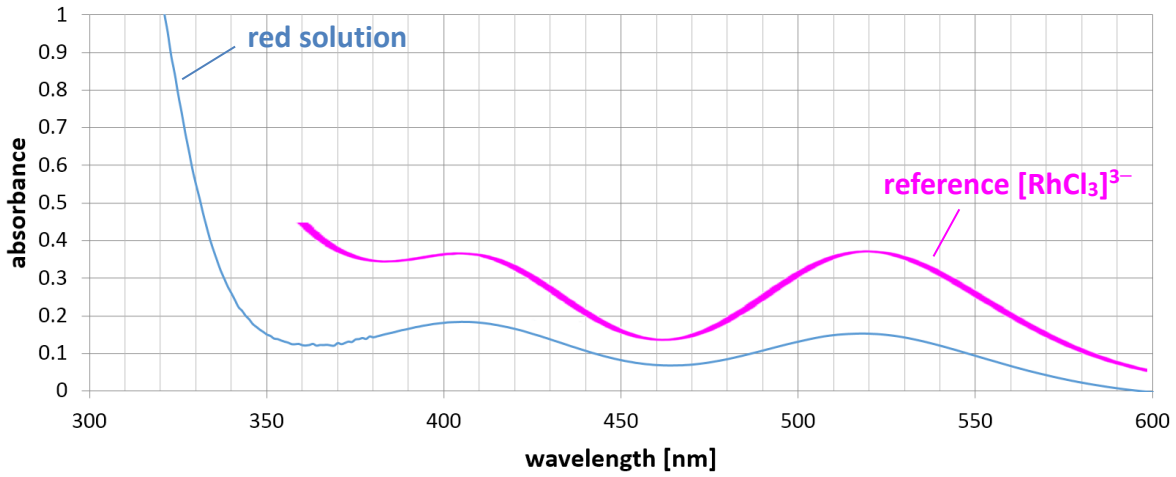

Figure 6.12: UV/VIS spectra of the originally yellow solution after adding HCl and KCl to it (blue graph). The spectrum is in very good accordance with the spectral data for $[RhCl_6]^{3-}$ (pink graph), which has been taken from [159].

As Rh(III)-complexes are often yellow, the color of the original solution might originate from the $[RhF_6]^{3-}$ anion, forming hexafluoridorhodic acid $H_3[RhF_6]$, which would most likely be structurally equivalent to $H_3[RhCl_6]$. In that case, the performed actions would be described by following equation

$$H_3[RhF_6] + KCl \xrightarrow{6M\ \ HCl,heat} K_3[RhCl_6] \qquad (46)$$

However, as RhF_3 is insoluble in water, a higher-valent Rh fluoride must have been formed under the conditions in the fluorination line.

6.3 Palladium

6.3.1 General aspects of palladium and its fluorides

Palladium completes the list of the platinum metals of the fifth period. It is of silvery-white appearance and possesses high ductility but relatively low hardness. Palladium is the most reactive of the platinum metals and is dissolved by concentrated nitric acid, aqua regia and hydrochloric acid in the presence of oxygen [105]. Palladium has the electron configuration [Kr] d^{10} and prefers oxidation state +II and +IV. Oxidation state +III often only formally has this number and is instead composed of +II/+IV mixed-valent compounds [160]. Palladium forms three known thermodynamically stable binary fluorides, which are listed in Table 6.5.

Table 6.5: Physico-chemical properties of the thermodynamically stable binary fluorides of palladium [34,154]. If no data could be found in literature, this is indicated by n.d. (= no data).

	PdF_2	Pd_2F_6	PdF_4
molar mass	144.4 g/mol	163.4 g/mol	182.4 g/mol
melting point	952 °C	230 °C (dec.)	n.d.
boiling point	n.d.	–	n.d.
appearance (SATP)	light purple solid	black or black-violet solid	red or pink solid

PdF_2 is of light purple, amethyst or light brown color and may be obtained by reduction of PdF_3 with elemental palladium at 350 – 900 °C for several days. Palladium is best applied in a highly dispersed form such as palladium black [161]. It is hydrolyzed on moist air and decomposes to the hydrated oxide at exposure to water [162].

The term palladium trifluoride PdF_3 is often found in literature, although palladium (II) hexafluoridopalladate (IV) Pd_2F_6 accommodates for its mixed-valence nature and therefore is the better denomination of this compound. An alternative notation is $PdPdF_6$ [154]. Ruff and Ascher describe it as a black solid and synthesized it by fluorination of $PdCl_2$ at 200 – 250 °C [163]. Serafin et al. describe its color to be of deep black-violet color and suggest a higher temperature of 350 – 400 °C. They also report a feasible reaction even by usage of elemental palladium as a starting material [161].

Rao and Bartlett describe PdF_4 as a pink solid. It is synthesized by the fluorination of one of the lower fluorides, preferably Pd_2F_6 at a pressure of 7 bar and a temperature of 300 °C over several days. It rapidly hydrolyzes when exposed to moist air [154].

PdF_6 has yet to be synthesized; theoretical studies anticipate it to be thermodynamically stable and as the other hexafluorides to form an octahedral molecule. A weak Jahn-Teller distortion is to be expected [164].

6.3.2 Reaction conditions

One experiment was performed investigating the fluorination behavior of palladium. For this experiment, palladium was exposed as a powder.

Table 6.6: Basic conditions of the etching experiment on palladium as a substrate material. The volume flow consisted of pure NF_3 and was kept constant the entire time. The time indicates only the fluorination at an elevated temperature of 190 °C.

Exp. No.	sample mass [mg]	Ar [sccm]	NF_3 [sccm]	time [min]	residual mass [mg]	reaction yield [%]	etching rate [mg/min]
1	194.6	0	4	90	218.9	–	–

The first 30 minutes of the experiment were performed without any additional heating. However, as the powder appeared to be unchanged and no deposition in the cold traps cold be observed, after 50 minutes the temperature was increased to 190 °C. At this temperature, the powder showed occasional sparking and an iridescent pattern appeared at the vertical part of the Monel carrier. After an additional 90 minutes, the fluorination was stopped, leading to a total fluorination time of 140 minutes.

Figure 6.13: Palladium powder before fluorination.

Figure 6.14: Palladium powder after fluorination for 90 minutes at a temperature of 190 °C.

Figure 6.15: Palladium powder after fluorination immediately after extraction from the reaction chamber. Three differently colored zones can be identified, a silver, a brown and a black zone.

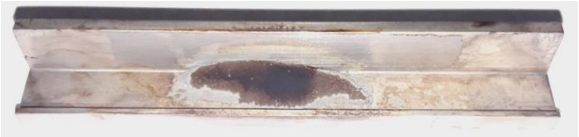

Figure 6.16: Palladium powder after being exposed to the lab atmosphere for seven minutes. A thin, colorful film deposits on the Monel carrier.

The extraction of the powder from the reaction tube is accompanied by the strong smell of hydrogen fluoride. Visual inspection of the powder shows three different zones characterized by different colors. The bottommost zone shows no change in color compared to the palladium powder before the fluorination. It follows a brownish zone merging into the topmost zone which has a blackish color. The compound or at least part of it seems to be very hygroscopic, as a thin colored film deposits on the Monel carrier around the Pd powder, as can be seen in Figure 6.16. This observation is in accordance with the descriptions from literature for PdF_2. The mass of the residues decreased during the time being exposed to the laboratory atmosphere.

XRPD of a sample of the topmost zone shows the presence of elemental palladium, palladium difluoride PdF_2 and palladium trifluoride PdF_3, as can be seen in Figure 6.17. No additional reflexes are present, making it to appear unlikely that PdF_4 was synthesized during the fluorination.

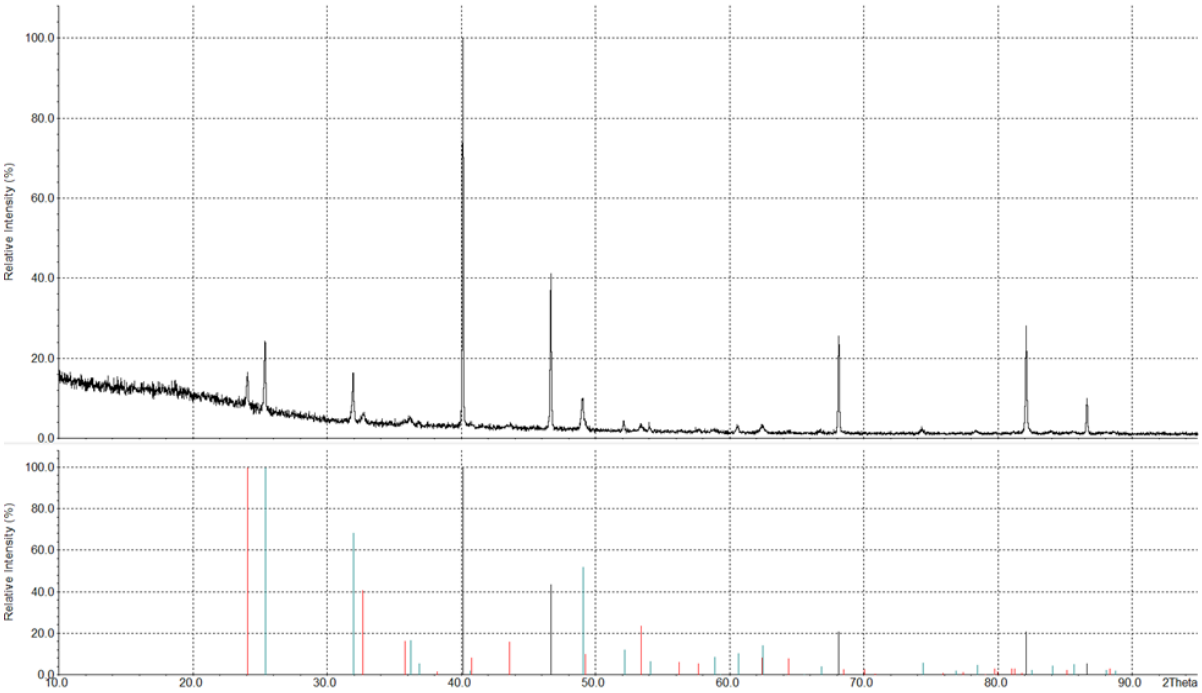

Figure 6.17: X-ray powder diffractogram of the topmost zone of palladium powder after fluorination. The strongest reflexes belong to elemental palladium (black lines, ICDD file [65-2867], quality mark C), the second strongest to PdF_2 (blue lines, ICDD file [72-1263], quality mark C), whereas the ones with the weakest intensities belong to PdF_3 (red lines, ICDD file [72-1182], quality mark C).

6.4 Tungsten

6.4.1 General aspects of tungsten and its fluorides

Tungsten was the first of the 5d transition metal hexafluorides to be investigated. Elemental tungsten is a silvery-white metal of great hardness and tensile strength. It possesses the highest melting point of all metals and the second highest of all elements only exceeded by the one of carbon. It is not dissolved by non-oxidizing acids due to passivation and only very slowly attacked by oxidizing acids such as concentrated sulfuric acid or aqua regia. However, tungsten is easily dissolved by hydrogen peroxide [105].

Table 6.7: Physico-chemical properties of the thermodynamically stable binary fluorides of tungsten [34,105]

	WF_4	WF_5	WF_6
molar mass	259.8 g/mol	278.8 g/mol	297.8 g/mol
melting point	–	–	2.3 °C
boiling point	800 °C (dec.)	80 °C (disp.)	17.1 °C
appearance (SATP)	red-brown solid	yellow solid	colorless gas

WF_4 is a reddish-brown solid, which may be prepared by the reduction of WF_6. Priest et al. thereby used benzene as a reducing agent [165]. It only possesses a low volatility.

WF_5 is volatile already at room temperature. At this temperature, it easily disproportionates into WF_4 and WF_6, if in contact with another surface. At a temperature of 200 °C, this disproportionation also takes place in absence of an additional surface [166].

WF_6 is a colorless gas at standard conditions. It is the only hexafluoride being used on an industrial scale, namely in the semiconductor industry. Here, it is used as the precursor for the deposition of thin tungsten layers, which serve as low resistance interconnects [167].

6.4.2 Reaction conditions

One experiment was performed investigating the fluorination of tungsten. The element was subjected to the etching agent in a massive form as a sheet.

Table 6.8: Basic conditions of the etching experiment using tungsten as a substrate material. The volume flow of NF_3 was kept constant the entire time, whereas Ar was only used for starting the RPS.

Exp. No.	sample mass [mg]	Ar [sccm]	NF_3 [sccm]	time [min]	residual mass [mg]	reaction yield [%]	etching rate [mg/min]
1	541.7	0	60	35	142.2	73.7	11.4

Tungsten shows sufficient etching rates in a massive form such as a thin sheet. Good etching results were achieved using pure NF_3 at a volume flow of 60 sccm, resulting in an average etching rate of 11.4 mg/min. The utilization of NF_3 is rather poor with 2.4 %. However, this yield might be increased at higher temperatures. During the entire experiment, no external heating was provided.

Figure 6.18: Tungsten sheet before fluorination.

Figure 6.19: Tungsten sheet after fluorination for 35 minutes.

After extraction from the reaction chamber, the sheet no longer shows a metallic gloss but is dull instead. Unlike its lighter congener molybdenum, tungsten does not show the formation of any solid residues but instead shows a complete reaction to tungsten hexafluoride.

Figure 6.20: Deposited WF_6 in in the first cold trap using LN_2 as a frigorific agent.

As tungsten was one of the first elements to be fluorinated, no spectroscopic analysis was performed as the measuring cell was constructed later.

6.5 Rhenium

6.5.1 General aspects of rhenium and its fluorides

Rhenium is the higher homologous element to technetium. Their atomic radii are similar; they therefore share many similarities concerning their chemical behavior. Thus, the behavior of rhenium during the fluorination process is of special interest. Rhenium is not considered to be a noble metal, but does not show a reaction with air at room temperature and does not lose its lustrous appearance. It is easily dissolved in oxidizing acids such as nitric acid and concentrated sulfuric acid [105]. Rhenium has the electron configuration [Xe] $4f^{14}5d^{5}6s^{2}$, therefore preferring higher oxidation numbers and reaching oxidation state +VII in numerous compounds. Rhenium forms four thermodynamically stable binary fluorides, that are listed in Table 6.9 [147].

Table 6.9: Physico-chemical properties of the thermodynamically stable binary fluorides of rhenium [34,168,169].

	ReF_4	ReF_5	ReF_6	ReF_7
molar mass	262.2 g/mol	281.2 g/mol	300.2 g/mol	319.2 g/mol
melting point	–	48 °C	18.5 °C	48.3 °C
boiling point	300 °C (subl.)	221.3 °C	33.8 °C	73.7 °C
appearance (SATP)	blue solid	yellow-green solid	yellow liquid or yellow solid	yellow solid

ReF_4 is a medium to dark blue solid at room temperature. It may be synthesized via reduction of ReF_6 by heating rhenium power to 550 °C in one end of a nickel tube and cooling the other end. ReF_4 tends to decompose in the presence of atmospheric gases and dissolves rapidly in water being hydrolyzed and depositing a black precipitate [170].

ReF_5 is a yellow-green solid at room temperature. It may be obtained by the reduction of ReF_6. Different reducing agents have been reported such as silicon powder, hydrogen or rhenium metal [169–171].

The preparation of ReF_6 is challenging requiring either high temperature or high pressure. Thus, it can be synthesized by passing fluorine gas at 330 mbar over rhenium metal at 300 – 400 °C or by fluorinating rhenium powder in an autoclave at 22 bar and 125 °C [123,168]. The same holds for ReF_7. Both compounds are often formed concurrently and can be subsequently separated by reduction of ReF_7 using elemental rhenium. A separation by fractional distillation also seems possible due to a significant difference in their thermodynamic properties.

The thermodynamic properties of ReF_6 and ReF_7 were studied by Malm and Selig [168]. They described the vapor pressure of ReF_6 for different temperature regimes by:

−10.5 °C to -3.5 °C $$p = 1.33 \cdot 10^{\left(-\frac{2303.6K}{T[K]} - 0.8327 \cdot \log(T[K]) + 12.70721\right)}\ mbar \qquad (47)$$

−3.5 °C to 18.5 °C $$p = 1.33 \cdot 10^{\left(-\frac{1765.4K}{T[K]} - 0.1790 \cdot \log(T[K]) + 9.12298\right)}\ mbar \qquad (48)$$

18.5 °C to 48.1 °C $$p = 1.33 \cdot 10^{\left(-\frac{1956.7K}{T[K]} - 3.599 \cdot \log(T[K]) + 18.20814\right)}\ mbar \qquad (49)$$

The vapor pressure of ReF_7 was described by the same authors by the following equations:

−14.5 °C to 48.3 °C $$p = 1.33 \cdot 10^{\left(-\frac{2205.8K}{T[K]} - 1.4703 \cdot \log(T[K]) - 13.04321\right)}\ mbar \qquad (50)$$

48.3 °C to 74.6 °C $$p = 1.33 \cdot 10^{\left(-\frac{244.28K}{T[K]} - 9.90825 \cdot \log(T[K]) - 21.58352\right)}\ mbar \qquad (51)$$

The corresponding graphs for both compounds for the different temperature regimes are depicted in Figure 6.21.

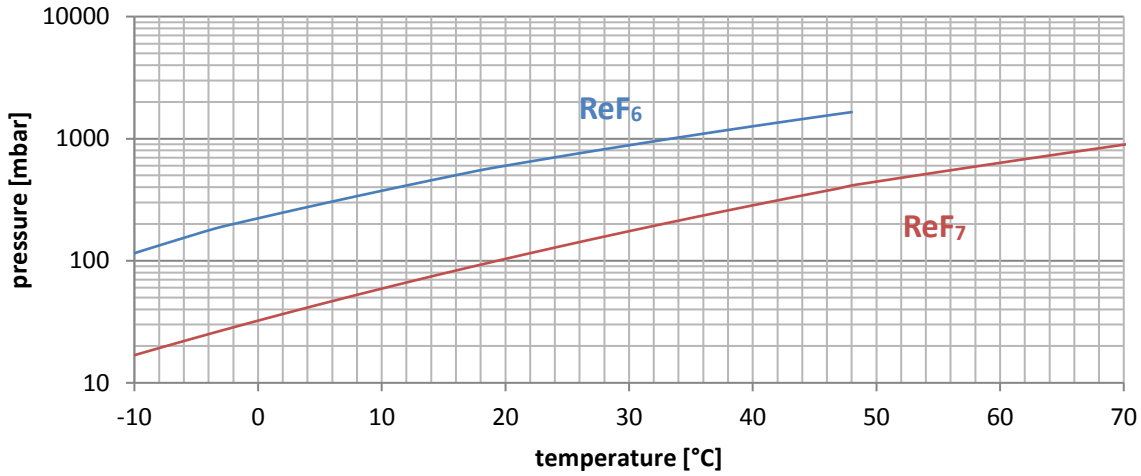

Figure 6.21: The vapor pressure of ReF_6 (blue graph) and ReF_7 (red graph) derived from equations (47) to (51).

6.5.2 Reaction conditions

A total number of four experiments was performed investigating the fluorination of rhenium. However, only two of these are listed in Table 6.10, as the rhenium used in the other two experiments showed to be contaminated with impurities. Thus, the rhenium applied in the two listed experiments was produced by dissolution of rhenium ingots in aqua regia, and subsequent reduction with hydrogen to elemental rhenium. The purity of the powder was verified by µXFS spectroscopy; explicitly no traces of copper could be detected. This information will become relevant in the discussion of the fluorination results. For the first experiment, the rhenium powder was arc melted into a spherical target and for the second trial applied as a powder.

Table 6.10: Basic conditions of the etching experiments on rhenium as a substrate material. For the first experiment, rhenium powder was melted into spheres by arc melting. In the second experiment, rhenium was applied as a powder.

Exp. No.	sample mass [mg]	Ar [sccm]	NF_3 [sccm]	time [min]	residual mass [mg]	reaction yield [%]	etching rate [mg/min]
1	3929.1	100	60	60	3929.0	0.0	0.0
2	195.1	0 − 8	2 − 8	60	2.7	98.6	–

If applied in a massive form, rhenium does not show any reaction even after prolonged exposure. Targets of spherical shape did not show a significant reduction in mass nor did they lose their metallic luster. However, if applied as a powder, rhenium reacts almost completely quite intensely under continuous sparking. Different settings of Ar and NF_3 were used during the reaction, and good etching results were achieved with a NF_3 : Ar ratio of 8 sccm : 8 sccm.

Figure 6.22: Rhenium powder before fluorination.

Figure 6.23: Residues of rhenium powder after fluorination for 60 minutes.

The extraction of the Monel carrier from the reaction chamber is accompanied by a strong smell of hydrogen fluoride. The residues are very low in mass, corresponding to only about 3 mg or 1 % of the applied rhenium mass. However, in addition to rhenium, XRPD also reveals the presence of CuF_2. As the possibility of a contamination of the rhenium powder can be eliminated, the copper most likely originates from the Monel carrier. The corresponding spectrum is depicted in Figure A.35.

The reaction products in the cold traps are of different color, depending on the temperature of the frigorific mixture used for the recovery of the reaction product. For the second experiment, the first cold trap was held at −78 °C using a dry ice/isopropanol mixture and its content was slightly darker with an orange shade. The second cold trap was held at −195 °C using LN_2 and its content was lighter having a more yellowish appearance. As the reaction is expected to produce both, ReF_6 as well as ReF_7, the difference in color may be attributed to a different ration of both components in each cold trap.

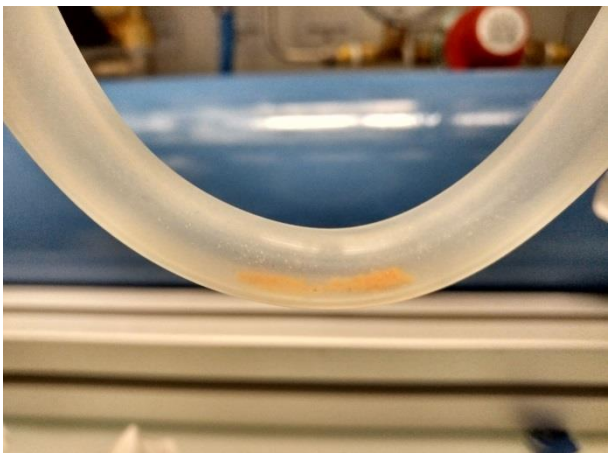

Figure 6.24: Mixture of deposited ReF_6 and ReF_7 in one of the cold traps.

A difficulty of the synthesis of rhenium hexafluoride is the concurrent synthesis of rhenium heptafluoride. As ReF_6 is more volatile than ReF_7, a separation based on the difference in vapor pressure by use of different frigorific mixtures seems possible in principle. In addition to the formation of these two fluorides, another compound synthesized during the reaction was $ReOF_5$. It was identified via IR and Raman as well as NMR spectroscopy (also see chapters 6.5.4, 6.5.5 and 6.5.6). $ReOF_5$ is a cream colored solid melting at 41 °C and boiling at 73 °C [172]. Its thermodynamic properties are therefore comparable with those of ReF_7 and it is likely the two will deposit under similar conditions.

A potential explanation for the origin of oxygen is the formation of a thin layer of rhenium oxide on the surface of the powder. A pretreatment with an H_2 plasma before fluorination therefore seems advisable for future experiments.

6.5.3 UV/VIS spectroscopy

UV/VIS spectroscopy was performed on the samples of the second experiment. These were the same samples, on which IR spectroscopy was performed. The corresponding spectrum was measured at a pressure of 46 mbar and is depicted in Figure 6.25. IR spectroscopy has revealed cold trap 1 holding significate amounts of $ReOF_5$, in addition UF_6, ReF_6 and ReF_7. The UV/VIS spectrum of ReF_6 is known and does not show structured absorption between 380 and 1690 nm. Its entire spectrum is depicted in Figure A.36. Furthermore, comparison with the UV/VIS spectrum of UF_6 shows the structure of the absorption bands not to originate from this compound and may therefore attributed to either ReF_7 or $ReOF_5$.

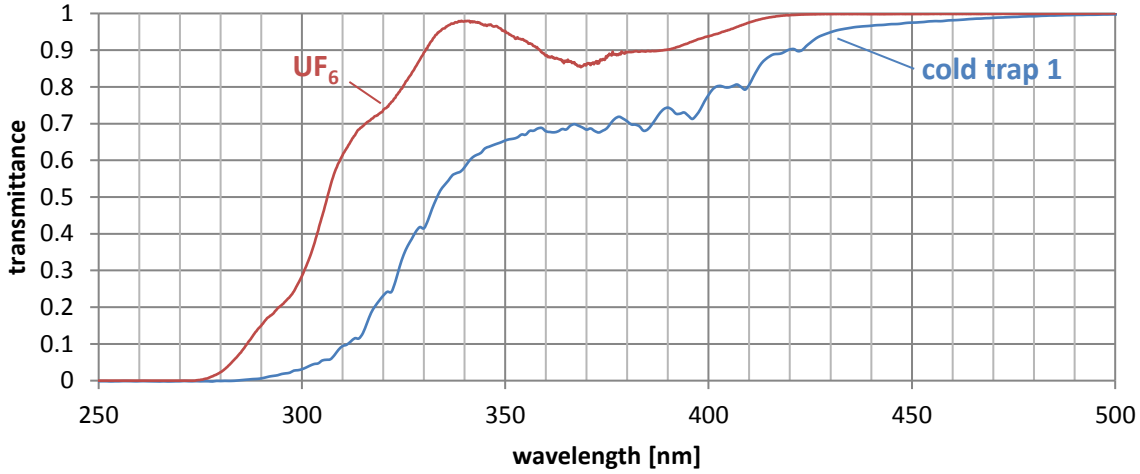

Figure 6.25: UV/VIS spectrum of the content of the first cold trap (blue graph) and in comparison the UV/VIS spectrum of UF_6 at 25 mbar. The pressure in the measuring chamber was 46 mbar.

The content of the second cold trap shows a completely different absorption behavior at a comparable pressure of 43 mbar. The shift in position of the absorption edge may therefore not be attributed to the pressure, but instead must be attributed to a difference composition of the constituents. Extrapolation of equations (47) and (50) leads to a vapor pressure of 0.13 mbar for ReF_6 and of 0.03 mbar for ReF_7 at −78 °C. According to the thermodynamic data, it is therefore more likely for ReF_6 to pass through the first cold trap and to deposit in the second. However, it should be noticed that this temperature lies significantly out of the range recorded by Malm and Selig [168].

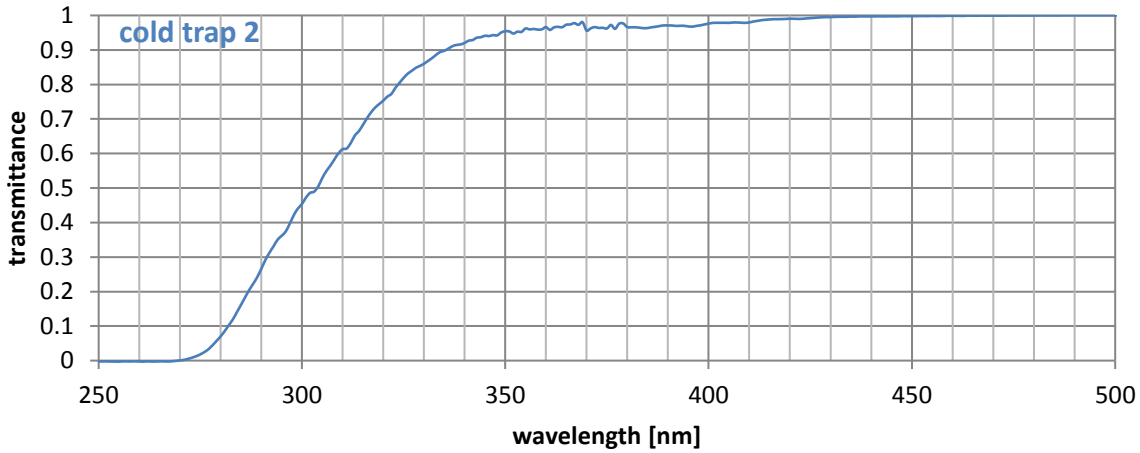

Figure 6.26: UV/VIS spectrum of the content of the second cold trap. The pressure in the measuring chamber was 43 mbar.

6.5.4 IR spectroscopy

IR spectroscopy was performed individually on the first and the second cold trap using the measuring cell. The IR spectrum of the first cold trap, which was cooled using an isopropanol/dry ice mixture, is shown in Figure 6.27. The most noticeable circumstance is the three-pointed band at 981, 989 and 999 cm^{-1}, respectively, which seemed very uncommon for a hexafluoride and indeed, it belongs to $ReOF_5$.

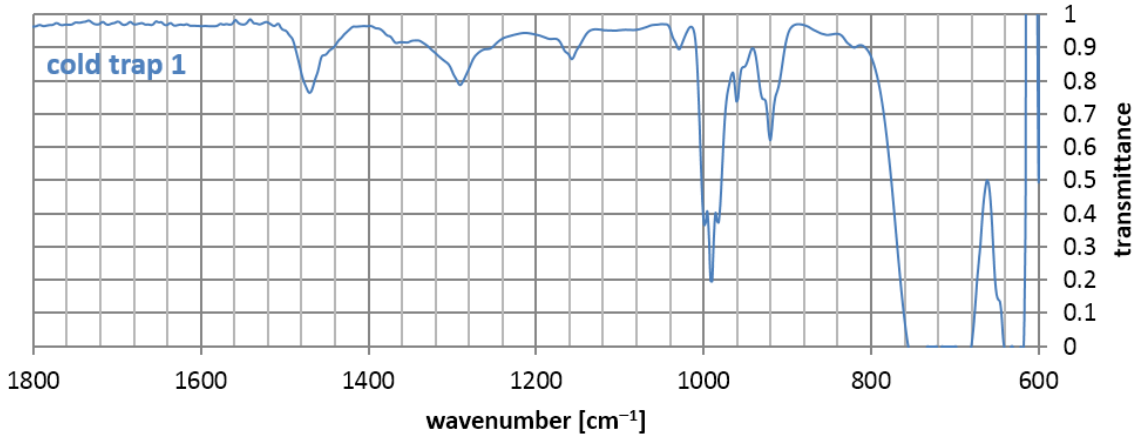

Figure 6.27: The IR spectrum of the content of first cold trap after the fluorination of rhenium powder. The pressure in the measuring cell was 46 mbar.

The IR spectrum of the content of the second cold trap shows the characteristic signal of $ReOF_5$ in the region around 990 cm^{-1} being significantly reduced. Thus, the major fraction deposits already at a temperature of −78 °C. The remaining spectrum does neither resemble the spectrum of pure ReF_6 nor of pure ReF_7. It therefore seems likely both compounds being present.

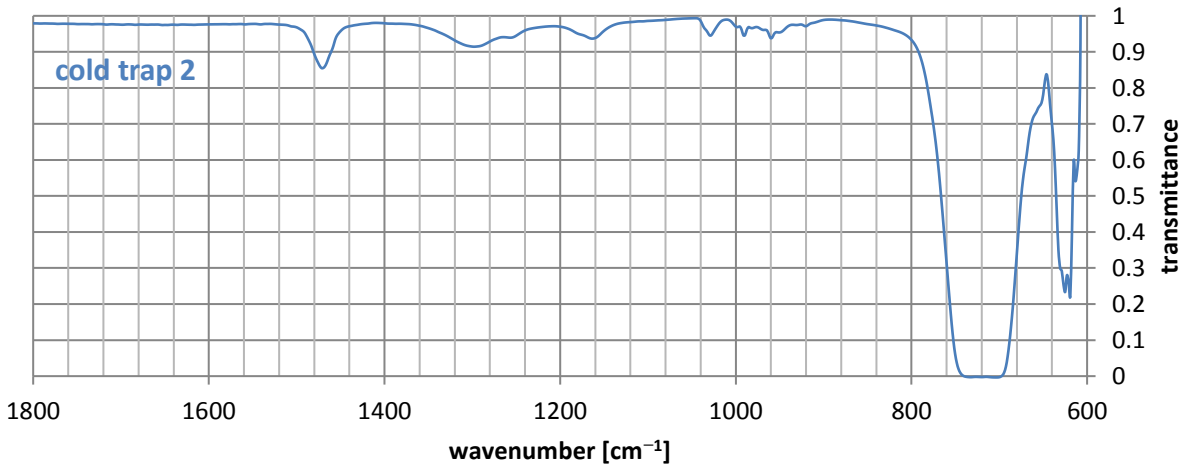

Figure 6.28: The IR spectrum of the content of the second cold trap after the fluorination of rhenium powder. The pressure in the measuring cell was 43 mbar.

6.5.5 Raman spectroscopy

As the presence of $ReOF_5$ and UF_6 had already been confirmed by IR spectroscopy and ReF_6 and ReF_7 are expected to be formed during the reaction, a total number of four compounds has to be taken into account at determining the signal position. The difficulty resulting from this circumstance may be illustrated by Figure 6.29, which shows the digitalized spectra of ReF_6, ReF_7 and $ReOF_5$. Many signals overlap, the quality of the background correction is questionable and the intensity of the fundamentals was not entirely recorded.

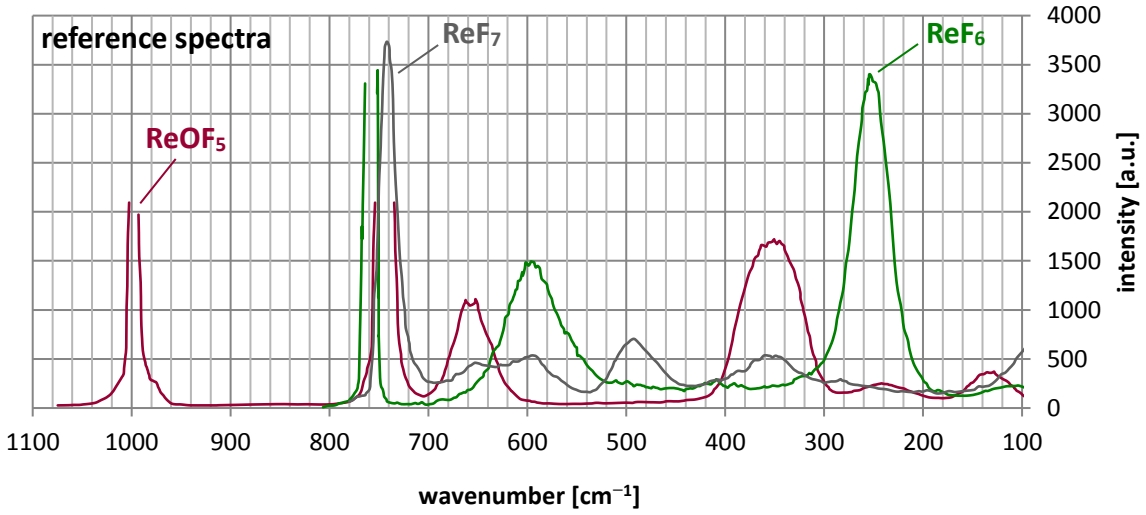

Figure 6.29: Raman reference spectra of ReF_6 gas at a temperature of 90 °C and a pressure of 3 bar (green graph) [173], ReF_7 vapor at a temperature of 75 °C and a pressure of 1 bar (grey graph) [174] and of $ReOF_5$ at 135 °C and a pressure of 1.5 bar (red graph) [175].

Raman spectroscopy was performed on the content of the first cold trap. Figure 6.30 shows the acquired spectrum after background correction and subtraction of the FEP reference spectrum. Although a quantitative analysis of this spectrum would be afflicted with a high level of uncertainty, a qualitative assignment of the signals is possible. The band at 995 cm^{-1} may clearly be assigned to $ReOF_5$, the band at 665 cm^{-1} to UF_6. The band at 757 cm^{-1} may be assigned to ReF_6.

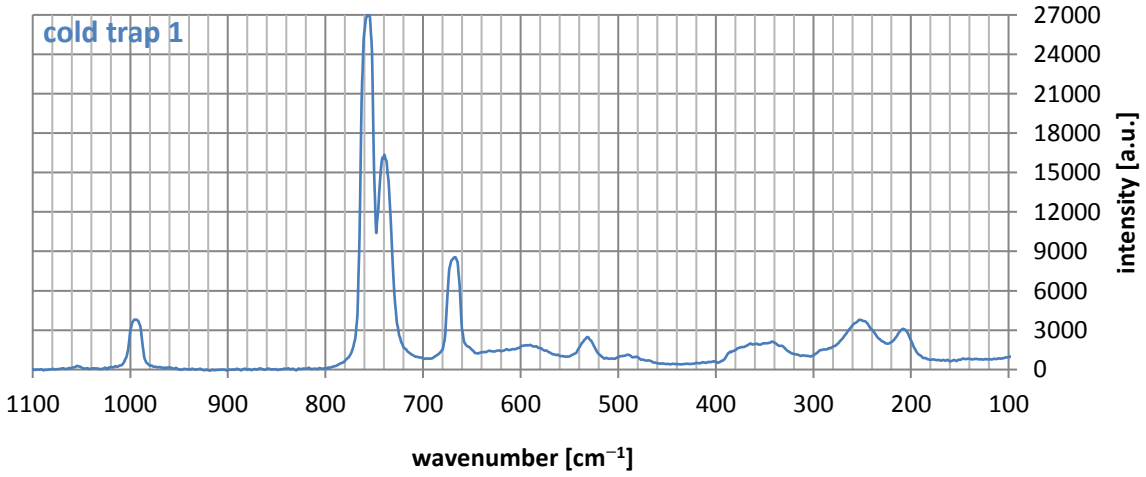

Figure 6.30: Raman spectrum of the content of the first cold trap after baseline correction and subtraction of the FEP spectrum.

6.5.6 NMR Spectroscopy

NMR spectroscopy was performed on the content of both cold traps. The first cold trap gave a total number of five sharp signals, at 4, 201, 288, 351 and 766 ppm w.r.t. $CFCl_3$. The second cold trap gave four clearly distinguishable signals as well as one that was very weak. In addition, these signals are much broader than the ones from the first cold trap, which most likely is to be attributed to the low filling level of the NMR tube. Their positions are slightly shifted to the ones of the first cold trap and are found at 10, 291, 354 and 769 ppm w.r.t. $CFCl_3$. The number of signals is consistent with what would be expected given the knowledge of the presence of the three compounds ReF_6, ReF_7 and $ReOF_5$ as well as a contamination with UF_6. As $ReOF_5$ is known to have C_{4v} symmetry [176], two signals would be expected for this compound.

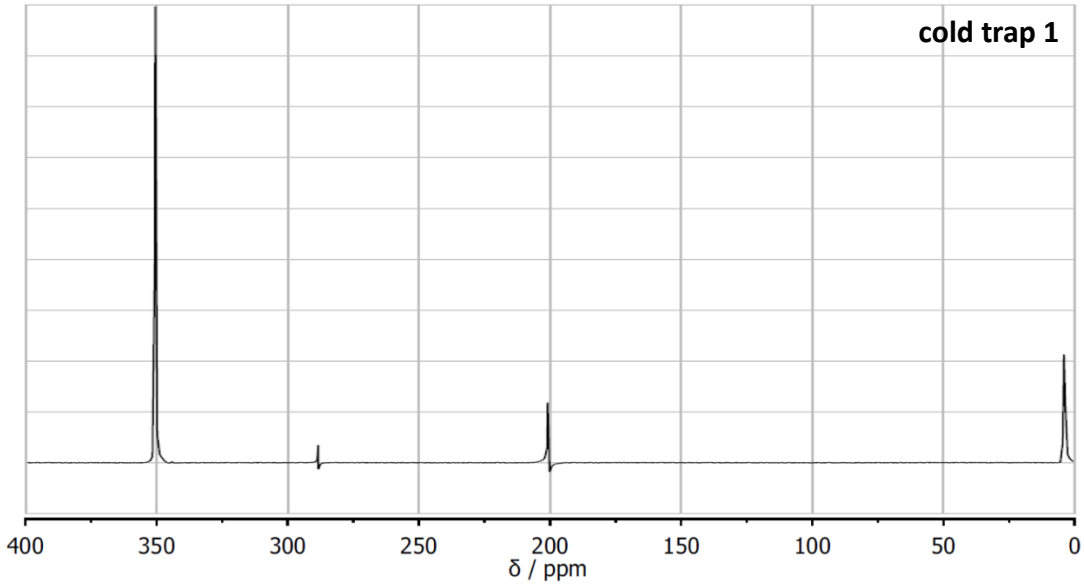

Figure 6.31: ^{19}F NMR of the first cold trap, which was cooled using an isopropanol/dry ice mixture.

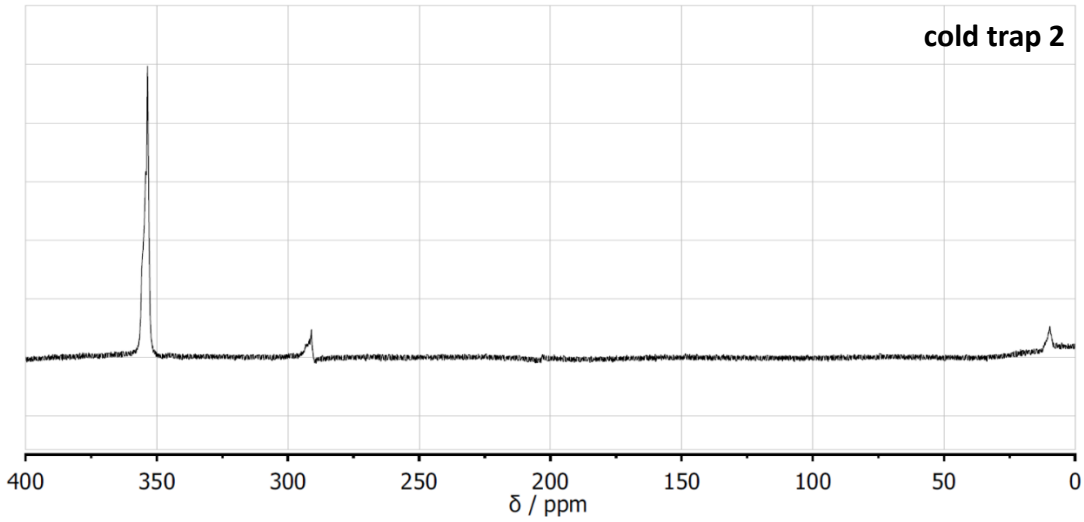

Figure 6.32: ^{19}F NMR of the second cold trap, which was cooled using LN_2.

Except for the first signal at 4 and 10 ppm, respectively, the difference in chemical shift is constantly 3 ppm. These signals may therefore assigned to the same compounds. Bartlett et al. had already investigated ReF_7 and $ReOF_5$ using ^{19}F NMR in [177]. However, their measurements were performed with respect to SiF_4 and gave a chemical shift of -510 ± 1 ppm for ReF_7 as well as -361.9 ± 0.5 and -159.6 ± 0.5 ppm for the equatorial and axial signal of $ReOF_5$, respectively. A conversion between different standards is possible in principle but may lead to a deviation of several ppm. The offset between SiF_4 and $CFCl_3$ is −158.8 ppm [178]. Accounting for the meanwhile opposite leading sign convention for the chemical shift, this leads to the signal of ReF_7 to be found at 351.2 ppm w.r.t. $CFCl_3$. The equatorial signal of $ReOF_5$ would be expected at 203.1 ppm and the axial signal at 0.8 ppm w.r.t.$CFCl_3$. The chemical shift of these signals is in very good agreement with the observations.

Table 6.11: Chemical shifts of $ReOF_5$ and ReF_7 as recorded by Bartlett et al. in [177], however measured w.r.t. SiF_4. As the measurements of the compounds extracted from the cold traps were performed w.r.t. $CFCl_3$, the conversion to this standard is also given. Comparison with the synthesized compounds shows good agreement.

	Bartlett, SiF_4	Bartlett, $CFCl_3$	cold trap 1	cold trap 2
$ReOF_5$, axial	−159.6 ± 0.5	0.8	4	10
$ReOF_5$, equatorial	−361.9 ± 0.5	203.1	201	–
ReF_7	−510 ± 1	351.2	351	354
ReF_6	–	–	288	291

The signal at 766 ppm is in good agreement with the previously determined chemical shift of UF_6 at 765 ppm w.r.t $CFCl_3$. The only signal remaining unassigned is found at 288 ppm. As Raman spectroscopy performed on the exact same sample has already confirmed the presence of ReF_6, it may be concluded this signal belonging to ReF_6.

6.6 Osmium

6.6.1 General aspects of osmium and its fluorides

Osmium is a very hard and brittle platinum metal of grey-blue color. Of all elements, it has the highest density. It is highly unreactive, not attacked by any acid and even insoluble in aqua regia [149]. It has the electron configuration $[Xe]4f^{14}5d^{6}6s^{2}$ and thus is able to reach the oxidation state +VIII as in OsO_4. However, its preferred oxidation state is +IV. Osmium forms three, maybe four, thermodynamically stable binary fluorides that are listed in Table 6.12 [147]. Although oxidation state +VII is known from compounds such as $OsOF_5$, there is some debate about the existence of OsF_7. Its preparation claimed by Glemser and Roesky could not be reproduced by Seppelt [179,180].

Table 6.12: Physico-chemical properties of the thermodynamically stable binary fluorides of osmium [34,169].

	OsF_4	OsF_5	OsF_6	OsF_7
molar mass	266.2 g/mol	285.2 g/mol	304.2 g/mol	323.2 g/mol
melting point	230 °C	70 °C	33.2 °C	–
boiling point	–	225.9 °C	47.5 °C	−100 (dec.)
appearance (SATP)	yellow-brown solid	blue or blue-green solid	yellow solid	yellow solid

OsF_4 is a yellow-brown solid at room temperature. Paine and Asprey describe its synthesis starting from OsF_5 by dissolving this compound in anhydrous HF and admitting H_2 gas to the resulting solution. This solution is subsequently photochemically reduced by UV irradiation using Pt gauze as a catalyst [169]. OsF_4 is very sensitive to moisture.

OsF_5 is a blue solid at room temperature. Paine and Asprey synthesized it by the reducing OsF_6 using silicon powder in anhydrous HF at room temperature and subsequently evaporating the HF [169]. Hargreaves et al. describe its color as blue-green, when in the solid state, as a green liquid just above the melting point and as a bright blue liquid just below the boiling point [181].

OsF_6 is a bright yellow substance and solid at ambient temperature. Weinstock and Malm report its synthesis by passing elemental fluorine over finely divided osmium at a pressure of 330 mbar [182]. They describe the osmium powder to be heated, but do not provide a specific temperature.

6.6.2 Reaction conditions

Two experiments investigating the etching behavior were performed. For both experiments, osmium was deposited as a powder and showed a fierce reaction. In each trial, more than 95 % of the deployed powder was converted into volatile species.

Table 6.13: Basic conditions of the etching experiments on osmium as a substrate material. During the first trial, the volume flows of both, Ar and NF_3 were kept constant. During the second trial, the volume flow of both components was varied until a promising set of parameters was identified.

Exp. No.	sample mass [mg]	Ar [sccm]	NF_3 [sccm]	time [min]	residual mass [mg]	reaction yield [%]	etching rate [mg/min]
1	208.6	8	2	75	6.6	96.8	2.7
2	842.3	0 – 7.5	3 – 15	41	41.2	95.1	–

Good etching results were achieved with pure NF_3 and no argon as a carrier gas at a volume flow of 15 sccm per minute, utilizing 60 % of the NF_3 for the conversion. In contrast, volume flows as little as NF_3 : Ar of 2 sccm : 8 sccm led to a utilization of the etching agent of only 30 %, however with a slightly higher utilization of the deployed osmium.

Figure 6.33: Osmium powder on the Monel boat before fluorination. A total mass of 208.6 mg was applied.

Figure 6.34 Residues of the osmium after being exposed to the plasma for 75 minutes. Mass of the residues equal to 6.6 mg, accounting for a reaction yield of about 97 %.

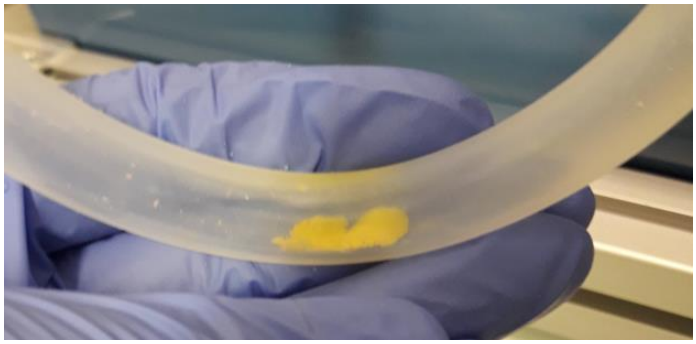

Figure 6.35: Deposition of OsF_6 in the first cold trap, as verified using UV/VIS and Raman spectroscopy.

All analytical measurements mentioned in the following chapters 6.6.3 to 6.6.6 have been performed on the content of the same cold trap.

6.6.3 UV/VIS spectroscopy

UV/VIS was performed on the reaction product from the second experiment. The sample was taken from the content of the first cold trap, which was cooled using a bath of isopropanol and dry ice.

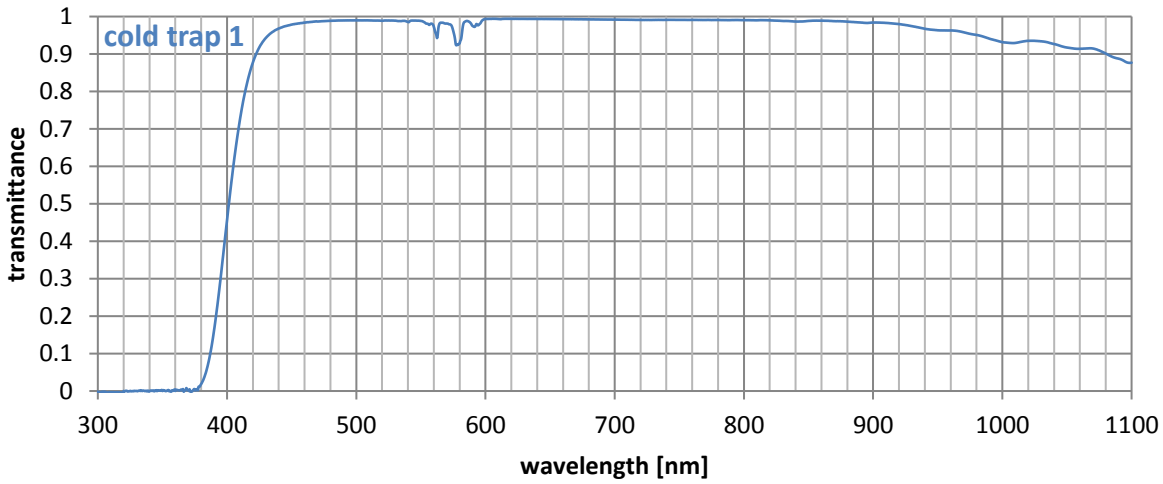

Figure 6.36: UV/VIS spectrum of the content of the first cold trap after the fluorination of osmium powder, acquired with the measuring cell at a pressure of 168 mbar.

The spectrum shows strong absorption in the UV-region below 380 nm, followed by a steep rise in the violet and blue region of the visible spectrum. An additional structure, consisting of relatively sharp absorption bands, is present in the region between 540 and 600 nm. Starting at 900 nm, OsF_6 again shows significant absorption. However, the bands become much wider and are not as sharply separated. Literature research only yielded one UV/VIS spectrum for OsF_6. As this spectrum was recorded as a function of wavenumber, the spectrum in Figure 6.36 was also converted. Unfortunately, these spectra are only qualitative in nature, therefore an overlay of literature and experimental data as done for UF_6 is inexpedient in this case. Instead, both spectra are shown side by side in Figure 6.37 and Figure 6.38.

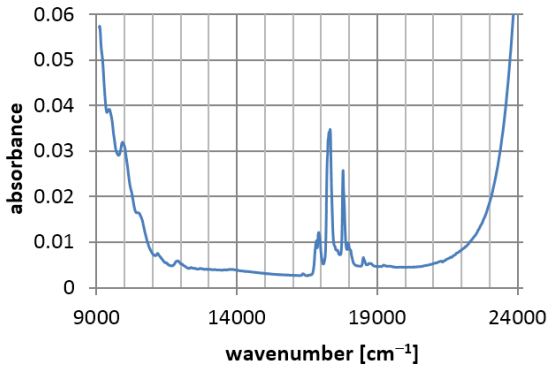

Figure 6.37: Section of the spectrum in Figure 6.36 containing the band positions in detail.

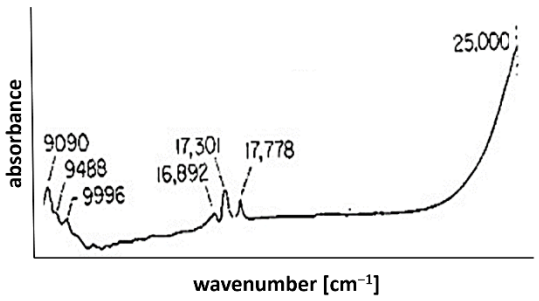

Figure 6.38: The absorption spectrum of osmium hexafluoride in the visible range [183].

In the recorded range, all bands assigned in the literature spectrum are also found in the spectrum of the sample synthesized using the fluorination line. Additional bands are also present, that have not been assigned in literature before. As impurities of IrF_6 have been found in the Raman spectrum, the positions of these bands have been compared to these of IrF_6 but may not be assigned. It may therefore be concluded, the impurities being of minor amount and therefore not showing any significant absorption in the UV/VIS range.

Table 6.14: The bands of the UV/VIS spectrum as assigned by Moffitt et al. in [183]. The last column lists the values found in the spectrum acquired during the course of this thesis, the second column the corresponding wavenumber for comparison with the data from literature.

Moffitt et al. wavenumber [cm^{-1}]	corresponding wavenumber [cm^{-1}]	measured wavelength [nm]
–	18484	541
–	17986	556
17778	17762	563
17301	17271	579
16892	16892	592
–	16835	594
–	11891	841
–	11161	896
–	10537	949
9996	9920	1008
9488	9443	1059

6.6.4 IR spectroscopy

IR spectroscopy was performed on the identical sample as UV/VIS spectroscopy. As the contained compound was clearly identified as OsF_6, the main bands found in the spectrum shown in Figure 6.39 also belong to OsF_6. However, as impurities have also been found in the spectrum of IrF_6, the presence of bands originating from previously synthesized compounds may not entirely be excluded. However, due to the absence of the ν_3 fundamental of UF_6, no bands may be assigned due to the presence of this compound.

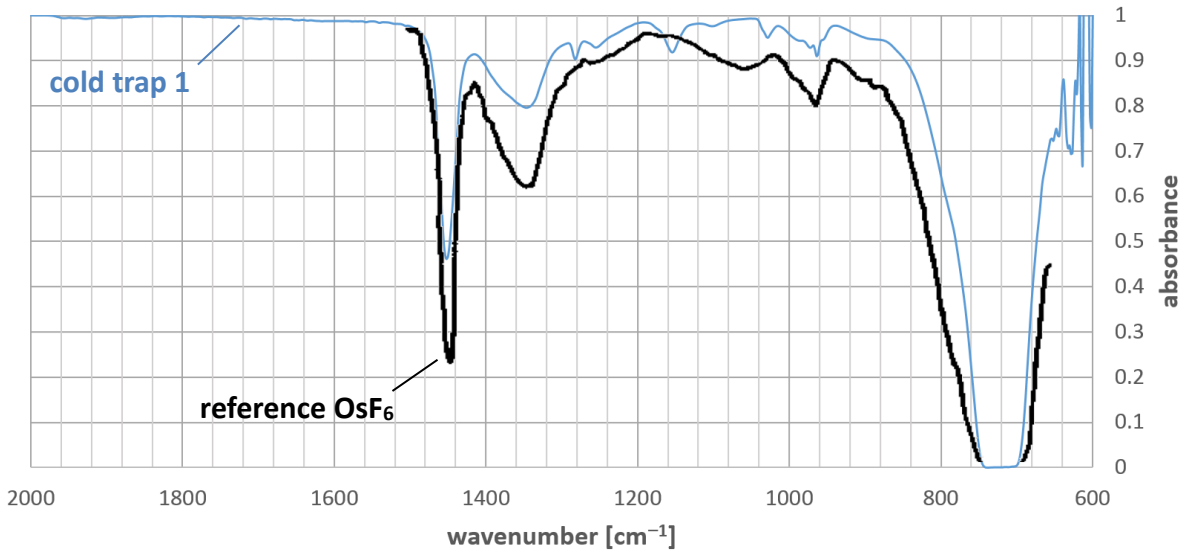

Figure 6.39: IR spectrum of the content of the first cold trap after the fluorination of osmium powder. Measurement was performed on the same sample as the acquisition of the UV/VIS spectrum in Figure 6.36 and Figure 6.37 using the measuring cell at a pressure of 168 mbar. The reference spectrum has been reported by Weinstock et al. [184].

The spectrum is in very good agreement with the data from literature and shows the typical structure of the other hexafluorides with a wide ν_3 fundamental in the region between 600 and 800 cm^{-1} and the prominent ($\nu_2 + \nu_3$) and ($\nu_1 + \nu_3$) combination bands between 1150 and 1500 cm^{-1}. However, OsF_6 also shows some peculiar features. First, the left flank of the ν_3 fundamental located at approximately 722 cm^{-1} is by far less steep than for the other hexafluorides. Second, whereas the named combination bands are similar in form and absorbance for the other hexafluorides, this is not the case here. ($\nu_1 + \nu_3$) at 1451 cm^{-1} is narrow and strong, ($\nu_2 + \nu_3$) at approximately 1362 cm^{-1} is much wider and has significantly lower intensity. Its width may be explained by the formation of different branches, as may be observed in the detailed view on the spectrum shown in Figure A.40.

The fundamentals ν_1 to ν_6 of OsF_6 have been reported by Weinstock et al. in [184] to be found at 733 (ν_1), 632 (ν_2), 720 (ν_3), 268 (ν_4), 252 (ν_5) and 230 cm^{-1} (ν_6). These allow the calculation of the combination bands of the OsF_6 spectrum and are listed in Table 6.15. Also listed are the bands observed by Weinstock.

Table 6.15: Positions of the bands in the IR spectrum of OsF_6 found during this work and comparison with the observed bands and calculated positions based on Weinstock et al. [184].

assignment	Weinstock calc. wavenumber [cm^{-1}]	Weinstock obs. wavenumber [cm^{-1}]	this work wavenumber [cm^{-1}]
ν_3	–	720	723
$\nu_2 + \nu_6$	862	–	–
$\nu_2 + \nu_4$	900	894	–
$\nu_3 + \nu_5$, P	972	–	954
$\nu_3 + \nu_5$, Q	972	–	963
$\nu_3 + \nu_5$, R	972	969	973
$\nu_1 + \nu_4$, P	1001	–	990
$\nu_1 + \nu_4$, R	1001	–	1101
–	–	–	1155
$(2\nu_1 - \nu_6)$	1236	–	1251
$(\nu_3 + 2\nu_4)$	1256	1268	1282
$\nu_2 + \nu_3$, P	1352	1352	1344
$\nu_2 + \nu_3$, R	1352	–	1380
$\nu_1 + \nu_3$	1453	1453	1451

The two elements fluorinated directly before the fluorination of osmium were first rhenium and subsequently iridium. However, due to its absorption behavior, a contamination with IrF_6 should have already been detected in the UV/VIS spectrum. A small contamination of the sample with ReF_6 or ReF_7 would most likely not be visible in the UV/VIS spectrum due to the very high absorption of OsF_6 in the region below 400 nm.

This contamination could explain the origin of the band at 1155 cm^{-1} and may as well partly contribute to the bands found at 1251 and 1282 cm^{-1}. The appearance of the latter two is much more prominent as has been reported in the literature spectrum as shown in Figure 6.39.

6.6.5 Raman spectroscopy

Raman spectroscopy was performed on a sample extracted from the first cold trap synthesized during the second experiment using a laser wavelength of 532 nm. The corresponding spectrum and the comparison with literature is shown in Figure 6.40. Some minor impurities of IrF_6 are visible, as iridium was the element fluorinated in the trials directly before this experiment. The reference spectrum was recorded by Molski and Seppelt on OsF_6 dissolved in HF at room temperature [41].

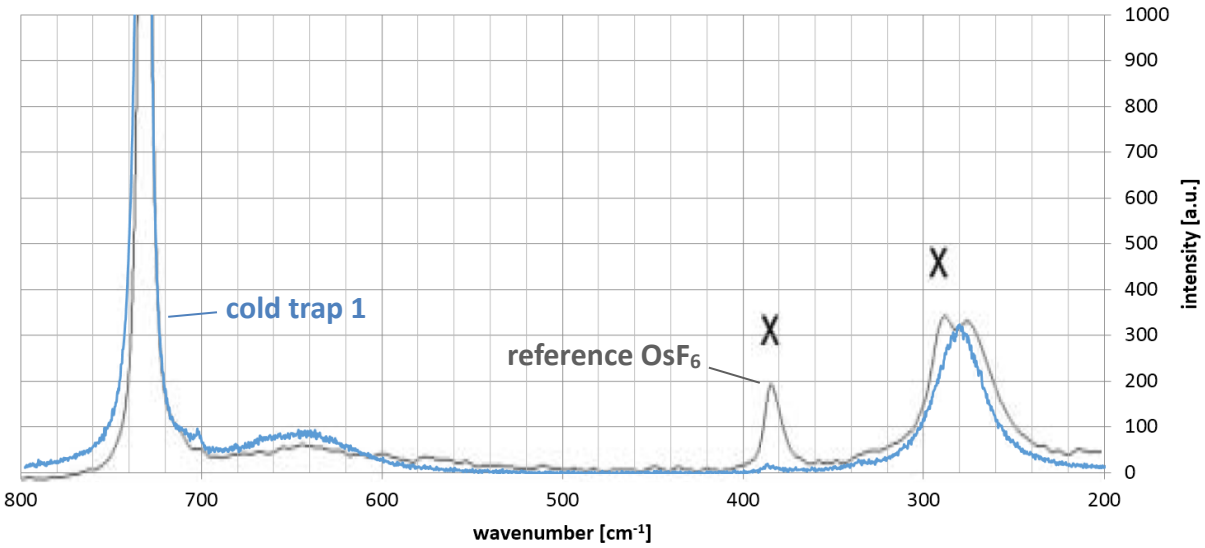

Figure 6.40: Raman spectrum of the reaction product of the fluorination of osmium powder extracted from the first cold trap in the second experiment. The grey graph is the reference spectrum reported by Molski and Seppelt, who measured OsF_6 in HF solution at room temperature. *x* marks bands of the PFA tube, in which the samples were measured [41].

As already observed in the IR spectrum, the Raman spectrum of OsF_6 also shows the typical structure of the other hexafluorides with some differences. The ν_1 fundamental is located in the region between 650 and 750 cm^{-1} and possesses the highest intensity of all fundamentals. The ν_2 fundamental is in relative proximity, but in difference to the other hexafluorides is very broad and comparably flat. None of the fundamentals shows signs of splitting into the different PQR-branches, even if measured at high resolution. The decomposition and analysis of the spectrum is depicted in Figure A.42 to Figure A.44.

In comparison with the spectra reported by Weinstock et al., the position of the ν_1 fundamental is in very good agreement. However, the deviations are becoming larger with smaller wavenumbers and the position of the ν_5 fundamental already shows a deviation of almost 10 % to the literature data. As both spectra were acquired using liquid OsF_6 as a sample, the possibility of the deviation originating from solid-to-liquid frequency shifts may be discarded.

Table 6.16: Comparison of the fundamental bands reported by Weinstock et al. [184] with the positions determined during the experiments of this thesis.

assignment	Weinstock et al. wavenumber [cm^{-1}]	this work wavenumber [cm^{-1}]
ν_5	252	280.1
ν_2	632	648.0
ν_1	733	732.1

6.6.6 NMR spectroscopy

The NMR spectrum of OsF_6 has only been rarely been investigated. Seppelt and Bartlett report a very broad signal hard to observe at 88.7 ppm w.r.t. $CFCl_3$ [185]. However, in this article the authors use a sign convention of the chemical shift contrary to present-day use. Therefore, a potential signal is to be expected at −88.7 ppm. Their measurement was performed at a frequency of 56.4 MHz. The OsF_6 sample was condensed into an FEP tube which was inserted into a glass tube.

The NMR measurements on OsF_6 were performed on the same sample as the Raman spectroscopy. The content of the first cold trap was therefore heated and sublimed into an FEP tube. The tube was heated to 323 K in order to ensure the sample being liquid. Three distinct signals may be observed between 0 and 1200 ppm with respect to $CFCl_3$, at 135 ppm, 358 ppm and 839 ppm. As all signals are very weak and obviously there is no possibility for all three signals belonging to OsF_6, side products also have to be taken into account. Bartlett et al. reported the equatorial signal of $OsOF_5$ at −215 ppm w.r.t SiF_4, what would correspond to 57 ppm w.r.t. $CFCl_3$. However, no signal in this region could be observed. The signal at 135 ppm has also been found at IrF_6 for high fluxes of NF_3. It therefore is reasonable to believe this signal belonging to NF_3, which is documented at 147 ppm for the pure substance. The signal at 358 ppm could belong to NF_3O, which is reported at 366 ppm for the pure substance. Very fine osmium powder is known to react with oxygen already at room temperature forming OsO_4, if stored on air [186]. This would explain the origin of the oxygen. The signal at 839 ppm is in reasonable proximity to 865 ppm, the reported signal of F_2O_2. In summary, all signals in the spectrum may be assigned to other substances than OsF_6. The position of the signal of OsF_6 at −88.7 ppm may therefore neither be confirmed nor confuted.

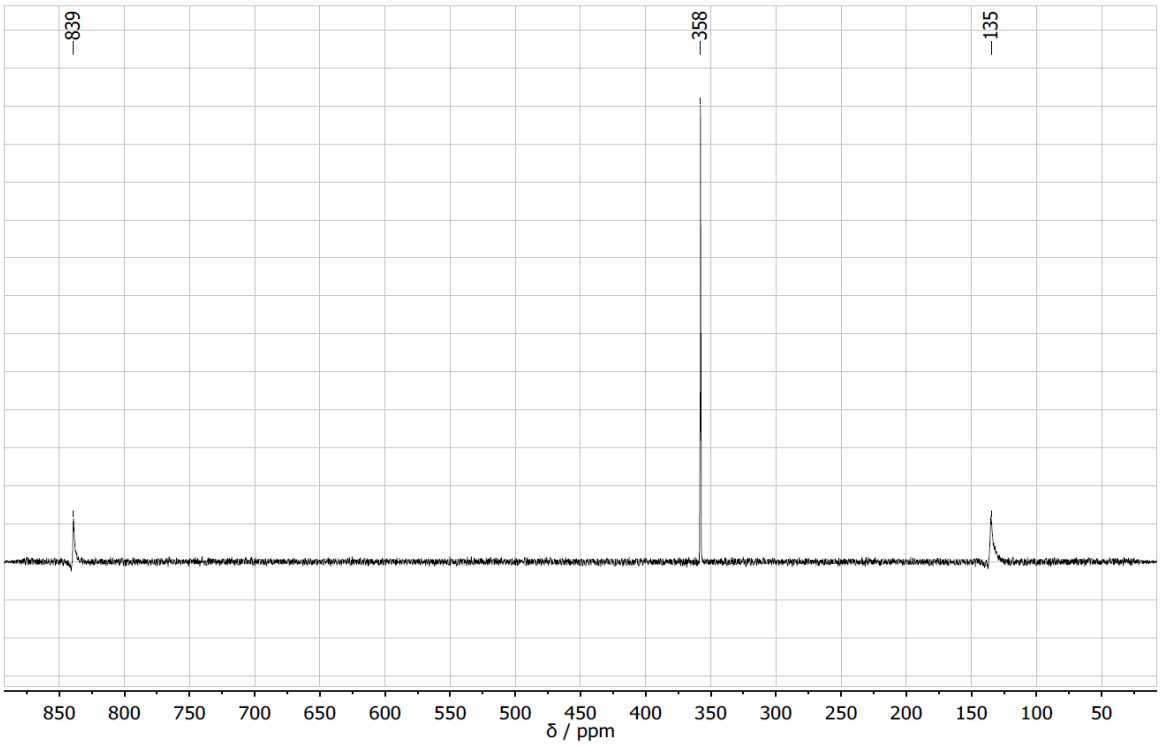

Figure 6.41: NMR spectrum of the reaction product of the fluorination of osmium powder.

6.7 Iridium

6.7.1 General aspects of iridium and its fluorides

Iridium is a silvery-white and brittle platinum metal. Out of these, it has the highest chemical inertness. It is resistant against acids in compact form, and is only dissolved as a very fine powder by aqua regia and concentrated sulfuric acid [105]. Iridium has the electron configuration [Xe] $4f^{14}5d^{7}6s^{2}$ and therefore prefers oxidation states +III and +IV. It forms four known thermodynamically stable binary fluorides that are listed in Table 6.17 [147].

Table 6.17: Physico-chemical properties of the thermodynamically stable binary fluorides of iridium [34,43,135,187]. If no data could be found in literature, this is indicated by n.d. (= no data).

	IrF_3	IrF_4	IrF_5	IrF_6
molar mass	249.2 g/mol	268.2 g/mol	287.2 g/mol	306.2 g/mol
melting point	250 °C (dec.)	n.d.	104.5 °C	44 °C
boiling point	–	~ 400 °C (disp.)	n.d.	53.6 °C
appearance (SATP)	black solid	red-brown or light brown solid	yellow or yellow-green solid	yellow solid

IrF_3 has been described as either a brownish-black or black solid, that is insoluble in water. It is thermodynamically stable up to 250 °C. Above that temperature, it starts to decompose into elemental iridium and fluorine. Relatively pure IrF_3 may be by synthesized by reducing IrF_4 in an atmosphere of sulfur tetrafluoride [188].

IrF_4 is described as light brown solid by Rao et al. and may efficiently be prepared by the reduction of IrF_5 with iridium metal sponge, although the direct synthesis from the elements at 310 °C is also possible [154]. Other sources describe its color as red-brown [149]. IrF_4 is thermodynamically stable until about 400 °C, at which temperature it starts to disproportionate into IrF_3 and IrF_5. IrF_4 slowly hydrolyses in moist air into a violet substance [154]. Exposed to water, it immediately hydrolyses into hydrated IrO_2 and HF [189].

IrF_5 is a yellow or yellow-green solid at room temperature. Bartlett et al. describe its synthesis by reacting a stoichiometric amount of iridium and fluorine at 350 – 380 °C over a period of 24 hours [187]. IrF_5 reacts with excess water forming a purple solution [162].

IrF_6 is a yellow solid at room temperature. It may be synthesized from the elements at a temperature of 300 – 400 °C [188]. IrF_6 may be handled in quartz glass only at temperatures below 200 °C and only if the glass has been thoroughly dried [190].

6.7.2 Reaction conditions

A total number of three experiments was performed investigating the fluorination of iridium. For all trials, iridium was presented as a powder with a very fine mesh. It was purchased from Smart-elements GmbH and according to the provider possessed a metal-based purity of 99.95 %. Investigation using µXFS did not reveal any impurities.

Table 6.18: Basic conditions of the etching experiments with iridium as a substrate material. All trials were performed without the use of Ar as a carrier gas.

Exp. No.	sample mass [mg]	Ar [sccm]	NF_3 [sccm]	time [min]	residual mass [mg]	reaction yield [%]	etching rate [mg/min]
1	286.2	0	60	7	233.4	18.4	7.5
2	495.9	0	3 – 6	21	161.8	67.3	–
3	722.2	0	3 – 23	62	39.3	94.6	–

All three trials were performed using pure NF_3 and no carrier gas. Argon was only used for plasma ignition and switched off with the injection of NF_3. In the first trial, intensive sparking was immediately initiated and lasted for about three minutes. At its end, a considerable amount of Ir powder was still present on the Monel carrier. No external heating was performed during the entire course of the reaction. For the second experiment, the NF_3 volume flow was held at 3 sccm for 13 minutes and then set to 6 sccm for an additional 8 minutes. The chamber was externally heated at 185 °C. The third trial must be considered the most successful with respect to the reaction yield. Different process parameters were tested, which identified a volume flow of 13 sccm at a temperature of 210 °C as being most successful.

Figure 6.42: Iridium powder on the Monel boat before fluorination. The applied mass in this picture amounts to 722.3 mg.

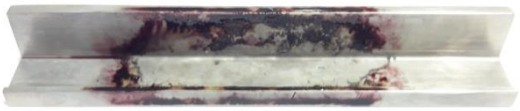

Figure 6.43 Residues of the iridium after being exposed to the plasma for 62 minutes. Mass of the residues equal to 39.2 mg. They are extremely hygroscopic starting to react immediately with the moisture in the lab atmosphere.

Extraction of the residues of the iridium powder from the reaction chamber after the fluorination is accompanied by the characteristic smell of HF. It is extremely hygroscopic and immediately starts reacting with the moisture of the laboratory atmosphere, resulting in a wet appearing, violet-colored substance.

The residues of the third trial are completely soluble in water, leading to the formation of a violet solution. This behavior has been described for both, IrF_4 and IrF_5, it therefore seems likely, the residues being one of the two.

Despite its high chemical stability, the synthesis of its hexafluoride in the fluorination line is much more readily achieved than for platinum. A reason may be found in its lower electron affinity as shown in Table 2.3. The deposited IrF_6 in one of the cold traps is shown in Figure 6.44.

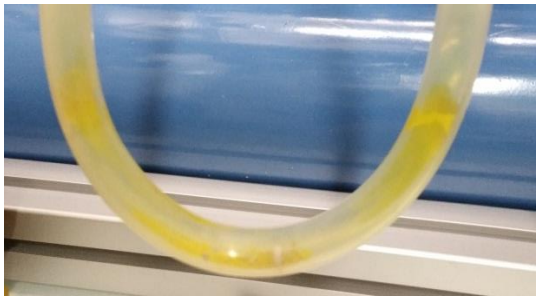

Figure 6.44: Deposited IrF_6 in the first cold trap using liquid nitrogen as a frigorific agent.

As no other hexafluoride, IrF_6 almost immediately starts to diffuse into the FEP cold traps if warmed to room temperature leaving them in a light purple color over the course of two days. Washing the cold traps with water directly after extraction of the hexafluoride only accelerates this process. However, IrF_6 could safely be stored at −45 °C for several months in a sealed FEP tube of the type shown in Figure 3.14. The FEP tube itself was thereby enclosed in a sealed stainless-steel container filled with argon.

6.7.3 UV/VIS spectroscopy

For the acquisition of its UV/VIS spectrum, IrF_6 was collected in the first cold trap and afterwards transferred via sublimation into the measuring cell. The sample was measured with a slit width of 0.5 nm for high resolution.

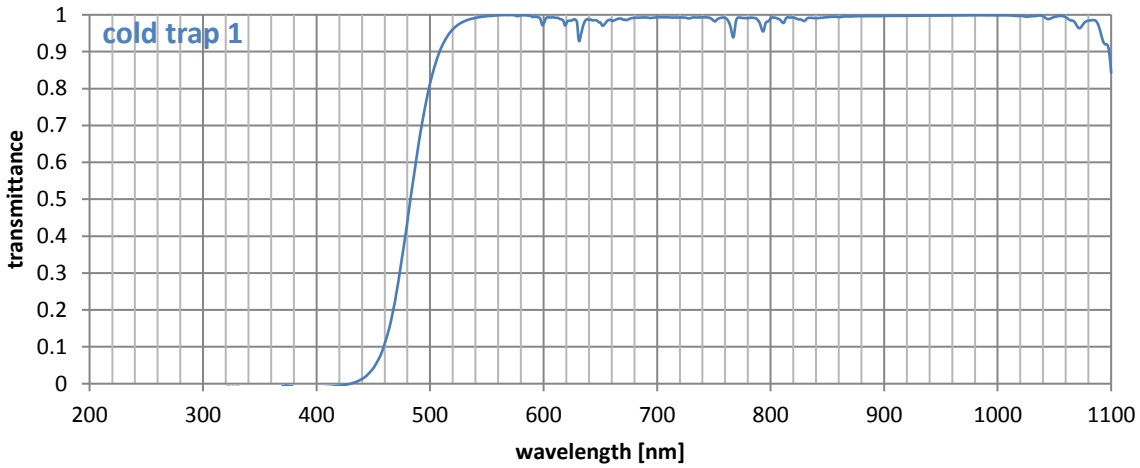

Figure 6.45: The UV/VIS spectrum of the content of first cold trap after fluorination of iridium, acquired using the measuring cell at a pressure of 76 mbar.

As expected from its color, IrF_6 shows strong absorption in the low visible wavelengths, especially below 440 nm. In addition, it possesses a rather rich absorption structure in the range between 570 and 860 nm. As was already the case for OsF_6, no true-to-scale spectrum was found in the accessible literature. Thus, also here, no overlay of experimental data and literature was performed.

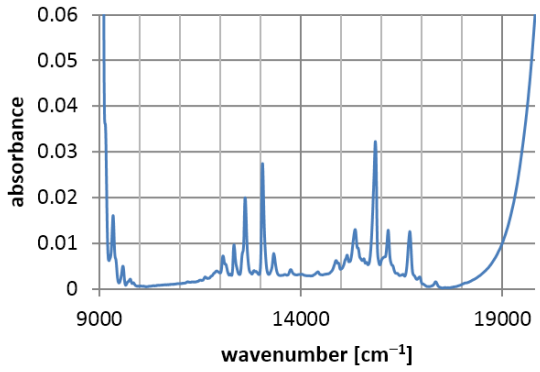

Figure 6.46: Section of the spectrum in Figure 6.45 containing the band positions in detail.

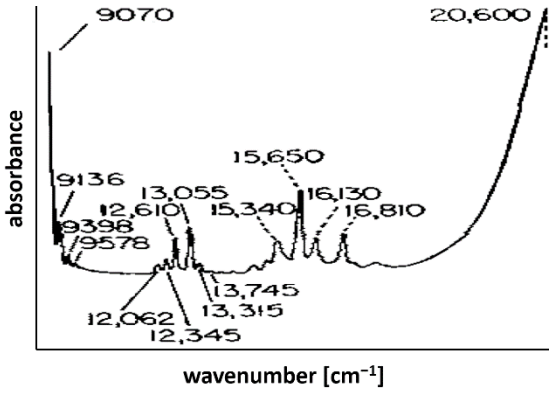

Figure 6.47: The absorption spectrum of iridium hexafluoride in the visible range [183].

All wavelengths assigned in Figure 6.47 may be also found in Figure 6.46, some with minor deviations. However, additional bands are also present and in part can also be identified in the spectrum taken from literature without having been assigned there. For example, the spectrum reported by Moffitt et al. shows at least two additional clearly distinguishable bands between 13745 and 15340 cm^{-1} that have not been indexed. It may therefore be concluded that it is not impurities that make up for these bands. An overview of all signals form literature and experimental data is given in the following Table 6.19.

Table 6.19: The bands of the UV/VIS spectrum as assigned by Moffitt et al. in [183] and Brand et al [191]. The last column lists the values found in the spectrum acquired during the course of this thesis, the third column the corresponding wavenumber for comparison with the data from literature.

Moffitt et al. wavenumber [cm^{-1}]	Brand et al. wavenumber [cm^{-1}]	corresponding wavenumber [cm^{-1}]	this work wavelength [nm]
–	–	17331	577
16810	–	16920	591
–	–	16694	599
16130	–	16155	619
15650	–	15822	632
15340	–	15337	652
–	–	15129	661
–	–	14859	673
–	–	14409	694
13745	12732	13736	728
13315	13321	13316	751
13055	13042	13038	767
12610	12605	12594	794
12345	12328	12330	811
12062	12051	12063	829
–	11609	11628	860
–	9759	9756	1025
9578	9579	9579	1044
9398	9393	9398	1064
–	9333	9337	1071
9136	9136	9141	1094
9070	9071	<9091	>1100

6.7.4 IR spectroscopy

IR spectroscopy was performed on the exact same sample, on which UV/VIS spectroscopy was performed as shown in Figure 6.45 and Figure 6.46. As this spectrum was already known from literature, it allowed the positive identification of the substance in the measuring cell to be IrF_6. However, due to the high reactivity of IrF_6 the question of its contamination with impurities arises. As an interesting finding, also the presence of UF_6 could be verified in the spectrum. This is remarkable, as no uranium has been fluorinated during the five preceding experiments. It seems as if small residues still present in the line have been converted back to UF_6 due to the by far higher fluorination potential of IrF_6.

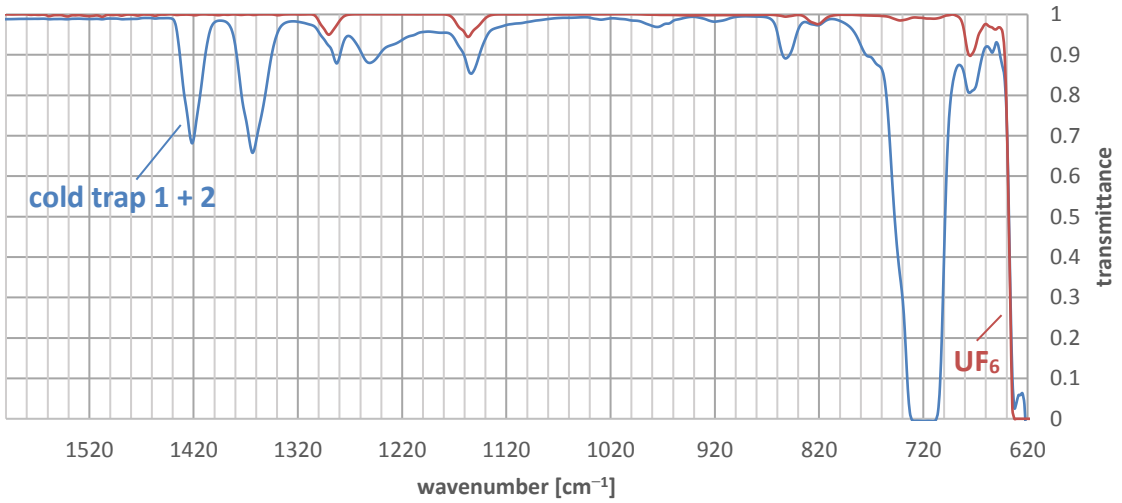

Figure 6.48: The IR spectrum of the content of the first two cold traps after the fluorination of iridium at a pressure in the measuring cell of 76 mbar (blue graph) and the spectrum of UF_6 at a pressure of 7.7 mbar (red graph).

The spectrum shown in Figure 6.49 was corrected by the subtraction of the UF_6 spectrum fitted on its band at 854 cm^{-1}, corresponding to a pressure of UF_6 of 7.7 mbar. Its comparison with the IR spectra of other hexafluorides preceding the fluorination of iridium did not show any conformity.

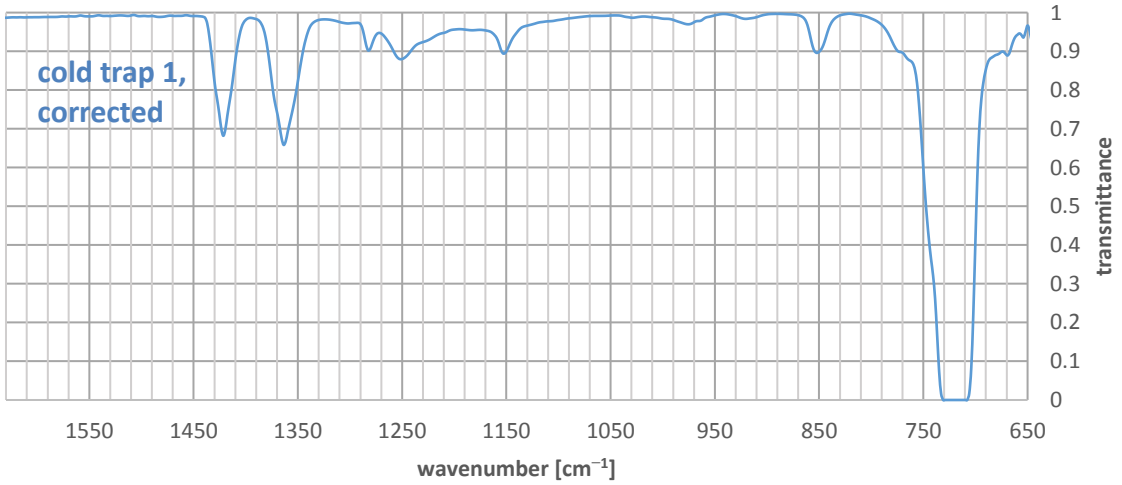

Figure 6.49: The IR spectrum of iridium hexafluoride IrF_6 at a pressure of 68 mbar. The background correction of the spectrum is based on its region between 2600 and 3100 cm^{-1}, as no absorption is observed in that part of the spectrum.

The fundamentals ν_1 to ν_6 of IrF_6 have been reported by Claassen et al. to be found at 702 (ν_1), 645 (ν_2), 719 (ν_3), 276 (ν_4), 267 (ν_5) and 206 cm^{-1} (ν_6) [116]. Many of the binary combination bands may be assigned based on these positions. Especially the prominent ($\nu_2 + \nu_3$) and ($\nu_1 + \nu_3$) combinations are found at the expected positions. However, indications of a more detailed structure are visible in Figure A.49, probably due to a splitting in P and R branches.

The region between 950 and 1300 cm^{-1} shows a number of additional bands. However, these cannot be assigned based on the fundamental mentioned above. Table 6.20 lists the calculated positions and the ones found during the course of this thesis.

Table 6.20: Comparison of the positions of the bands in the IR spectrum of IrF_6 found during this work and calculated based in the fundamentals reported by Claassen et al. [116].

assignment	calc. from Claassen wavenumber [cm^{-1}]	this work wavenumber [cm^{-1}]
ν_3	719	720
$\nu_2 + \nu_6$	851	851
$\nu_2 + \nu_4$	921	919
$\nu_1 + \nu_4$	978	963
$\nu_3 + \nu_5$	986	976
–	–	999
–	–	1031
$\nu_1 + \nu_5 + \nu_6$	1175	1151
$2\nu_1 - \nu_6$	1198	1183
–	–	1227
–	–	1251
$\nu_3 + 2\nu_4$	1271	1282
$\nu_2 + \nu_3$	1364	1362
$\nu_1 + \nu_3$	1421	1422

6.7.5 Raman spectroscopy

Raman spectroscopy was performed on a sample in the liquid phase extracted from the first cold trap synthesized during the second experiment using a laser wavelength of 532 nm. The corresponding spectrum and the comparison with literature is shown in Figure 6.50. The reference spectrum was reported by Rotger et al. on IrF_6 in the gas phase [192].

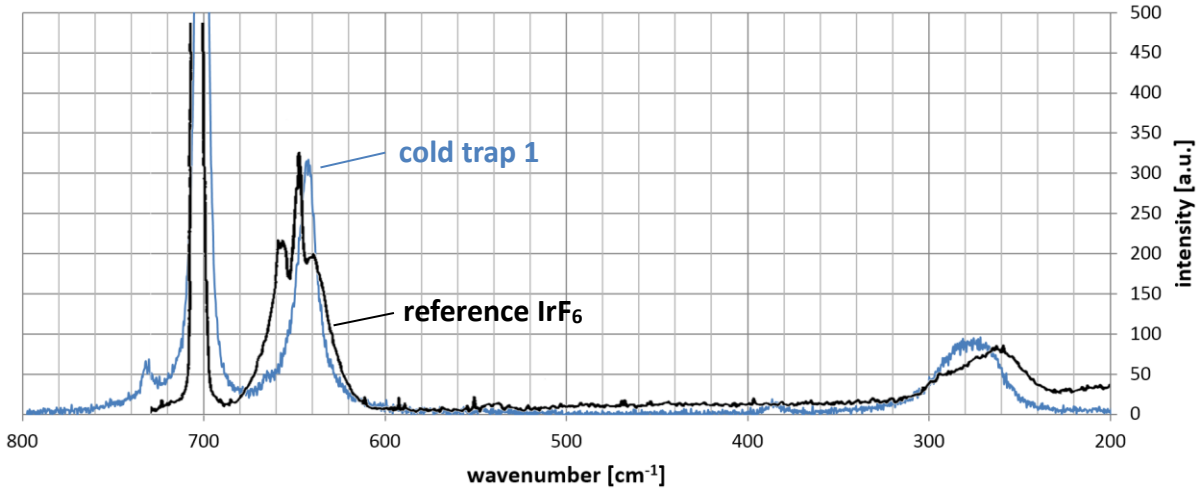

Figure 6.50: Raman spectra of the content of the first cold trap of the third experiment measured at a laser wavelength of 532 nm and a groove density of 1800 g/mm (blue graph). Reference data of IrF_6 was reported by Rotger et al. [192] (black graph).

The Raman spectrum of IrF_6 shows the presence of the three fundamental vibrations ν_1, ν_4 and ν_5. These show no signs of underlying structure, even if measured at a high resolution. In addition, no signs of overtones are present. The decomposition of the spectrum is depicted in Figure A.51 to Figure A.53.

As has been the case before for OsF_6, also for IrF_6 the position of the ν_1 fundamental is in very good accordance with the value previously reported, but shows increasing deviations with smaller wavenumbers.

Table 6.21: Comparison of the fundamental bands of IrF_6 reported by Rotger et al. [192] as well as Claassen et al. with the positions determined during the experiments of this thesis. Rotger reports the wavenumber of the first overtone of the ν_4 fundamental found by Claassen to be 542 cm^{-1} in [192]. However, Claassen reports the position of the fundamental itself at 276 cm^{-1} in [116], the first overtone evaluating to 552 cm^{-1}.

assignment	Claassen et al. wavenumber [cm^{-1}]	Rotger et al. wavenumber [cm^{-1}]	this work wavenumber [cm^{-1}]
ν_5	267	265.2	277.6
$2\nu_4$	542 (552)	540.0	–
ν_2, P	–	639.7	–
ν_2, Q	645	647.3	643.2
ν_2, R	–	656.7	–
ν_1	701.7	701.1	701.6

6.7.6 NMR spectroscopy

NMR spectroscopy has been performed on the two samples that have also been investigated using Raman spectroscopy. Thus, the presence of IrF_6 has been verified before. IrF_6 has barely been investigated using NMR spectroscopy. Seppelt and Bartlett report a "very broad signal hard to observe" at −205 ppm with respect to $CFCl_3$ [185]. As this region overlaps with the signal from the FEP tube and the glass tube (see Figure 3.17), which cannot quantitatively be subtracted from the IrF_6 signal, it is not possible to confirm their observation.

An additional signal is observed at 1086 ppm with respect to $CFCl_3$. Its origin is unknown as no substance found in literature creates a signal at this chemical shift. However, it has been found in the spectrum of both, the second as well as the third experiment as shown in Figure 6.51 and Figure 6.52. This signal has also not been observed in any previous measurements of the other hexafluorides. Quantum chemical calculation could help to determine, whether a signal in this region is to be expected for IrF_6.

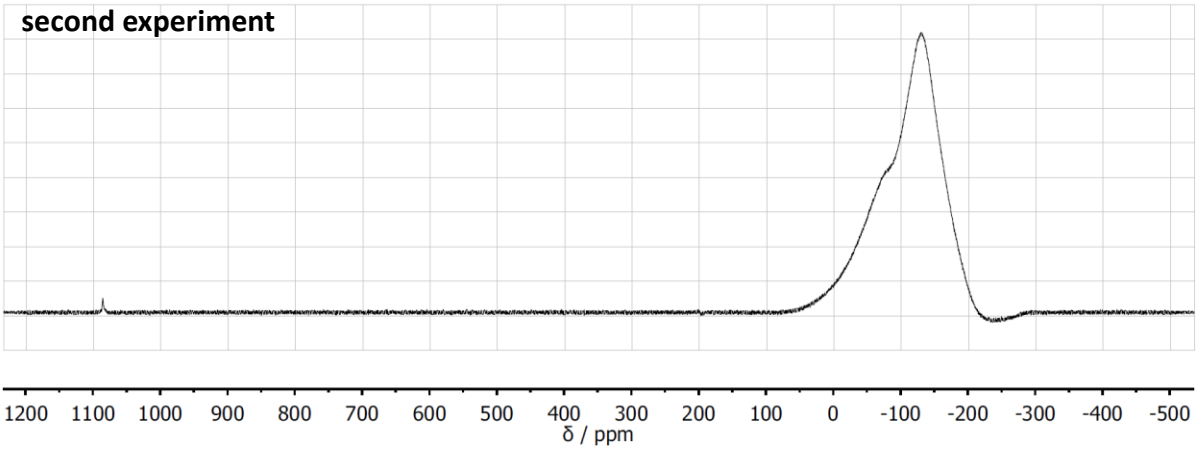

Figure 6.51: The NMR spectrum of IrF_6 synthesized during the second experiment.

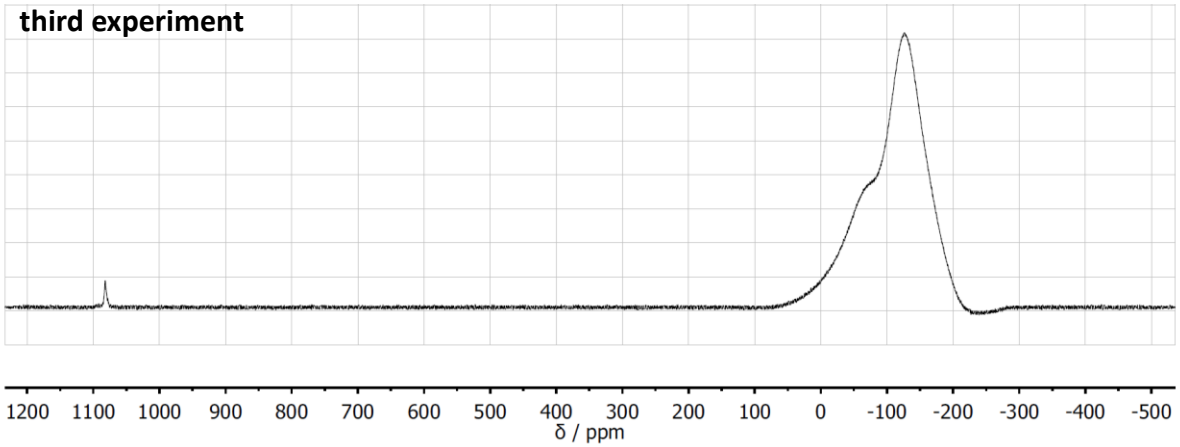

Figure 6.52: The NMR spectrum of IrF_6 synthesized during the third experiment.

6.8 Platinum

6.8.1 General aspects of platinum and its fluorides

Platinum is a precious metal and eponymous for a group of itself and five further precious metals (ruthenium, rhodium, palladium, osmium, iridium), which together are the constituents of the platinum metal group. It is a grey-white and ductile metal with rather low hardness. Platinum is soluble in aqua regia and in HCl in presence of air. It is attacked by HNO_3 only above 100 °C [105]. Platinum has the electron configuration [Xe] $4f^{14}5d^{9}6s^{1}$ and therefore prefers oxidation state +IV, although +II is also quite common. Platinum forms three known thermodynamically stable fluorides, which are listed in Table 6.22 [147].

Table 6.22: Physico-chemical properties of the thermodynamically stable binary fluorides of platinum [43,105,149].

	PtF_4	PtF_5	PtF_6
molar mass	271.1 g/mol	290.1 g/mol	309.1 g/mol
melting point	600 °C	80 °C	61.3 °C
boiling point	–	–	69.1 °C
appearance (SATP)	brownish-yellow solid	deep red solid	deep red solid

PtF_4 is a yellow-brown solid at room temperature. Sharpe proposed a synthesis starting from $PtCl_4$ and reacting it with BrF_3. By evaporating the resulting red solution in vacuo and subsequently heating the precipitate to 180 – 200 °C, contaminated PtF_4 is formed [156]. Bartlett reports, additional evacuation and heating are able to remove the remaining BrF_3 contamination [193]. As reported by Ruff, PtF_4 quickly decomposes in an exothermic reaction into platinum dioxyhydrate and hydrofluoric acid when exposed to water [194].

PtF_5 is a deep red solid at room temperature. It is prepared by reacting $PtCl_2$ with fluorine at 350 °C. Three parts fluorine were thereby slightly diluted with one part nitrogen. PtF_5 under vacuum disproportionates at 130 °C into PtF_4 and PtF_6 [193]. PtF_5 is a highly reactive species reported to be able to oxidize water to oxygen [105]. It reacts exothermally with water, partly yielding platinum dioxide as a precipitate, whereas the remainder forms the hexafluoridoplatinate [193].

PtF_6 is an extremely reactive species able to oxidize oxygen and even xenon. In fact, the first compounds with a noble gas, a variety of xenon hexafluoridoplatinates $Xe(PtF_6)_x$ with $1 \leq x \leq 2$, were synthesized by Bartlett using PtF_6 as an oxidizing agent [195,196]. The synthesis of PtF_6 is challenging and involves the electric heating of a platinum wire under fluorine atmosphere in a brass device, whose walls are cooled with liquid nitrogen. The heat of formation of PtF_6 is negative [197], the reaction therefore is self-sustaining, once the ignition temperature of the Pt wire is reached. As the heat of formation of PtF_4 is larger than for PtF_6 [198], the formation of the former is favored at lower temperatures. PtF_6 exposed to water leads to the formation of fluoroplatinic acid and elemental oxygen [198].

6.8.2 Reaction conditions

Three trials have been performed investigating the fluorination of platinum. As its resistance to fluorination had already been observed before, in a first experiment a different approach introduced platinum silicide PtSi produced in an arc melting furnace. As silicon reacts easily with fluorine forming SiF_4, it was hoped to thereby improve the etching behavior. For the second and third experiment, platinum was introduced to the fluorination line as a fine powder. This powder was produced by Chempur Feinchemikalien und Forschungsbedarf GmbH, had a metal-based purity of 99.9 % and a mesh size of 60 micron.

Table 6.23: Basic conditions of the etching experiments with platinum as a substrate material.

Exp. No.	sample mass [mg]	Ar [sccm]	NF_3 [sccm]	time [min]	residual mass [mg]	reaction yield [%]	etching rate [mg/min]
1	932.4	6	2	90	932.2	0.0	–
2	357.8	0 – 100	2 – 100	188	369.8	–	–
3	254.0	0	15	62	–	–	–

The first approach using PtSi was unsuccessful, as also in this case no significant reduction in mass could be observed. In addition, the slug did not lose its metallic luster. However, it seems possible, that higher contents of silicon might induce a reaction. This possibility was not investigated further.

For the second experiment, a pure argon plasma was applied for 65 minutes without additional heating at a volume flow of 100 sccm, followed by the application of a hydrogen plasma for 300 minutes at a set temperature of 150 °C and an average volume flow of 300 sccm. The intention of this routine was the removal of a potential oxide layer, that might have been present on the platinum powder. The actual fluorination took place at an NF_3 : Ar ratio of 2.0 sccm : 8.0 sccm for 120 minutes, subsequently raised to 54.0 sccm : 10.0 sccm for 45 minutes. No additional heating was performed during the fluorination. Also during this experiment, platinum showed great resistance to fluorination. Sparking of the particles or glowing could not be observed at any moment.

The third experiment was performed at a constant volume flow of NF_3 of 15 sccm for 62 minutes with no carrier gas. The reaction chamber was externally heated to 200 °C. No pre-treatment of the substrate such as hydrogenation was performed. As the substrate was directly transferred into a glovebox after fluorination, no mass measurements could be performed.

Figure 6.53: Platinum powder after fluorination for 150 minutes at an elevated temperature of 190 °C. Although there is no change in appearance under the microscope, the powder agglomerates much easier.

Figure 6.54: Residues of platinum, possibly PtF_4, after removal of the powder.

The removal of the powder from the reaction chamber for both, the second and the third experiment, is accompanied by the strong smell of hydrogen fluoride. During the second trial with hydrogen pretreatment as described above, the removal of the powder shows the presence of an ocher-brownish residue adhering to the Monel carrier, as seen in Figure 6.54. This substance was only present, where the platinum stood in direct contact to the Monel carrier. Unfortunately, the opportunity to perform XRPD analysis on this compound was missed. However, due to its color it is believed to be PtF_4. Visual inspection of the residues of the third experiment does not reveal any difference in the superficial appearance except for an easier agglomeration of the powder; it seems to be stickier. Aside from its increased tendency for agglomeration, the optical appearance of the residual substrate differed between the various experiments. At trials without hydrogen pretreatment and lower temperatures, the entire powder still had a silvery appearance. However, the Monel carrier showed black spots, where it stood in contact with the platinum powder.

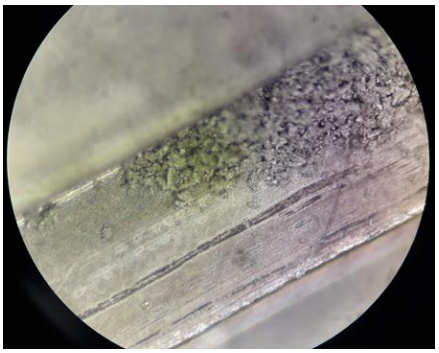

Figure 6.55: Sample of platinum powder before fluorination.

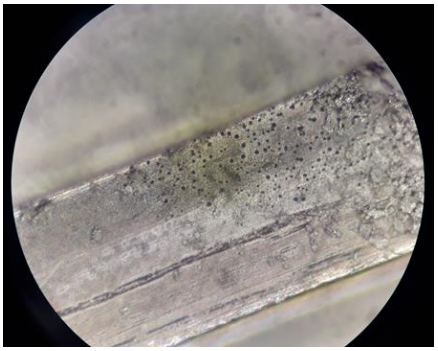

Figure 6.56: Sample of platinum powder after fluorination for 50 minutes. The Monel boat shows black spots, where it had contact to platinum.

The observations match well with an effect known as atomic fluorine spillover. This phenomenon has been known for more than 50 years and was studied in detail for nickel and platinum by Chilingarov et al. in [199]. There, they placed a Pt plate on a weakly fluorinated Ni plate and exposed this arrangement to elemental fluorine obtained by the thermal decomposition of TbF_4. They observed the diffusion of atomic fluorine over the surface of the weakly passivated Ni plate towards the Pt plate, where over several hours a thin layer of Pt_2F_6-PtF_4 was formed. These observations are similar to the ones during the plasma fluorination and as Ni is a major constituent of Monel, the underlying mechanism might by similar in nature.

All of the following analysis refers to the platinum powder of the third experiment that appeared to be unchanged during the reaction. A detailed microscopic examination of the platinum, before and after exposition in the fluorination line shows a reduction of the average particle size (see Figure 6.57 and Figure 6.58). The sample was stored in a glass vial under ambient atmosphere for several days prior to examination. The glass showed to be significantly etched, especially but not exclusively, where it stood in direct contact to the powder. Both images were acquired using optical microscopy and combining a number of images with different focal planes in order to sharply display all particles. A loss of particles during the evacuation process seems unlikely, as it was performed very slowly and carefully. In addition, the powder agglomerates much easier, keeping the particles together. Last, the smaller and therefore lighter particles would be expected to be lost first, if the gas flow during the evacuation was the underlying cause.

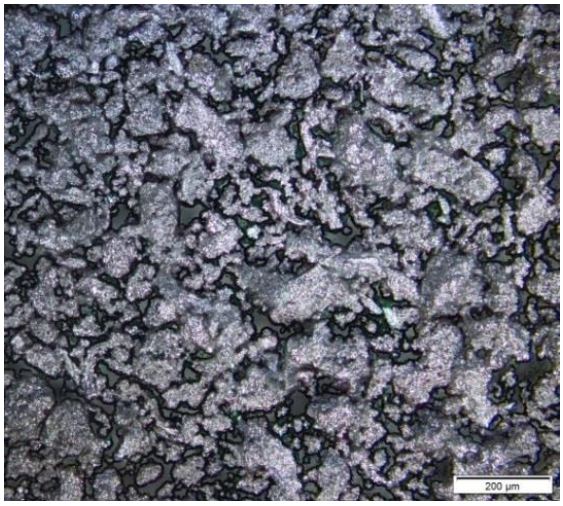

Figure 6.57: Sample of platinum powder before fluorination. The image was taken as a z-stack in order to maintain a continuous focus.

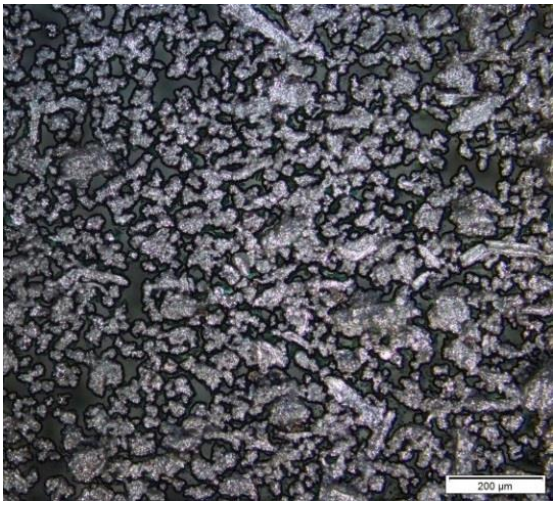

Figure 6.58: Sample of platinum powder after fluorination for 50 minutes. The average grain size decreased. The image was taken as a z-stack in order to maintain a continuous focus.

XRPD was performed on the overhead part of the remaining powder, which reveals the presence of elemental platinum, as expected. For this analysis, the substrate was removed from the fluorination line under Ar counter flow and under protective Ar atmosphere deposited on Scotch tape. Aside from Pt, additional reflections are initially also present (blue arrows in Figure 6.59). However, these reflections vanish, if the sample is measured for a longer period of time. The reflections cannot be assigned, as they are not found in the WinXPOW database [200]. They explicitly do not belong to neither PtF_6 nor PtF_4.

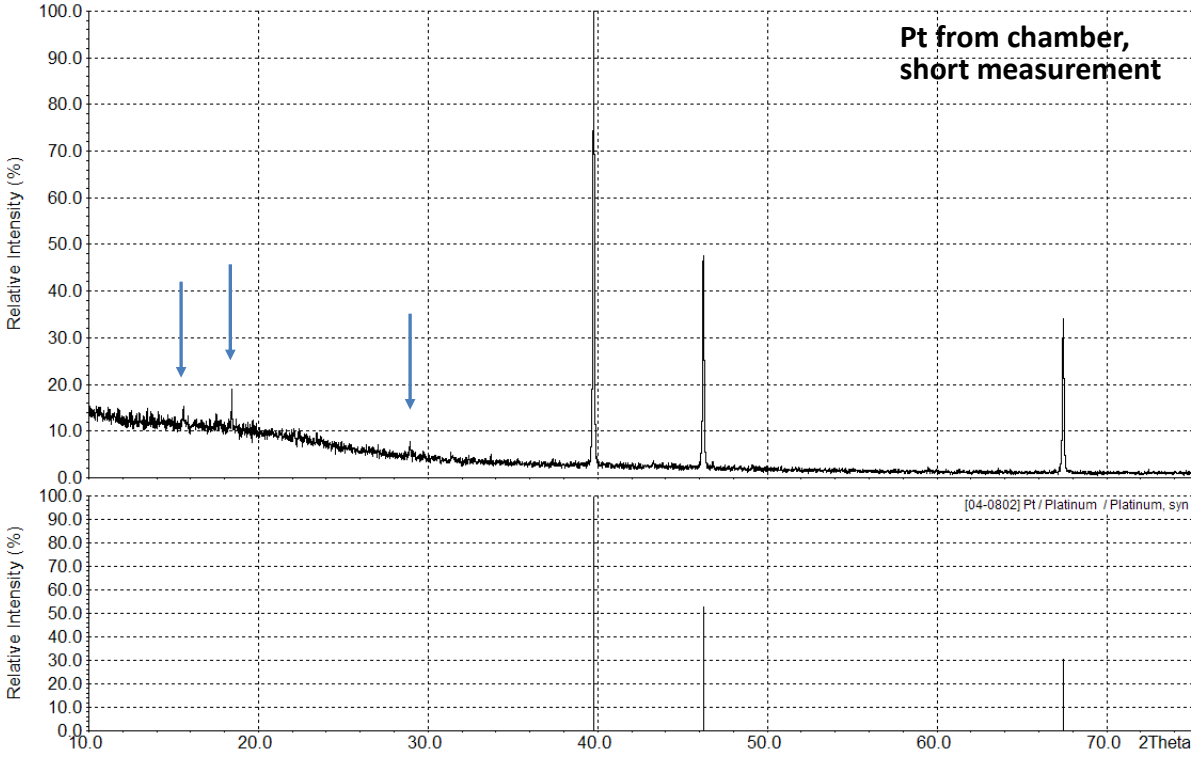

Figure 6.59: X-ray powder diffractogram of platinum powder from the reaction chamber after fluorination, step size 5°, measuring time per step 10 s, resulting in a total measurement time of 4 minutes.

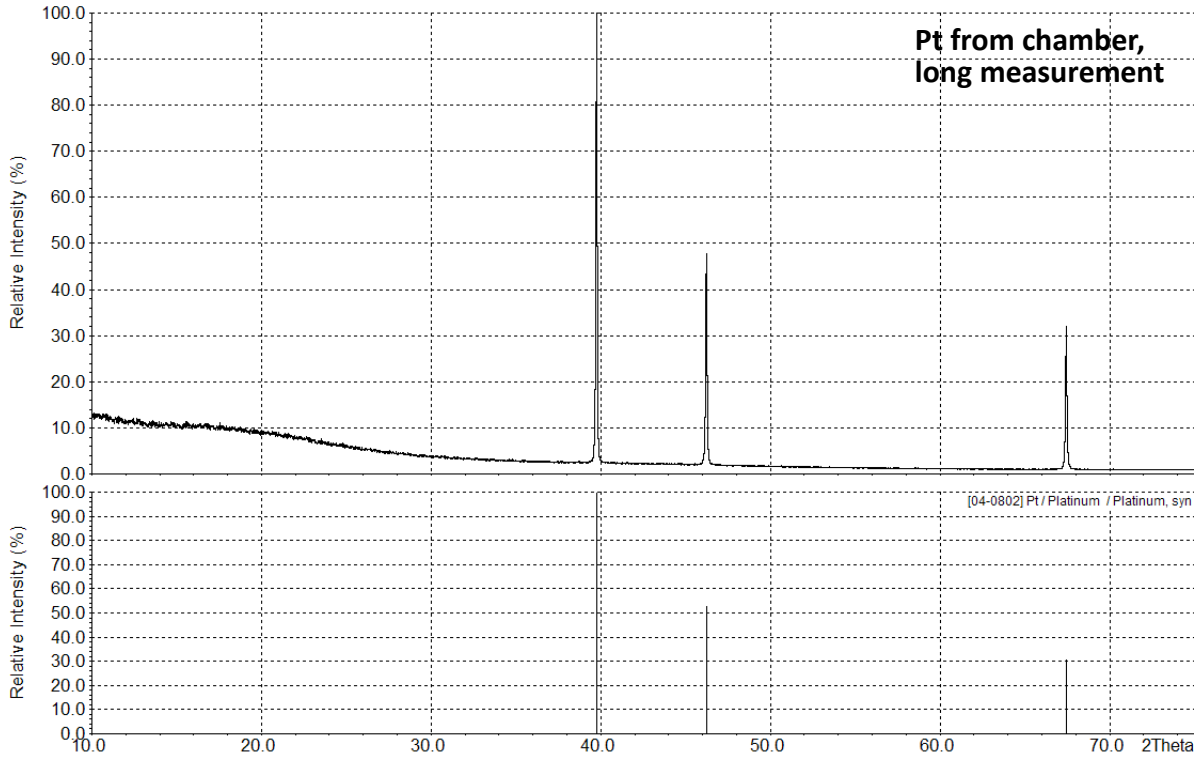

Figure 6.60: X-ray powder diffractogram of platinum powder from the reaction chamber after fluorination, step size 2°, measuring time per step 180 s, resulting in a total measurement time of 131 minutes. The sample is the same as in Figure 6.59 and was neither altered nor removed in-between the two measurements.

Dumping of the residual powder into water leads to the formation of an acidic yellow-brownish solution with pH ≈ 1. The solution is decanted and a fibrous and spongy precipitate settles on the ground of the container overnight, whereas the solution loses part of its color. XRPD of the precipitate was unsuccessful; the substance seems to be amorphous.

Figure 6.61: Yellow-brownish solution above the Pt powder after fluorination when exposed to water.

Figure 6.62: Settling of an orange precipitate from the solution overnight at concurrent decolorization of the solution.

Lohmann in his thesis [201] describes PtF_4 to quickly dissolve in water forming a yellow-brownish solution. This solution is unstable and decomposes over time into HF and the hydrated dioxide of platinum, which is described by him as being of orange color. However, the actual color of the hydrate depends on its water content and has also been described by Wöhler as brown or deep black [202]. In general, the observations of Lohmann are in good agreement with the ones described above, so it seems likely that also in that case PtF_4 was originally formed during the fluorination process.

The UV/VIS spectrum of the decanted solution shows two distinct absorption bands at 272 and 318 nm. According to Clark and Perros [203], hexafluoridoplatinic acid $H_2[PtF_6]$, shows two distinct absorption bands in the UV/VIS region at 275 and 318 nm, respectively.

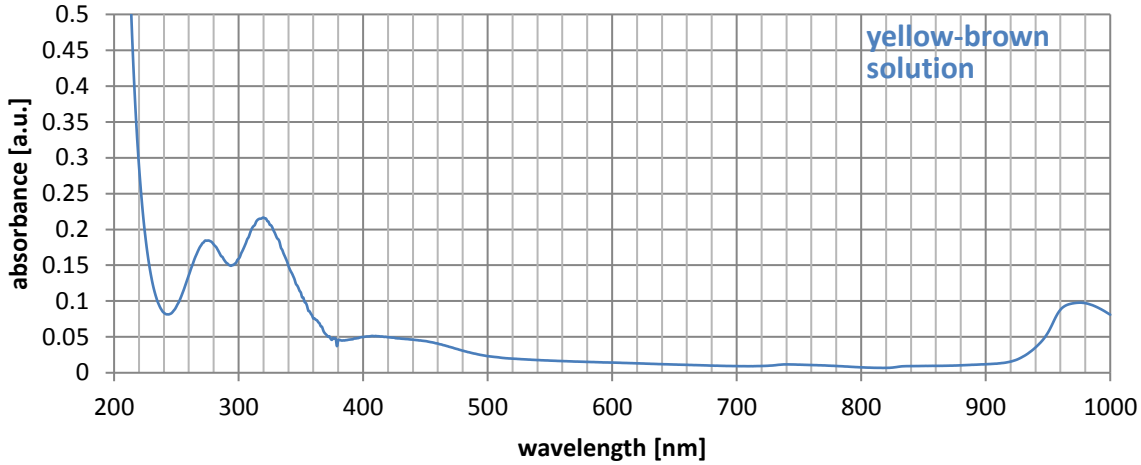

Figure 6.63: UV/VIS spectrum of the solution acquired by putting the residues from the holder into water. Measured in a quartz cuvette.

Furthermore, the decanted solution was concentrated with HCl and afterwards diluted ammonia solution was added, resulting in a yellowish powder. XRPD on this powder revealed it to be ammonium hexachloridoplatinate(IV) $(NH_4)_2[PtCl_6]$.

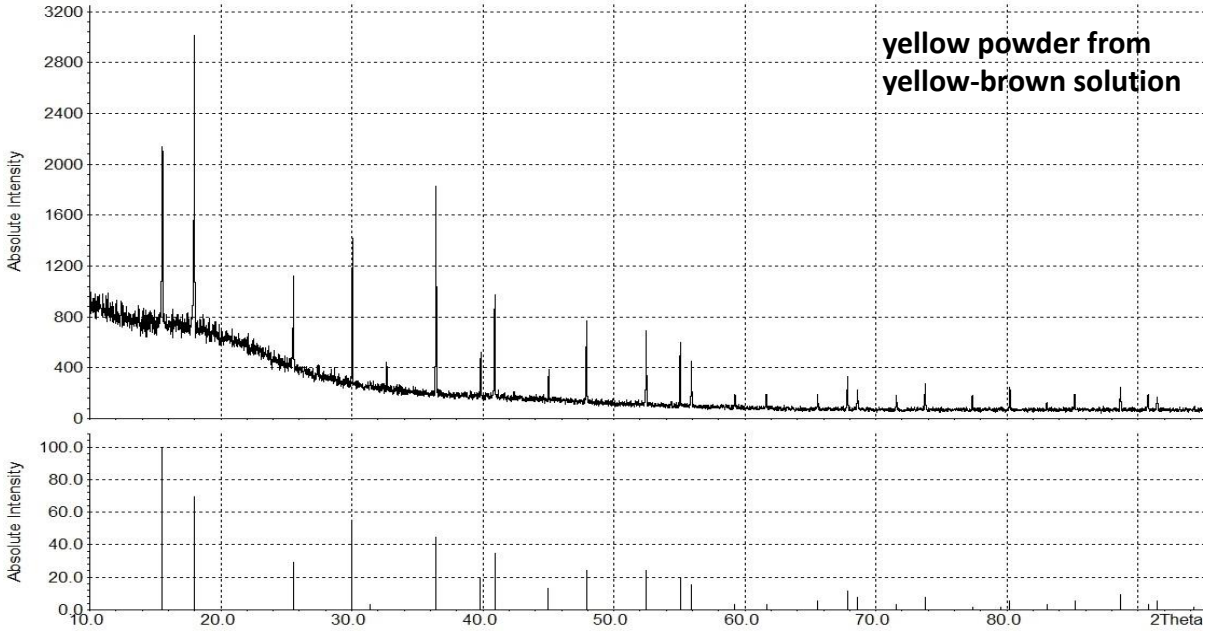

Figure 6.64: X-ray powder diffractogram of ammonium hexachloridoplatinate(IV) $(NH_4)_2[PtCl_6]$.

It may therefore by concluded the yellow solution being $H_2[PtF_6]$. The following reactions are proposed in order to explain the findings. During the fluorination process, a thin layer of PtF_4 was formed on the surface of the platinum particles. As a hygroscopic compound, it extracts humidity from the air, forming a surface layer of platinum oxide hydroxide $PtO_2 \cdot n\,H_2O$ according to equation (52) as proposed by Lohmann, leading to the increased tendency for agglomeration of the powder.

$$PtF_4 + 3\ H_2O \rightarrow PtO_2 \cdot 2\ H_2O + 4\ HF \quad (52)$$

If dumped into water, in addition to equation (52) in the presence of HF, PtF_4 may form $H_2[PtF_6]$, according to equation (53):

$$PtF_4 + 2\ HF \rightarrow H_2[PtF_6] \quad (53)$$

As all observations may be explained without the presence of PtF_6, it seems questionable, whether it is formed under the present conditions.

6.9 Tellurium

6.9.1 General aspects of tellurium and its fluorides

Tellurium was the only main group element investigated. The fluorination behavior of its lighter congeners sulfur and selenium was not studied due to their ability to form large polymeric molecules. The use of SF_6 as a precursor in plasma etching is known for its potential to contaminate components with difficult-to-remove polymeric residues (also see chapter 4.1.2). The fluorination behavior of tellurium is also of major relevance for the separation process as the amount produced during the fission process amounts to almost 30 wt% of the produced molybdenum.

Tellurium as its crystalline allotrope is a brittle metalloid with lustrous, silvery-gray appearance. It is chemically stable on air and is not attacked by non-oxidizing acids. Nitric acid, sulfuric acid and aqua regia easily dissolve crystalline tellurium already at low temperatures [204]. Tellurium is a chalcogen with the electron configuration [Kr] $4d^{10}5s^25p^4$ and therefore prefers oxidation state –II, +IV and +VI. Thus, two thermodynamically stable binary fluorides of tellurium are known, tellurium tetrafluoride TeF_4 and tellurium hexafluoride TeF_6. There is some debate about the existence of Te_2F_{10}, whose successful characterization was first claimed by Campbell and Robinson [205]. However, Watkins doubts the reported compound to be Te_2F_{10} and instead suspects it to be $Te_2F_{10}O$ [206]. The physico-chemical properties of TeF_4, TeF_6 and the proposed Te_2F_{10} are listed in Table 6.24.

Table 6.24: Physico-chemical properties of the binary fluorides of tellurium [204,205].

	TeF_4	Te_2F_{10}	TeF_6
molar mass	203.6 g/mol	445.2 g/mol	241.6 g/mol
melting point	129 °C	−33.7 °C	−38.4 °C
boiling point	195 °C (dec.)	59 °C	−38.2 °C (subl.)
appearance (SATP)	colorless needles	colorless liquid	colorless liquid

TeF_4 is a white solid at room temperature. It is synthesized by an endothermic reaction of TeF_6 with elemental Te at 180 °C over a period of 100 hours. TeF_4 is hygroscopic and reacts to TeO_2 and HF if exposed to water [207].

The compound proposed by Campbell et al. as T_2F_{10} is a colorless liquid at room temperature. It is prepared by reacting oxygen-diluted fluorine with mixtures of Te and TeO_2. As this compound could only be obtained in the presence of TeO_2, whereas reactions in complete absence of oxygen yielded TeF_4 and TeF_6 instead, the formation of an oxyfluoride seems more likely [206].

TeF_6 is a colorless liquid and may be synthesized from the elements already at ambient temperature [204]. It hydrolyses in the presence of water into telluric acid [204].

6.9.2 Reaction conditions and evaluation

Only one etching experiment investigated the fluorination behavior of tellurium using Te chunks. The tellurium used was produced by Alfa Aesar and according to the producer possessed a purity of 99.999 %.

Table 6.25: Basic conditions of the etching experiment using tellurium as a substrate material. The volume flow of NF_3 and Ar was kept constant the entire time.

Exp. No.	sample mass [mg]	Ar [sccm]	NF_3 [sccm]	time [min]	residual mass [mg]	reaction yield [%]	etching rate [mg/min]
1	552.0	8.0	8.0	35	0.0	100.0	15.8

Tellurium is easily fluorinated, even if presented in a solid form. Here, good etching results were achieved with an NF_3 : Ar ratio of 8.0 sccm : 8.0 sccm, resulting in an average etching rate of 15.8 mg/min and a utilization of NF_3 of 70 %. No additional heating of the samples proved to be necessary.

Figure 6.65: Tellurium chunks on a Monel boat before fluorination. Total mass of this sample is 552 mg.

Figure 6.66: Residues after fluorination. The reaction is complete, the residing mass within the limits of the accuracy of the scale.

The reaction product was collected in the first cold trap using liquid nitrogen as a frigorific agent. It is highly volatile and starts evaporating shortly after the LN_2 cooling has been removed.

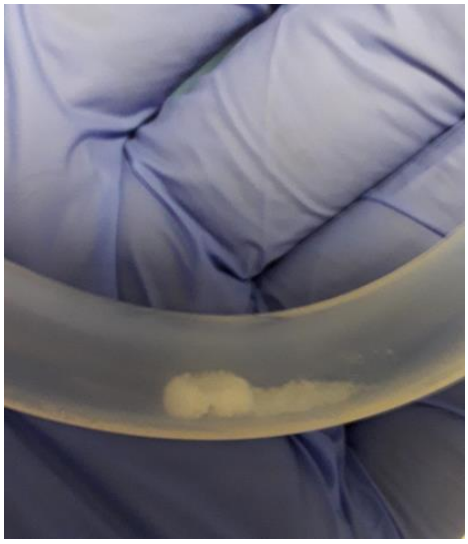

Figure 6.67: Deposition of tellurium hexafluoride in the first cold trap using LN_2 as a frigorific agent.

6.9.3 UV/VIS spectroscopy

The content of the first cold trap was transferred into the measuring cell and investigated via UV/VIS spectroscopy. The spectrum shows a steep flank in the region of 200 nm with a maximum around 298 nm followed by a local minimum around 400 nm.

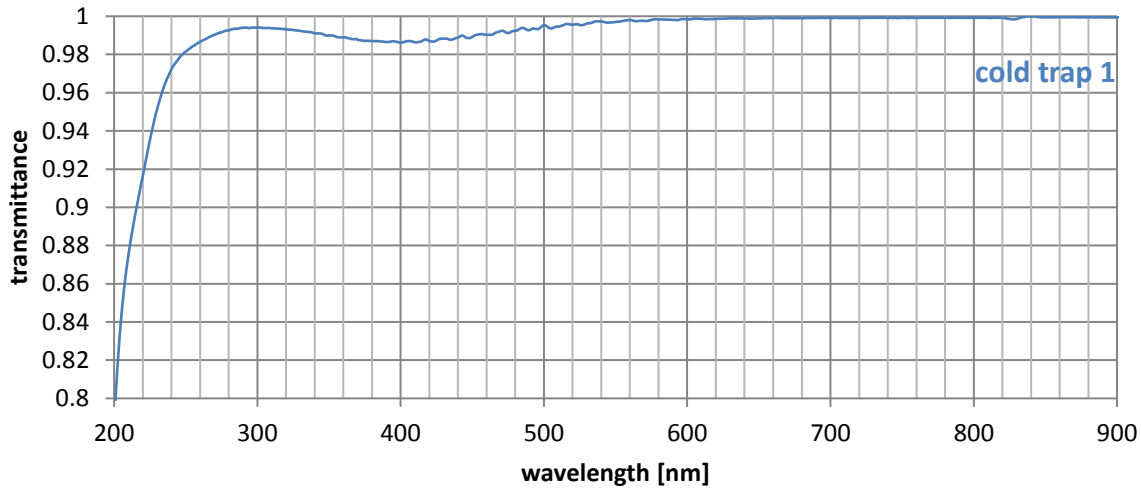

Figure 6.68: UV/VIS spectrum of the content of the first cold trap after fluorination of tellurium. Pressure in the measuring cell was 90.6 mbar.

A detailed examination shows this macrostructure superimposed by an oscillation with a wavelength between 11 and 14 nm.

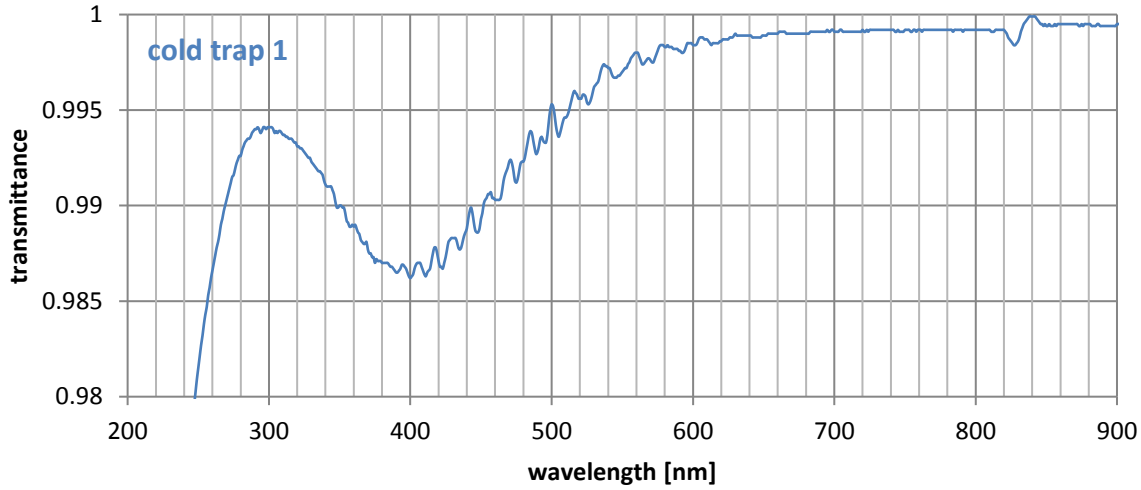

Figure 6.69: Detailed view of the of the spectrum depicted in Figure 6.69.

6.9.4 IR spectroscopy

IR spectroscopy was performed on the same sample as UV/VIS spectroscopy. The corresponding spectrum is shown in Figure 6.68. It shows the ν_3 fundamental as the strongest signal to be found at approximately 751 cm^{-1}. The precision of the position must be considered rather poor, as only the flanks of the band could be used for its determination.

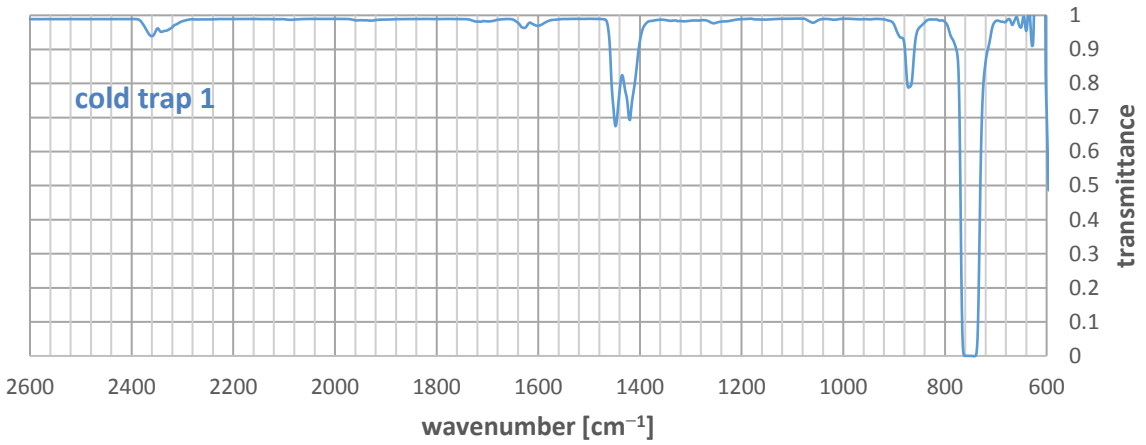

Figure 6.70: IR spectrum of the content of the first cold trap at a pressure of 90.6 mbar acquired with the measuring cell.

The (ν_2 + ν_6) combination band reported by McDowell at 871 cm^{-1} may be resolved into its three branches at 866, 873 and 890 cm^{-1}. As for the other hexafluorides the ($\nu_2 + \nu_3$) and ($\nu_1 + \nu_3$) combination bands are very prominent and lie comparably close together. Several weaker bands are also present but have not been assigned in literature. They will therefore not be treated here any further.

All determination of the position of the bands and their potential decomposition are depicted in Figure A.54 to Figure A.57.

Table 6.26: Observed bands for the IR spectrum of TeF_6 by McDowell et al. [208] and of this work based on the IR spectrum depicted in Figure 6.70.

assignment	McDowell et al. wavenumber [cm^{-1}]	this work wavenumber [cm^{-1}]
ν_3	753	751
$\nu_2 + \nu_6$, P	–	866
$\nu_2 + \nu_6$, Q	871	873
$\nu_2 + \nu_6$, R	–	890
$\nu_3 + \nu_5$	1060	1060
$\nu_2 + \nu_3$	1420	1420
$\nu_1 + \nu_3$	1449	1448

6.9.5 Raman spectroscopy

Raman spectroscopy was performed on a liquid sample of the first cold trap in an FEP tube at ambient temperature under intrinsic pressure using a laser wavelength of 532 nm and a groove density of 1800 g/mm.

In comparison with the spectrum reported by Claassen et al. [116], who measured TeF_6 in the gas phase, only four bands may be observed with certainty. These four bands are the three fundamentals ν_1, ν_2 and ν_5. As distinguished from previous works only reporting one signal around 700 cm^{-1} for TeF_6, this fundamental actually splits into two branches peaking at 696.5 as well as 699.7 cm^{-1}. The position of the other two very weak combination bands may not precisely be determined. The band reported at 394 cm^{-1} is in direct vicinity of the band at 396 cm^{-1} belonging to FEP. The band at 626 cm^{-1} may not be resolved at all. The original spectrum without the overlay of literature and FEP data is depicted in Figure A.58.

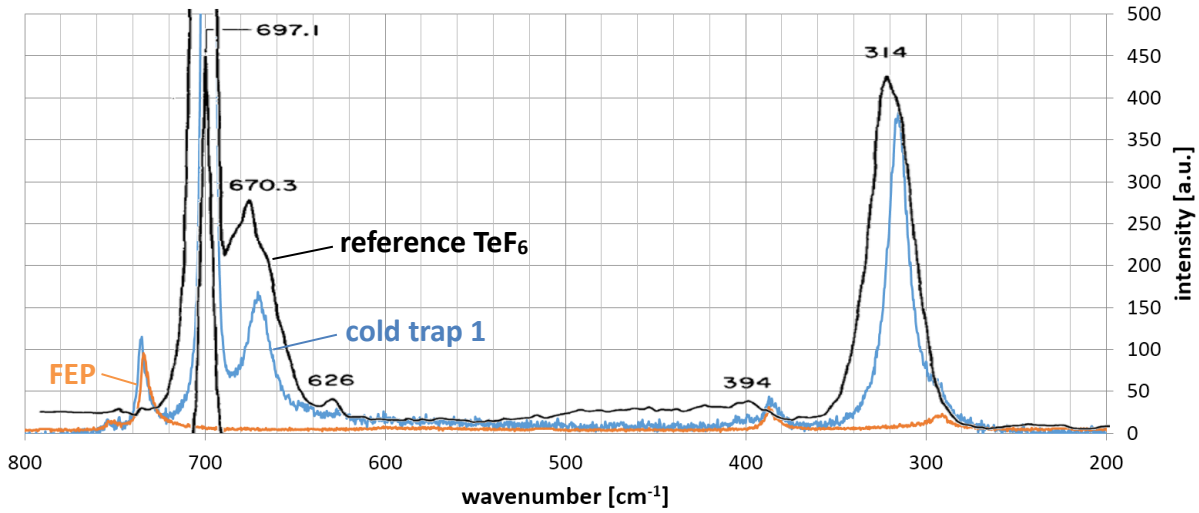

Figure 6.71: Raman spectrum of the content of the first cold trap at 22 °C under intrinsic pressure (blue graph). Underlying are the Raman spectrum of FEP (orange graph) and for comparison with literature the Raman spectrum of TeF_6 gas at 23 °C and 1 bar (black graph) [116].

The determination of the exact position of the peaks was performed stepwise using pseudo-Voigt profiles and is depicted in Figure A.59 and Figure A.60.

Table 6.27: Comparison of the fundamental bands reported by Claassen et al. [116] with the positions determined during the experiments of this thesis.

assignment	Claassen et al. wavenumber [cm^{-1}]	this work wavenumber [cm^{-1}]
ν_5	314	315.5
$2\ \nu_5$	626	–
$2\ \nu_6$	394	–
ν_2	670.3	670.7
ν_1, P	697.1	696.5
ν_1, R	–	699.7

6.9.6 NMR spectroscopy

Tellurium has five stable isotopes and an additional three unstable isotopes. However, out of these, the shortest-lived has a half-life of $9.2 \cdot 10^{16}$ years. With an atomic number of 52, the number of protons is even and only odd-numbered isotopes carry spin other than zero and are therefore NMR active. This is the case for ^{123}Te and ^{125}Te, which both carry spin I = ½.

NMR spectroscopy was performed on liquid TeF_6 in an FEP tube at ambient temperature under intrinsic pressure, the exact same sample used for Raman spectroscopy. The corresponding spectrum is shown in Figure 6.72. The main signal is found at −57.0 ppm w.r.t. $CFCl_3$, with satellites at −53.7 and −60.3 ppm as well as −53.0 and −60.9 ppm. These satellites originate most likely from heteronuclear spin-spin coupling of ^{19}F and ^{123}Te and ^{125}Te. This is in very good accordance with the position of −56.4 ppm w.r.t. $CFCl_3$ reported by Seppelt [117].

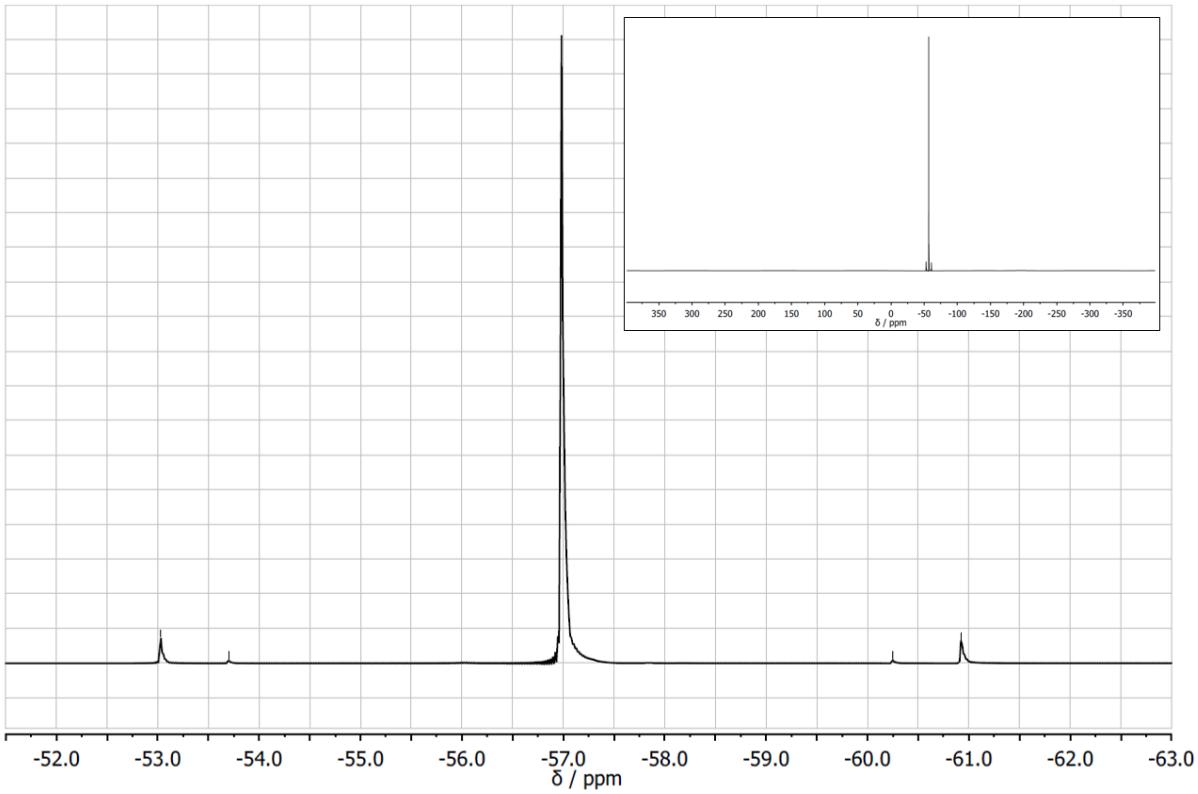

Figure 6.72: NMR spectrum of liquid TeF_6 under intrinsic pressure at room temperature.

6.10 Summary of reaction conditions and spectroscopic analysis

The following chapter gives a summary of the reaction conditions for all investigated elements as well as the spectroscopic data of the compounds that could be synthesized without a major amount of impurities.

Table 6.28 lists the conditions, at which a synthesis was most successfully performed and which fluoride could be obtained under these conditions.

Table 6.28: Overview over the basic conditions of the etching experiments for the different elements.

substrate	obtained fluoride	Ar/NF_3 [sccm]	heating [°C]	time [min]	reaction yield [%]	etching rate [mg/min]	H_2 pre-treatment
Mo sheets	MoF_3	100/60	no	30	–	–	no
	MoF_6	35/35	no	45	92.2	45.2	no
Ru powder	RuF_5	8/2	190	100	88.0	2.7	no
Rh powder	RhF_4 (?)	8/2	160	60	–	–	yes
Pd powder	PdF_2 PdF_3	0/4	190	60	–	–	no
W sheets	WF_6	0/60	no	35	73.7	11.4	no
Re powder	ReF_6 ReF_7	8/8	no	60	98.6	–	highly advisable
Os powder	OsF_6	0/15	no	40	95.1	–	no
Ir powder	IrF_6	0/13	210	60	94.6	–	no
Pt powder	PtF_4 (?)	54/10	no	45	–	–	yes
Te chunks	TeF_6	8/8	no	35	100.0	15.8	no
U sheets	UF_4	20/20	no	40	–	–	no
	UF_6	35/35	no	65	93.3	43.9	no

Figure 6.73 to Figure 6.76 show the spectroscopic data for the compounds MoF_6, TeF_6, OsF_6, IrF_6 as well as UF_6. These compounds could be synthesized relatively pure. The spectra of the reaction products from the fluorination of rhenium are not shown, as they contained a number of compounds with partly overlapping bands that could not clearly be assigned.

Figure 6.73 shows the IR spectra of the five hexafluorides. The transmittance thereby ranges between 0 and 1 for each compound. Figure 6.74 depicts their Raman spectra with the corresponding intensity given in arbitrary units. Figure 6.75 gives an overview over the UV/VIS spectra of the five hexafluorides. The transmittance here also ranges between 0 and 1 for each compound. Figure 6.76 depicts their NMR spectra.

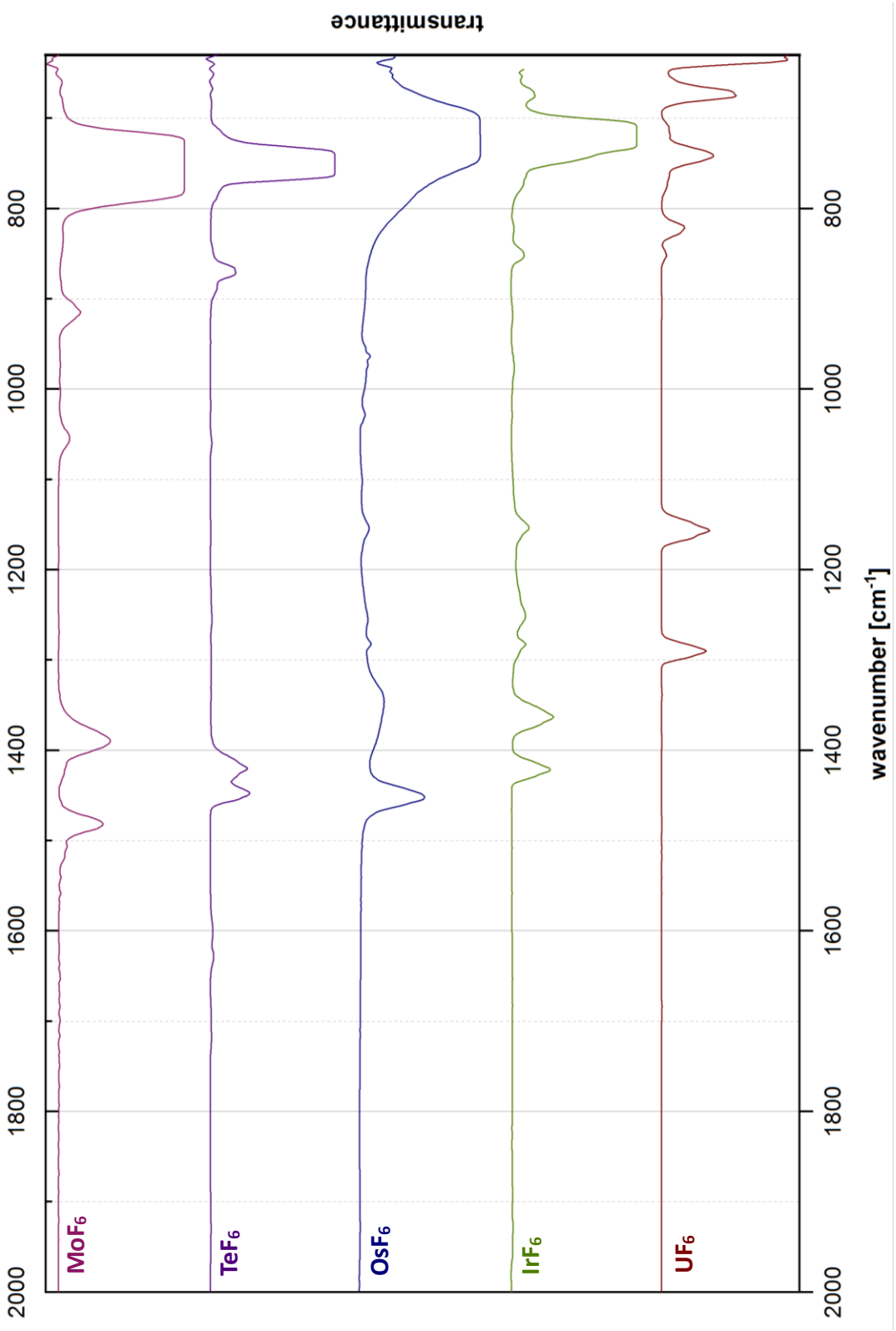

Figure 6.73: IR spectra of the hexafluorides that were successfully synthesized without a major amount of impurities.

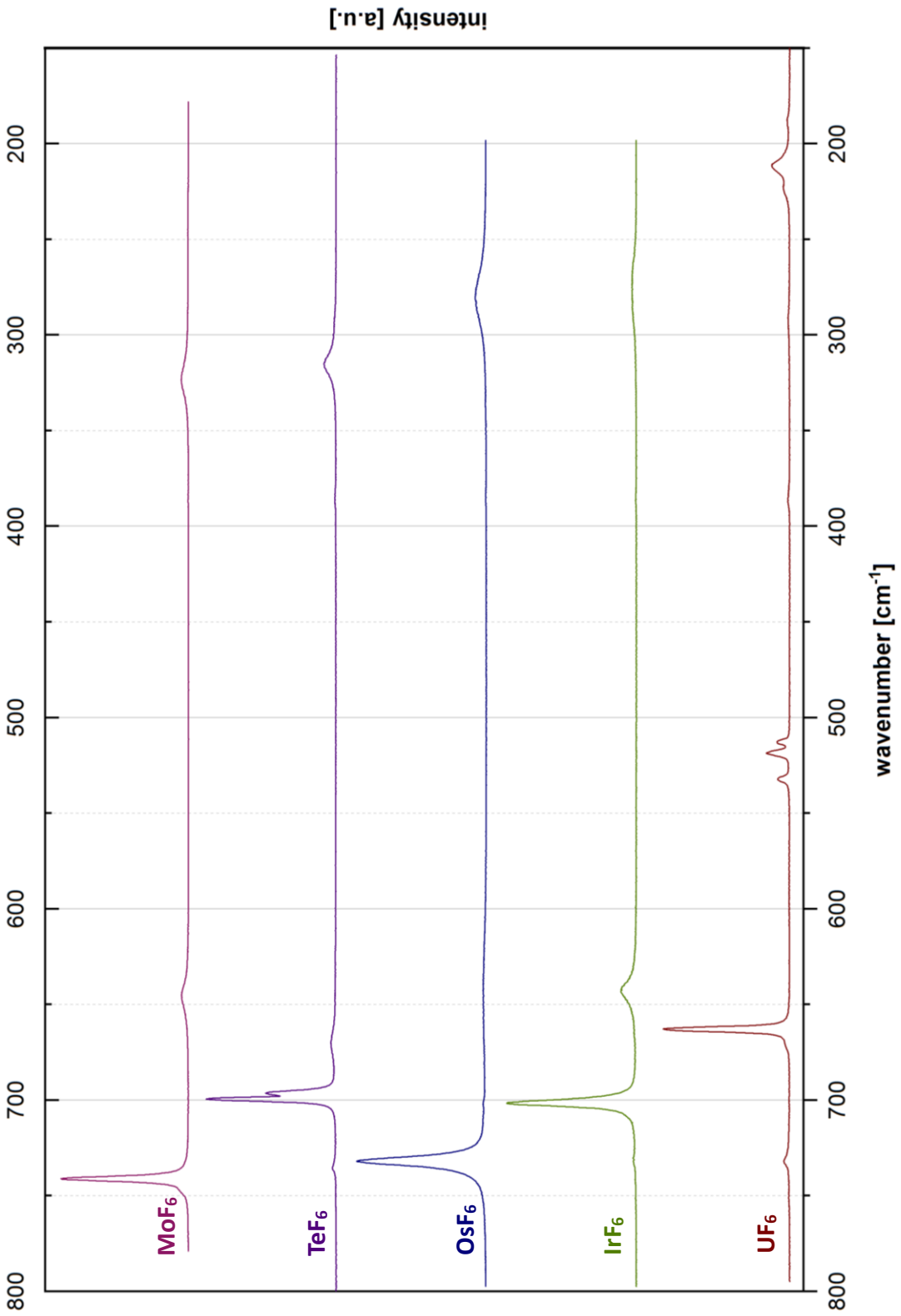

Figure 6.74: Raman spectra of the hexafluorides that were successfully synthesized without a major amount of impurities.

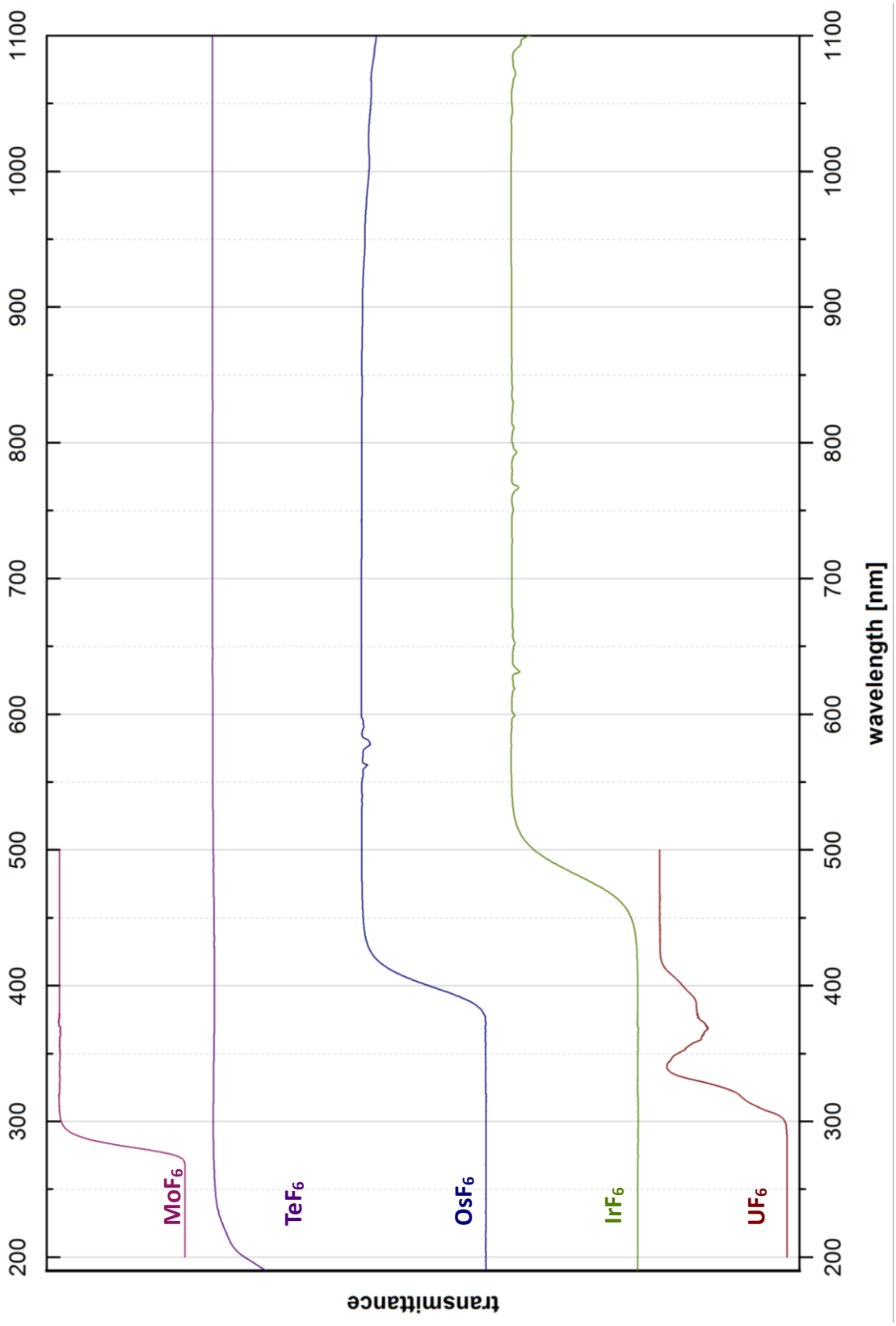

Figure 6.75: UV/VIS spectra of the hexafluorides that were successfully synthesized without a major amount of impurities.

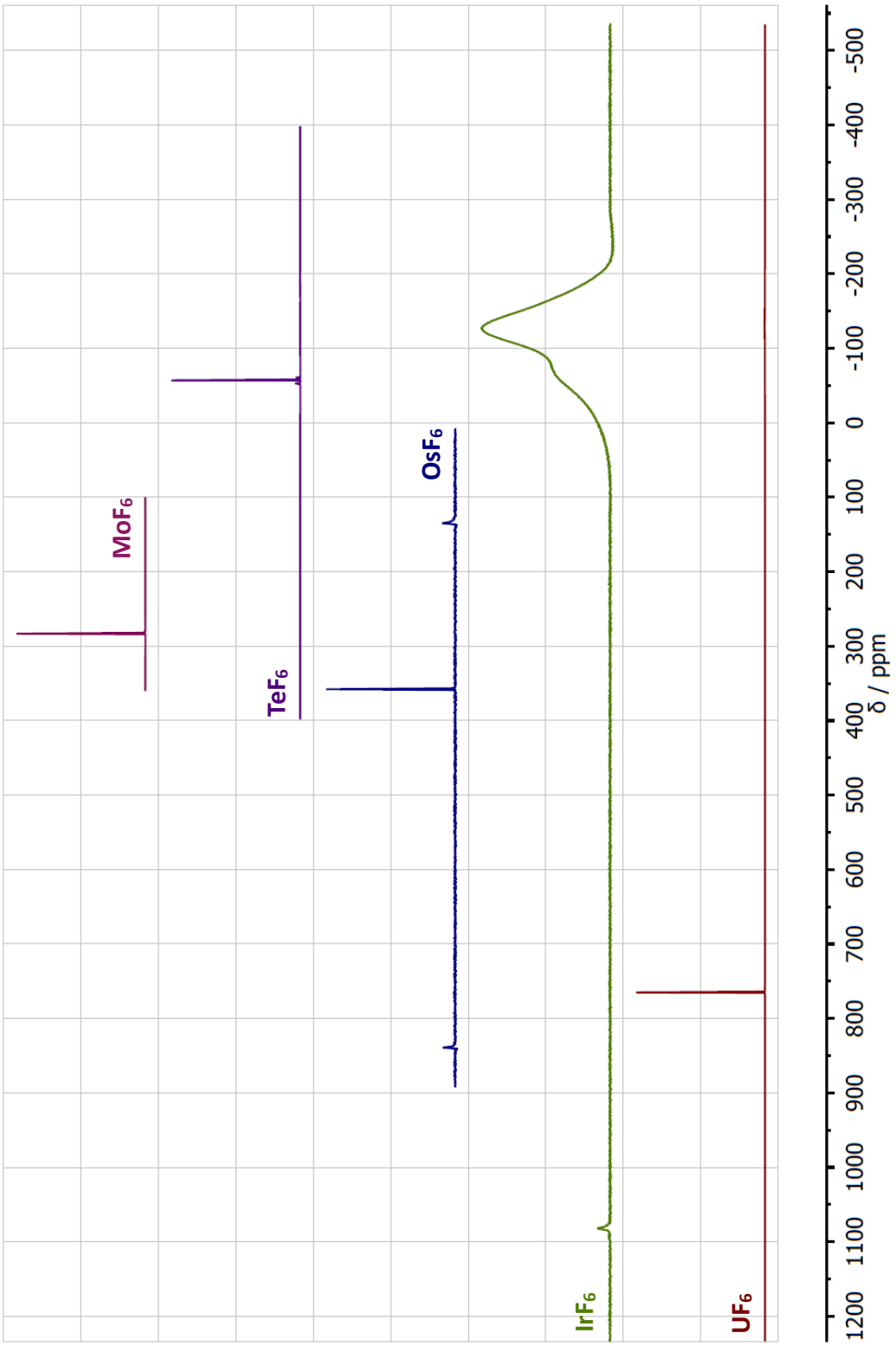

Figure 6.76: NMR spectra of the hexafluorides that were successfully synthesized without a major amount of impurities.

7 Conclusion and Future Prospects

7.1 Conclusion

The aim of this thesis was the development of a dry-chemical process for the separation of molybdenum from uranium that could be applied for ^{99}Mo production. In order to solve this task, a fluorination line using a remote plasma source was developed, built and commissioned. This line is able to fluorinate UMo targets to uranium hexafluoride and molybdenum hexafluoride and collect these in three subsequently arranged cold traps. The reaction rate of the targets thereby is a function of a multitude of parameters including the applied power of the plasma source, the substrate temperature, the etching agent, the absolute flow of the etching agent, the ratio of the etching agent and a potential carrier gas as well as the etching time. As an investigation of the exact influence of the entirety of these parameters to the full extent was impossible during the course of this work, instead a well-suited parameter set resulting in good etching rates was identified. This parameter set allowed for a reaction yield of up to 99.98 % and an etching rate of 95.8 mg/min for UMo targets. In addition, a potential pre-separation based on a difference in the vapor pressure of UF_6 and MoF_6 was studied. Hereby, the uranium recovery and molybdenum losses were investigated in dependency of the etching rate and the temperature of the first cold trap. Thereby, a temperature of −69 °C and an etching rate of 37 mg/min led to a recovery of 80.8 % of the deployed molybdenum and at the same time increased its mass ratio from originally 0.1 % to 2.3 %.

However, as a complete separation of UF_6 and MoF_6 could not be achieved by this method itself, a second chemical separation step was tested. A comparison of the UV/VIS spectra of UF_6 and MoF_6 showed significant differences in the absorbance between 340 and 420 nm. As literature had already described the formation of UF_5 via photoreduction at 390 nm and MoF_6 did not show any absorption at all at this wavelength, it stood to reason taking a photochemical approach. In order to avoid a back reaction, a fluorine scavenger was added. As the scavenger preferably had to be well suited for a dry-chemical process, CO was chosen. This reaction had also already been known from literature and experiments of a colleague, Ms. Riane Stene [142], with gaseous CO and an irradiation at 395 nm had shown to be successful. However, as the reaction showed to be rather long for a potential separation process, the suitability of CO in the liquid and supercritical phase was investigated. The use of liquid CO at ambient pressure demanded a reaction temperature below −192 °C and thus the cooling of the reaction vessel with liquid nitrogen. The experiments performed at this temperature did either show no reduction of UF_6 at all or only a greatly reduced reaction rate. In either case, a separation of the two hexafluorides could not be achieved.

The investigations on supercritical CO as a fluorine scavenger demanded for much more sophisticated technical requirements. Thus, a high-pressure container was constructed, that allowed the use of CO up to 70 bar and could therefore be operated at ambient temperature. Gaseous UF_6 and MoF_6 could be condensed into the container using a cooling system operated on LN_2. This concept in principle permits an integration of this component into the fluorination line. The irradiation of the hexafluorides could be performed through a sapphire window using a high-power LED. The reaction time could be reduced

from originally 48 hours for the use of gaseous CO to only 60 minutes using supercritical CO. During this time, 88.9 % of the original deployed uranium mass could be removed from the molybdenum side. The amount of molybdenum found on the uranium side after separation only amounts to about $1-2$ %, therefore most likely allowing for an efficient separation. However, the use of supercritical CO leads to the formation of $(COF)_2$, a compound not observed during the separation experiments using gaseous CO. This compound has rather unfavorable thermodynamic properties such as a relatively high boiling point of −3 °C, compared to the boiling points to CO at −191.5 °C and COF_2 at −84.6 °C. The separation of this compound from MoF_6 has to be subject to further investigations.

In order to investigate its suitability for different target materials, the fluorination behavior of U_3Si_2 targets was also investigated. U_3Si_2 has several advantages as a target material, as it possesses a relatively high uranium density of up to 6.0 g/cm^3 in dispersed form and behaves well under irradiation. As a potential monolithic target material, its uranium density may be as high as 11.3 g/cm^3. During the course of the experiments, the fluorination line also proved to be well suited for the processing of this target material. All U_3Si_2 targets could entirely be transformed into UF_6 and SiF_4. A separation of MoF_6 and SiF_4 can most likely be performed purely by physical means, as SiF_4 has a very low boiling point of −86 °C.

As the first fluorination experiments with molybdenum and tungsten were highly successful, the idea was born to investigate its suitability for the synthesis of additional high-valent fluorides that can otherwise only be obtained by sophisticated experimental techniques. Especially the synthesis of the hexafluorides of the platinum metals includes the use of high temperatures, high pressures and elemental fluorine. The fluorination line proved to be able to provide an easy and comfortable access to their synthesis. In addition, the reduced corrosivity due to the use of NF_3 significantly extends the life of the utilized components. The performance of the reactions at pressures in the low millibar range furthermore greatly increases the procedural safety, as a leakage in the system does not lead to a release of highly reactive species.

The hexafluorides of the rhenium, osmium and iridium could be easily synthesized with high reaction yields of over 95 %. An advantageous set of reaction parameters with respect to volume flow of the etching agent and the carrier gas as well as the reaction temperature was identified for each element. The named metals have to be presented in a finely dispersed form such as a powder, as a reaction deploying them in a massive form was unsuccessful. Base metals such as tungsten may also be presented in a massive form such as a sheet. The synthesis of the hexafluorides of the platinum metals of the fifth period was not successful. The fluorination of ruthenium resulted in the synthesis of its pentafluoride, for rhodium most likely only the tetrafluoride was obtained. The fluorination of palladium resulted in its difluoride as well as its trifluoride. However, the reaction yield for each of these three elements was very low. For each of the synthesized hexafluorides, spectroscopic data was collected including UV/VIS, IR, Raman and NMR spectroscopy.

7.2 Future Prospects

7.2.1 Uranium plasma processing

The process has proven to provide a possibility to synthesize UF_4 of high purity starting from metallic uranium. In addition, the synthesis of UF_4 from other compounds should be investigated, namely from UO_2 and U_3O_8. UF_4 is of high interest for certain types of generation IV nuclear reactor designs, namely molten salt reactors [209], and the plasma fluorination process might allow an easy access to this compound completely without the need for HF.

7.2.2 Uranium and molybdenum separation

As the use of supercritical CO in combination with irradiation at 395 nm has produced very promising results for the separation of MoF_6 and UF_6, this procedure should be studied in further detail. Thereby, the design of the high-pressure container should be altered by equipping it with a more efficient cooling system. The transfer of UF_6 and MoF_6 into the container could thereby be significantly accelerated. Furthermore, it has to be investigated, whether the presence of $(COF)_2$ provokes any problems for the further separation and how it could be removed, if necessary. In addition, the separation of uranium and molybdenum proposes only the first step of an alternative dry-chemical extraction process. Following experiments will also have to concentrate on the separation of the other elements of the nuclide vector. A complete surrogate material containing all listed elements would provide the most robust data with respect to comparability with actual irradiated targets. However, as such a surrogate material will be most difficult to obtain due to the wide range of melting and boiling points of the constituents, some of them could be introduced in form of their fluorides (e.g. RbF).

7.2.3 U_3Si_2 processing

Additional experiments should be performed in order to study the suitability of the process for the fluorination of $U(AlSi)_3$, as this compound is present in irradiated U_3Si_2 dispersion fuels and causes difficulties during the dissolution of the targets.

7.2.4 Platinum metal hexafluoride synthesis

The question, whether or not the hexafluorides of the three platinum metals rhodium, palladium and platinum have been synthesized at least in traces, cannot be answered. Up to date, no substantive evidence in form of spectroscopic data could be provided. This should yet not be seen as a general inability to provide an access to these compounds via plasma fluorination. Instead, the installation of the following improvements will significantly increase the chances of their successful synthesis:

The simplest but most beneficial modifications may be made with regard to the reaction chamber. By decreasing its cross section, the reaction yield of NF_3 should easily be increased. Furthermore, a mechanism to place the Monel carrier in a reproducible manner would eliminate the uncertainty arising from differences of the flow profile due to a tilt of the carrier or due to the position of the substrate in the current. In addition, it is essential for future investigations to retrofit the reaction chamber in order to allow for a more efficient recovery of the substrate under Ar atmosphere in case it has not reacted or formed non-volatile compounds.

The possibility of the investigation of the influence of higher temperatures on the reaction course should be introduced into the line. In order to reduce the thermal load on the structural components of the line and of the reaction chamber in particular, isolated heating of the substrate would thereby be desirable. One potential extension to the reaction chamber would therefore be a laser heater irradiating the substrate only through an additional sapphire window on top of the reaction chamber.

Additional changes aiming on a reduction of the tubing between the RPS and the first cold trap should be made. It seems very likely, that the conditions necessary for a successful synthesis of the hard-to-obtain hexafluorides such as high temperature are also unfavorable for their continuous existence. A rapid thermal quenching may therefore increase the possibility of their successful recovery.

A. Appendix

A.1 Additional spectra and diffractograms

A.1.1 Supporting material to chapter 2.4

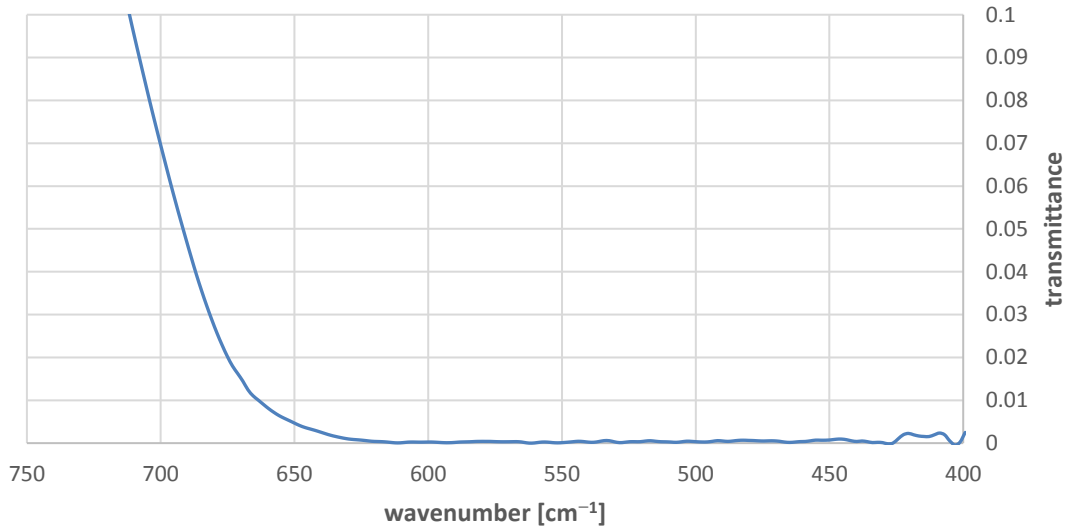

Figure A.1: IR spectrum of BaF_2 in the region between 400 and 750 cm^{-1}. The transmittance falls under 10 % at 711 cm^{-1}, under 1 % at 663 cm^{-1} and under 0.1 % at 628 cm^{-1}.

A.1.2 Supporting material to chapter 3.4

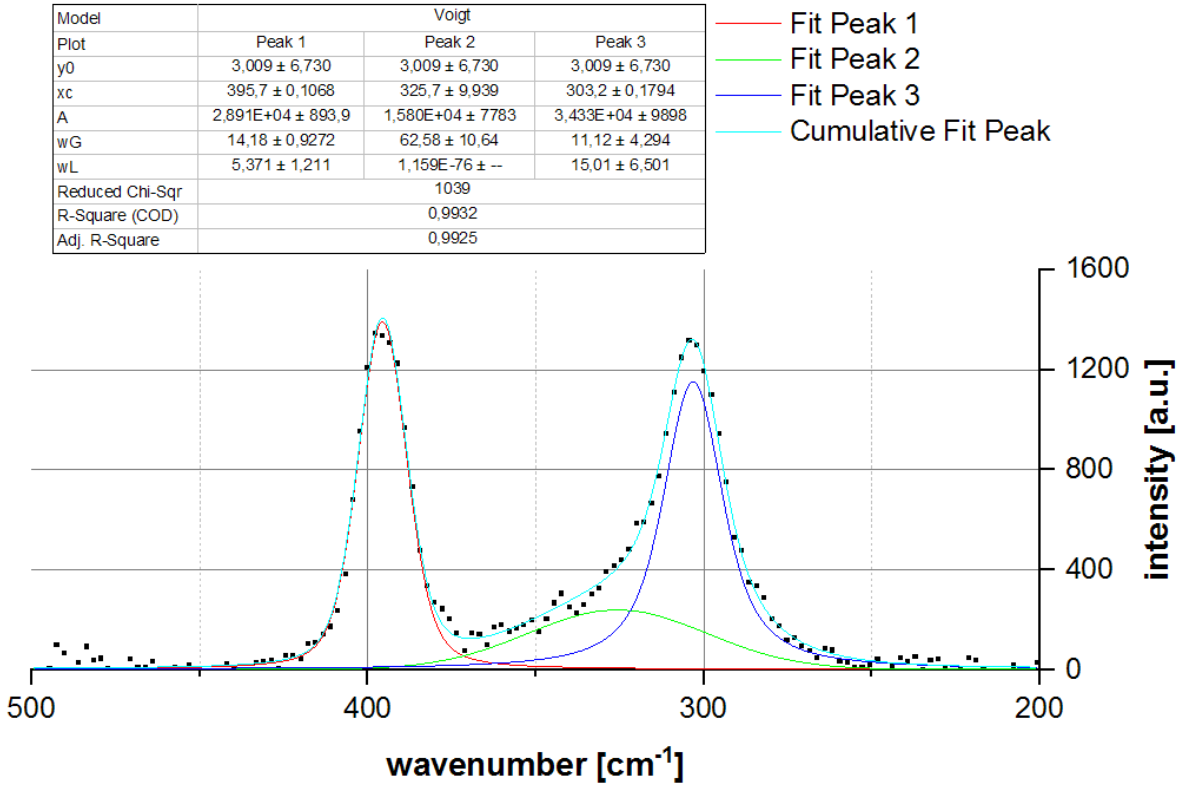

Figure A.2: Raman spectrum of FEP in the range between 200 and 500 cm^{-1}, measured at a wavelength of 532 nm and a groove density of 300 g/mm.

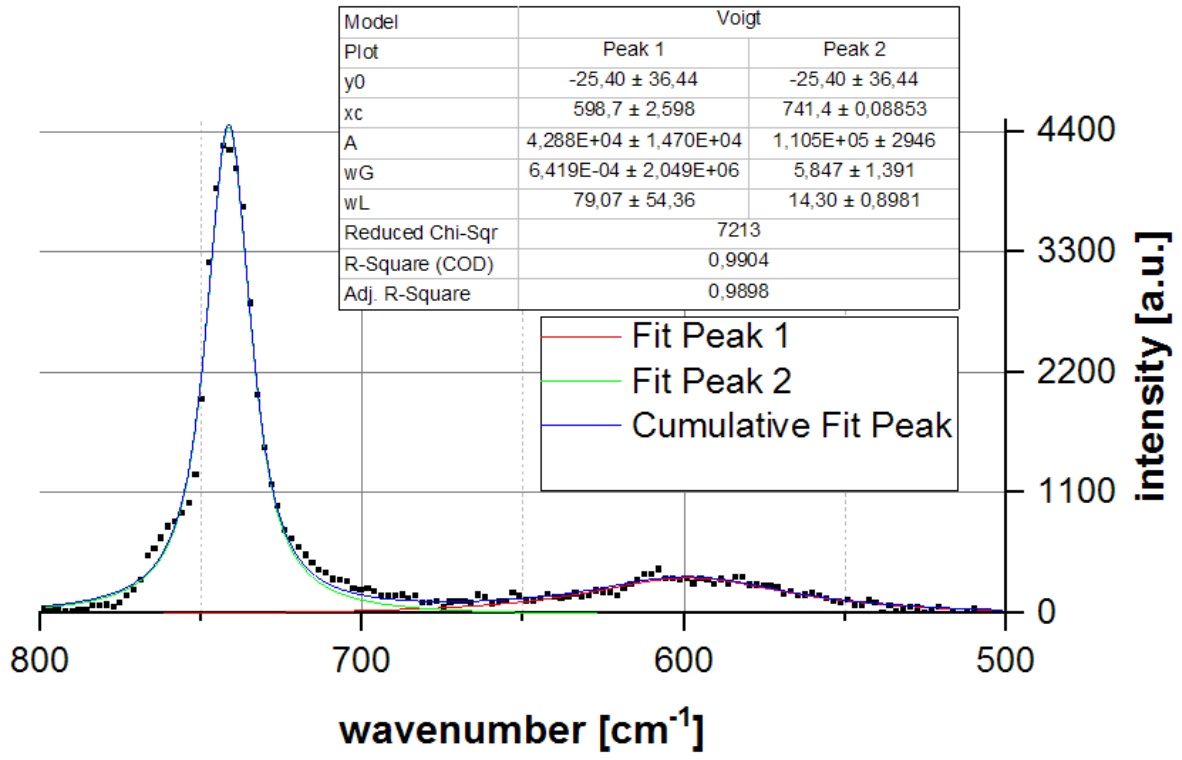

Figure A.3: Raman spectrum of FEP in the range between 500 and 800 cm^{-1}, measured at a wavelength of 532 nm and a groove density of 300 g/mm.

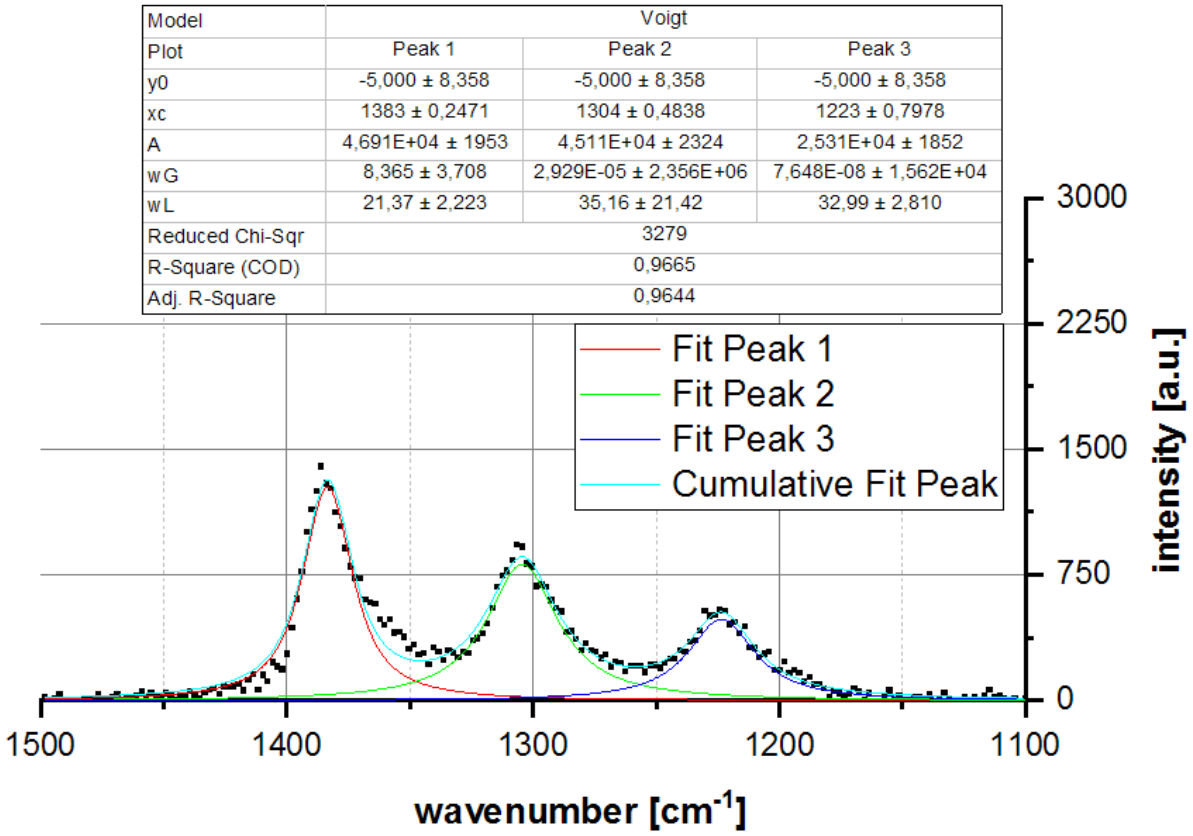

Figure A.4: Raman spectrum of FEP in the range between 1100 and 1500 cm^{-1}, measured at a wavelength of 532 nm and a groove density of 300 g/mm.

A.1.3 Supporting material to chapter 5.1

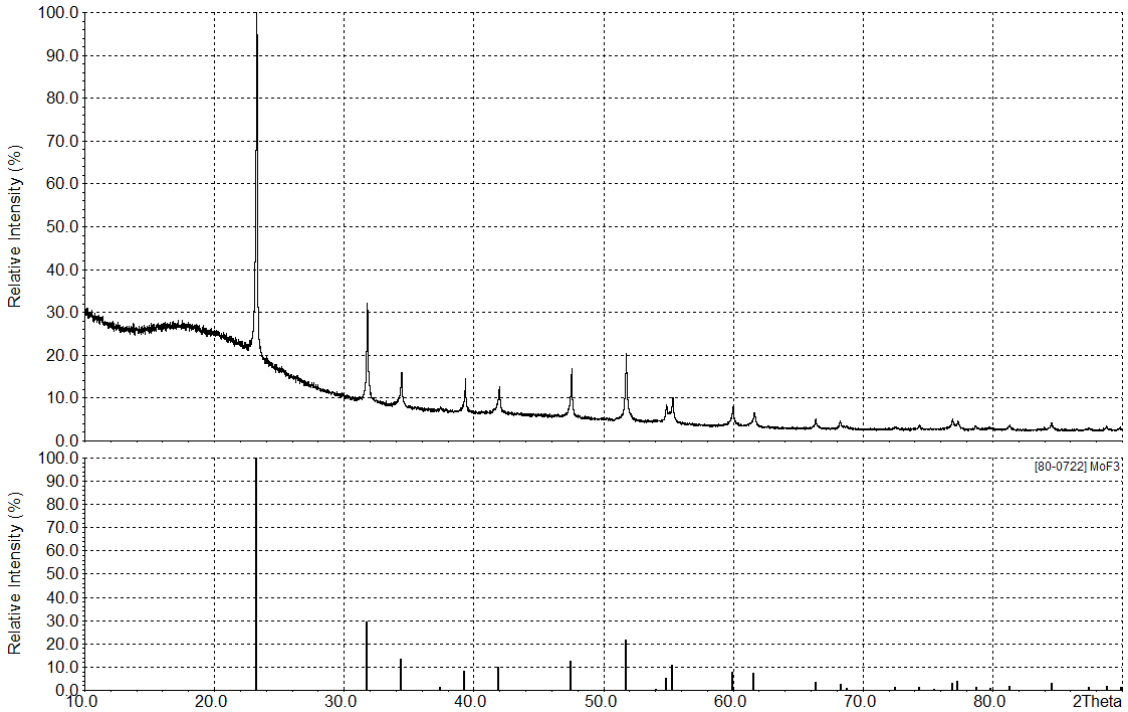

Figure A.5: X-ray powder diffractogram of the residues in the combustion boat in Figure 5.4. The reflections are in very good agreement with MoF_3, taken from ICDD-File [80-0722] rated with quality mark C.

A.1.4 Supporting material to chapter 5.1.4

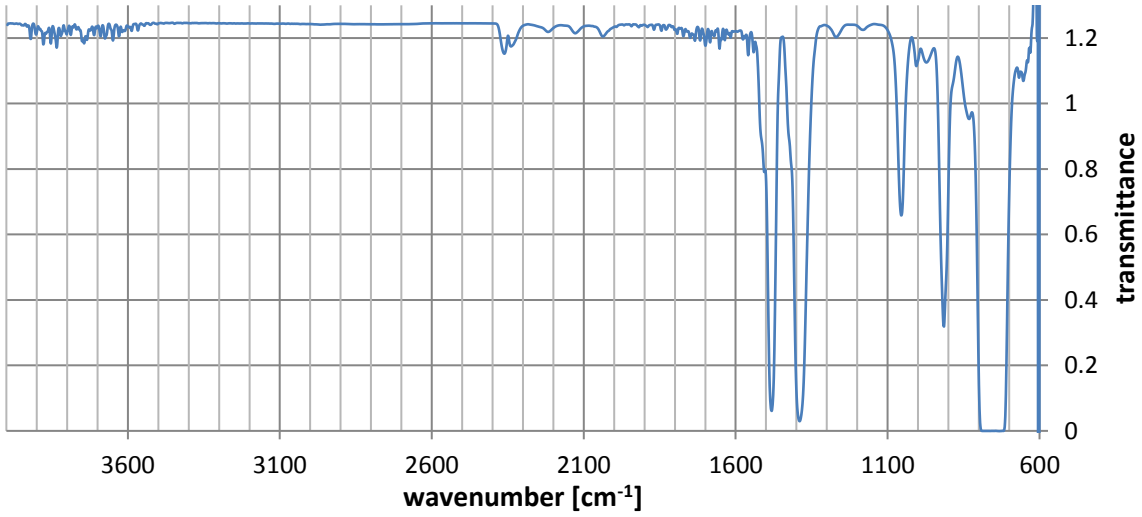

Figure A.6: IR spectrum of MoF_6 in the gas phase at 500 mbar measured with a resolution of 4 cm^{-1}.

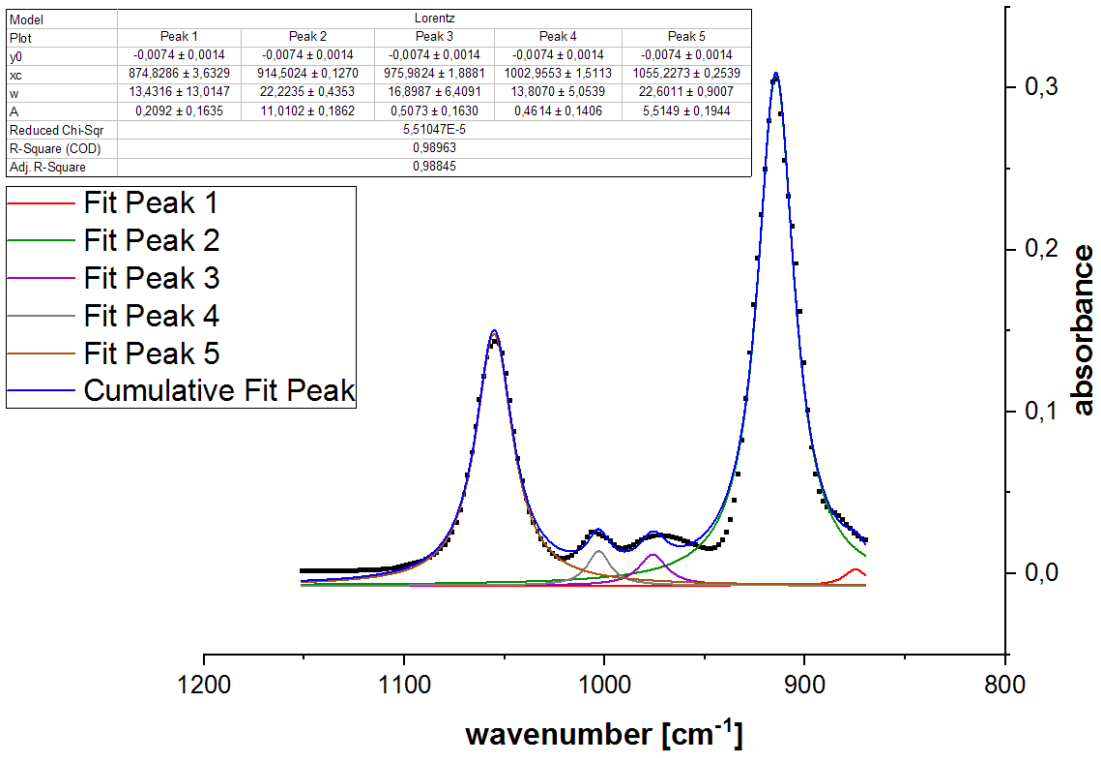

Figure A.7: IR spectrum of gaseous MoF_6 at 255 mbar and fit for determination of position of absorption bands between 870 and 1150 cm^{-1}.

Model	Voigt	
Plot	Peak 1	Peak 2
y0	0,0013308 ± 9,2286E-05	0,0013308 ± 9,2286E-05
xc	1268,7 ± 0,15634	1181,2 ± 0,33929
A	0,46383 ± 0,017505	0,15374 ± 0,0059456
wG	25,167 ± 1,5116	25,371 ± 0,91905
wL	7,0191 ± 2,2030	1,2313E-17 ± 0,0000
Reduced Chi-Sqr	1,5726E-07	
R-Square (COD)	0,99002	
Adj. R-Square	0,98920	

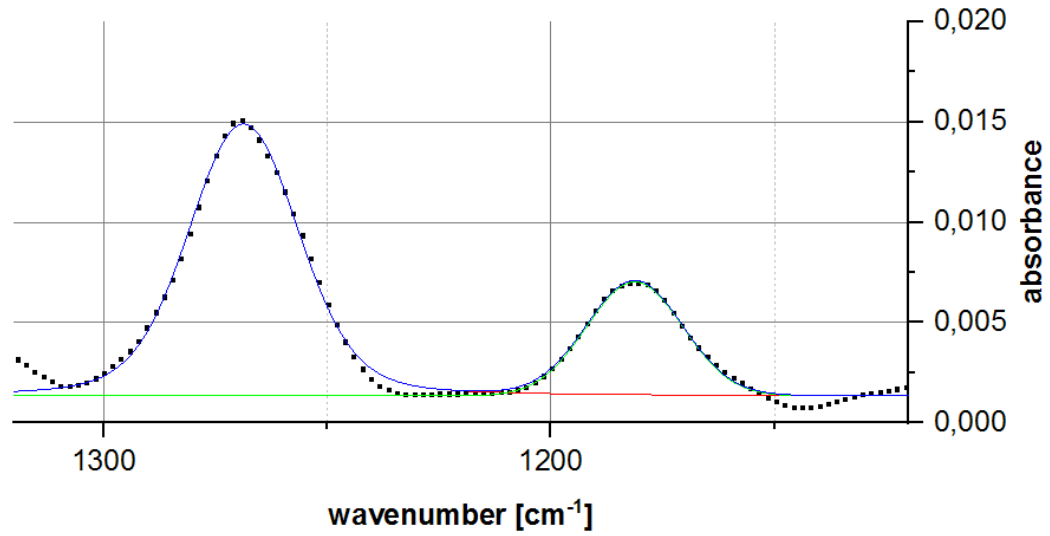

Figure A.8: IR spectrum of gaseous MoF_6 at 500 mbar and fit for determination of position of absorption bands between 1120 and 1320 cm^{-1}.

Model	Gauss		
Plot	Peak1(B)	Peak2(B)	Peak3(B)
y0	0,01013 ± 9,562E-04	0,01013 ± 9,562E-04	0,01013 ± 9,562E-04
xc	1482 ± 0,04225	1507 ± 0,8863	1519 ± 1,222
w	16,23 ± 0,1116	10,40 ± 1,436	9,068 ± 1,717
A	6,326 ± 0,04925	0,4931 ± 0,08333	0,2773 ± 0,08425
Reduced Chi-Sqr	7,959E-06		
R-Square (COD)	0,9994		
Adj. R-Square	0,9992		

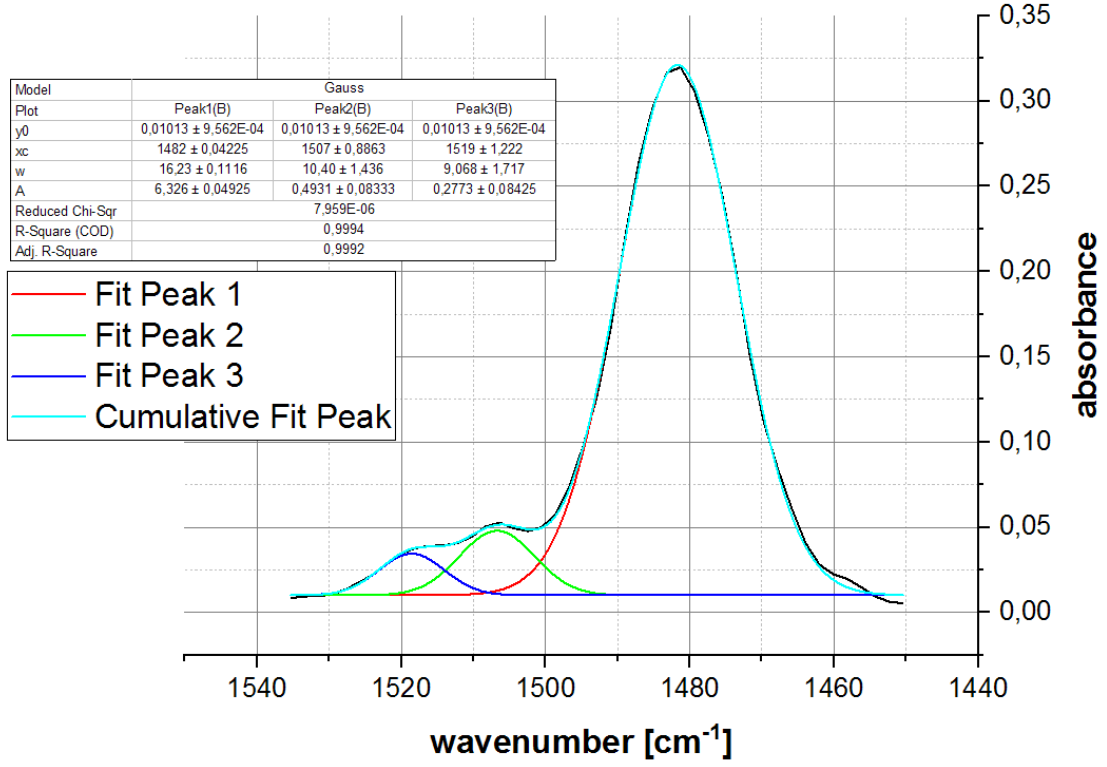

Figure A.9: IR spectrum of gaseous MoF_6 at 255 mbar and fit for determination of position of absorption bands between 1450 and 1535 cm^{-1}.

Model	Voigt	
Plot	Peak 1	Peak 2
y0	-0,032851 ± 0,0087865	-0,032851 ± 0,0087865
xc	1388,6 ± 0,10064	1427,5 ± 1,8667
A	61,806 ± 1,7749	0,60000 ± 0,25062
wG	17,733 ± 1,3740	10,852 ± 4,6330
wL	16,299 ± 1,6003	7,4513E-15 ± 0,0000
Reduced Chi-Sqr	8,8767E-04	
R-Square (COD)	0,99675	
Adj. R-Square	0,99636	

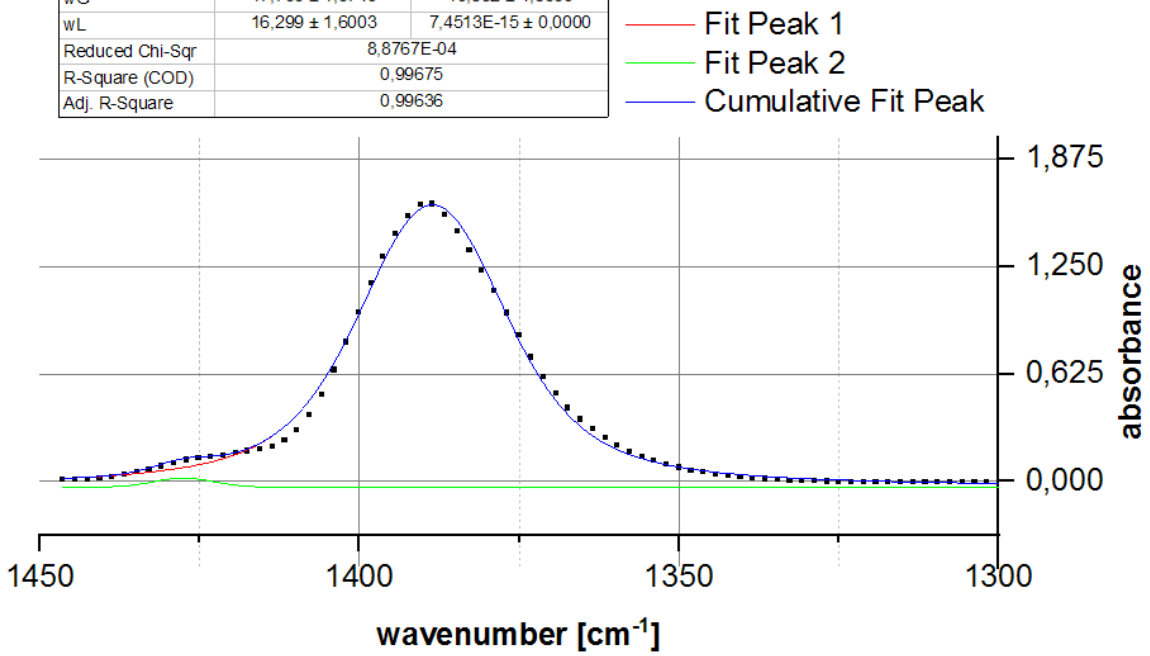

Figure A.10: IR spectrum of gaseous MoF_6 at 500 mbar and fit for determination of position of absorption bands between 1300 and 1450 cm^{-1}.

Model	Voigt		
Plot	Peak1(B)	Peak2(B)	Peak3(B)
y0	9,5269E-04 ± 1,1308E-04	9,5269E-04 ± 1,1308E-04	9,5269E-04 ± 1,1308E-04
xc	2217,8 ± 0,38959	2126,5 ± 0,28375	2034,3 ± 0,23050
A	0,43650 ± 0,020013	0,29557 ± 0,015598	0,65841 ± 0,024234
wG	1,8329E-05 ± 1,3261E+06	28,157 ± 2,3994	4,7258 ± 8,0376
wL	34,134 ± 11,741	3,1722 ± 3,5103	31,693 ± 2,2789
Reduced Chi-Sqr	2,2134E-07		
R-Square (COD)	0,98070		
Adj. R-Square	0,97934		

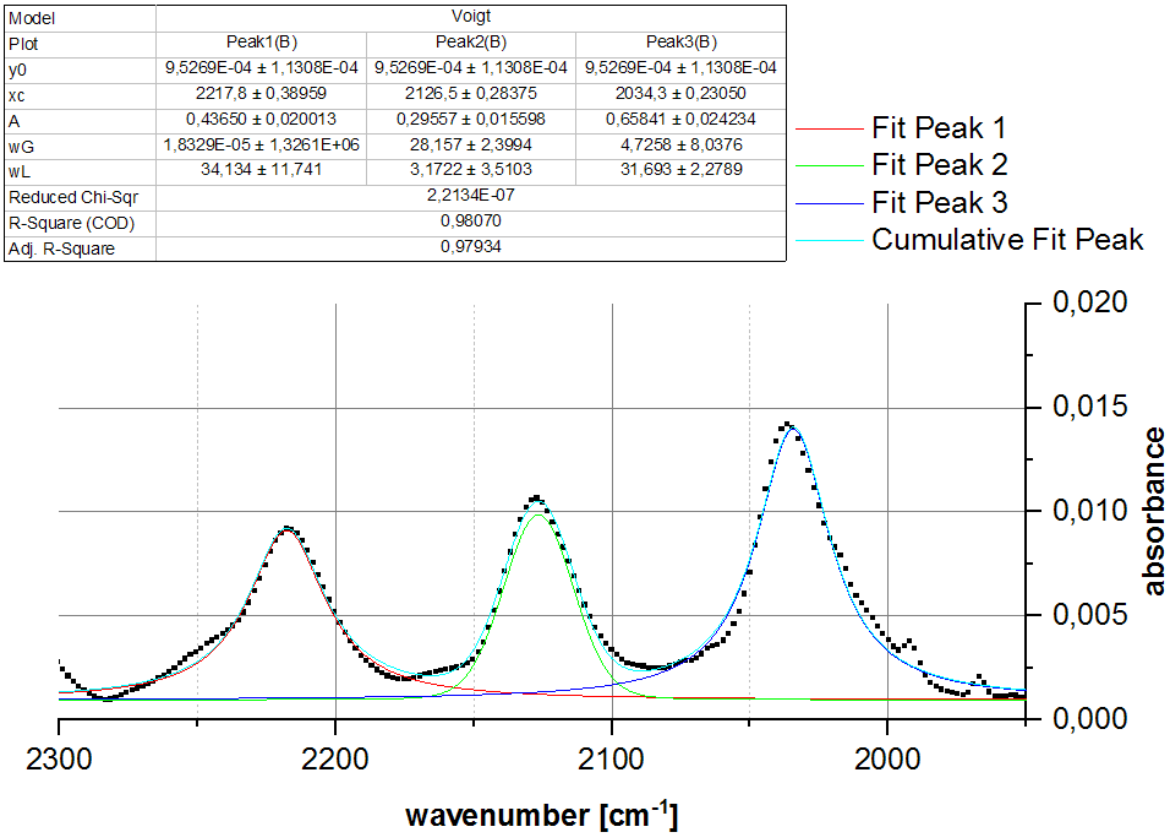

Figure A.11: IR spectrum of gaseous MoF_6 at 500 mbar and fit for determination of position of absorption bands between 1950 and 2300 cm^{-1}.

A.1.5 Supporting material to chapter 5.1.5

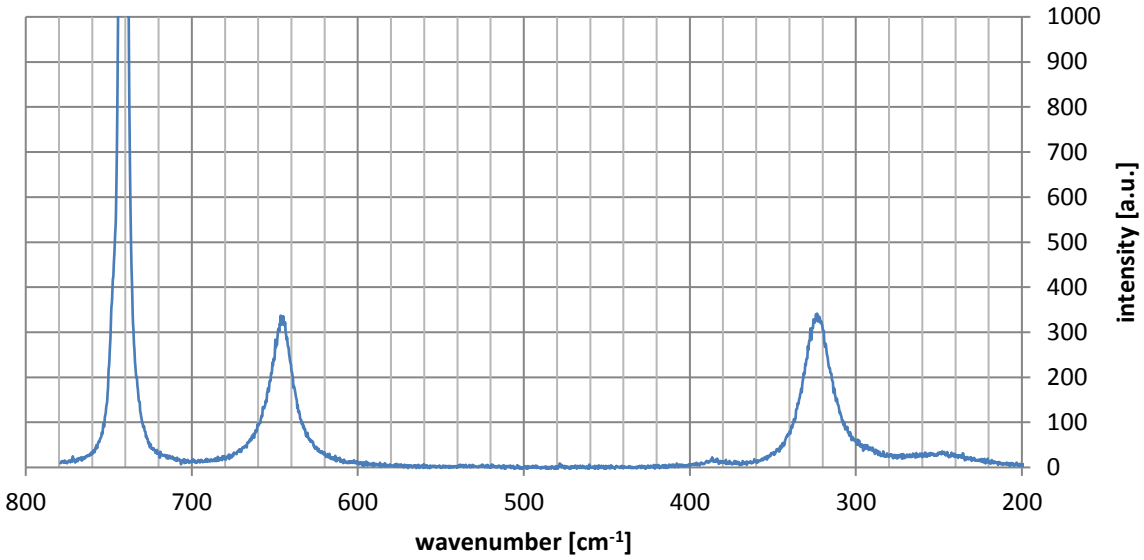

Figure A.12: Raman spectrum of liquid MoF_6 measured with a laser wavelength of 532 nm and a groove density of 1800 g/mm.

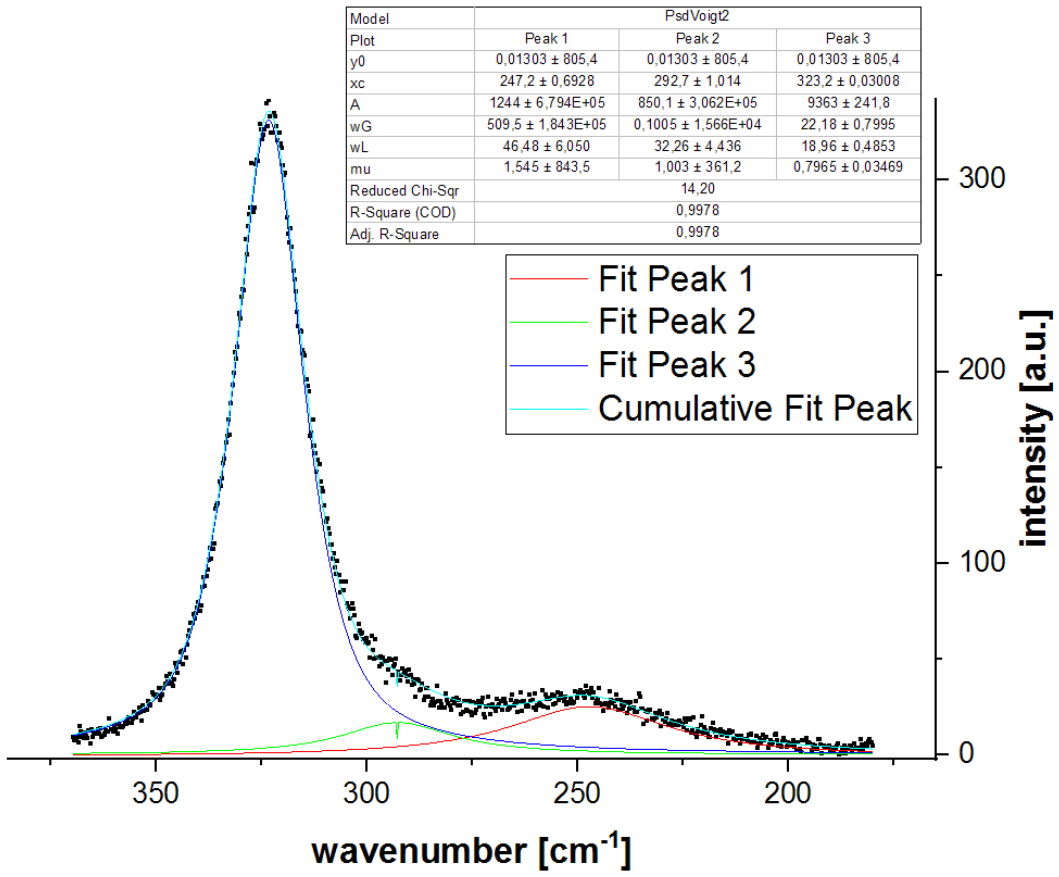

Figure A.13: Raman spectrum of liquid MoF_6 measured at 532 nm and a groove density of 1800 g/mm. The peak at 293 cm^{-1} belongs to FEP.

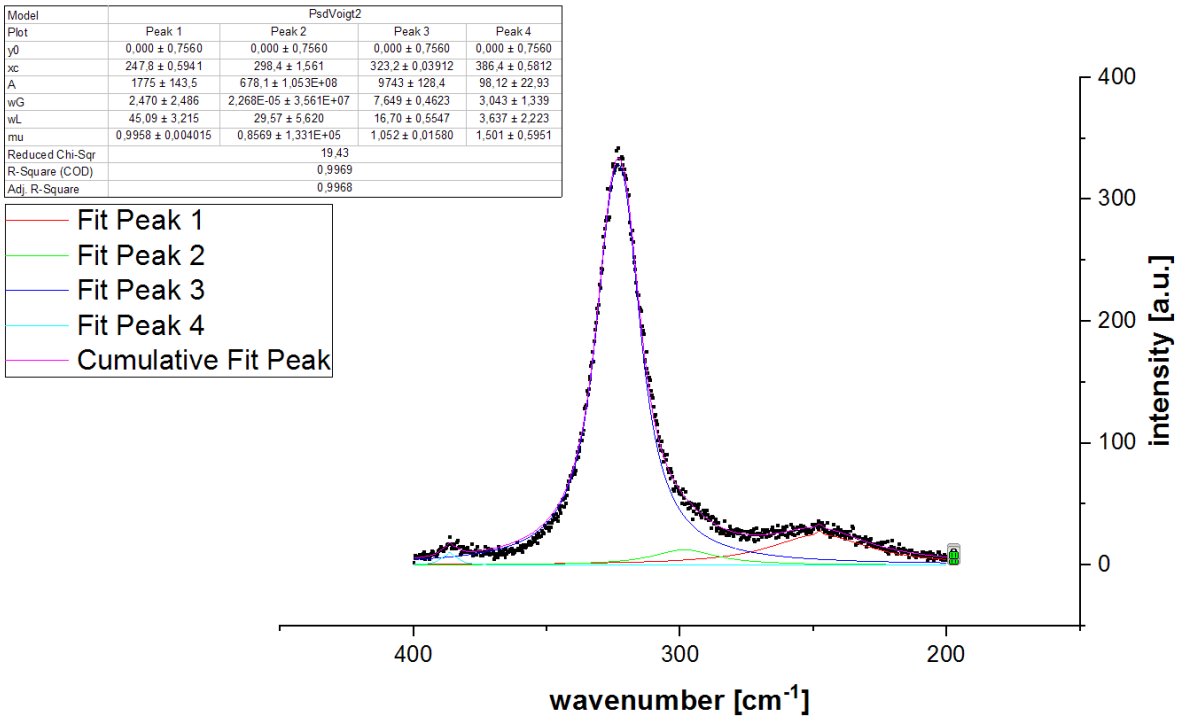

Figure A.14: Raman spectrum of liquid MoF_6 measured at 532 nm and a groove density of 1800 g/mm.

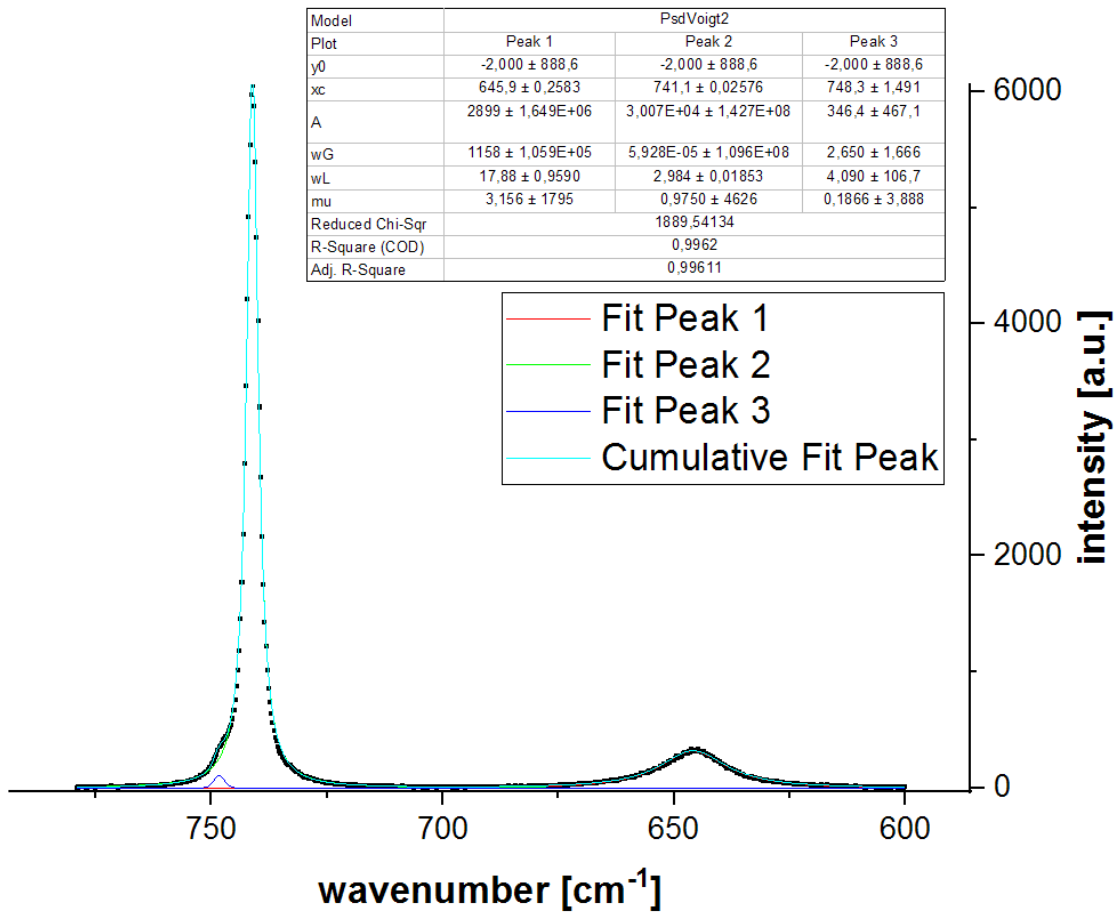

Figure A.15: Raman spectrum of liquid MoF_6 measured at 532 nm and a groove density of 1800 g/mm.

A.1.6 Supporting material to chapter 5.2

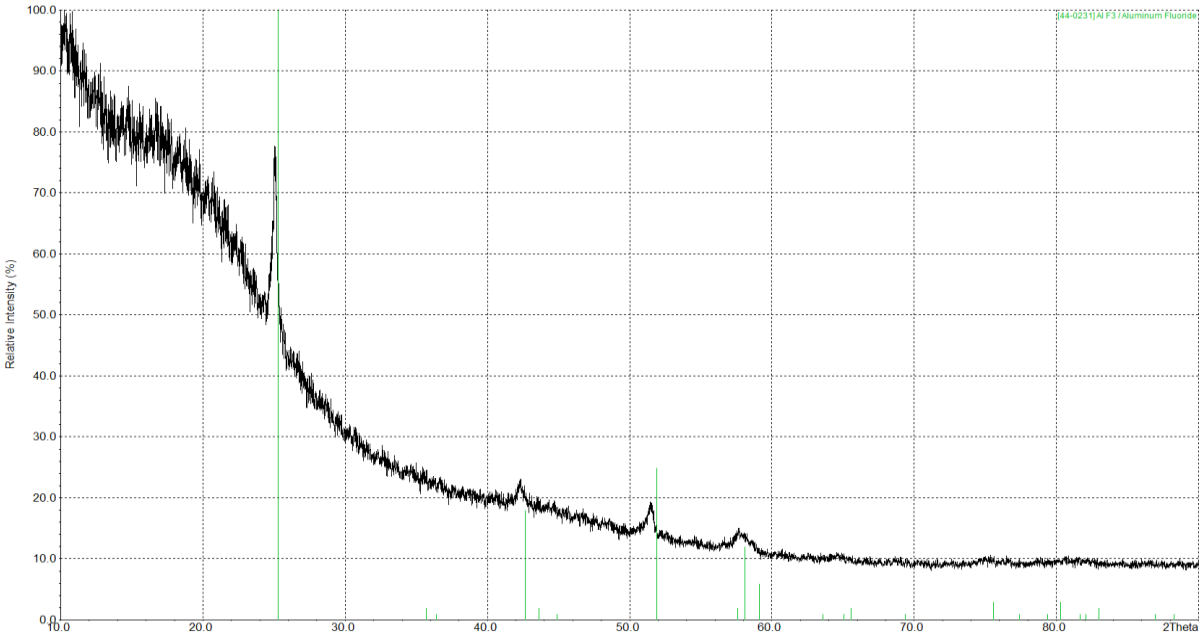

Figure A.16: X-ray powder diffractogram of the white residues left after fluorination of uranium targets. The reflections show a slight shift but are still in good agreement with AlF_3; data taken from ICDD-File [44-0231] rated with quality mark S.

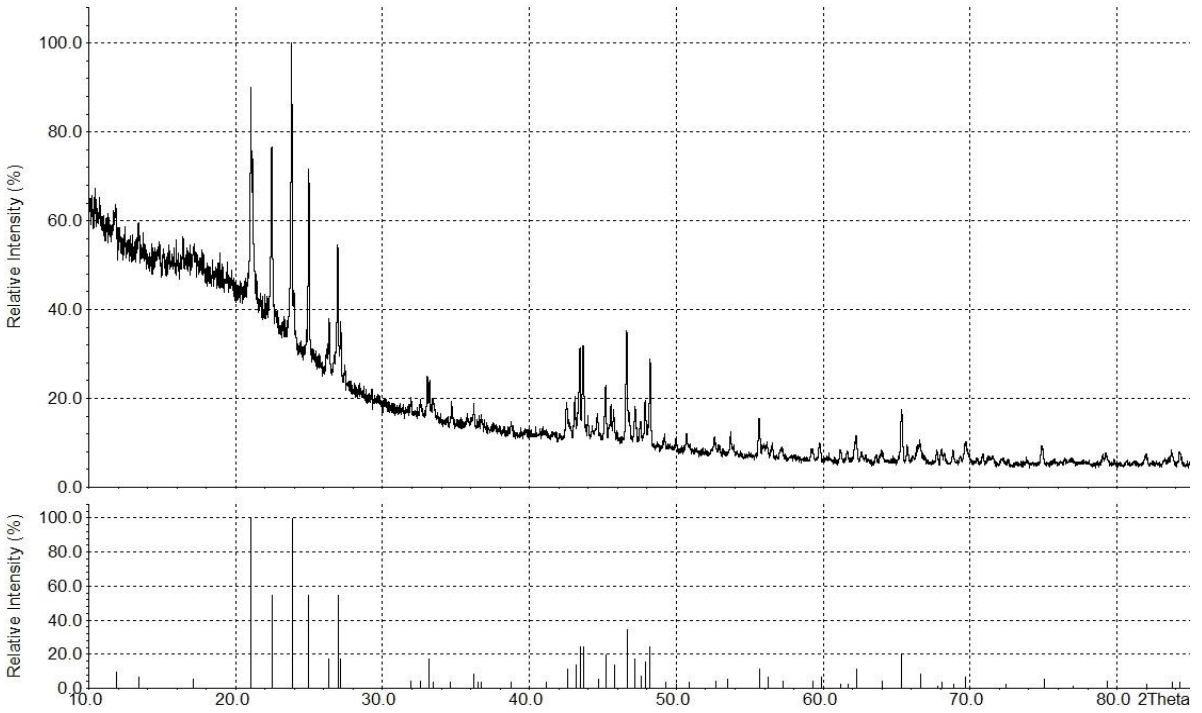

Figure A.17: X-ray powder diffractogram of the black residues of the reaction with low flow. The lower spectrum is the one of UF_4 calculated from single crystal diffraction.

A.1.7 Supporting material to chapter 5.2.4

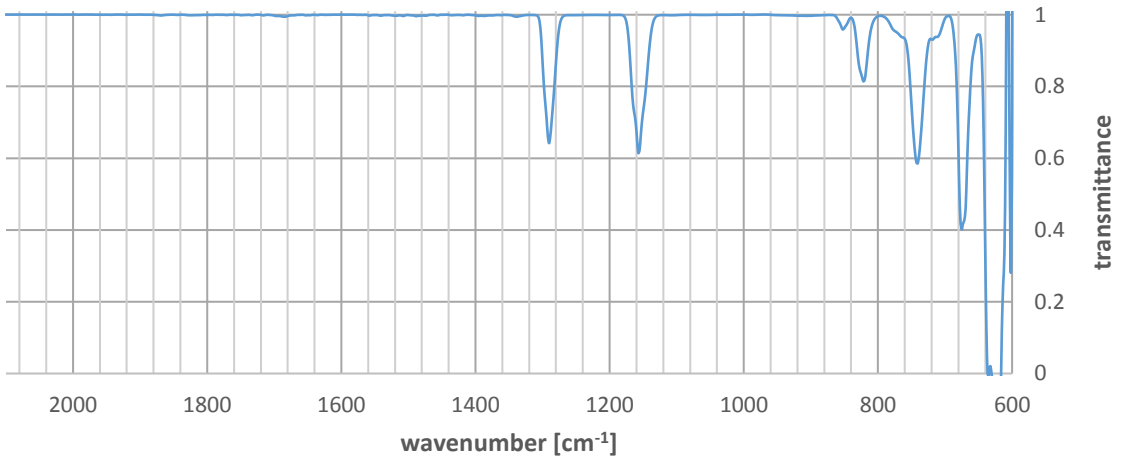

Figure A.18: IR spectrum of UF_6 in the gas phase at 66 mbar measured with a resolution of 4 cm^{-1}. The band at 741 cm^{-1} does not belong to UF_6 put is the ν_3 fundamental of minor impurities of MoF_6.

Model	Lorentz	
Plot	Peak 1	Peak 2
y0	-0,005491 ± 0,004044	-0,005491 ± 0,004044
xc	677,0 ± 0,06391	670,1 ± 0,1169
w	5,515 ± 0,2173	9,179 ± 0,3542
A	4,739 ± 0,2347	7,451 ± 0,3445
Reduced Chi-Sqr	1,735E-04	
R-Square (COD)	0,9970	
Adj. R-Square	0,9966	

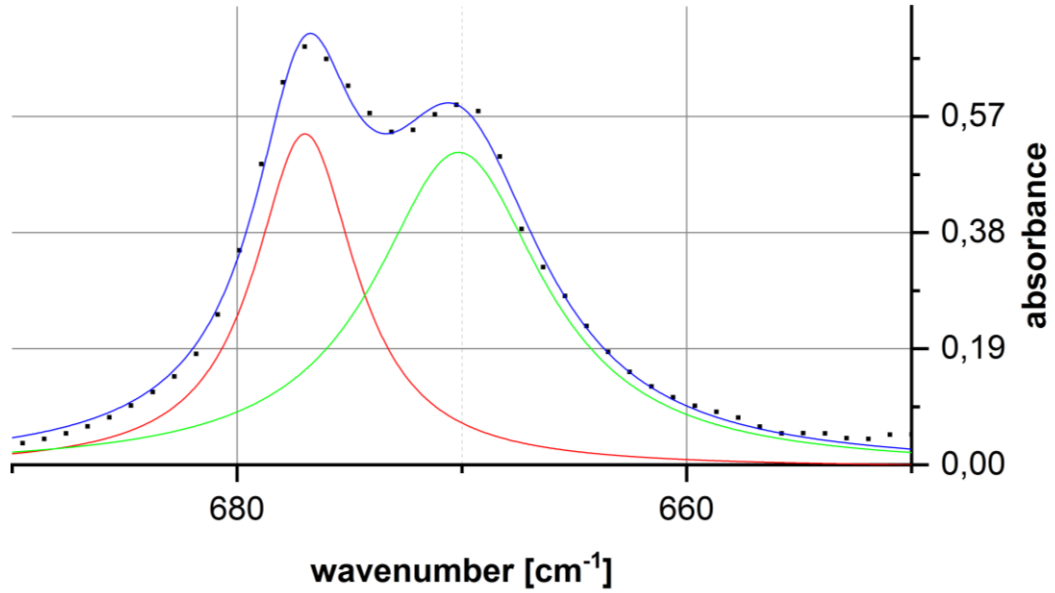

Figure A.19: IR spectrum of gaseous UF_6 at 99.3 mbar measured with a resolution of 2 cm^{-1} and fit for determination of position of absorption bands between 650 and 690 cm^{-1}.

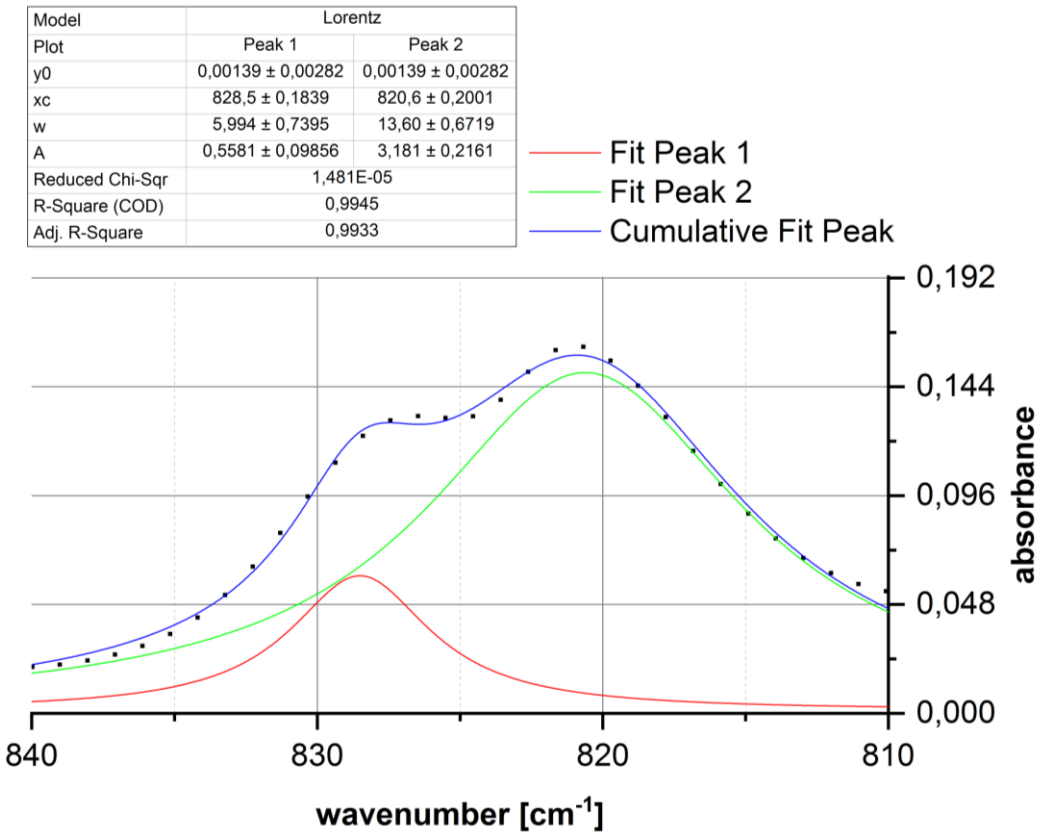

Figure A.20: IR spectrum of gaseous UF_6 at 99.3 mbar measured with a resolution of 2 cm^{-1} and fit for determination of position of absorption bands between 840 and 870 cm^{-1}.

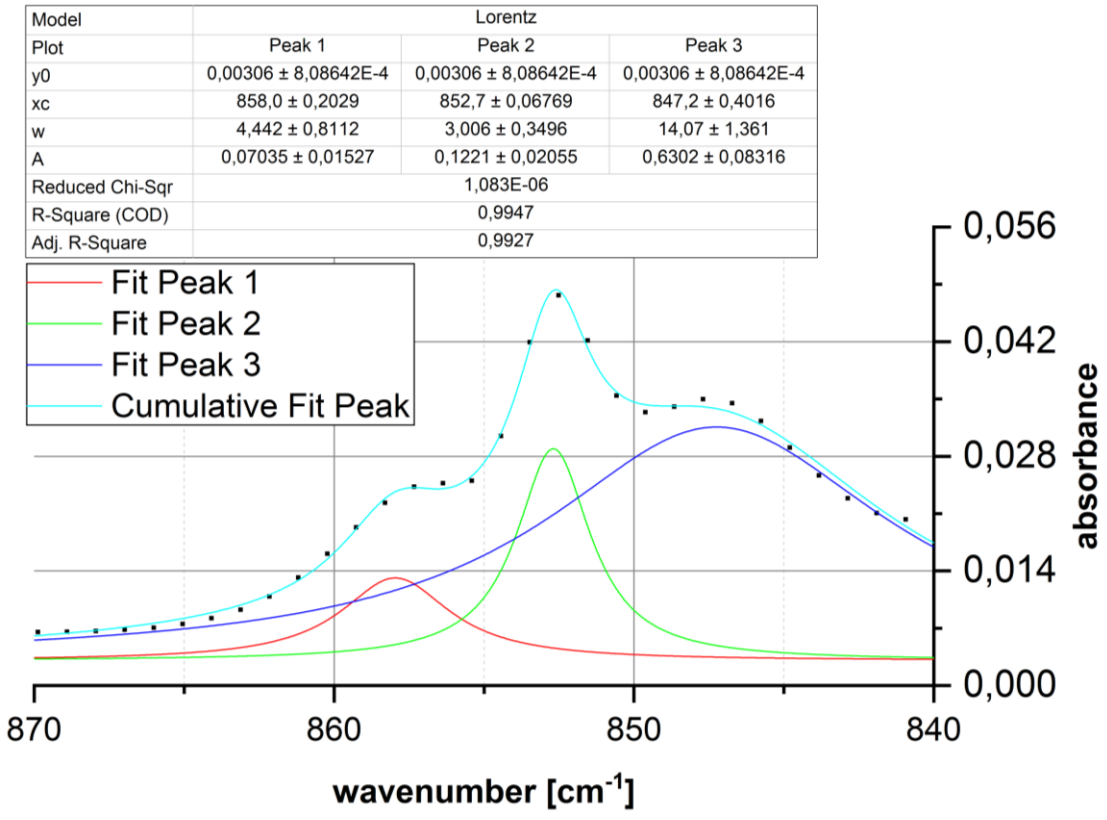

Figure A.21: IR spectrum of gaseous UF_6 at 99.3 mbar measured with a resolution of 2 cm^{-1} and fit for determination of position of absorption bands between 840 and 870 cm^{-1}.

Model	Lorentz		
Plot	Peak 1	Peak 2	Peak 3
y0	-0,003622 ± 5,585E-04	-0,003622 ± 5,585E-04	-0,003622 ± 5,585E-04
xc	741,4 ± 0,1456	717,6 ± 0,4828	709,6 ± 0,4023
w	17,88 ± 0,5579	9,470 ± 1,523	7,873 ± 1,242
A	2,078 ± 0,06225	0,4058 ± 0,08096	0,3312 ± 0,06981
Reduced Chi-Sqr	4,292E-06		
R-Square (COD)	0,9920		
Adj. R-Square	0,9904		

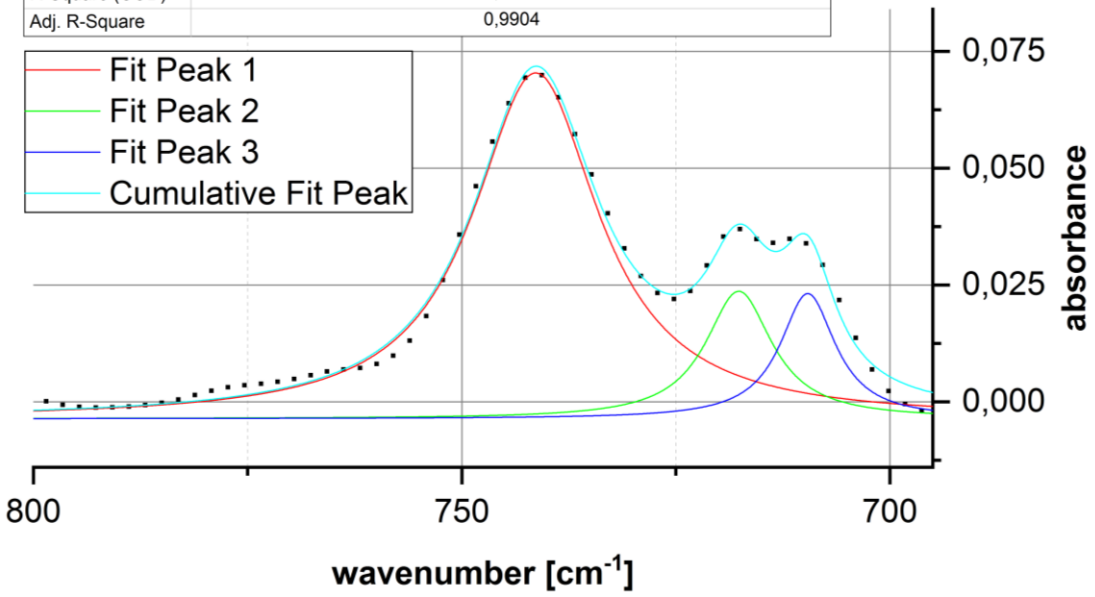

Figure A.22: IR spectrum of gaseous UF_6 at 98 mbar and fit for determination of position of absorption bands between 1120 and 1200 cm^{-1}. The band at 741.4 cm^{-1} is the ν_3 of MoF_6.

Model	Lorentz		
Plot	Peak1(B)	Peak2(B)	Peak3(B)
y0	-0,0050000 ± 0,001529	-0,0050000 ± 0,001529	-0,0050000 ± 0,001529
xc	1164,8 ± 0,16056	1156,7 ± 0,090332	1148,3 ± 0,27945
w	6,8419 ± 0,52975	7,5842 ± 0,47756	10,324 ± 0,75967
A	1,6269 ± 0,15214	3,6384 ± 0,29077	2,3807 ± 0,23899
Reduced Chi-Sqr	6,4174E-05		
R-Square (COD)	0,99473		
Adj. R-Square	0,99410		

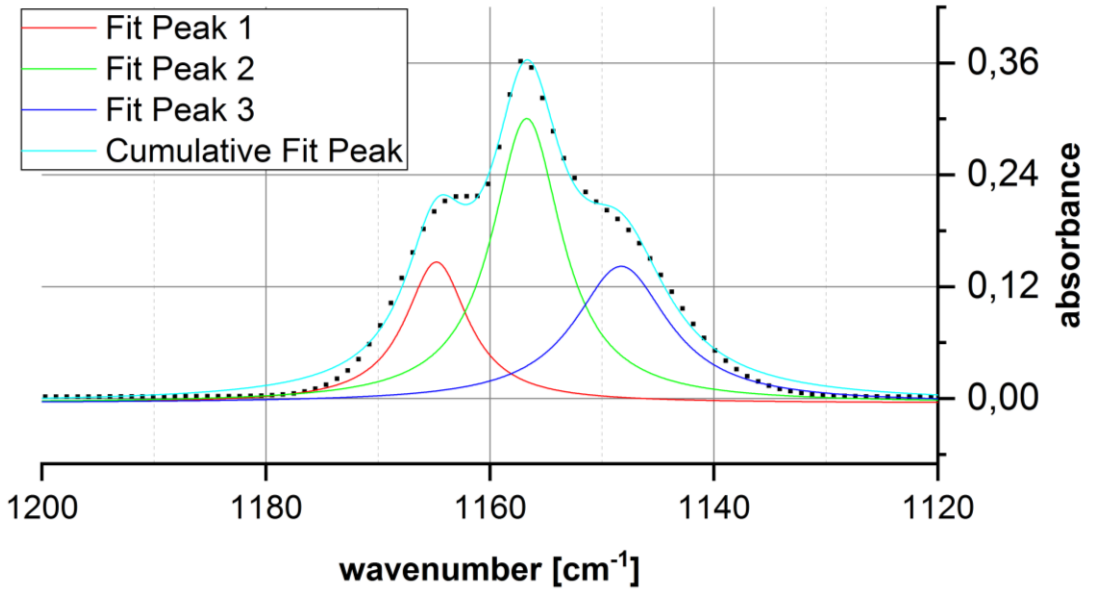

Figure A.23: IR spectrum of gaseous UF_6 at 99.3 mbar measured with a resolution of 2 cm^{-1} and fit for determination of position of absorption bands between 1120 and 1200 cm^{-1}.

Model	Lorentz		
Plot	Peak 1	Peak 2	Peak 3
y0	-0,01 ± 0,00178	-0,01 ± 0,00178	-0,01 ± 0,00178
xc	1297,3 ± 0,15009	1290,9 ± 0,12204	1284,8 ± 0,39378
w	4,5966 ± 0,54909	6,9836 ± 0,65086	9,7004 ± 0,80909
A	0,82631 ± 0,12680	2,9230 ± 0,40765	2,2982 ± 0,36449
Reduced Chi-Sqr	5,2738E-05		
R-Square (COD)	0,99546		
Adj. R-Square	0,99471		

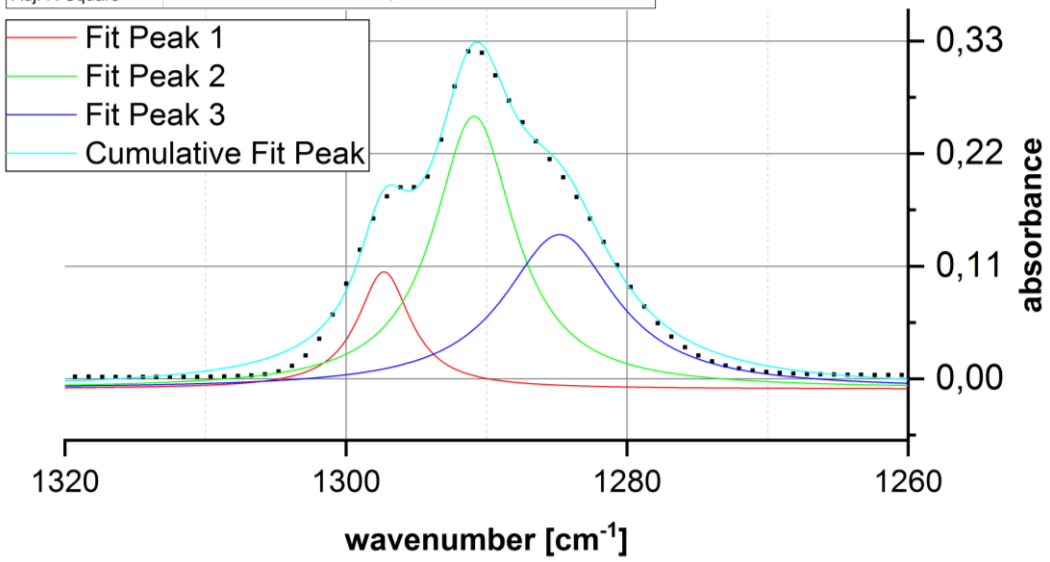

Figure A.24: IR spectrum of gaseous UF_6 at 99.3 mbar measured with a resolution of 2 cm^{-1} and fit for determination of position of absorption bands between 1260 and 1320 cm^{-1}.

A.1.8 Supporting material to chapter 5.2.5

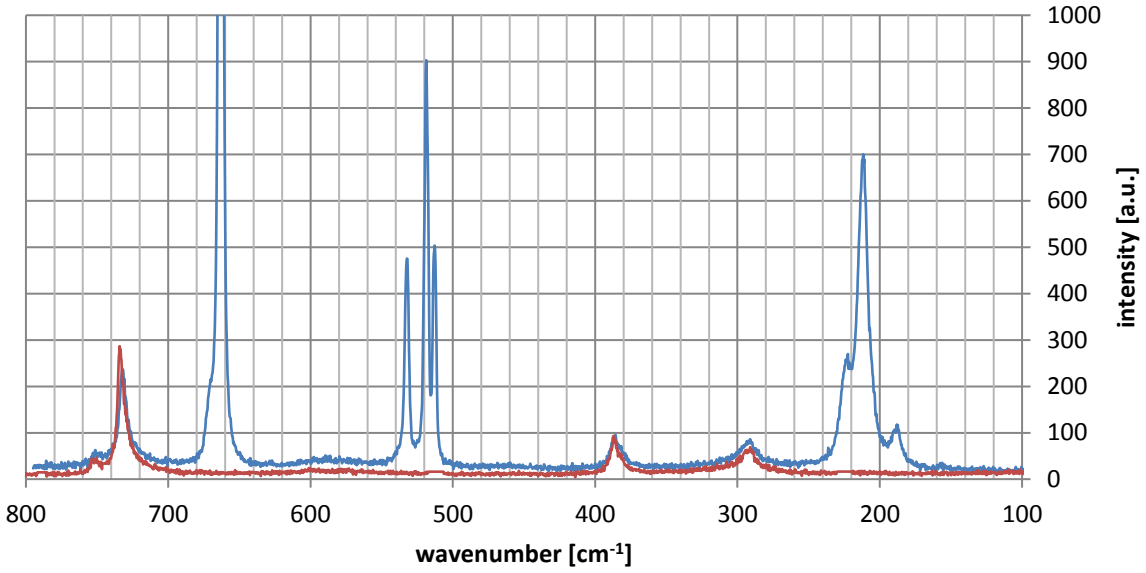

Figure A.25: Raman spectrum of solid UF_6 measured at 488 nm and a groove density of 1800 g/mm. The red graph is the reference spectrum of FEP.

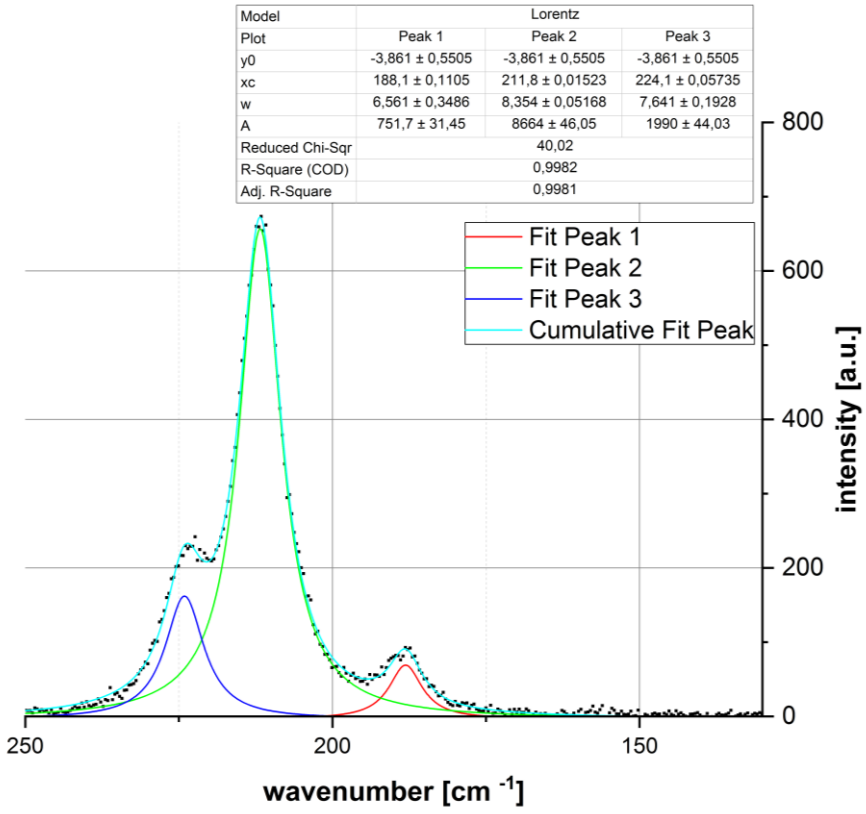

Figure A.26: Raman spectrum of solid UF_6 between 125 and 250 cm^{-1} measured at 488 nm and a groove density of 1800 g/mm and fitting for determination of band positions.

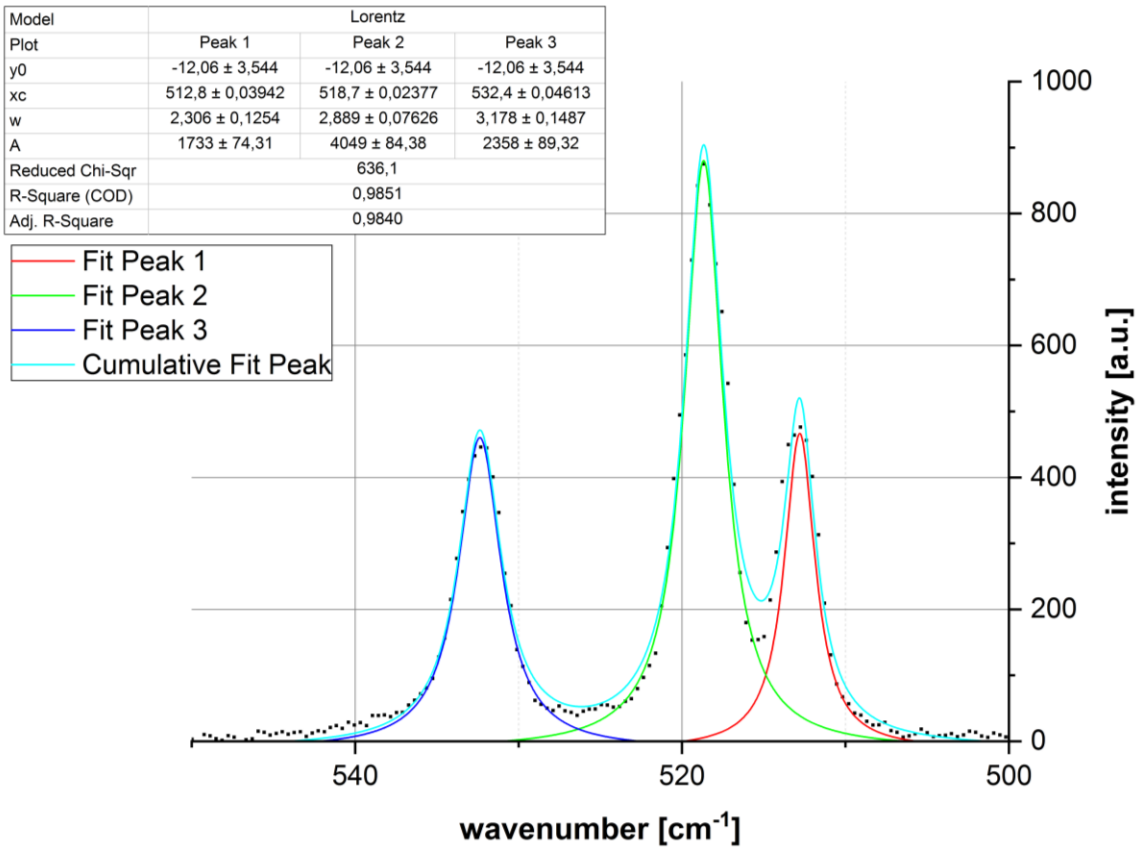

Figure A.27: Raman spectrum of solid UF_6 between 500 and 550 cm^{-1} measured at 488 nm and a groove density of 1800 g/mm and fitting for determination of band positions.

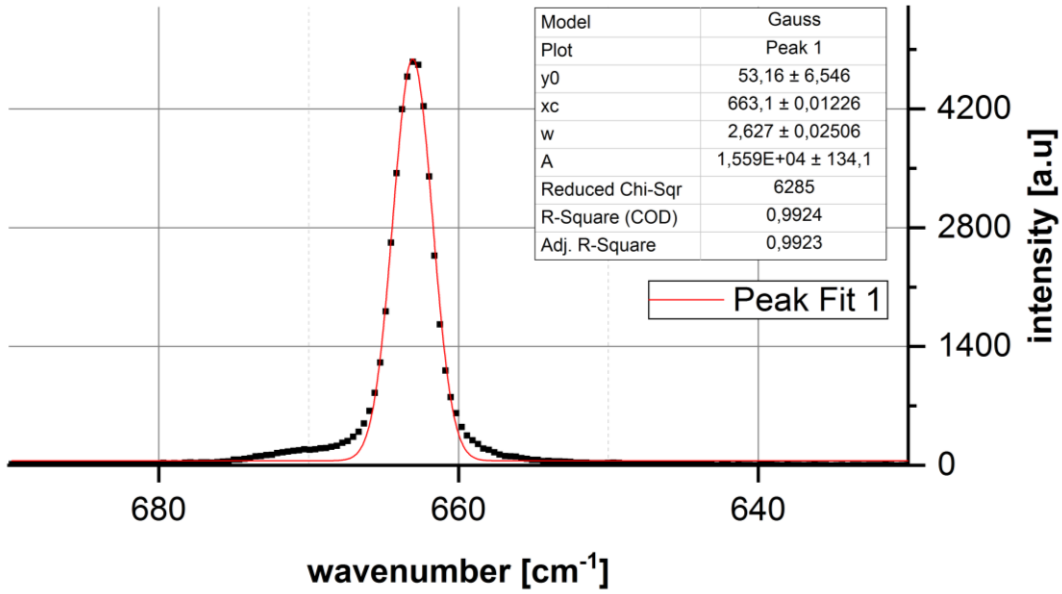

Figure A.28: Raman spectrum of solid UF_6 between 630 and 690 cm^{-1} measured at 488 nm and a groove density of 1800 g/mm and fitting for determination of band positions.

A.1.9 Supporting material to chapter 5.3

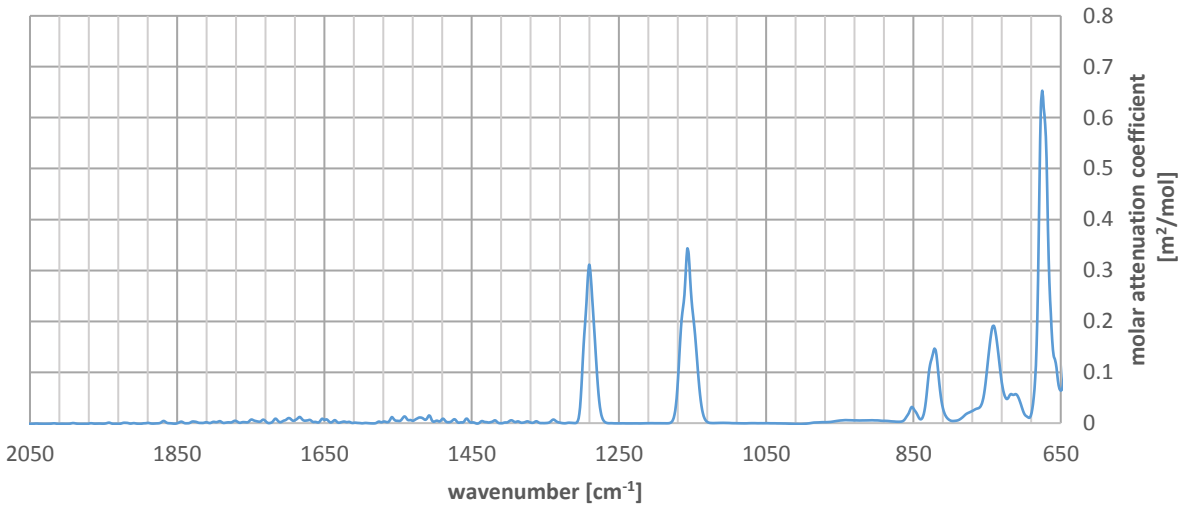

Figure A.29: Molar attenuation coefficient of UF_6 as determined by IR spectroscopy on a TENSOR 37 at a resolution of 4 cm^{-1}. However, the band at 740 cm^{-1} does not belong to UF_6 but has to be accounted to impurities of MoF_6.

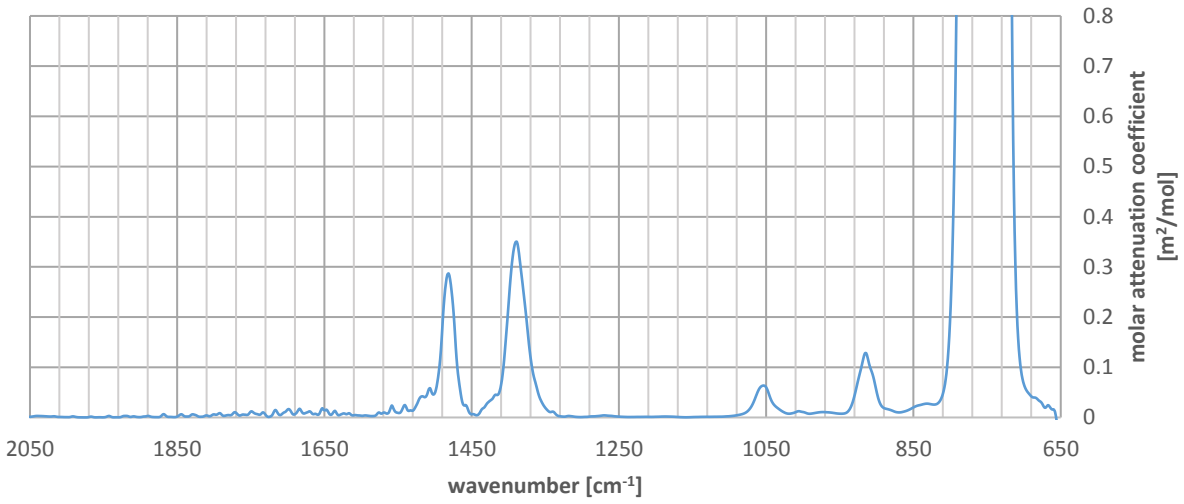

Figure A.30: Molar attenuation coefficient of MoF_6 as determined by IR spectroscopy on a TENSOR 37 at a resolution of 4 cm^{-1}.

A.1.10 Supporting material to chapter 5.4

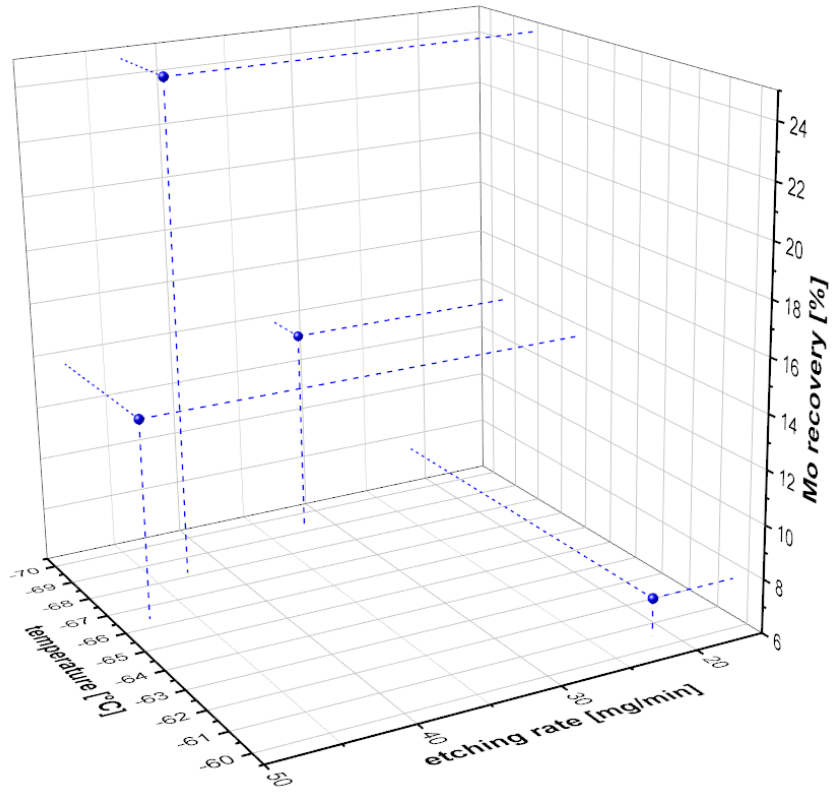

Figure A.31: Recovery of molybdenum in the first cold trap in dependence of etching rate and cold trap temperature for UMo05 targets.

A.1.11 Supporting material to chapter 5.5

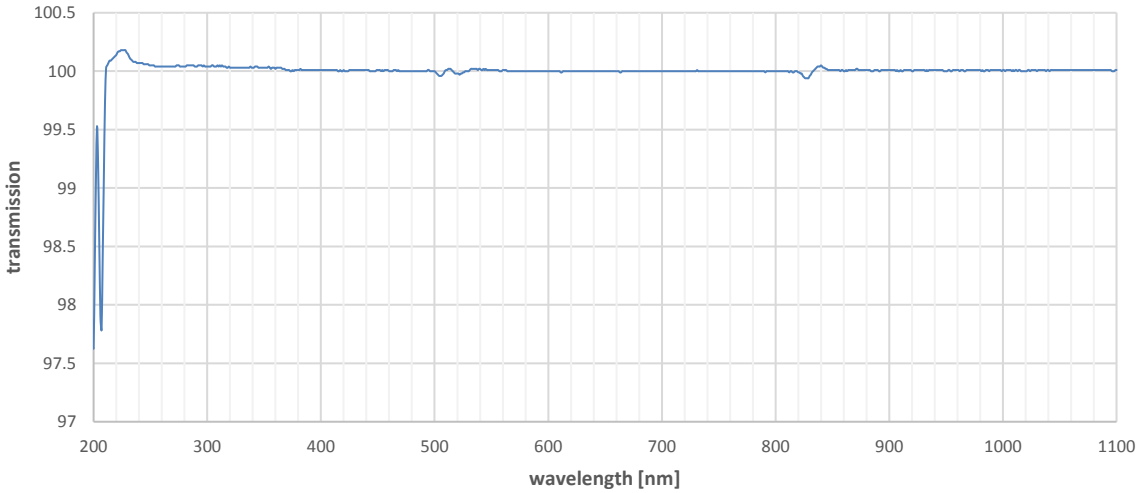

Figure A.32: UV/VIS spectrum of carbon monoxide at a pressure of 1 bar acquired using the measuring cell. Optical path length was 10 cm.

A.1.12 Supporting material to chapter 5.5.3

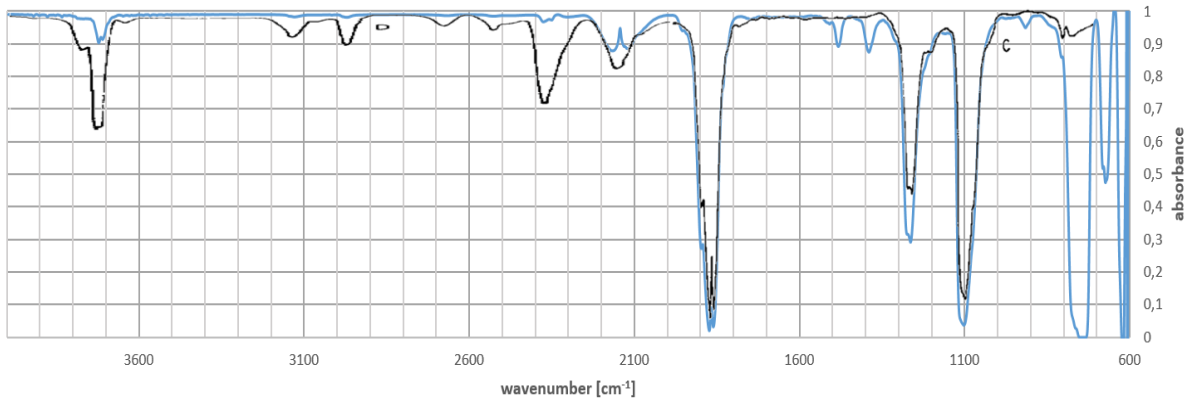

Figure A.33: Spectrum of the content of the high-pressure container (blue graph) and the spectrum of oxalyl fluoride (black graph) taken from literature [210]. The literature spectrum has been collected at different pressure; Region C between 700 and 2000 cm^{-1} was collected at 5.3 mbar, region D between 2000 and 4000 cm^{-1} was collected at 266 mbar.

A.1.13 Supporting material to chapter 5.6

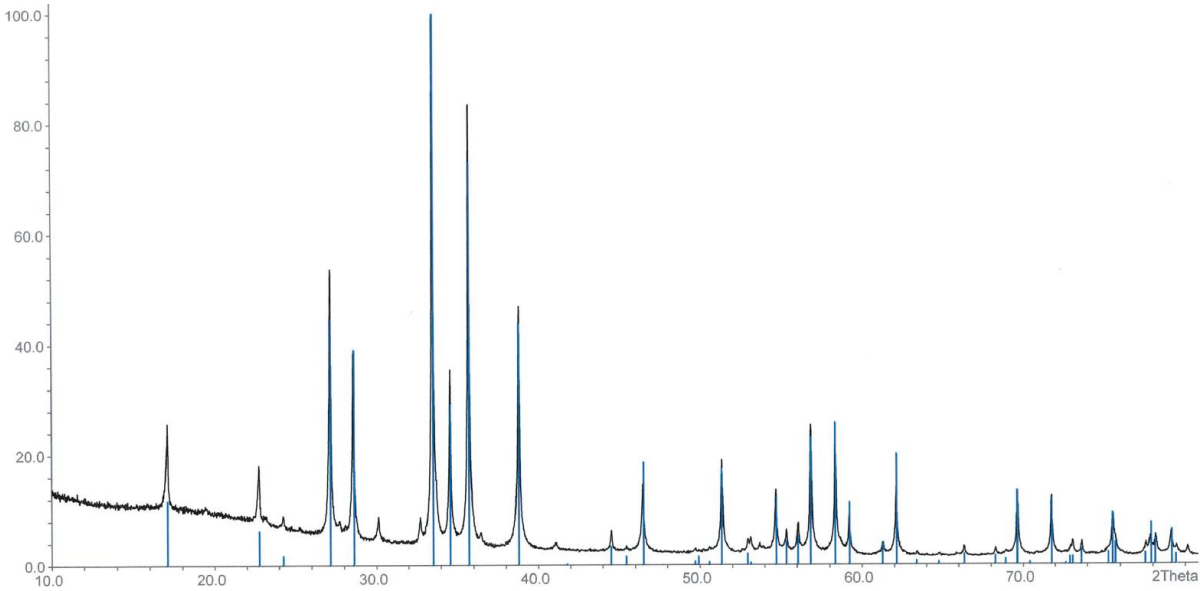

Figure A.34: Powder diffractogram of the U_3Si_2 slug for verification.

A.1.14 Supporting material to chapter 6.5

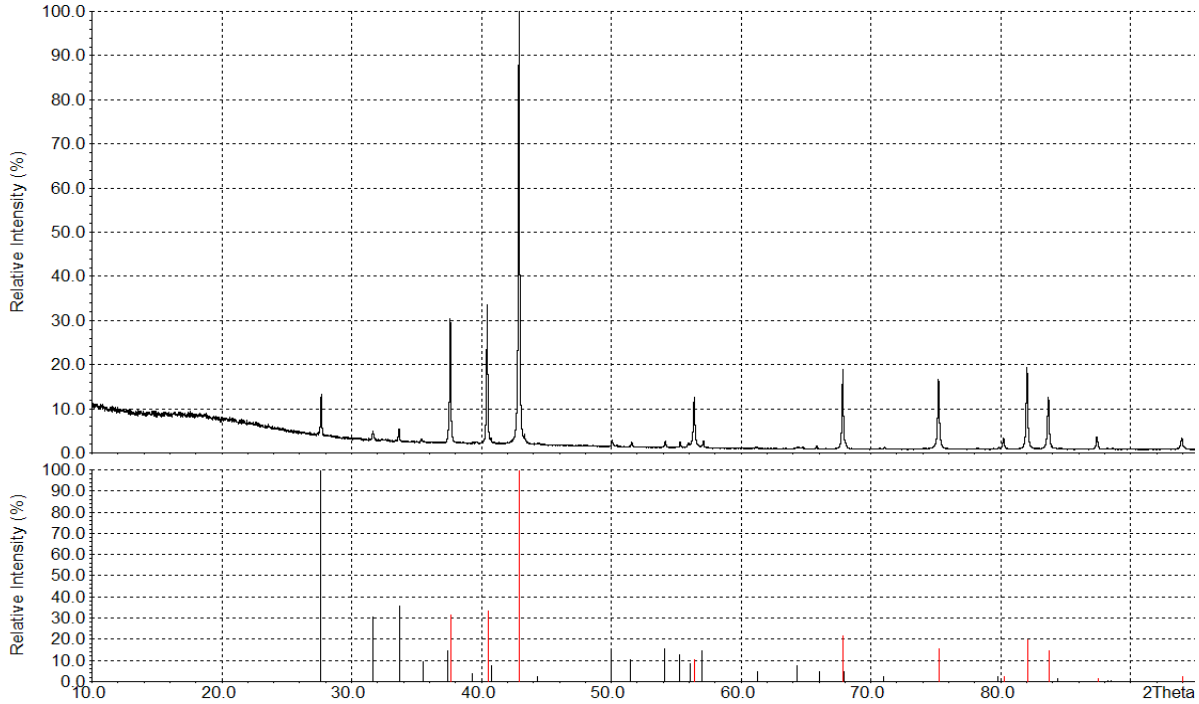

Figure A.35: X-ray powder diffractogram of the residues of the rhenium powder after fluorination as shown in Figure 6.23. All reflections can be assigned to either rhenium (red lines, ICDD file [05-0702], quality mark I) and copper fluoride CuF_2 (black lines, ICDD file [42-1244], quality mark I)

A.1.15 Supporting material to chapter 6.5.3

Figure A.36: UV/VIS spectrum of ReF_6 [183].

A.1.16 Supporting material to chapter 6.6.4

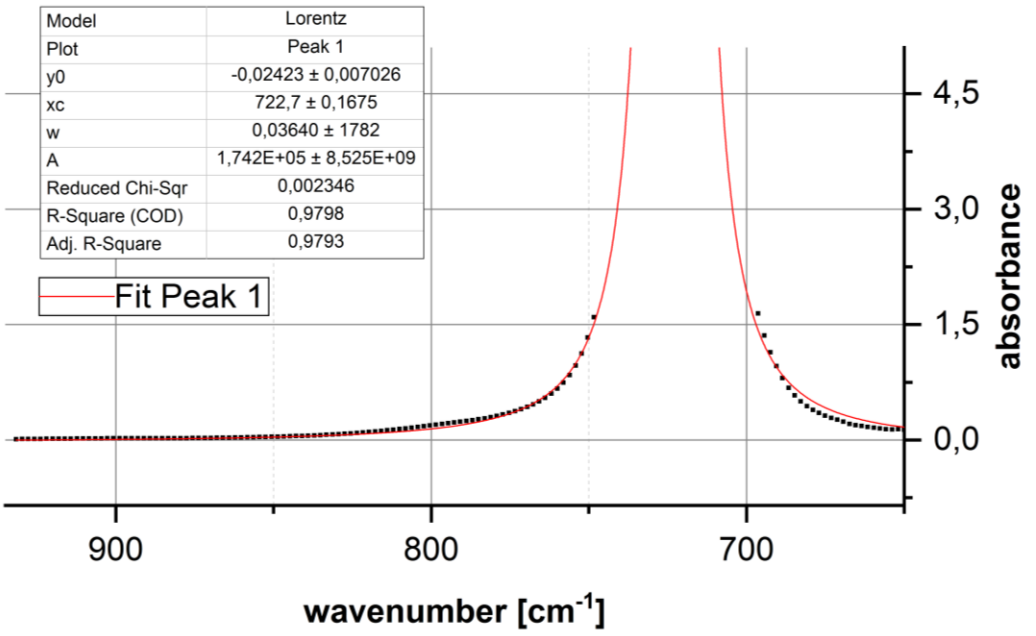

Figure A.37: Lorentzian fit for the determination of the band positions in the IR spectrum of OsF_6 between 650 and 940 cm^{-1}.

Model	Lorentz			
Plot	Peak 1	Peak 2	Peak 3	Peak 4
y0	0,00677 ± 6,35966E-4	0,00677 ± 6,35966E-4	0,00677 ± 6,35966E-4	0,00677 ± 6,35966E-4
xc	954,2 ± 0,3686	963,4 ± 0,1238	973,2 ± 0,3507	989,5 ± 0,8678
w	8,900 ± 1,334	6,903 ± 0,6192	12,30 ± 1,841	28,63 ± 2,839
A	0,1381 ± 0,02375	0,2758 ± 0,03119	0,2971 ± 0,06228	0,6893 ± 0,1039
Reduced Chi-Sqr	5,506E-07			
R-Square (COD)	0,9946			
Adj. R-Square	0,9925			

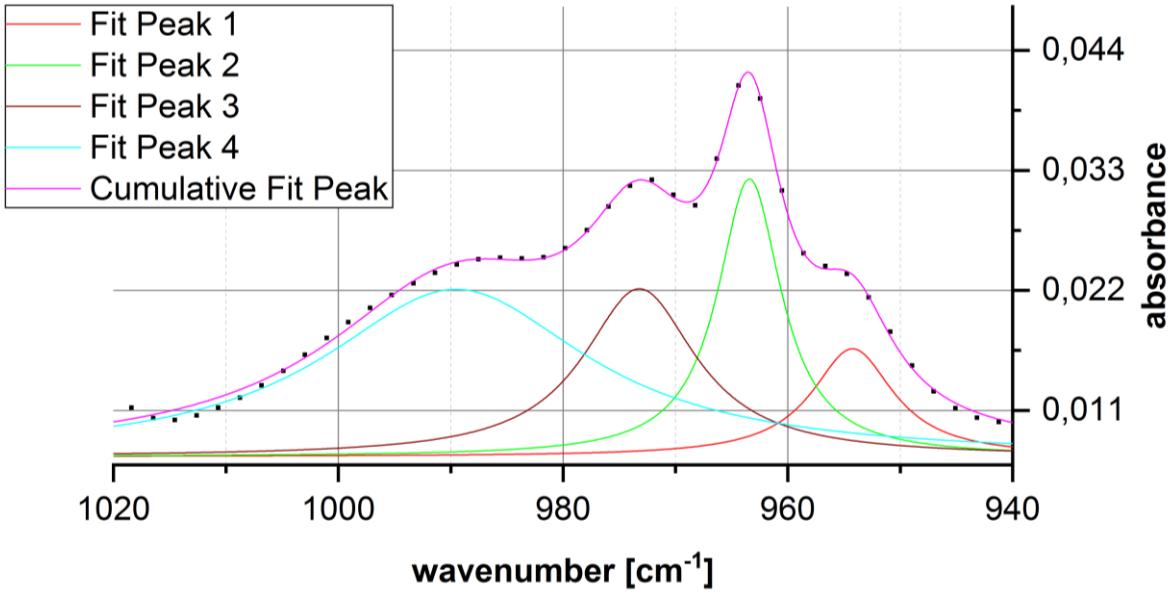

Figure A.38: Lorentzian fit for the determination of the band positions in the IR spectrum of OsF_6 between 940 and 1020 cm^{-1}.

Model	Lorentz	
Plot	Peak 1	Peak 2
y0	0,00328 ± 1,80047E-4	0,00328 ± 1,80047E-4
xc	1155 ± 0,1199	1101 ± 0,6125
w	22,70 ± 0,4258	19,35 ± 2,162
A	1,188 ± 0,02048	0,1827 ± 0,01833
Reduced Chi-Sqr	5,554E-07	
R-Square (COD)	0,9930	
Adj. R-Square	0,9925	

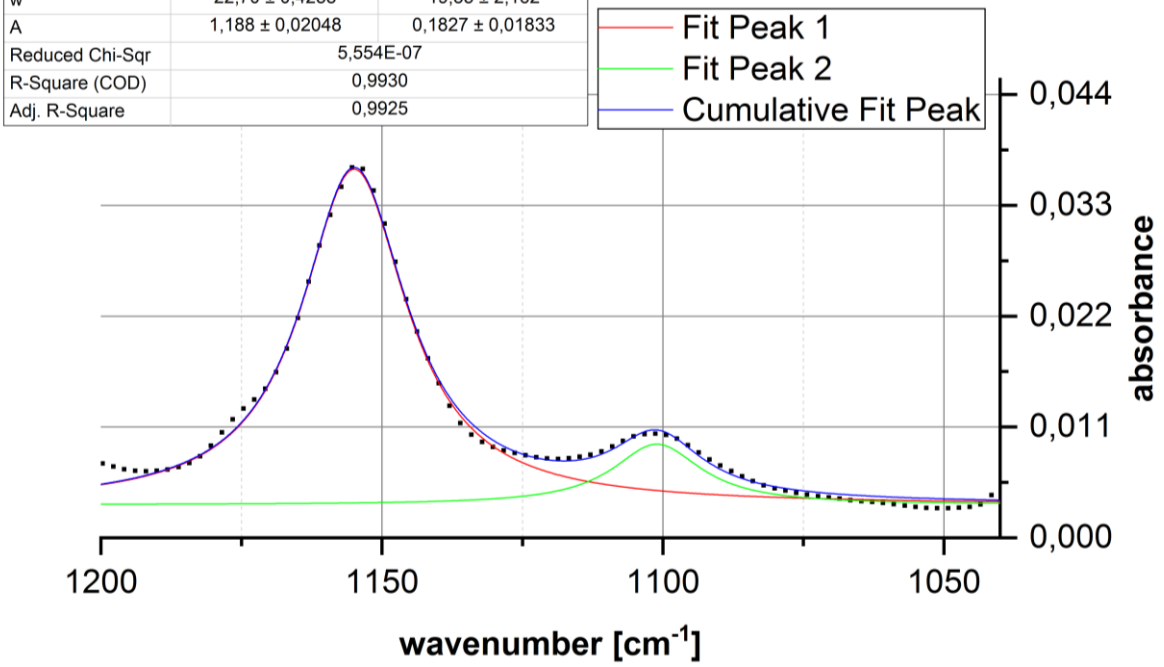

Figure A.39: Lorentzian fit for the determination of the band positions in the IR spectrum of OsF_6 between 1040 and 1200 cm^{-1}.

Model	Lorentz				
Plot	Peak 1	Peak 2	Peak 3	Peak 4	Peak 5
y0	-0,00255 ± 8,3351E-4	-0,00255 ± 8,3351E-4	-0,00255 ± 8,3351E-4	-0,00255 ± 8,3351E-4	-0,00255 ± 8,3351E-4
xc	1451 ± 0,08037	1380 ± 1,855	1344 ± 1,317	1282 ± 0,8172	1251 ± 2,961
w	18,88 ± 0,2632	40,48 ± 5,596	50,20 ± 3,711	7,837 ± 3,034	56,04 ± 10,18
A	10,24 ± 0,1166	2,945 ± 0,6484	6,950 ± 0,7578	0,2713 ± 0,09888	2,089 ± 0,3663
Reduced Chi-Sqr	3,252E-05				
R-Square (COD)	0,9923				
Adj. R-Square	0,9917				

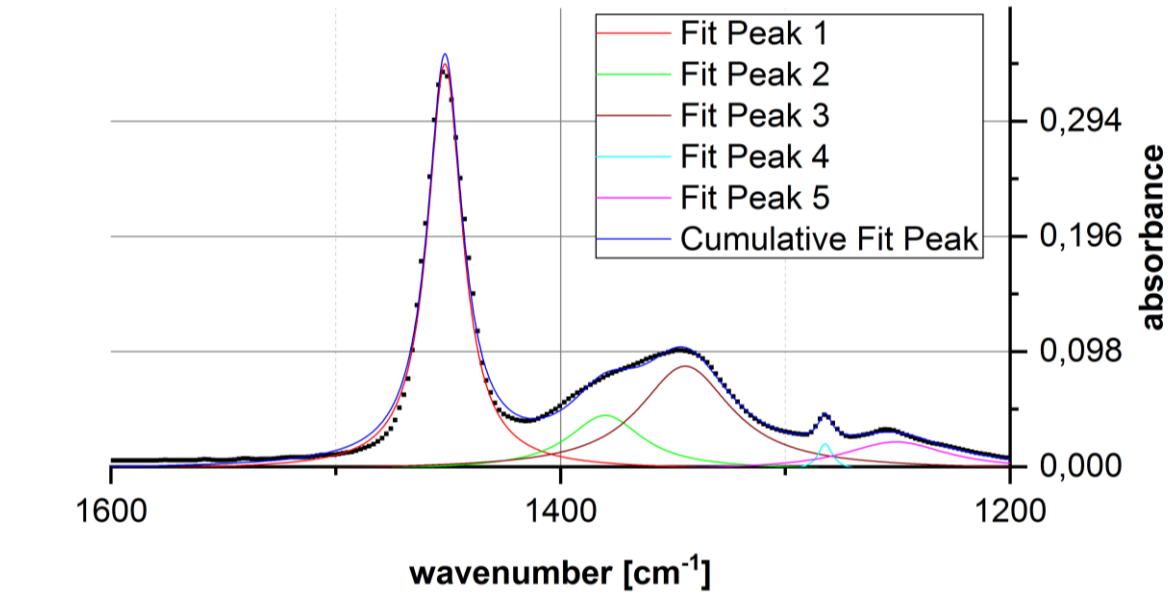

Figure A.40: Lorentzian fit for the determination of the band positions in the IR spectrum of OsF_6 between 1200 and 1600 cm^{-1}.

A.1.17 Supporting material to chapter 6.6.5

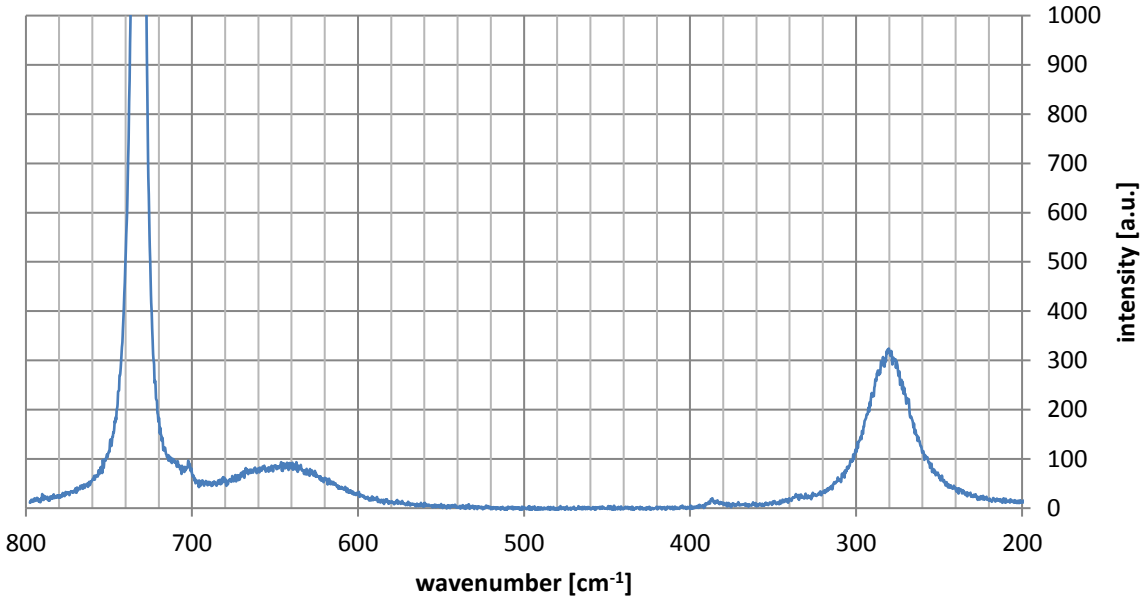

Figure A.41: Raman spectrum of liquid OsF_6 measured at a laser wavelength of 532 nm and a groove density of 1800 g/mm. The minor bands at 701 cm^{-1} does not belong to OsF_6, but instead to small impurities of IrF_6.

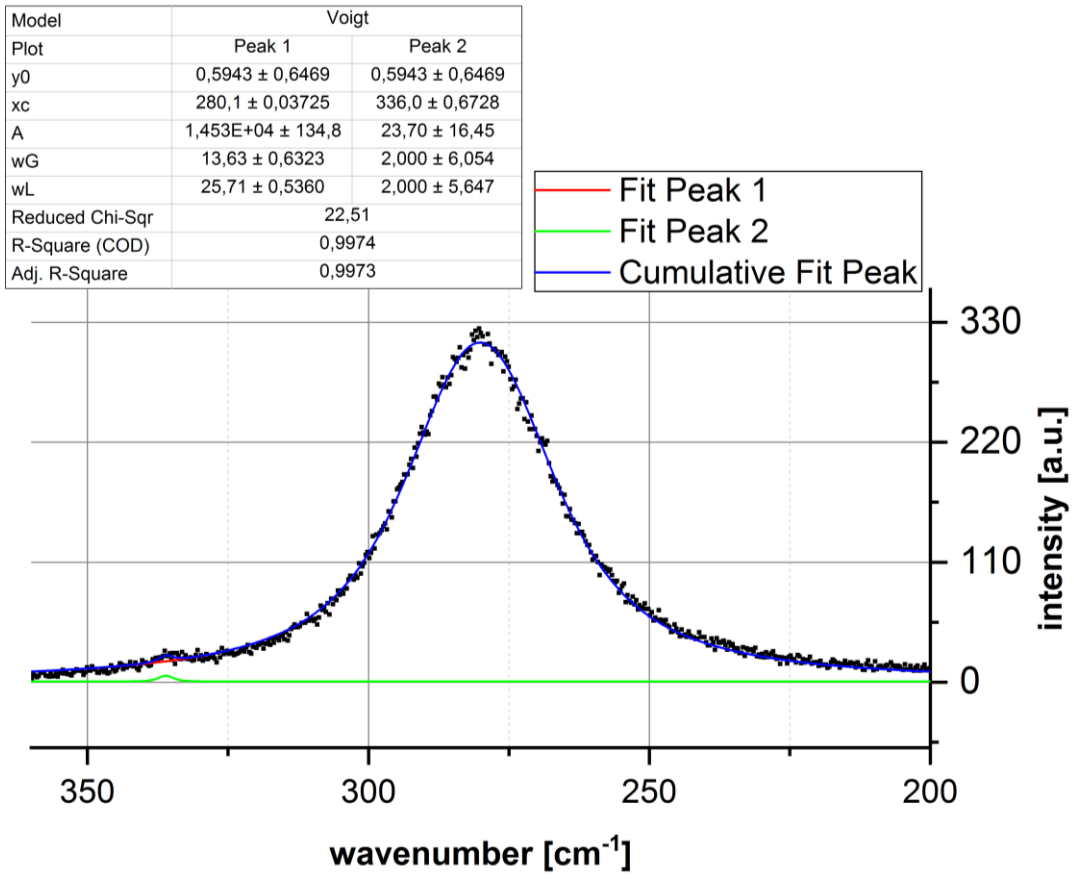

Figure A.42: Voigt fit for the determination of the band positions in the Raman spectrum of OsF_6 between 200 and 360 cm^{-1}.

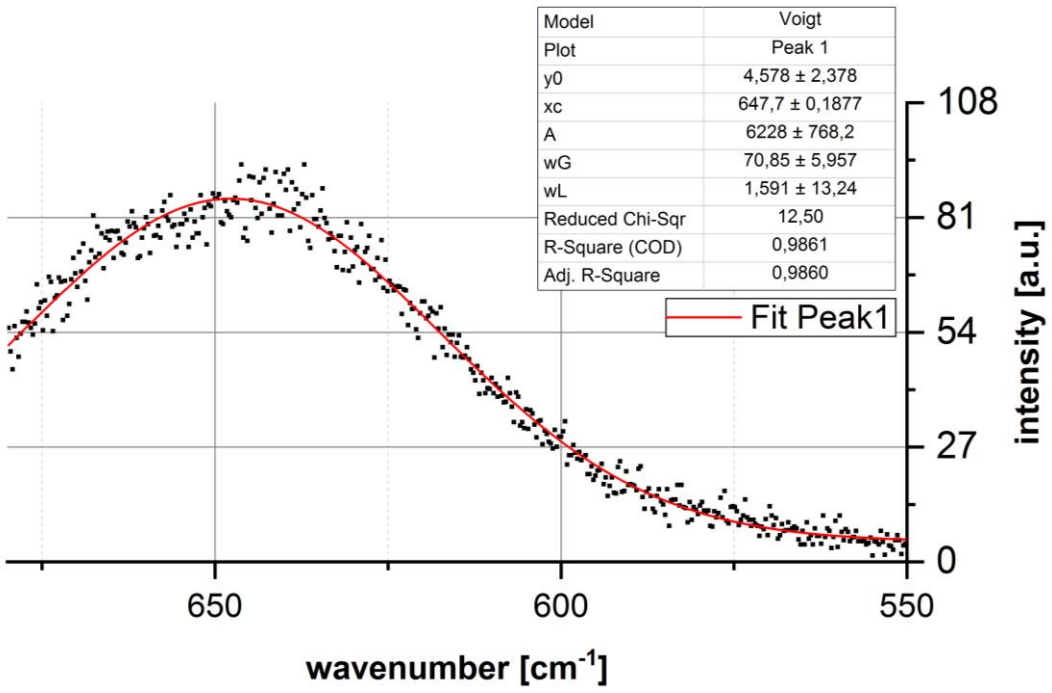

Figure A.43: Voigt fit for the determination of the band positions in the Raman spectrum of OsF_6 between 550 and 680 cm^{-1}.

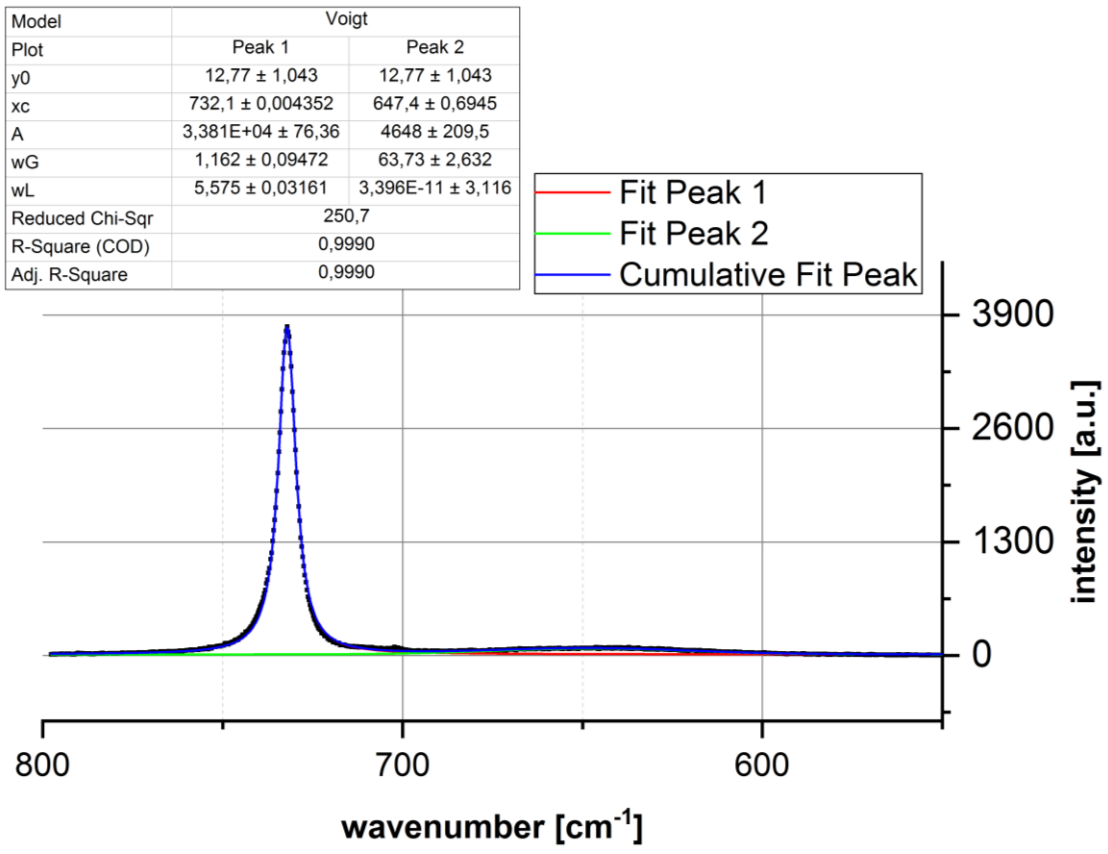

Figure A.44: Voigt fit for the determination of the band positions in the Raman spectrum of OsF_6 between 550 and 800 cm^{-1}.

A.1.18 Supporting material to chapter 6.7.4

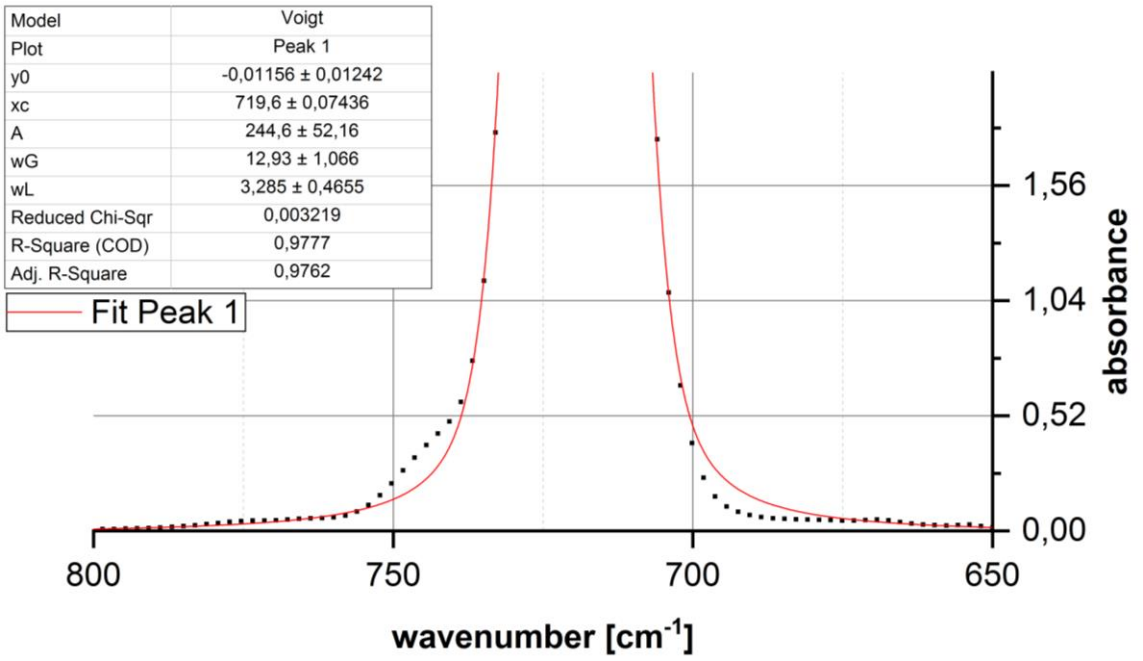

Figure A.45: IR spectrum of gaseous IrF_6 at 75.8 mbar measured with a resolution of 4 cm^{-1} and fit for determination of position of absorption bands between 650 and 800 cm^{-1}.

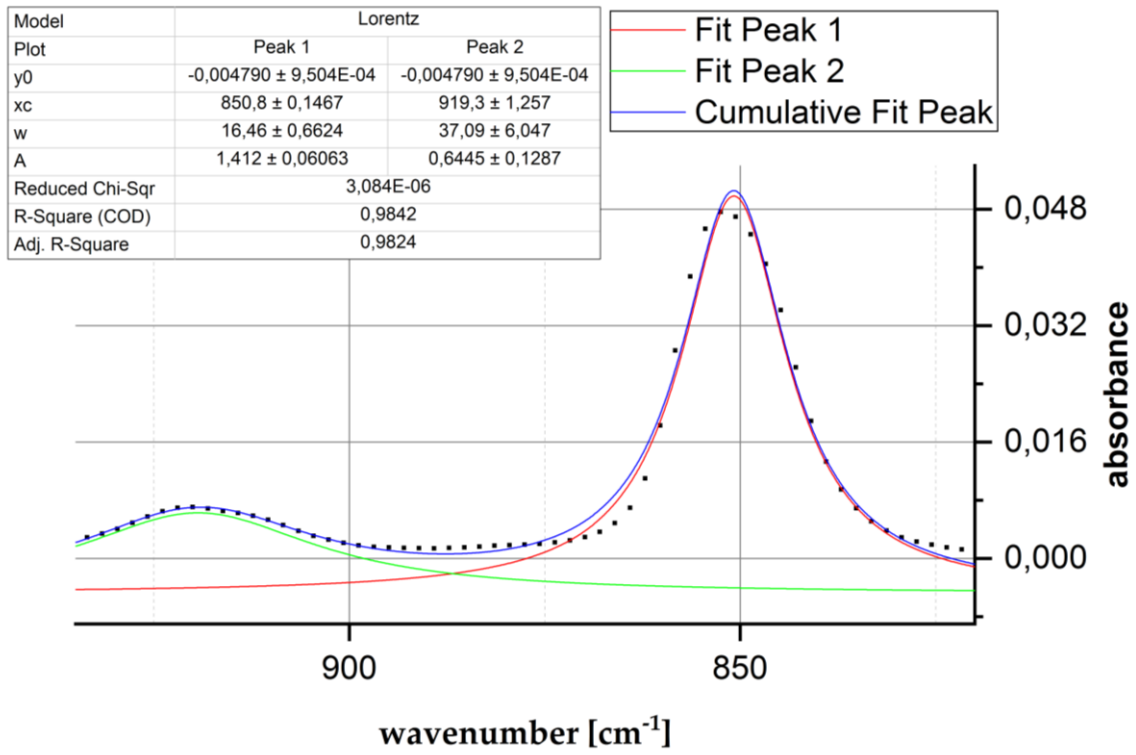

Figure A.46: IR spectrum of gaseous IrF_6 at 75.8 mbar measured with a resolution of 4 cm^{-1} and fit for determination of position of absorption bands between 820 and 935 cm^{-1}.

Model	Lorentz			
Plot	Peak 1	Peak 2	Peak 3	Peak 4
y0	6,945E-04 ± 2,637E-04	6,945E-04 ± 2,637E-04	6,945E-04 ± 2,637E-04	6,945E-04 ± 2,637E-04
xc	1031 ± 1,006	999,4 ± 1,702	976,3 ± 0,4189	963,4 ± 0,4629
w	29,38 ± 4,285	26,96 ± 7,964	24,09 ± 2,523	6,518 ± 2,508
A	0,1706 ± 0,03464	0,1248 ± 0,05233	0,4356 ± 0,06573	0,02651 ± 0,01349
Reduced Chi-Sqr	1,442E-07			
R-Square (COD)	0,9887			
Adj. R-Square	0,9860			

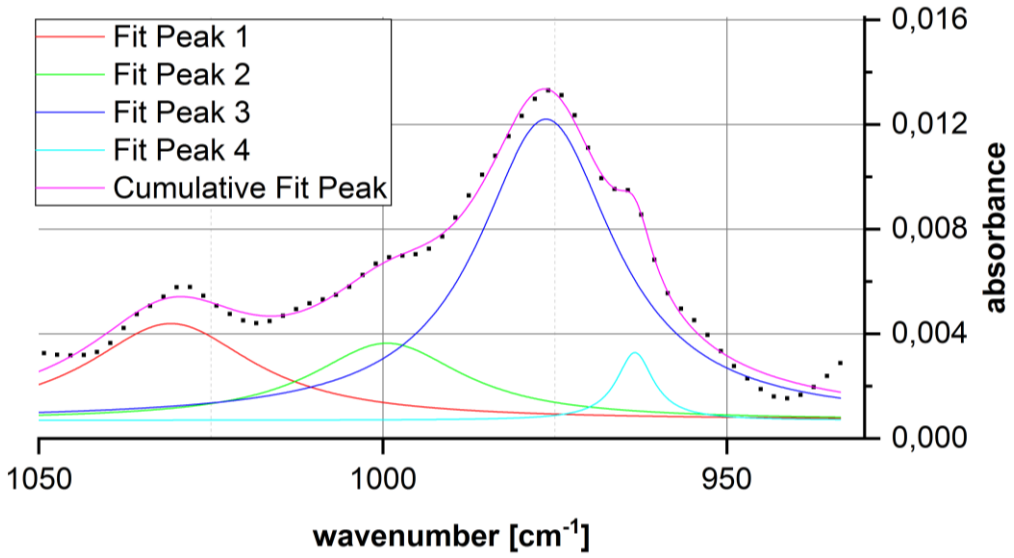

Figure A.47: IR spectrum of gaseous IrF_6 at 75.8 mbar measured with a resolution of 4 cm^{-1} and fit for determination of position of absorption bands between 935 and 1050 cm^{-1}.

Model	Lorentz				
Plot	Peak 1	Peak 2	Peak 3	Peak 4	Peak 5
y0	0,007014 ± 3,540E-04	0,007014 ± 3,540E-04	0,007014 ± 3,540E-04	0,007014 ± 3,540E-04	0,007014 ± 3,540E-04
xc	1282 ± 0,1069	1251 ± 0,3186	1227 ± 1,680	1183 ± 1,997	1151 ± 0,1632
w	6,964 ± 0,3635	24,26 ± 1,250	39,98 ± 6,974	36,61 ± 10,48	16,48 ± 0,6605
A	0,3542 ± 0,01566	1,604 ± 0,1485	1,010 ± 0,2566	0,3729 ± 0,1342	0,9742 ± 0,04390
Reduced Chi-Sqr	1,379E-06				
R-Square (COD)	0,9927				
Adj. R-Square	0,9915				

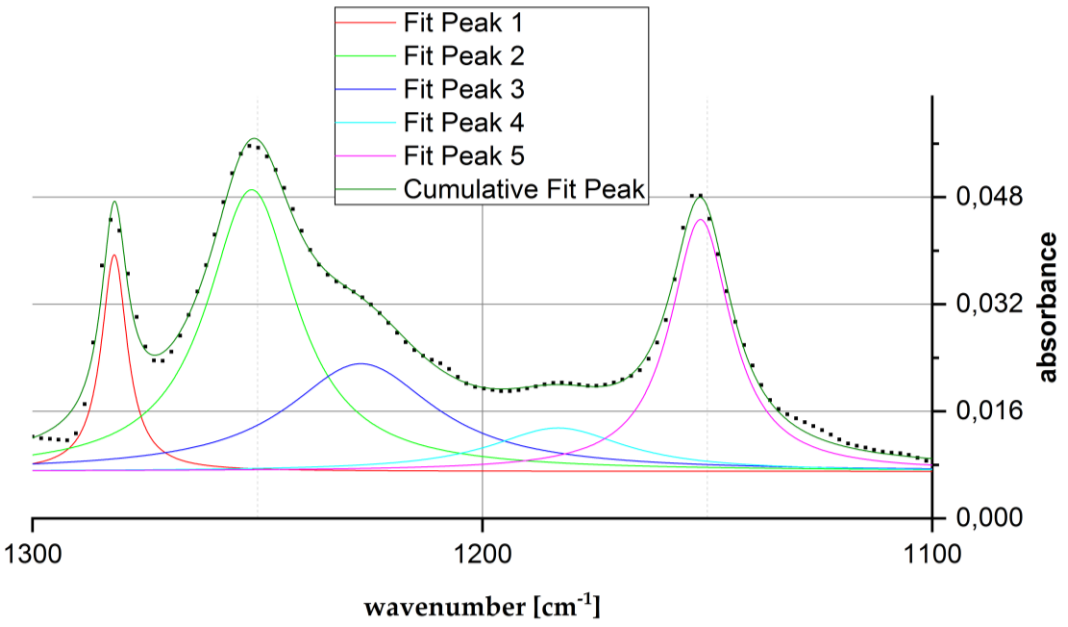

Figure A.48: IR spectrum of gaseous IrF_6 at 75.8 mbar measured with a resolution of 4 cm^{-1} and fit for determination of position of absorption bands between 1100 and 1300 cm^{-1}.

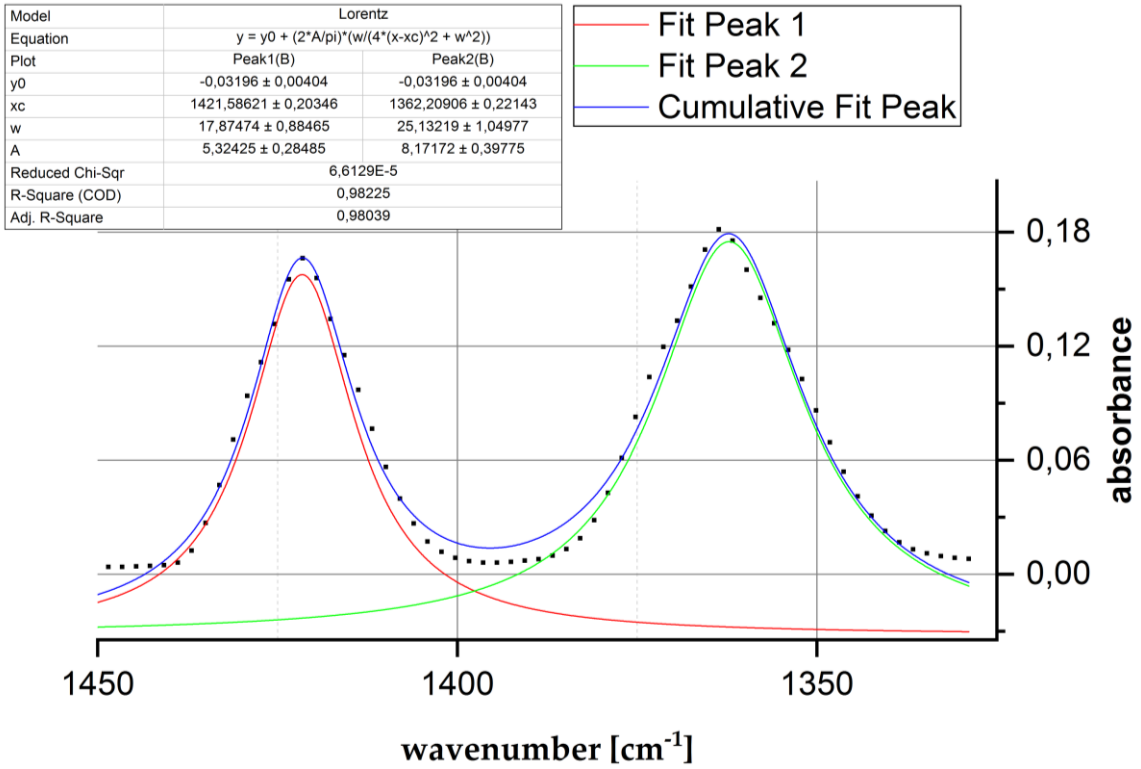

Figure A.49: IR spectrum of gaseous IrF_6 at 75.8 mbar measured with a resolution of 4 cm^{-1} and fit for determination of position of absorption bands between 1330 and 1450 cm^{-1}.

A.1.19 Supporting material to chapter 6.7.5

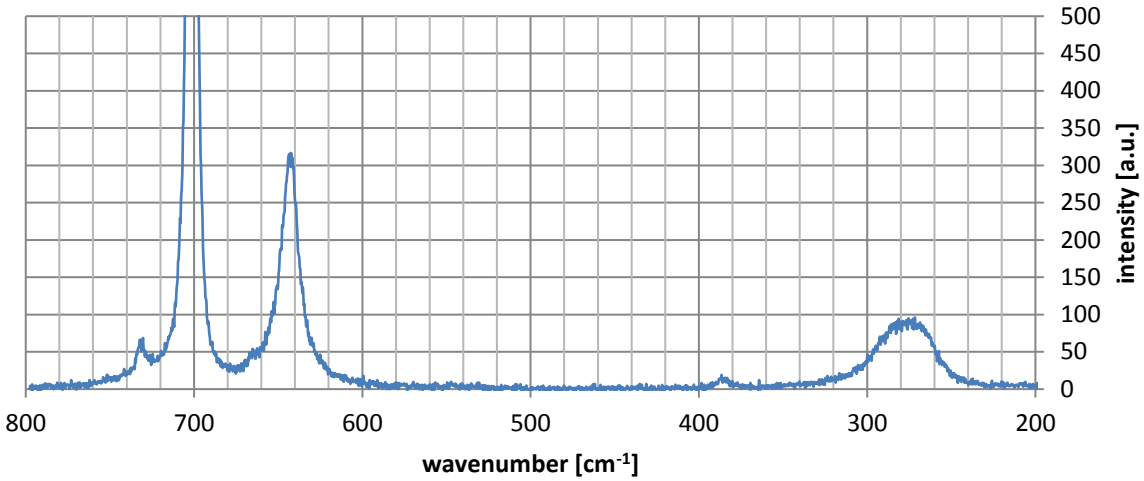

Figure A.50: Raman spectrum of liquid IrF_6 measured with a laser wavelength of 532 nm and a groove density of 1800 g/mm.

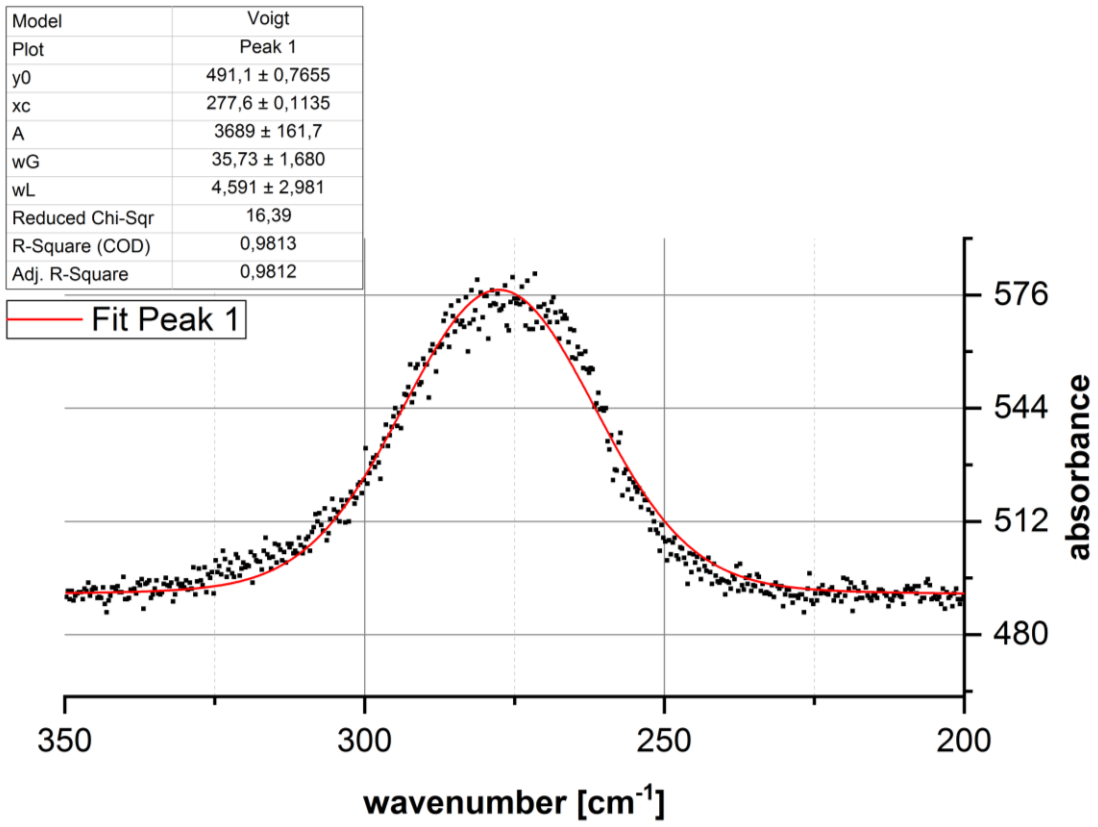

Figure A.51: Fit for determination of position of absorption bands between 200 and 350 cm^{-1} of IrF_6.

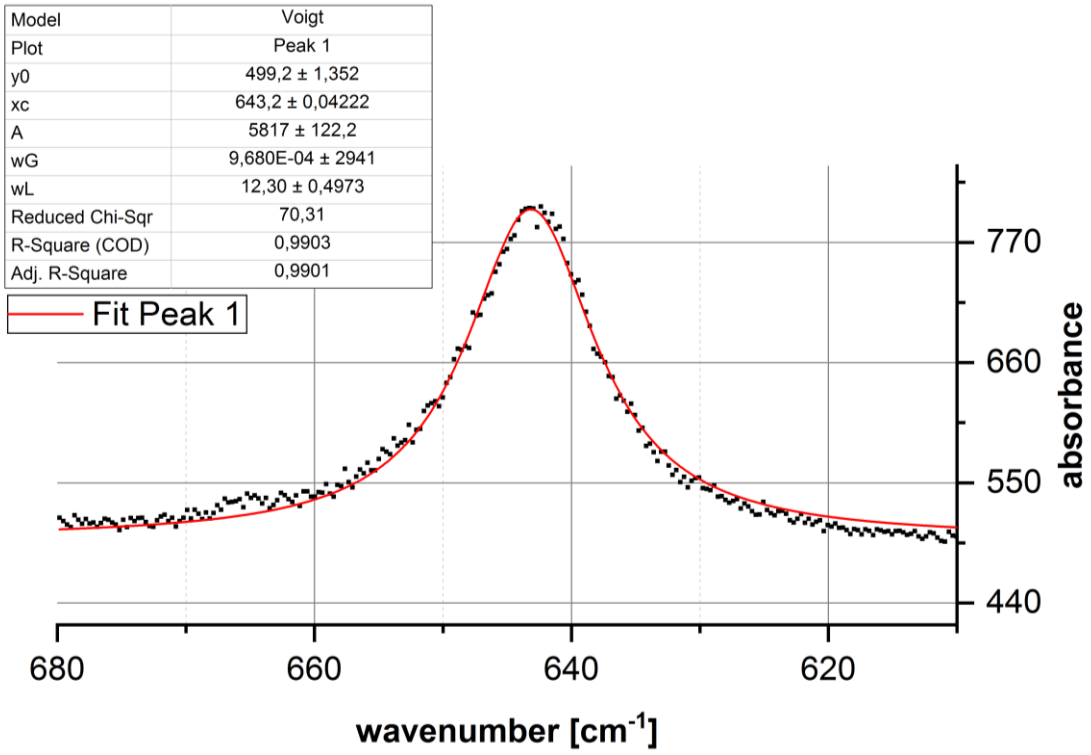

Figure A.52: Fit for determination of position of absorption bands between 610 and 680 cm^{-1} of IrF_6.

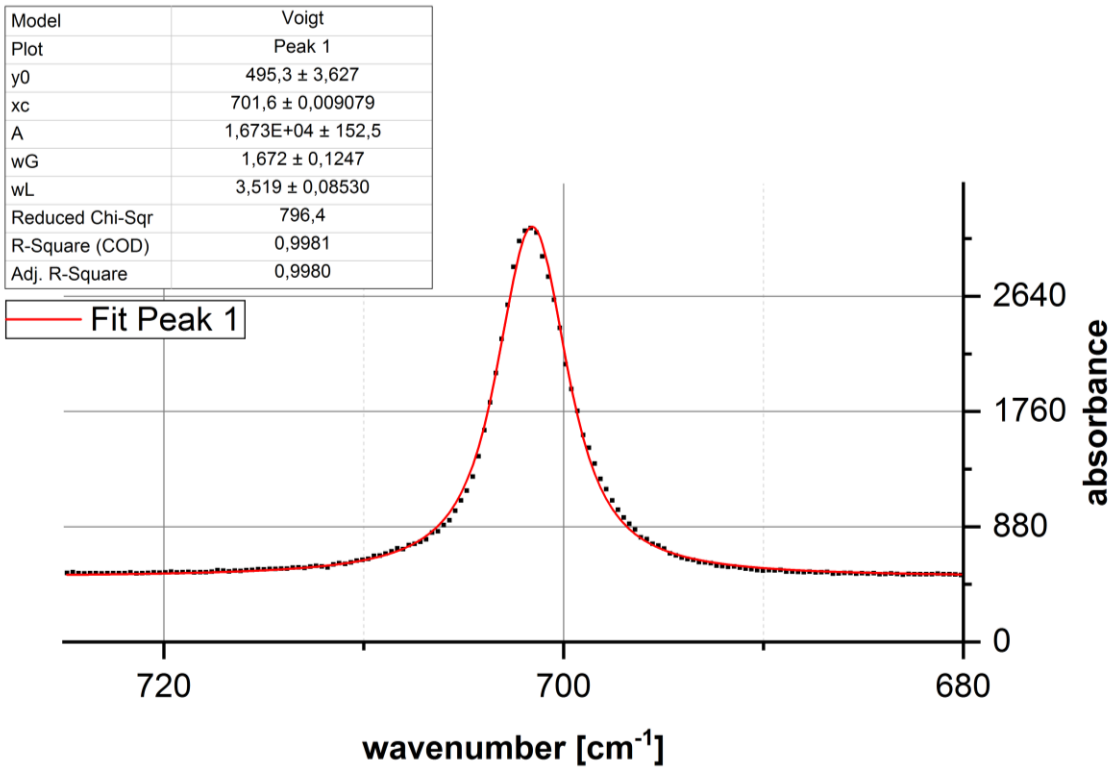

Figure A.53: Fit for determination of position of absorption bands between 680 and 730 cm^{-1} of IrF_6.

A.1.20 Supporting material to chapter 6.9.4

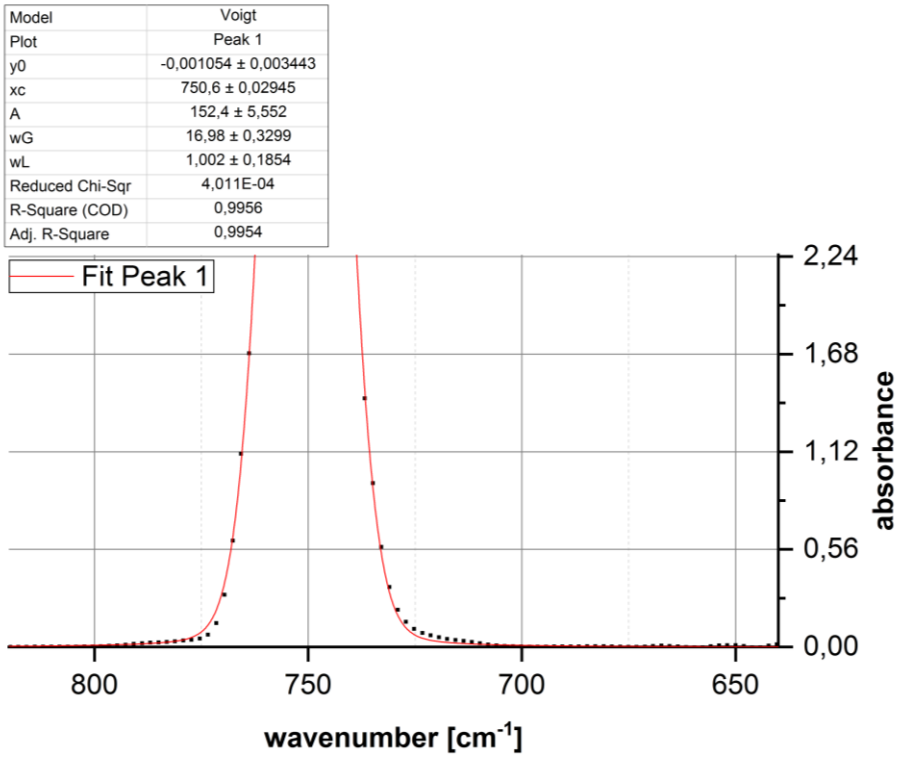

Figure A.54: IR spectrum of gaseous TeF_6 at 90.6 mbar measured with a resolution of 4 cm^{-1} and fit for determination of position of absorption bands between 640 and 820 cm^{-1}.

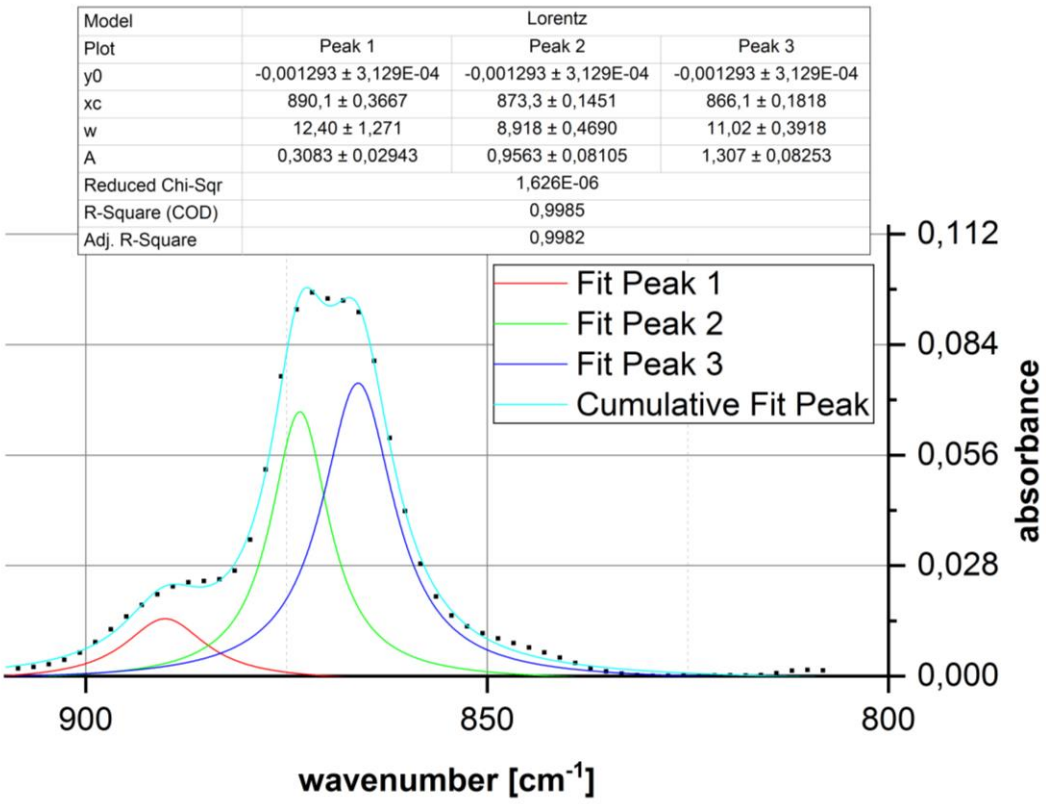

Figure A.55: IR spectrum of gaseous TeF_6 at 90.6 mbar measured with a resolution of 4 cm^{-1} and fit for determination of position of absorption bands between 810 and 910 cm^{-1}.

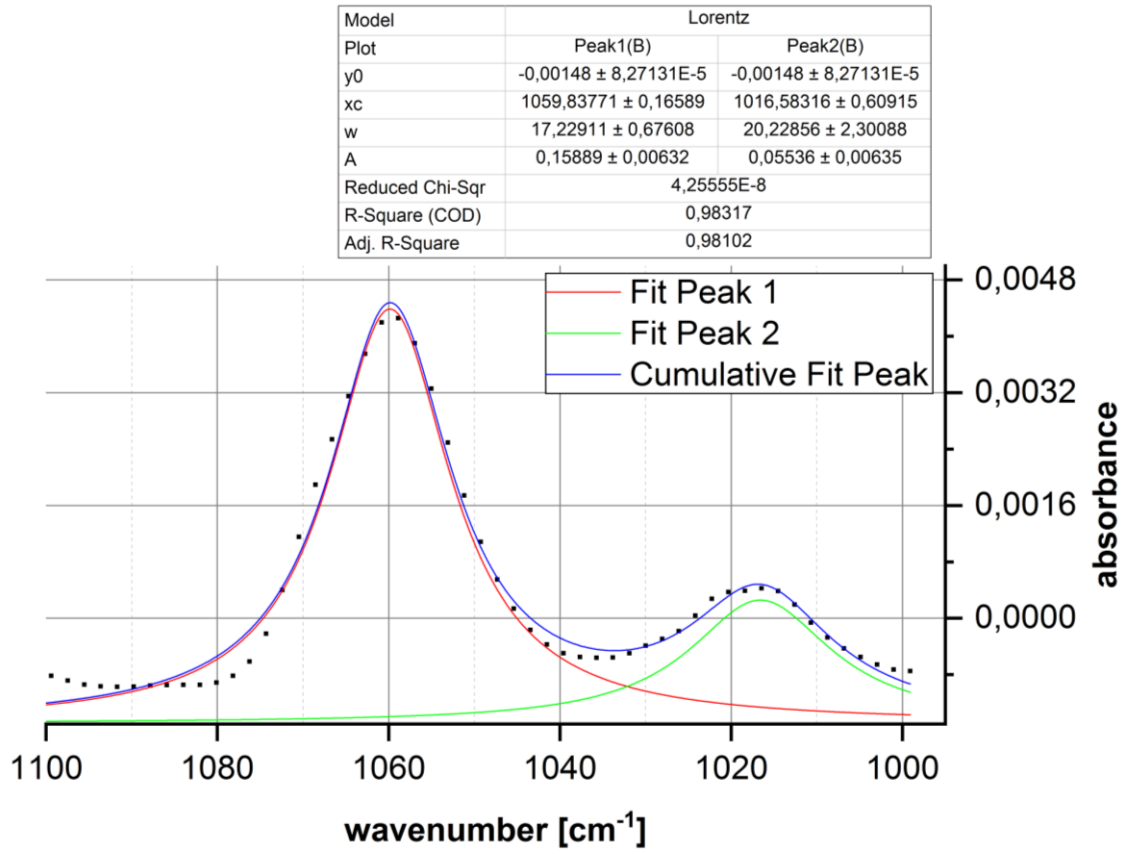

Figure A.56: IR spectrum of gaseous TeF_6 at 90.6 mbar measured with a resolution of 4 cm^{-1} and fit for determination of position of absorption bands between 1000 and 1100 cm^{-1}.

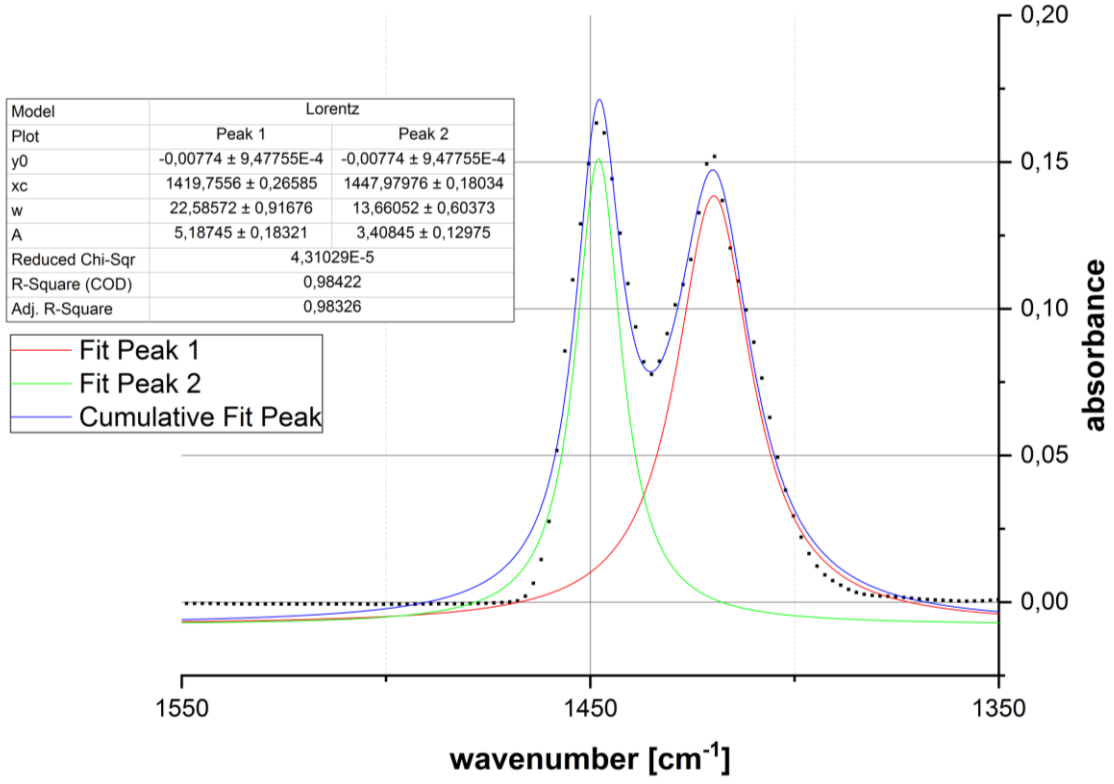

Figure A.57: IR spectrum of gaseous TeF_6 at 90.6 mbar measured with a resolution of 4 cm^{-1} and fit for determination of position of absorption bands between 1350 and 1550 cm^{-1}.

A.1.21 Supporting material to chapter 6.9.5

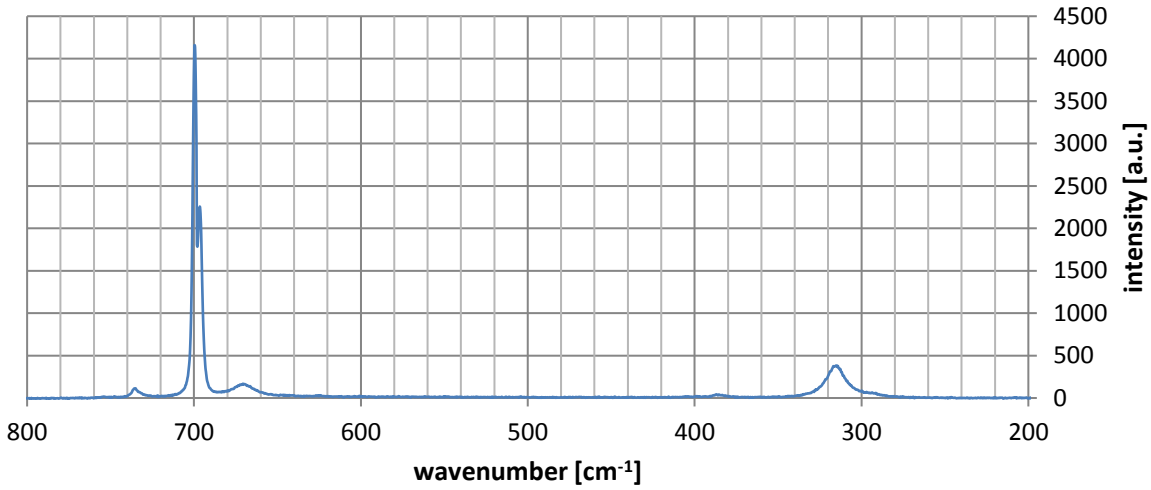

Figure A.58: Raman spectrum of liquid TeF_6 at 22 °C under intrinsic pressure measured at a laser wavelength of 532 nm and a groove density of 1800 g/mm.

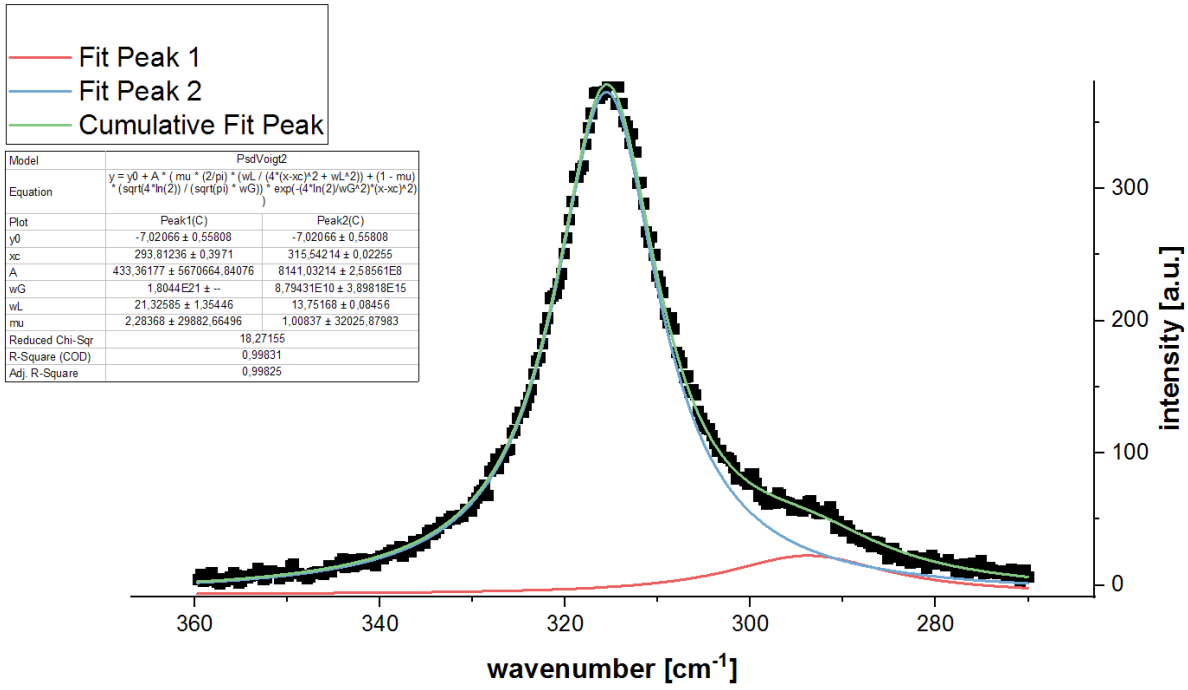

Model	PsdVoigt2	
Equation	y = y0 + A * (mu * (2/pi) * (wL / (4*(x-xc)^2 + wL^2)) + (1 - mu) * (sqrt(4*ln(2)) / (sqrt(pi) * wG)) * exp(-(4*ln(2)/wG^2)*(x-xc)^2))	
Plot	Peak1(C)	Peak2(C)
y0	-7,02066 ± 0,55808	-7,02066 ± 0,55808
xc	293,81236 ± 0,3971	315,54214 ± 0,02255
A	433,36177 ± 5670664,84076	8141,03214 ± 2,58561E8
wG	1,8044E21 ± --	8,79431E10 ± 3,89818E15
wL	21,32585 ± 1,35446	13,75168 ± 0,08456
mu	2,28368 ± 29882,66496	1,00837 ± 32025,87983
Reduced Chi-Sqr	18,27155	
R-Square (COD)	0,99831	
Adj. R-Square	0,99825	

Figure A.59: Fit of the Raman spectrum of TeF_6 between 270 and 360 cm^{-1}.

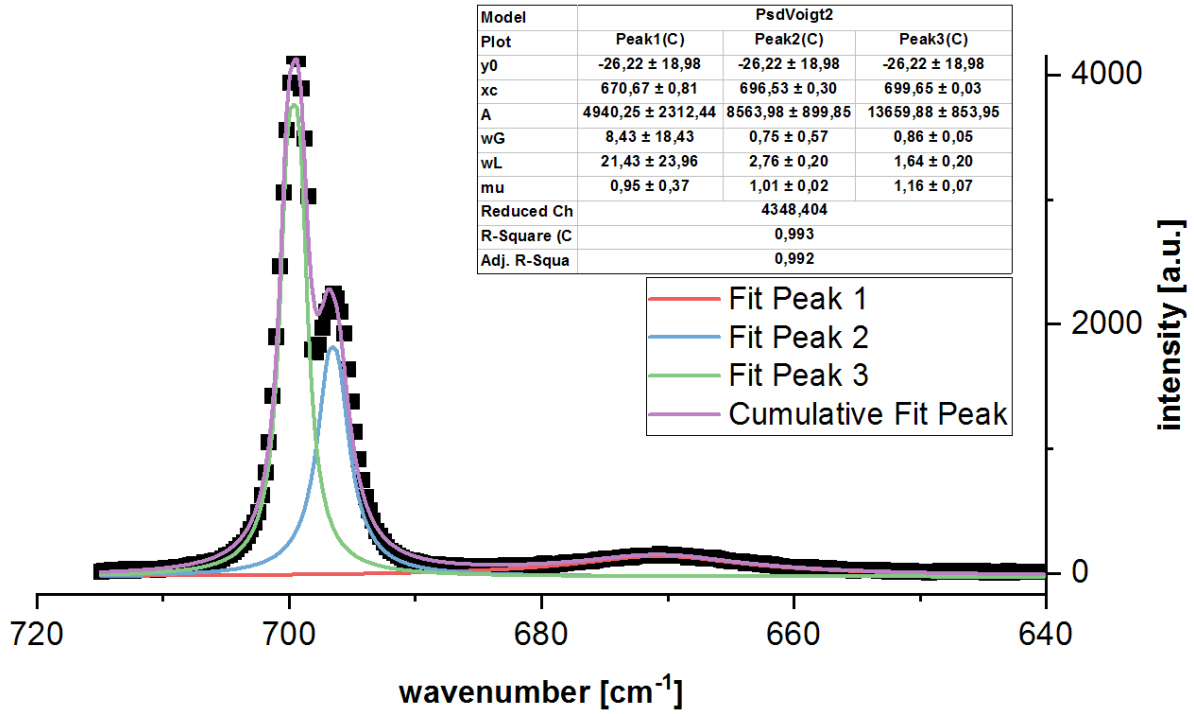

Figure A.60: Fit of the Raman spectrum of TeF_6 between 640 and 720 cm^{-1}.

A.2 Technical Drawings

The entire design of the fluorination line is documented in technical drawings. In order to keep the handling of this thesis comfortable, only the most important ones are shown here.

A.2.1 The high-pressure container

POS-NR.	BENENNUNG	MATERIAL	MENGE
1	Druckkörper		1
2	FFKM O-Ring 21x1.5mm		1
3	Saphirscheibe 25x5mm		1
4	Oberteil		1
5	Stopfen		1

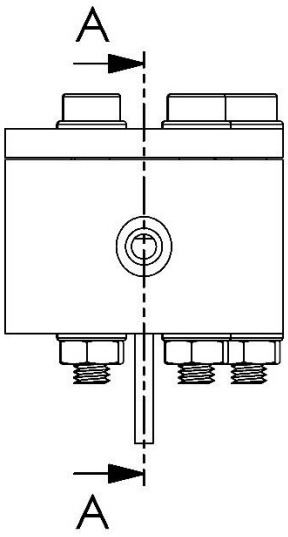

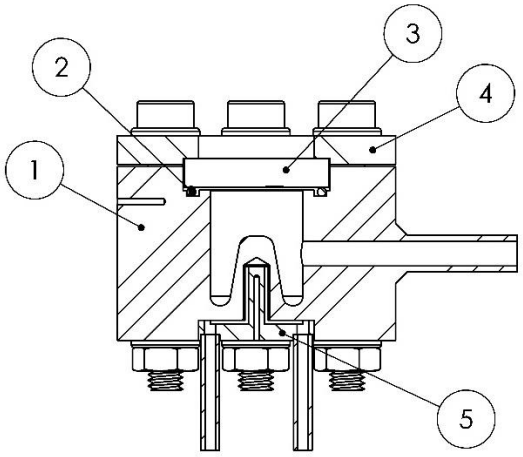

SCHNITT A-A

WENN NICHT ANDERS DEFINIERT: BEMASSUNGEN SIND IN MILLIMETER OBERFLÄCHENBESCHAFFENHEIT: TOLERANZEN: LINEAR: WINKEL:	OBERFLÄCHENGÜTE:	ENTGRATEN UND SCHARFE KANTEN BRECHEN	ZEICHNUNG NICHT SKALIEREN	ÄNDERUNG		
	NAME	SIGNATUR	DATUM	BENENNUNG:		
GEZEICHNET	Chemnitz		12.02.2020	High-pressure chamber		
GEPRÜFT						
GENEHMIGT						
PRODUKTION						
QUALITÄT				WERKSTOFF:	ZEICHNUNGSNR.	A4
				GEWICHT:	MASSSTAB:1:1	BLATT 1 VON 1

Figure A.61: High-pressure container, all parts mounted.

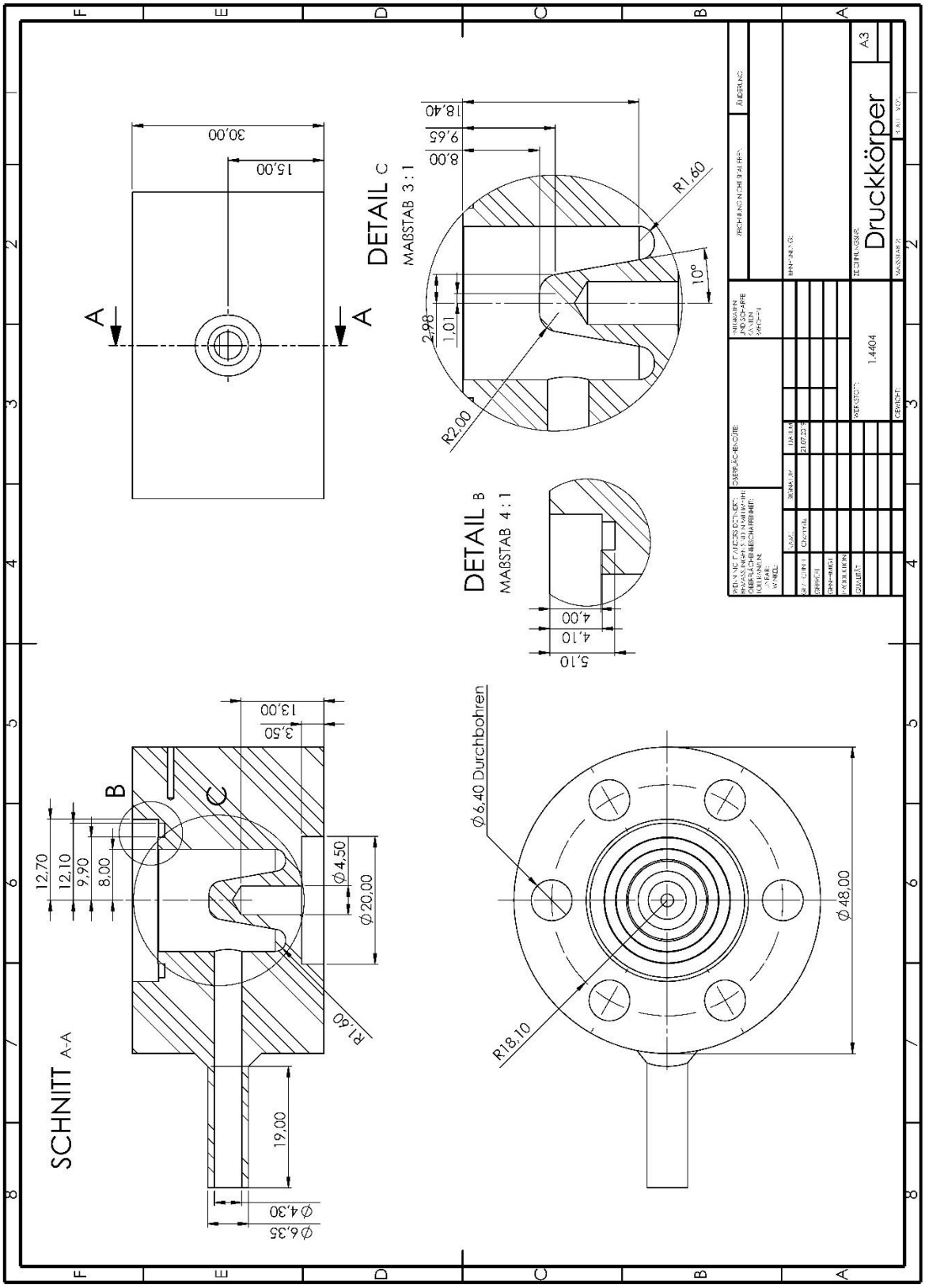

Figure A.62: Pressure hull (in German Druckkörper).

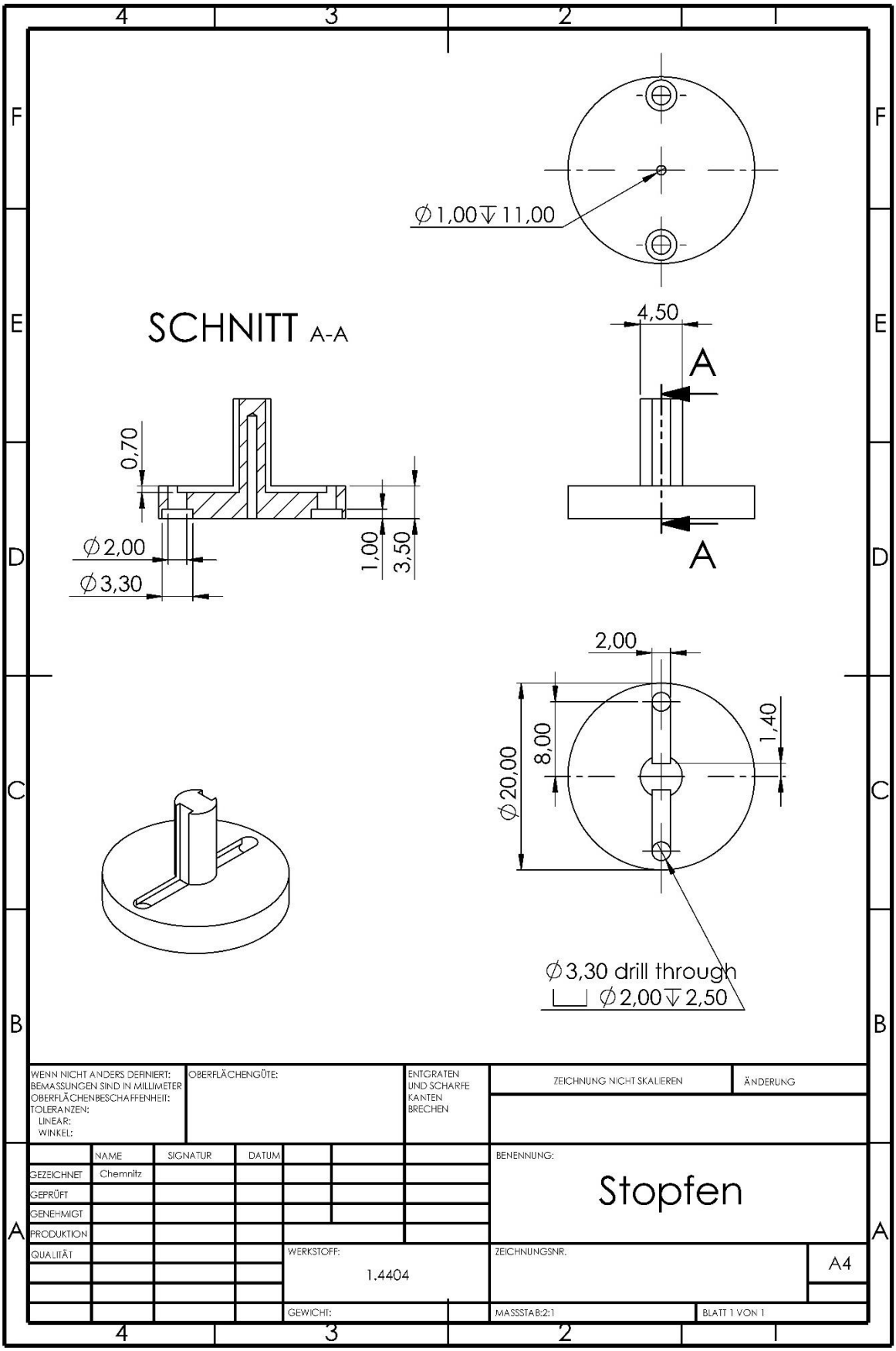

Figure A.63: The plug (Stopfen in German) allows the cooling of the cool finger with liquid nitrogen. It is soldered onto the pressure hull.

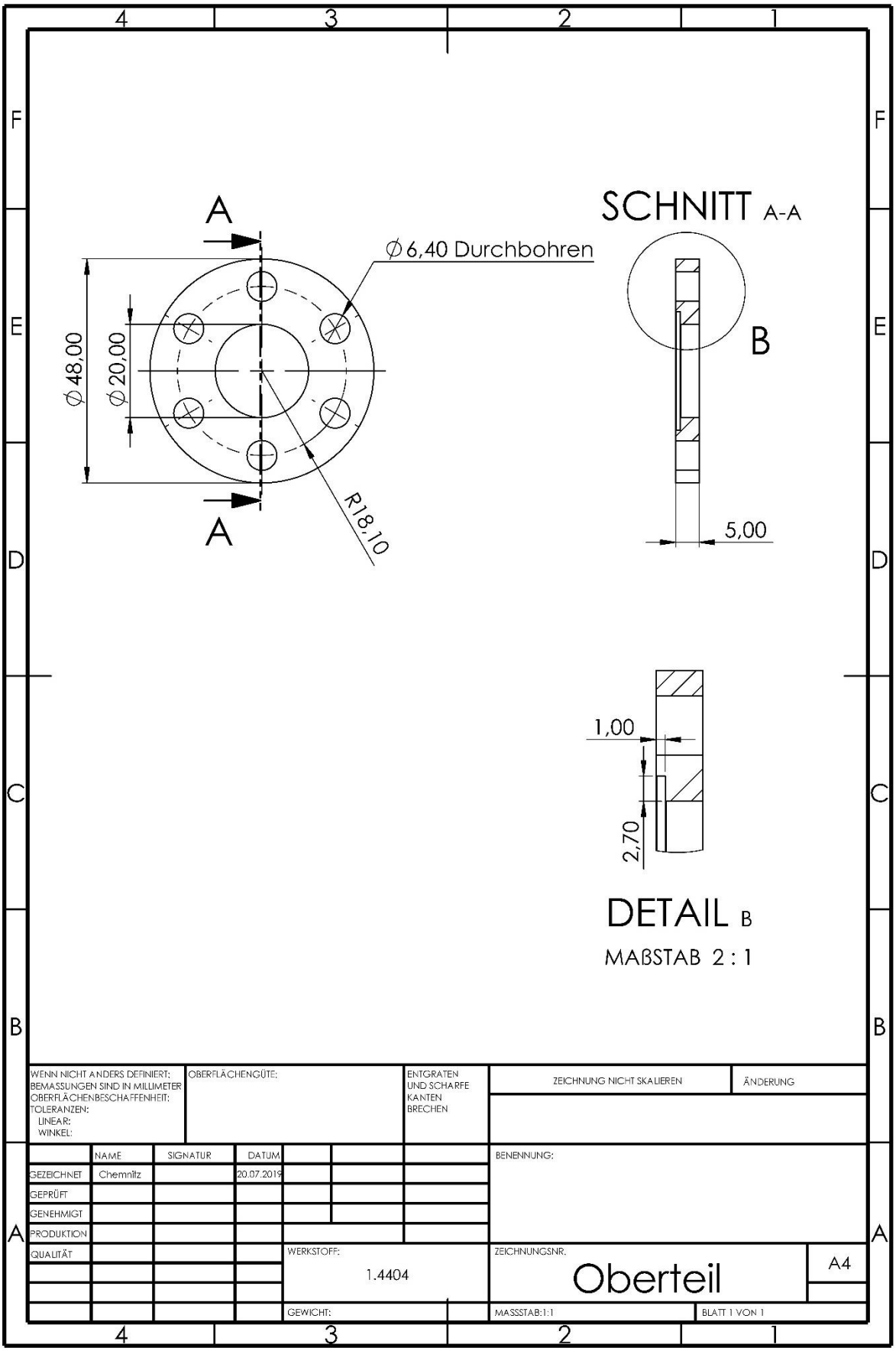

Figure A.64: The lid (Oberteil in German) tightening the sapphire window to the pressure hull.

A.2.2 The measuring cell

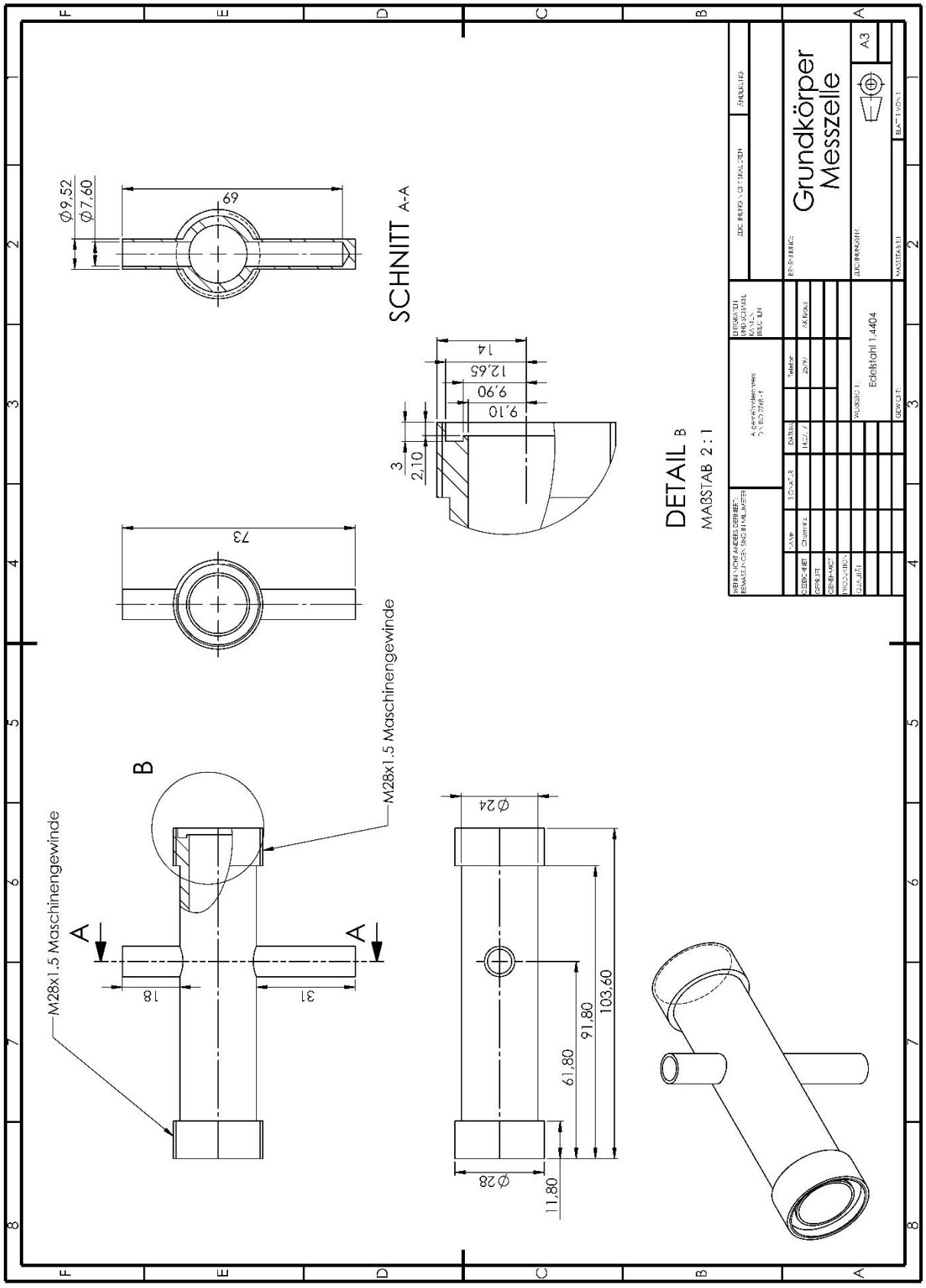

Figure A.65: The main body of the measuring cell as used for the acquisition of all gas phase IR spectra.

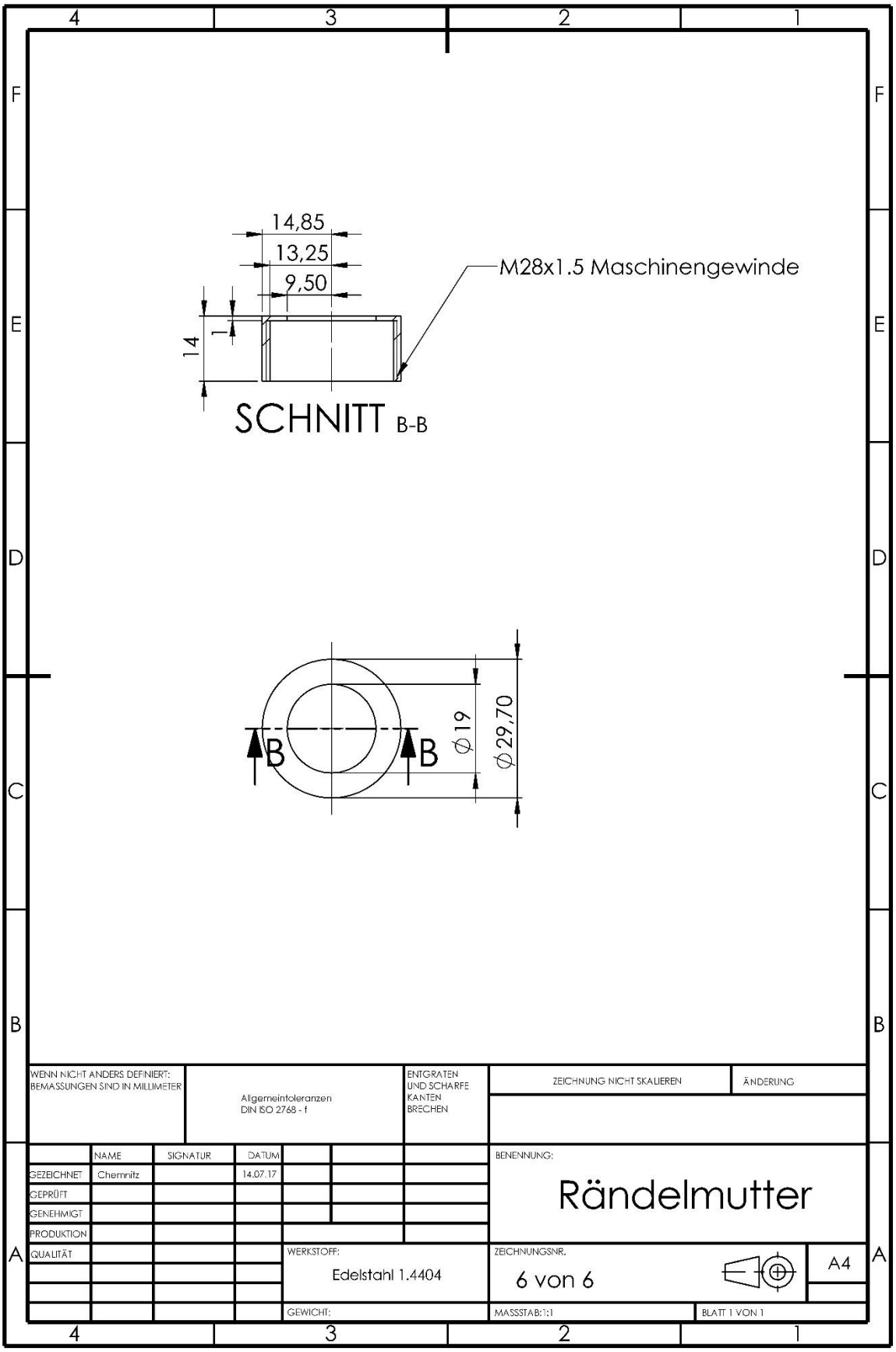

Figure A.66: The two knurled nuts (German term Rändelmutter) holding the sapphire windows in pla

List of Figures

List of Tables

Own Publications

The following own publications are related to this work:

Preparation of Metal Fluorides and Separation Processes
Tobias Chemnitz, Florian Kraus, Winfried Petry, Riane Stene, Stefan Rudel, Christian Steyer
PCT application, submitted to the European Patent Office, March 2020

A new Approach in Molybdenum Separation
Tobias Chemnitz, Riane Stene, Winfried Petry, Florian Kraus
presented at the European Research Reactor Conference (RRFM), 2019, Swemieh, Jordan

Reductive Photo-Chemical Separation of the Hexafluorides of Uranium and Molybdenum
Riane E. Stene, Tobias Chemnitz, Winfried Petry, Florian Kraus, to be published

References

[1] IAEA, Nuclear Technology Review 2010. GC(54)/INF/3, Wien, 2010.

[2] Deutsche Gesellschaft für Nuklearmedizin e.V., Der Radionuklidengpass: Ursachen und Lehren, Göttingen, 2009.

[3] C.o.M.I.P.W.H.E. Uranium, N.a.R.S. Board, D.o.E.a.L. Studies, N.R. Council, Medical Isotope Production Without Highly Enriched Uranium, National Academies Press, 2009.

[4] H.L. Deubner, Nuklearmedizinische Diagnoseverfahren am Beispiel der Szintigraphie.

[5] B. Sattler, T. Scholz, T. Philipp, B. Habermann, Physik und Technik der Nuklearmedizin: Studienbrief MPT0009, Kaiserslautern, 2018.

[6] M.u. Hassan, H.J. Ryu, Radioactive Waste Issues Related to Production of Fission-based ^{99}Mo by using Low Enriched Uranium (LEU), J. of Nucl. Fuel Cycle and waste Technol. 13 (2015) 155–161. https://doi.org/10.7733/jnfcwt.2015.13.2.155.

[7] I. Zolle, Technetium-99m Pharmaceuticals: Preparation and Quality Control in Nuclear Medicine, first. Aufl., Springer-Verlag, s.l., 2007.

[8] F.J. Wackers, D.S. Berman, J. Maddahi, D.D. Watson, G.A. Beller, H.W. Strauss, C.A. Boucher, M. Picard, B.L. Holman, R. Fridrich, Technetium-99m hexakis 2-methoxyisobutyl isonitrile: human biodistribution, dosimetry, safety, and preliminary comparison to thallium-201 for myocardial perfusion imaging, J. Nucl. Med. 30 (1989) 301–311.

[9] OECD/NEA, The Supply of Medical Isotopes: An Economic Diagnosis and Possible Solutions, OECD, Paris, 2019.

[10] D.I. Hamilton, P.J. Riley, Diagnostic Nuclear Medicine: A Physics Perspective, Springer Berlin / Heidelberg, Berlin, Heidelberg, 2013.

[11] F. Kraus, Picture of Mo-99/Tc-99 Generator. personally taken picture.

[12] C.H. Green, Technetium-99m production issues in the United Kingdom, J. Med. Phys. 37 (2012) 66–71. https://doi.org/10.4103/0971-6203.94740.

[13] GE Healthcare, Package leaflet: Information for the user: Drytec 2.5-100 GBq radionuclide generator.

[14] The National Academies of Sciences, Engineering, Medicine, Molybdenum-99 for Medical Imaging, Washington, DC, 2016.

[15] NEA/SEN/HLGMR, The Supply of Medical Radioisotopes: The Path to Reliability, 2011.

[16] NEA/SEN/HLGMR, The Supply of Medical Radioisotopes: 2019 Medical Isotope Demand and Capacity Projection for the 2019-2024 Period, 2019.

[17] E. Bradley, Non-HEU production technologies for molybdenum-99 and technetium-99m, International Atomic Energy Agency, Vienna, 2013.

[18] NEA/SEN/HLGMR, The Supply of Medical Radioisotopes: Market Impacts of Converting to Low-enriched Uranium Targets for Medical Isotope Production, 2012.

[19] S.-K. Lee, G.J. Beyer, J.S. Lee, Development of Industrial-Scale Fission ^{99}Mo Production Process Using Low Enriched Uranium Target, Nuclear Engineering and Technology 48 (2016) 613–623. https://doi.org/10.1016/j.net.2016.04.006.

[20] S.A. Ali, H.J. Ache, Production Techniques of Fission Molybdenum-99, Radiochimica Acta 41 (1987). https://doi.org/10.1524/ract.1987.41.23.65.

[21] IAEA, Management of radioactive waste from ^{99}Mo production. IAEA-TECDOC-1051, Wien, 1998.

[22] C.K. Sivaramakrishnan, A.V. Jadhav, Preparation of High Purity Fission Produced Molybdenum-99, Bombay, 1976.

[23] IAEA, Feasibility of Producing Molybdenum-99 on a Small Scale Using Fission of Low Enriched Uranium or Neutron Activation of Natural Molybdenum, IAEA, Vienna, 2015.

[24] J. Snelgrove, Qualifications Status of 6-gU/cm^3 U_3Si_2 Dispersion Targets for ^{99}Mo Production, 2011.

[25] M. Giourges, Mo-99 Bestrahlungsanlage: Erläuterungsbericht für die Errichtung und den Betrieb, 2015.

[26] Construction of the Mo-99 irradiation facility - TUM FRMII, 2020. https://www.frm2.tum.de/en/mo-99/construction-of-the-mo-99-irradiation-facility/ (accessed 4 May 2020).

[27] B. Ponsard, The new BR2 Reactor: Perspectives for Radioisotope Production, Mechelen, 2017.

[28] C. Reiter, Serpent 2: FRM II core model, München, 2016.

[29] T. Hollmer, Development of a PVD-based manufacturing process of monolithic LEU irradiation targets for ^{99}Mo production. Dissertation, Technische Universität München, 2015.

[30] J. Leppänen, M. Pusa, T. Viitanen, V. Valtavirta, T. Kaltiaisenaho, The Serpent Monte Carlo Code: Status, Development and Applications in 2013, in: SNA + MC 2013 - Joint International Conference on Supercomputing in Nuclear Applications + Monte Carlo, Paris, France, EDP Sciences, Les Ulis, France, October 27-31, 2013, p. 6021.

[31] C. Reiter, Serpent 2: Burnup calculations for ^{99}Mo, München, 2017.

[32] T. Hollmer, W. Petry, A novel monolithic LEU foil target based on a PVD manufacturing process for ^{99}Mo production via fission, Applied Radiation and Isotopes 118 (2016) 290–296.

[33] A. Röhrmoser, Isotope-Vector. E-Mail, Garching, 2014.

[34] D.R. Lide (Ed.), CRC handbook of chemistry and physics: A ready-reference book of chemical and physical data, 84th ed., CRC Press, Boca Raton, 2003.

[35] C. Reiter, Serpent 2: Activity calculations for ^{99}Mo LEU and HEU targets, 2020.

[36] J. Schmedt auf der Günne, M. Mangstl, F. Kraus, Elementares Fluor F_2 in der Natur - In-situ-Nachweis und Quantifizierung durch NMR-Spektroskopie, Angew. Chem. 124 (2012) 7968–7971. https://doi.org/10.1002/ange.201203515.
[37] Universitätsklinikum Jena, Flusssäureverätzung und Kontakt: Arbeitsanweisung, Jena, 2018.
[38] National Academies Press (US), Acute Exposure Guideline Levels for Selected Airborne Chemicals: Volume 4, Washington (DC), 2004.
[39] F. Kraus, Periodic Table for DFG Grant. Microsoft Word file, 2016.
[40] E. Capelli, R.J.M. Konings, Thermodynamic assessment of the niobium-fluorine system by coupling density functional theory and CALPHAD approach, Journal of Fluorine Chemistry 208 (2018) 55–64. https://doi.org/10.1016/j.jfluchem.2018.01.011.
[41] M.J. Molski, K. Seppelt, The transition metal hexafluorides, Dalton Trans. (2009) 3379–3383. https://doi.org/10.1039/b821121c.
[42] N. Bartlett, The Oxidizing Properties of the Third Transition Series Hexafluorides and Related Compounds, Angew. Chem. Int. Ed. Engl. 7 (1968) 433–439. https://doi.org/10.1002/anie.196804331.
[43] W.M. Haynes, CRC Handbook of Chemistry and Physics, 95th Edition, ninthfifthth ed., CRC Press, Hoboken, 2015.
[44] R. Craciun, D. Picone, R.T. Long, S. Li, D.A. Dixon, K.A. Peterson, K.O. Christe, Third row transition metal hexafluorides, extraordinary oxidizers, and Lewis acids: electron affinities, fluoride affinities, and heats of formation of WF_6, ReF_6, OsF_6, IrF_6, PtF_6, and AuF_6, Inorg. Chem. 49 (2010) 1056–1070. https://doi.org/10.1021/ic901967h.
[45] R. Craciun, R.T. Long, D.A. Dixon, K.O. Christe, Electron affinities, fluoride affinities, and heats of formation of the second row transition metal hexafluorides: MF(6) (M = Mo, Tc, Ru, Rh, Pd, Ag), J. Phys. Chem. A 114 (2010) 7571–7582. https://doi.org/10.1021/jp1022949.
[46] R.N. Compton, On the formation of positive and negative ions in gaseous UF_6, J. Chem. Phys. 66 (1977) 4478–4485. https://doi.org/10.1063/1.433699.
[47] B.L. Moiseiwitsch, On the Electron Affinities of Atomic Fluorine, Oxygen and Lithium, Proc. Phys. Soc. A 67 (1954) 25–32. https://doi.org/10.1088/0370-1298/67/1/305.
[48] NASA - JPL, GUIDELINE NO. GD-ED-2206: Selection of compatible Materials for Use with Fluorine.
[49] M. Woite GmbH, 1.4401, Erkrath, 2005.
[50] M. Woite GmbH, 1.4404, Erkrath, 2005.
[51] C.P. Dillon, Alloy selection for service in hydrogen fluoride, hydrofluoric acid and fluorine: A guide to the use of nickel-containing alloys, 2019.
[52] K. Hauffe, Gegen Fluor und Fluorwasserstoff korrosionsbeständige Werkstoffe, Mat.-wiss. u. Werkstofftech. 15 (1984) 427–435. https://doi.org/10.1002/mawe.19840151206.

[53] M. Woite GmbH, 2.4360, Erkrath, 2005.
[54] D.J. McAdam, R.W. Mebs, Report No. 696: Tensile Elastic Properties of Typical Stainless Steels and Nonferrous Metals as affected by Plastic Deformation and by Heat Treatment, 1940.
[55] DuPont Fluoroproducts, Teflon PTFE: Properties Handbook, Wilmington, 1996.
[56] C.C. Ibeh, Thermoplastic materials: Properties, manufacturing methods, and applications, CRC Press, Boca Raton, Fla., 2011.
[57] Du Pont, Teflon FEP fluoropolymer resin: Product and Properties Handbook, Wilmington.
[58] H. Domininghaus, Die Kunststoffe und ihre Eigenschaften, fifth., völlig neu bearb. und erw. Auflage, Springer Berlin Heidelberg, Berlin, Heidelberg, 1998.
[59] Material: Bariumfluorid (BaF_2) - Korth Kristalle GmbH, 2020.000Z. https://www.korth.de/index.php/material-detailansicht/items/9.html (accessed 22 June 2020).
[60] Material: Saphir (Al_2O_3) - Korth Kristalle GmbH, 2020.000Z. https://www.korth.de/index.php/material-detailansicht/items/5.html (accessed 22 June 2020).
[61] A.A. Luginina, A.E. Baranchikov, A.I. Popov, P.P. Fedorov, Preparation of barium monohydrofluoride $BaF_2 \cdot HF$ from nitrate aqueous solutions, Materials Research Bulletin 49 (2014) 199–205. https://doi.org/10.1016/j.materresbull.2013.08.074.
[62] J.R. Ferraro, C.W. Brown, K. Nakamoto, Introductory Raman spectroscopy, second ed., Academic Press, Amsterdam, Boston, 2003.
[63] I.R. McNab, Rotational Spectroscopy, Theory, in: J.C. Lindon, G.E. Tranter, J.L. Holmes (Eds.), Encyclopedia of spectroscopy and spectrometry, Academic Press, San Diego, CA, 2000, pp. 2017–2028.
[64] H. Günzler, H.-U. Gremlich, IR-Spektroskopie, Wiley-VCH Verlag GmbH & Co. KGaA, Weinheim, Germany, 2003.
[65] W. Demtröder, Atoms, Molecules and Photons, Springer Berlin Heidelberg, Berlin, Heidelberg, 2018.
[66] M. Bradley, Curve Fitting in Raman and IR Spectroscopy: Basic Theroy of Line Shapes and Applications, Madison, WI, 2007.
[67] N.W. Ashcroft, N.D. Mermin, Festkörperphysik, fourth., verb. Aufl., Oldenbourg, München, 2013.
[68] R. Gross, A. Marx, Festkörperphysik, thirdrd ed., De Gruyter Inc, Berlin/Boston, 2018.
[69] STOE & Cie GmbH, STADI MP: Brochure.
[70] Soorya N Kabekkodu, Powder Diffraction File: Recent Developments in Quality Control.

[71] X-ray Diffraction Shared Experimental Facility, Abridged Guide to Retrieving Reference Patterns and other Uses of Jade for XRPD Analysis, Cambridge.
[72] M.F. Vitha, Spectroscopy: Principles and instrumentation, Wiley, Hoboken, 2018.
[73] Analytik Jena AG, Grundlagen: Instrumentation und Techniken der UV VIS Spektroskopie, Jena.
[74] Analytik Jena AG, SPECORD PLUS: UV VIS Spectrophotometer. Betriebsanleitung, Jena, 2013.
[75] T. Hecht, Physikalische Grundlagen der IR-Spektroskopie: Von mechanischen Schwingungen zur Vorhersage und Interpretation von IR-Spektren, firstst ed. twentiethnineteenth, Springer Fachmedien Wiesbaden; Springer Spektrum, Wiesbaden, 2019.
[76] T. Hasegawa, Quantitative Infrared Spectroscopy for Understanding of a Condensed Matter, Springer Japan, Tokyo, 2017.
[77] Profactor, InfraRed: Bruker Tensor 37.
[78] Bruker Optik GmbH, TENSOR: Benutzerhandbuch, Ettlingen, 2011.
[79] P.F. Kane, G.B. Larrabee, Characterization of Solid Surfaces, Springer US, Boston, MA, 1974.
[80] P.J. Larkin, Infrared and Raman spectroscopy: Principles and spectral interpretation, first. Aufl., Elsevier professional, 2011.
[81] SyntPot, ALPHA II Wine Analyzer, 2020.000Z. https://syntpot.ee/product/alpha-ii-wine-analyzer/ (accessed 22 June 2020).
[82] D.N. Sathyanarayana, Vibrational spectroscopy: Theory and applications, New Age International, New Delhi, 2004.
[83] E. Smith, G. Dent, Modern Raman Spectroscopy - A Practical Approach, John Wiley & Sons, Ltd, Chichester, UK, 2004.
[84] Spectroscopy & Imaging GmbH, MonoVista CRS+, 2020.000Z. http://www.s-and-i.eu/index.php/products/monovista-crs (accessed 6 June 2020).
[85] W.-D. Herzog, M. Messerschmidt, NMR-Spektroskopie für Anwender, VCH, Weinheim, 1995.
[86] O. Zerbe, S. Jurt, Applied NMR Spectroscopy for Chemists and Life Scientists, John Wiley & Sons, Incorporated, Weinheim, Germany, 2014.
[87] J. Keeler, Understanding NMR spectroscopy, Wiley, Chichester, 2009.
[88] T. James, Nuclear magnetic Resonance in biochemistry, Elsevier Science, Burlington, 2012.
[89] L. Lajunen, Spectrochemical Analysis by Atomic Absorption and Emission, Royal Society of Chemistry, Cambridge, 2007.
[90] I. Agilent Technologies, Microwave Plasma Atomic Emission Spectroscopy (MP-AES): Application eHandbook, 2016.

[91] I. Agilent Technologies, Agilent 4200 Mikrowellenplasma-Atomemissionsspektrometer: Es liegt was in der Luft, 2015.
[92] A.A. Fridman, Plasma chemistry, Cambridge Univ. Press, Cambridge, 2008.
[93] W. Tsang, J.T. Herron, Kinetics and thermodynamics of the reaction $SF_6 \rightleftarrows SF_5 + F$, J. Chem. Phys. 96 (1992) 4272–4282. https://doi.org/10.1063/1.462821.
[94] Intergovernmental Panel on Climate Change, Climate Change 2013 - The Physical Science Basis, Cambridge University Press, Cambridge, 2014.
[95] Atmospheric chemistry, emissions, & lithosphere, first. ed., 2006.
[96] Nitrogen trifluoride, 2017. https://encyclopedia.airliquide.com/nitrogen-trifluoride (accessed 10 April 2017).
[97] Crystran Ltd, The Design of Pressure Windows, Dorset, 2014.
[98] Leybold GmbH, CERAVAC CTR 100 N | Leybold, 2020. https://www.leyboldproducts.de/produkte/vakuum-mess-und-analysegeraete/druckmessung-und-anzeigegeraete/aktive-sensoren/ceravac-transmitter/transmitter/1806/ceravac-ctr-100-n (accessed 3 May 2020).
[99] Thyracont Vacuum Instruments GmbH, VSC43MV Vacuum Transducer: Operating Instructions, 2019.
[100] A.E. Kubba, A. Hasson, A.I. Kubba, G. Hall, A micro-capacitive pressure sensor design and modelling, J. Sens. Sens. Syst. 5 (2016) 95–112. https://doi.org/10.5194/jsss-5-95-2016.
[101] Swagelok Company, PGI-40M-LG1.6-LASX, 2020. https://www.swagelok.ru/en/catalog/Product/Detail?part=PGI-40M-LG1.6-LASX (accessed 3 May 2020).
[102] Encyclopaedia Britannica, Bourdon-tube gauge. https://www.britannica.com/technology/Bourdon-tube-gauge#/media/1/75797/7008 (accessed 3 May 2020).
[103] Swagelok Company, LD16 Series Diaphragm Valves: Service Instructions, 2002.
[104] Swagelok Company, Bellows-Sealed Valves: H and HK Series, 2019.
[105] A.F. Holleman, E. Wiberg, N. Wiberg, Lehrbuch der anorganischen Chemie, tenthfirst., verb. u. stark erw. Aufl. / von Nils Wiberg, de Gruyter, Berlin u.a., 1995.
[106] R.F. Krause, T.B. Douglas, The melting temperature, vapor density, and vapor pressure of molybdenum pentafluoride, The Journal of Chemical Thermodynamics 9 (1977) 1149–1163. https://doi.org/10.1016/0021-9614(77)90116-1.
[107] H. Jehn, W. Kurtz, D. Schneider, U. Trobisch, J. Wagner, Molybdenum and Fluorine, in: H. Katscher, W. Kurtz, F. Schröder (Eds.), Mo Molybdenum, Springer Berlin Heidelberg, Berlin, Heidelberg, s.l., 1989, pp. 67–243.

[108] D.E. LaValle, R.M. Steele, M.K. Wilkinson, H.L. Yakel, The Preparation and Crystal Structure of Molybdenum (III) Fluoride, J. Am. Chem. Soc. 82 (1960) 2433–2434. https://doi.org/10.1021/ja01495a010.

[109] R.D. Peacock, Proceedings of the Chemical Society: February 1957, Proc. Chem. Soc. (1957) 33. https://doi.org/10.1039/ps9570000033.

[110] R.E. Stene, B. Scheibe, C. Pietzonka, A.J. Karttunen, W. Petry, F. Kraus, MoF_5 revisited. A comprehensive study of MoF_5, Journal of Fluorine Chemistry 211 (2018) 171–179. https://doi.org/10.1016/j.jfluchem.2018.05.002.

[111] A.J. Edwards, R.D. Peacock, R.W.H. Small, The preparation and structure of molybdenum pentafluoride, J. Chem. Soc. (1962) 4486. https://doi.org/10.1039/jr9620004486.

[112] N.I. Giricheva, O.G. Krasnova, G.V. Girichev, Simultaneous electron diffraction and mass-spectrometric study of the structure of the MoF_5 molecule, J Struct Chem 38 (1997) 54–61. https://doi.org/10.1007/BF02768807.

[113] K. Seppelt, Molecular Hexafluorides, Chem. Rev. 115 (2015) 1296–1306. https://doi.org/10.1021/cr5001783.

[114] G.H. Cady, G.B. Hargreaves, 305. The vapour pressures of some heavy transition-metal hexafluorides, J. Chem. Soc. (1961) 1563. https://doi.org/10.1039/jr9610001563.

[115] T.G. Burke, D.F. Smith, A.H. Nielsen, The Molecular Structure of MoF_6, WF_6, and UF_6 from Infrared and Raman Spectra, The Journal of Chemical Physics 20 (1952) 447–454. https://doi.org/10.1063/1.1700440.

[116] H.H. Claassen, G.L. Goodman, J.H. Holloway, H. Selig, Raman Spectra of MoF_6, TcF_6, ReF_6, UF_6, SF_6, SeF_6, and TeF_6 in the Vapor State, The Journal of Chemical Physics 53 (1970) 341–348. https://doi.org/10.1063/1.1673786.

[117] K. Seppelt, Molecular Hexafluorides, Chem. Rev. 115 (2015) 1296–1306. https://doi.org/10.1021/cr5001783.

[118] L. Gmelin, R.J. Meyer, E.H.E. Pietsch, E. Fluck, Gmelins Handbuch der anorganischen Chemie: Uran - Ergänzungsband C 8. Verbindungen mit Fluor, eighth. ed., Verl. Chemie, Berlin, 1980.

[119] R.W.M. D'Eye, F.S. Martin, 349. The barium fluoride–uranium trifluoride system, J. Chem. Soc. 0 (1957) 1847–1851. https://doi.org/10.1039/JR9570001847.

[120] A.S. Wolf, J.C. Posey, K.E. Rapp, α-Uranium Pentafluoride: I. Characterization, Inorg. Chem. 4 (1965) 751–754. https://doi.org/10.1021/ic50027a034.

[121] B. Scheibe, J. Bruns, G. Heymann, M. Sachs, A.J. Karttunen, C. Pietzonka, S.I. Ivlev, H. Huppertz, F. Kraus, UF_4 and the High-Pressure Polymorph HP-UF_4, Chemistry 25 (2019) 7366–7374. https://doi.org/10.1002/chem.201900639.

[122] U.S. Department of Energy, Depleted Uranium Hexafluoride Management Plan, Oak Ridge National Lab, 2001.

[123] G. Brauer, Handbuch der Präparativen Anorganischen Chemie, third., umgearb. Aufl., Ferdinand Enke Verlag, Stuttgart, 1978.

[124] J.C. Taylor, A.B. Waugh, Neutron diffraction study of β-uranium pentafluoride between 77 and 403 K, Journal of Solid State Chemistry 35 (1980) 137–140. https://doi.org/10.1016/0022-4596(80)90485-5.

[125] C.B. Amphlett, L.W. Mullinger, L.F. Thomas, Some physical properties of uranium hexafluoride, Trans. Faraday Soc. 44 (1948) 927. https://doi.org/10.1039/tf9484400927.

[126] D.R. Llewellyn, Some Physical Properties of Uranium Hexafluoride, J. Chem. Soc. (1953) 28. https://doi.org/10.1039/jr9530000028.

[127] G.D. Oliver, H.T. Milton, J.W. Grisard, The Vapor Pressure and Critical Constants of Uranium Hexafluoride, J. Am. Chem. Soc. 75 (1953) 2827–2829. https://doi.org/10.1021/ja01108a011.

[128] C. Steyer, Plasma- und festkörperphysikalische Optimierung eines Beschichtungsverfahrens für monolithische UMo-Kernbrennstoffe. Dissertation, München, 2019.

[129] H.M. Feder, C.L. Rosen, N.R. Chellew, Interaction of uranium and its alloys with ceramic oxides, Chicago, 1957.

[130] G. Meyer, L.R. Morss (Eds.), Synthesis of Lanthanide and Actinide Compounds, Springer, Dordrecht, 1991.

[131] W.B. Lewis, L.B. Asprey, L.H. Jones, R.S. McDowell, S.W. Rabideau, A.H. Zeltmann, R.T. Paine, Electronic and vibronic states of uranium hexafluoride in the gas and in the solid phase at very low temperatures, J. Chem. Phys. 65 (1976) 2707–2714. https://doi.org/10.1063/1.433414.

[132] R.S. McDowell, Vibrational spectrum and force field of uranium hexafluoride, J. Chem. Phys. 61 (1974) 3571. https://doi.org/10.1063/1.1682537.

[133] K. Seppelt, Kovalente Uranverbindungen des Typs $F_xU(OTeF_5)_{6-x}$, Chem. Ber. 109 (1976) 1046–1052. https://doi.org/10.1002/cber.19761090325.

[134] I. Ursu, D.E. Demco, M. Bogdan, P. Fitori, A. Darabont, Indirect NMR detection of ^{235}U in gaseous uranium hexafluoride, J. Phyique Lett. 46 (1985) 493–497. https://doi.org/10.1051/jphyslet:019850046011049300.

[135] P.W. Wilson, Preparation of uranium oxide tetrafluoride, J. Chem. Soc., Chem. Commun. (1972) 1241. https://doi.org/10.1039/c39720001241.

[136] O. Glemser, G. Lutz, Über Molybdänblau, Z. Anorg. Allg. Chem. (Zeitschrift für anorganische und allgemeine Chemie) 264 (1951) 17–33. https://doi.org/10.1002/zaac.19512640104.

[137] L.E. TREVORROW, M.J. STEINDLER, D.V. STEIDL, J.T. SAVAGE, Condensed Phase Equilibria in the Molybdenum Hexafluoride-Uranium Hexafluoride System, in:

P.R. Fields, T. Moeller (Eds.), Lanthanide-Actinide Chemistry, AMERICAN CHEMICAL SOCIETY, Washington, Jan. 1967, pp. 308–319.

[138] Air Liquide, Carbon monoxide: Physical Properties, 2018. https://encyclopedia.airliquide.com/carbon-monoxide (accessed 5 June 2020).

[139] G.W. Halstead, P. Gary Eller, R.T. Paine, 35. Uranium(V) Fluorides and Alkoxides, in: J.P. Fackler (Ed.), Inorganic syntheses: Volume 21, Wiley, New York, 1982, pp. 162–167.

[140] E. Borsella, F. Catoni, G. Freddi, Study of UF_6 photodissociation through light scattering of UF_5 particles, J. Chem. Phys. 73 (1980) 316–321. https://doi.org/10.1063/1.439877.

[141] E.L. Pace, M.A. Reno, Thermodynamic Properties of Carbonyl Fluoride from 12°K to Its Boiling Point. The Entropy from Molecular and Spectroscopic Data, J. Chem. Phys. 48 (1968) 1231–1235. https://doi.org/10.1063/1.1668786.

[142] R.E. Stene, Development of Dry and Non-Aqueous Techniques for the Separation of Molybdenum from Uranium and Investigations of Group Six Metal Fluoride and Oxyfluoride Chemistry. Dissertation, München, 2020.

[143] E. Cardoso, Contribution à l'étude du point critique de quelques gaz difficilement liquéfiables azote, oxyde de carbone, oxygène, méthane, J. Chim. Phys. 13 (1915) 312–356. https://doi.org/10.1051/jcp/1915130312.

[144] E.L. Pace, J.S. Mosser, Thermodynamic Properties of Silicon Tetrafluoride from 15°K to Its Triple Point. The Entropy from Molecular and Spectroscopic Data, J. Chem. Phys. 39 (1963) 154–158. https://doi.org/10.1063/1.1733993.

[145] J. Heicklen, V. Knight, The infrared spectrum of SiF_4, Spectrochimica Acta 20 (1964) 295–298. https://doi.org/10.1016/0371-1951(64)80026-6.

[146] National Institute of Standards and Technology, Silicon tetrafluoride, 2020. https://webbook.nist.gov/cgi/cbook.cgi?ID=C7783611&Type=IR-SPEC&Index=1 (accessed 26 February 2020).

[147] E. Riedel, C. Janiak, Anorganische Chemie, de Gruyter, 2007.

[148] J.H. Holloway, R.D. Peacock, Ruthenium pentafluoride and ruthenium oxytetrafluoride, J. Chem. Soc. (1963) 527. https://doi.org/10.1039/jr9630000527.

[149] S.A. Cotton, Chemistry of Precious Metals, first ed., Blackie Academic & Professional, London, 1997.

[150] W.J. Casteel, A.P. Wilkinson, H. Borrmann, R.E. Serfass, N. Bartlett, Preparation and structure of ruthenium tetrafluoride and a structural comparison with ruthenium trifluoride and ruthenium pentafluoride, Inorg. Chem. 31 (1992) 3124–3131. https://doi.org/10.1021/ic00040a024.

[151] T. Sakurai, A. Takahashi, Behavior of ruthenium in fluoride-volatility processes: Conversions of $RuOF_4$, RuF_4, and RuF_5 into RuO_4, Journal of Inorganic and Nuclear Chemistry 41 (1979) 681–685. https://doi.org/10.1016/0022-1902(79)80354-1.

[152] H.H. Claassen, H. Selig, J.G. Malm, C.L. Chernick, B. Weinstock, Ruthenium Hexafluoride, J. Am. Chem. Soc. 83 (1961) 2390–2391. https://doi.org/10.1021/ja01471a039.

[153] V.B. Sokolov, V.G. Tsinoev, A.V. Ryzhkov, Mössbauer effect and the vibrational spectra of AuF_5 and $KrF_2 \cdot AuF_5$, Theor Exp Chem 16 (1981) 270–274. https://doi.org/10.1007/BF00517277.

[154] P.R. Rao, A. Tressaud, N. Bartlett, The tetrafluorides of iridium, rhodium and palladium, Journal of Inorganic and Nuclear Chemistry 28 (1976) 23–28. https://doi.org/10.1016/0022-1902(76)80588-X.

[155] A.V. Dzhalavyan, E.G. Rakov, A.S. Dudin, Platinum Metal Fluorides, Russ. Chem. Rev. 52 (1983) 960–972. https://doi.org/10.1070/RC1983v052n10ABEH002908.

[156] A.G. Sharpe, Simple and complex fluorides of some noble metals, J. Chem. Soc. (1950) 3444. https://doi.org/10.1039/jr9500003444.

[157] J.H. Holloway, P.R. Rao, N. Bartlett, Quinquevalent rhodium compounds: RhF_5 and $CsRhF_6$, Chem. Commun. (London) (1965) 306. https://doi.org/10.1039/c19650000306.

[158] C.L. Chernick, H.H. Claassen, B. Weinstock, Rhodium Hexafluoride, J. Am. Chem. Soc. 83 (1961) 3165–3166. https://doi.org/10.1021/ja01475a046.

[159] L. Svecova, N. Papaïconomou, I. Billard, Rh(III) Aqueous Speciation with Chloride as a Driver for Its Extraction by Phosphonium Based Ionic Liquids, Molecules 24 (2019). https://doi.org/10.3390/molecules24071391.

[160] N. Bartlett, P.R. Rao, New Fluorides of Palladium: Palladium(II) Hexafluoropalladate(IV) and Related Compounds and Palladium Tetrafluoride, Proceedings of the Chemical Society (1964) 393.

[161] M. Serafin, B.G. Müller, Komplexe Fluoride von Palladium(II) – eine kurze Übersicht, Z. Anorg. Allg. Chem. (Zeitschrift für anorganische und allgemeine Chemie) 633 (2007) 2523–2536. https://doi.org/10.1002/zaac.200700377.

[162] R.P. Rao, New flourides of the noble metals, University of British Columbia, 1965.

[163] O. Ruff, E. Ascher, Die Fluoride der VIII. Gruppe des periodischen Systems, Z. Anorg. Allg. Chem. 183 (1929) 193–213. https://doi.org/10.1002/zaac.19291830113.

[164] G. Aullón, S. Alvarez, On the existence of molecular palladium(VI) compounds: palladium hexafluoride, Inorg. Chem. 46 (2007) 2700–2703. https://doi.org/10.1021/ic0623819.

[165] H.F. PRIEST, W.C. SCHUMB, Tungsten fluorides and related compounds, J. Am. Chem. Soc. 70 (1948) 3378. https://doi.org/10.1021/ja01190a047.

[166] J.R. Creighton, Selectivity loss during tungsten chemical vapor deposition: The role of tungsten pentafluoride, Journal of Vacuum Science & Technology A: Vacuum, Surfaces, and Films 7 (1989) 621–624. https://doi.org/10.1116/1.575854.

[167] J.G. Black, D.J. Ehrlich, J.H.C. Sedlacek, A.D. Feinerman, H.H. Busta, Rapid low-resistance interconnects by selective tungsten deposition on laser-direct-written polysilicon, IEEE Electron Device Lett. 7 (1986) 422–424. https://doi.org/10.1109/EDL.1986.26423.

[168] J.G. Malm, H. Selig, The vapour-pressures and other properties of ReF_6 and ReF_7, Journal of Inorganic and Nuclear Chemistry 20 (1961) 189–197. https://doi.org/10.1016/0022-1902(61)80267-4.

[169] R.T. Paine, L.B. Asprey, Reductive syntheses of transition metal fluoride compounds. Synthesis of rhenium, osmium, and iridium pentafluorides and tetrafluorides, Inorg. Chem. 14 (1975) 1111–1113. https://doi.org/10.1021/ic50147a030.

[170] D.E. LaValle, R.M. Steele, W.T. Smith, Rhenium nitrogen fluoride and rhenium tetrafluoride, Journal of Inorganic and Nuclear Chemistry 28 (1966) 260–263. https://doi.org/10.1016/0022-1902(66)80256-7.

[171] E.G. Rakov, A.S. Dudin, A.A. Opalovskii, Rhenium Fluorides, Russ. Chem. Rev. 49 (1980) 958–967. https://doi.org/10.1070/RC1980v049n10ABEH002520.

[172] W.A. Sunder, F.A. Stevie, The synthesis and characterization of some oxide fluorides of rhenium and osmium, Journal of Fluorine Chemistry 6 (1975) 449–463. https://doi.org/10.1016/S0022-1139(00)81685-1.

[173] H.H. Claassen, H. Selig, J.G. Malm, Vibrational Spectra of MoF_6 and TcF_6, J. Chem. Phys. 36 (1962) 2888–2890. https://doi.org/10.1063/1.1732396.

[174] H.H. Claassen, E.L. Gasner, H. Selig, Vibrational Spectra of IF_7 and ReF_7, J. Chem. Phys. 49 (1968) 1803–1807. https://doi.org/10.1063/1.1670310.

[175] J.H. Holloway, H. Selig, H.H. Claassen, Vibrational Spectra of IOF_5, $OsOF_5$, and $ReOF_5$, J. Chem. Phys. 54 (1971) 4305–4311. https://doi.org/10.1063/1.1674677.

[176] I.S. Alekseichuk, V.V. Ugarov, V.B. Sokolov, N.G. Rambidi, An electron diffraction study of the structure of the $ReOF_5$ molecule in the gaseous phase, J Struct Chem 22 (1982) 795–796. https://doi.org/10.1007/BF00746454.

[177] N. Bartlett, S. Beaton, L.W. Reeves, E.J. Wells, ^{19}F N.M.R. Spectra of Heptavalent Fluorides and Oxide Pentafluorides, Can. J. Chem. 42 (1964) 2531–2540. https://doi.org/10.1139/v64-371.

[178] C. Rissom, Untersuchungen zur Abtrennung von Hexafluorosilicat aus Ätzbädern. Dissertation, Freiberg, 2013.

[179] O. Glemser, H.W. Roesky, K.-H. Hellberg, H.-U. Werther, Darstellung und Eigenschaften von Osmiumheptafluorid, Chem. Ber. 99 (1966) 2652–2662. https://doi.org/10.1002/cber.19660990834.

[180] H. Shorafa, K. Seppelt, Osmium(VII) fluorine compounds, Inorg. Chem. 45 (2006) 7929–7934. https://doi.org/10.1021/ic0608290.

[181] G.B. Hargreaves, R.D. Peacock, Two fluorides of osmium, J. Chem. Soc. (1960) 2618. https://doi.org/10.1039/jr9600002618.

[182] B. Weinstock, J.G. Malm, Osmium Hexafluoride and its Identity with the Previously Reported Octafluoride 1,2, J. Am. Chem. Soc. 80 (1958) 4466–4468. https://doi.org/10.1021/ja01550a007.

[183] W. Moffitt, G.L. Goodman, M. Fred, B. Weinstock, The colours of transition metal hexafluorides, Molecular Physics 2 (1959) 109–122. https://doi.org/10.1080/00268975900100101.

[184] B. Weinstock, H.H. Claassen, J.G. Malm, Vibrational Spectra of OsF_6 and PtF_6, J. Chem. Phys. 32 (1960) 181–185. https://doi.org/10.1063/1.1700895.

[185] K. Seppelt, N. Bartlett, Kernresonanzuntersuchungen an Hexafluoriden, Z. Anorg. Allg. Chem. 436 (1977) 122–126. https://doi.org/10.1002/zaac.19774360114.

[186] C.E. Housecroft, A.G. Sharpe, Inorganic chemistry, second ed., Prentice Hall, Harlow, 2006.

[187] N. Bartlett, P.R. Rao, Iridium pentafluoride, Chem. Commun. (London) (1965) 252. https://doi.org/10.1039/c19650000252.

[188] P.L. Robinson, G.J. Westland, The simple fluorides of iridium, including the new trifluoride, J. Chem. Soc. (1956) 4481. https://doi.org/10.1039/jr9560004481.

[189] H.J. Kandiner, Iridium, Achte völlig neu bearbeitete Auflage, Springer Berlin Heidelberg, Berlin, Heidelberg, 1971.

[190] O. Ruff, J. Fischer, Iridiumfluoride, Z. Anorg. Allg. Chem. 179 (1929) 161–185. https://doi.org/10.1002/zaac.19291790113.

[191] J.C.D. Brand, G.L. Goodman, B. Weinstock, The Optical Absorption of Iridium Hexafluoride, Journal of Molecular Spectroscopy 37 (1971) 464–485. https://doi.org/10.1016/0022-2852(71)90177-9.

[192] M. Rotger, V. Boudon, A.T. Nguyen, D. Avignant, Spontaneous Raman Scattering Spectrum of Gaseous IrF_6 in the Ground Electronic State, J. Raman Spectrosc. 27 (1996) 145–148. https://doi.org/10.1002/(SICI)1097-4555(199602)27:2<145:AID-JRS938>3.0.CO;2-2.

[193] N. Bartlett, D.H. Lohmann, 124. Fluorides of the noble metals. Part III. The fluorides of platinum, J. Chem. Soc. (1964) 619. https://doi.org/10.1039/jr9640000619.

[194] O. Ruff, Über die Fluoride der Edelmetalle, Ber. Dtsch. Chem. Ges. 46 (1913) 920–929. https://doi.org/10.1002/cber.191304601120.

[195] N. Bartlett, Xenon Hexafluoroplatinate(V) $Xe^{+}[PtF_6]^{-}$, Proceedings of the Chemical Society (1962) 218. https://doi.org/10.1039/ps9620000197.

[196] L. Graham, Concerning the nature of $XePtF_6$, Coordination Chemistry Reviews 197 (2000) 321–334. https://doi.org/10.1016/S0010-8545(99)00190-3.

[197] M.V. Korobov, V.V. Nikulin, N.S. Chilingarov, L.N. Sidorov, Enthalpy of formation of platinum hexafluoride, The Journal of Chemical Thermodynamics 18 (1986) 235–240. https://doi.org/10.1016/0021-9614(86)90051-0.

[198] B. Weinstock, J.G. Malm, E.E. Weaver, The Preparation and Some Properties of Platinum Hexafluoride, J. Am. Chem. Soc. 83 (1961) 4310–4317. https://doi.org/10.1021/ja01482a002.

[199] N.S. Chilingarov, A.Y. Borschevsky, B.V. Romanovsky, L.N. Sidorov, Remote Fluorination by Spillover of Atomic Fluorine, J. Phys. Chem. C 122 (2018) 26372–26377. https://doi.org/10.1021/acs.jpcc.8b05464.

[200] STOE & Cie GmbH, WinXPOW: Powder Diffraction Software, Darmstadt, 2015.

[201] D.H. Lohmann, The fluorides of platinum and related compounds, University of British Columbia, 1961.

[202] L. Wöhler, Die Oxyde des Platins, Z. Anorg. Chem. 40 (1904) 423–464. https://doi.org/10.1002/zaac.19040400126.

[203] R.S. Clarke, T.P. Perros, The Fluoroplatinates: II. Fluoroplatinic Acid, J. Am. Chem. Soc. 75 (1953) 5734–5735. https://doi.org/10.1021/ja01118a506.

[204] E. Pietsch (Ed.), Tellur, Springer Berlin Heidelberg, Berlin, Heidelberg, s.l., 1969.

[205] R. Campbell, P.L. Robinson, 668. The fluorination of tellurium. Ditellurium decafluoride and tellurium oxyfluorides, J. Chem. Soc. (1956) 3454. https://doi.org/10.1039/jr9560003454.

[206] P.M. Watkins, Ditellurium decafluoride- A continuing myth, J. Chem. Educ. 51 (1974) 520. https://doi.org/10.1021/ed051p520.

[207] J.H. Junkins, H.A. Bernhardt, E.J. Barber, Preparation and Properties of Tellurium Tetrafluoride, J. Am. Chem. Soc. 74 (1952) 5749–5751. https://doi.org/10.1021/ja01142a052.

[208] R.S. McDowell, R.F. Holland, W.H. McCulla, Infrared Spectroscopy of TeF_6, Journal of Molecular Structure 145 (1986) 243–256. https://doi.org/10.1016/0022-2860(86)85028-1.

[209] J. Serp, M. Allibert, O. Beneš, S. Delpech, O. Feynberg, V. Ghetta, D. Heuer, D. Holcomb, V. Ignatiev, J.L. Kloosterman, L. Luzzi, E. Merle-Lucotte, J. Uhlíř, R. Yoshioka, D. Zhimin, The molten salt reactor (MSR) in generation IV: Overview and perspectives, Progress in Nuclear Energy 77 (2014) 308–319. https://doi.org/10.1016/j.pnucene.2014.02.014.

[210] J.L. Hencher, G.W. King, Oxalyl halides, Journal of Molecular Spectroscopy 16 (1965) 168–178. https://doi.org/10.1016/0022-2852(65)90095-0.

Acknowledgement

At this point, I would like to thank all people, who made this thesis possible. My special gratitude goes to **Prof. Dr. Winfried Petry** for giving me the great possibility to earn my doctorate at this great research facility, for believing in my ideas and for providing me with both, the means and the freedom to develop this new system.

I would like to thank **Prof. Dr. Florian Kraus** for the outstanding mentorship during my thesis. I would further like to thank him and his working group for all the effort and time they spent to introduce me to the topic of fluorine chemistry: **Dr. Matthias Conrad**, **Dr. Stefan Rudel**, **Jascha Bandemehr**, **Lars Deubner**, **Malte Sachs**, **Benjamin Scheibe**, **Riane Stene** and our secretary **Stella Maris Schenk**. I truly appreciate it and it was a pleasure being part of the Fluorine Chemistry Group of the Philipps-University Marburg. And my thanks would of course be utterly incomplete if I would forget the working group for Be chemistry at this point, **Dr. Magnus Buchner**, **Matthias Müller** and **Nils Spang**.

Many of the experiments could not have been performed without the necessary equipment. I therefore want to thank the entire team of the mechanical workshop of the Philipps-University Marburg under the direction of **Friedbert Bepperling** and **Stefan Staubitz** as well as **Daniel Bieker** and **Tarek Oehler** for coping with all my crazy ideas and crafting instruments of highest quality, thereby allowing the research performed.

Great thanks goes to **Dr. Christian Reiter** for performing the simulations with Serpent 2 and for off-topic talks during the coffee breaks. But I mostly thank him for not ignoring my calls, even in the late evening and at the weekend, if some random idea came to my mind, which I immediately had to share or if I had to get his opinion on my interpretations of data.

I would further like to thank **Dr. Christian Steyer and Bruno Baumeister** for countless discussions about ideas and concepts as well as valuable input on their implementation.

Finally, my special thanks go to the all people, who kept me motivated during the sometimes tensed up and challenging times, especially my parents **Frank** and **Beate Chemnitz** as well as my brother **Torsten Chemnitz**. Their moral support during the final weeks of writing helped me a great deal to finish this work. Mom, finally you are good to say: “I am the mother.”